**Title**

Transition Metal Confinement Effects on Catalysis in Two-dimensional Materials

**Permalink**

https://escholarship.org/uc/item/0mx5k595

**Author**

Younan, Sabrina Mary

**Publication Date**

2023

Peer reviewed|Thesis/dissertation

UNIVERSITY OF CALIFORNIA SAN DIEGO

SAN DIEGO STATE UNIVERSITY


Transition Metal Confinement Effects on Catalysis in Two-Dimensional Materials


A Dissertation submitted in partial satisfaction of the requirements
for the degree Doctor of Philosophy


in


Chemistry


by


Sabrina M. Younan


Committee in charge:

      University of California, San Diego

           Professor Clifford Kubiak
           Professor Kimberly Schurmeier

      San Diego State University

           Professor Jing Gu, Chair
           Professor Samuel Kassegne
           Professor Yong Yan


2023

The Dissertation of Sabrina M. Younan is approved, and it is acceptable in quality and form for publication on microfilm and electronically.

_____

_____

_____

_____

_____
Chair

University of California San Diego

San Diego State University

2023

EPIGRAPH

Atoms or elementary particles
Themselves are not real.
They form a world of possibilities
Rather than one of things or facts.

Werner Heisenberg


No great mind
Has ever existed
Without a touch
Of madness.

Aristotle

TABLE OF CONTENTS

# LIST OF FIGURES

# LIST OF TABLES

# LIST OF ABBREVIATIONS

| | |
|---|---|
| $\Delta$ | Crystal field splitting energy |
| $\Delta G_{H^*}$ | Free energy of $H^*$ adsorption |
| $\Delta G_{H_2O}$ | Free energy of $H_2O$ dissociation |
| $\eta$ | Overpotential |
| 1D | One-dimensional |
| 2D | Two-dimensional |
| 3D | Three-dimensional |
| AC-STEM | Aberration-corrected scanning transmission electron microscopy |
| $A_w$ | Warburg constant |
| Bpy | 2,2'-bipyridine |
| ADF | Annular dark field |
| Ag | Silver |
| CD | Circular dichroism |
| CFP | Carbon fiber paper |
| CISS | Chiral-induced spin selectivity |
| Co | Cobalt |
| CO | Carbonyl |
| $CO_2$ | Carbon dioxide |
| CNT | Carbon nanotube |
| CPE | Constant phase element |
| Cu | Copper |
| CV | Cyclic voltammetry |

| | |
|---|---|
| DI | Deionized |
| DFT | Density functional theory |
| ECSA | Electrochemically active surface area |
| EIS | Electrochemical impedance spectroscopy |
| EDX | Energy dispersive X-ray spectroscopy |
| EPR | Electron paramagnetic resonance spectroscopy |
| EXAFS | Extended X-ray absorption fine structure |
| Fe | Iron |
| FTIR | Fourier transform infrared spectroscopy |
| GO | Graphene oxide |
| $h$-BN | Hexagonal boronitride |
| $H^+$ | Protons |
| $H_2$ | Hydrogen |
| $H_2O$ | Water |
| HAADF | High-angle annular dark field imaging |
| HCl | Hydrochloric acid |
| HER | Hydrogen evolution reaction |
| HOMO | Highest occupied molecular orbital |
| $HNO_3$ | Nitric acid |
| HRTEM | High resolution transmission electron microscopy |
| HS | High spin |
| ICP-OES | Inductively coupled plasma optical emission spectroscopy |
| IPCE | Incident photon to current efficiency |

| | |
|---|---|
| IR | Infrared |
| LA | Longitudinal acoustic |
| LS | Low spin |
| LSV | Linear sweep voltammetry |
| LUMO | Lowest occupied molecular orbital |
| MACE | Metal-assisted chemical etching |
| Mn | Manganese |
| Mo | Molybdenum |
| MOF | Metal-organic framework |
| $MoO_3$ | Molybdenum trioxide |
| $MoS_2$ | Molybdenum disulfide |
| $N_2$ | Nitrogen |
| $-NH_2$ | Amine |
| Ni | Nickel |
| NRR | Nitrogen reduction reaction |
| NSC | N, S co-doped carbon |
| $O, O_2$ | Oxygen |
| PDOS | Partial density of states |
| PEC | Photoelectrochemistry |
| POM | Polyoxometalate |
| Pt | Platinum |
| $R_s$ | Electrolyte resistance |
| $R_{CT}$ | Charge transfer resistance |

| | |
|---|---|
| S | Sulfur |
| SAs | Single atoms |
| SACs | Single atom catalysts |
| Sc | Scandium |
| $ScCl_3$ | Scandium(III) chloride |
| Si | Silicon |
| SiNWs | Silicon nanowires |
| $SiO_x$ | Silicon oxide |
| $SO_4^{2-}$ | Sulfate ion |
| STEM | Scanning transmission electron microscopy |
| TA | Transverse acoustic |
| TMD | Transition metal dichalcogenide |
| TOF | Turnover frequency |
| TON | Turnover number |
| UV | Ultraviolet |
| UV-Vis | UV-Visible spectroscopy |
| XAS | X-ray absorption spectroscopy |
| XANES | X-ray absorption near edge structure |
| XPS | X-ray photoelectron spectroscopy |
| XRD | X-ray diffraction |
| Zn | Zinc |

# ACKNOWLEDGEMENTS

First and foremost, I would like to thank my advisor Jing Gu for her support and friendship throughout my graduate career. I appreciate not only the support, kindness, and confidence that she has provided me but also the freedom to pursue my own path in research that enabled me to become the independent scientist I am today.

Next, I would like to thank all of the members of the Gu lab since Fall 2017. To all of my undergraduate mentees, Michael Fairchild, Audrey Washington, Gabriella Trulson, Nini Demetrashvili, and Mariami Utiashvili: you all were a pleasure to mentor and I wouldn't be the scientist and mentor I am today if it weren't for you all. To Nicholas Williams, you were an amazing colleague and such an amazing support system. Thank you for always helping me when I needed it. To my best friend, Maggie Patrick: together we brought so much laughter and madness to the lab. I'm so grateful that grad school brought us together. Zhida Li, working by your side was an absolute pleasure. We accomplished so much together and I hope to visit you in China someday soon. Antonio Trammel, Honxing Kang, Gonto Johns, Jackie Johnson, and Chris Turciano: thank you for making my time in the Gu lab so memorable. I will miss you all dearly.

To Braden Silva, I am so lucky to have you in my life. Your love and support carried me through all the trials of graduate school and I am a better person with you by my side. You are a brilliant scientist. I love being able to bounce ideas off of you. You make me a better person and I appreciate you more than you'll ever know.

To my sister, Ariane Hussainy, thank you for pushing me through hard times, for calling me out on my nonsense, and for being the sister I never knew I needed. To Patrick Infante-Younan, you are the best brother in the world. You inspire me to be the best person I can be and I thank you so much for being my best friend. To my dear friend Ashley Nguyen, thank you for going through

all the steps of obtaining a Ph.D. with me. I couldn't have asked for a better person to experience grad school with. Cissle will miss you and her bestie Oliver.

To my fur babies, Odi and Cissle: mommy loves you more than you could ever know. Finally, I would like to thank my parents, Basim and Zean Younan, my Khalas, and my cousins for their love and support throughout my studies. It means the world to me and I appreciate you all so much.

Chapter 1 contains unpublished material introducing the research fields of interest that were pursued in this dissertation. The dissertation author was the primary author of this chapter.

Chapter 2, in full, is a reprint of the material as it appears in "Improving the Stability of Silicon Nanowires during Photoelectrochemical Hydrogen Generation with Zinc 1T-phase Molybdenum Disulfide." *Advanced Materials Interfaces* 2022, 2200178. Younan, S., Li, Z., Fairchild, M., Williams, N., Huang, Y., Gu, J. The dissertation author was the primary investigator and author of this paper.

Chapter 3, in full, is a reprint of the material as it appears in "Zinc Single Atom Confinement Effects on Catalysis in 1T-phase Molybdenum Disulfide." *ACS Nano* 2023, 17, 2, 1414-1426. Younan, S., Li, Z., Yan, X., He, D., Hu, W., Demetrashvili, N., Trulson, G., Washington, A., Xiao, X., Pan, X., Huang, J., Gu, J. The dissertation author was the primary investigator and author of this paper.

Part of Chapter 4 contains unpublished material describing the catalytic effects of confining Sc SAs near basal plane active sites in 1T-MoS$_2$. The portion of data in Chapter 4 discussing Zn SAs confined within 1T-MoS2 is a reprint of the material as it appears in "Zinc Single Atom Confinement Effects on Catalysis in 1T-phase Molybdenum Disulfide." *ACS Nano* 2023, 17, 2, 1414-1426. Younan, S., Li, Z., Yan, X., He, D., Hu, W., Demetrashvili, N., Trulson, G.,

Washington, A., Xiao, X., Pan, X., Huang, J., Gu, J. The dissertation author was the primary investigator and author of this paper and chapter.

Chapter 5, in part is currently being prepared for submission for publication of the material. The dissertation author was the primary researcher and author of this chapter.

Chapter 6 contains unpublished material describing future directions in this field. The dissertation author was the primary author of this chapter.

VITA

2018    Bachelor of Science in Chemistry, San Diego State University

2023    Doctor of Philosophy in Chemistry, University of California San Diego and San Diego State University

PUBLICATIONS

**Younan, S.**, Li, Z., Yan, X., He, D., Hu, W., Demetrashvili, N., Trulson, G., Washington, A., Xiao, X., Pan, X., Huang, J., Gu, J. "Zinc Single Atom Confinement Effects on Catalysis in 1T-phase Molybdenum Disulfide." *ACS Nano* 2023, 17, 2, 1414-1426. https://doi.org/10.1021/acsnano.2c09918

Capobianco, M., **Younan, S.**, Tayvah, U., Pattengale, B., Neu, J., Gu, J., Brudvig, G. "Terahertz Conductivity of Semiconducting 2H and Metallic 1T Phases of Molybdenum Disulfide." *Journal of Physical Chemistry Letters* 2022, 13, 8319-8326. https://doi.org/10.1021/acs.jpclett.2c02283

Li, Z., Yan, X., He, D., Hu, W., **Younan, S.**, Ke, Z., Patrick, M., Xiao, X., Huang, J, Wu, H., Pan, X., Gu, J. "Manipulating Coordination Structures of Mixed Valence Copper Single Atoms on 1T-$MoS_2$ for Efficient Hydrogen Evolution." *ACS Catalysis* 2022, 12, 13, 7686-7695. https://doi.org/10.1021/acscatal.2c00759

**Younan, S.**, Li, Z., Fairchild, M., Williams, N., Huang, Y., Gu, J. "Improving the Stability of Silicon Nanowires during Photoelectrochemical Hydrogen Generation with Zinc 1T-phase Molybdenum Disulfide." *Advanced Materials Interfaces* 2022, 2200178. https://doi.org/10.1002/admi.202200178

Ke, Z., Williams, N., Yan, X., **Younan, S.,** He, D., Song, X., Pan, X., Xiao, X., Gu, J. "Solar-Assisted Co-Electrolysis of Glycerol and Water for Concurrent Production of Formic Acid and Hydrogen." *Journal of Materials Chemistry A* 2021. https://doi.org/10.1039/d1ta02654b

Pattengale, B., Huang, Y., Yan, X., Yang, S., **Younan, S.,** Hu, W., Li, Z., Lee, S., Pan, X., Gu, J., Huang, J. "Dynamic evolution and reversibility of single-atom Ni(II) active site in 1T-$MoS_2$ electrocatalysts for hydrogen evolution." *Nature Communications* 11, 4114 (2020). https://doi.org/10.1038/s41467-020-17904-z

Li, Z., He, D., Yan, X., Dai, S., **Younan, S.**, Ke, Z., Pan, X., Xiao, X., Wu, H., and Gu, J. "Size-dependent Ni-based electrocatalysts for selective $CO_2$ reduction." *Angewandte Chemie International Edition* 10.1002/anie/202000318 (2020). https://doi.org/10.1002/anie/202000318

Yang, F., Aguiar, J. A., Fairchild, M., Vakki, W., **Younan, S.**, Zhou, Y., Zhou, L., and Gu, J. "Dual protection layer strategy to increase photoelectrode–catalyst interfacial stability: a case study on black silicon photoelectrodes." *Advanced Materials Interfaces* 6 (8), 1802085 (2019). https://doi.org/10.1002/admi.201802085

Huang, Y., Sun, Y., Zheng, X., Aoki, T., Pattengale, B., Huang, J., He, X., Bian, W., **Younan, S.**, Williams, N., Hu, J., Ge, J., Pu, N., Yan, X., Pan, X., Zhang, L., Wei, Y., and Gu, J. "Atomically engineering activation sites onto metallic 1T-MoS$_2$ catalysts for enhanced electrochemical hydrogen evolution." *Nature Communications* 10, 982 (2019). https://doi.org/10.1038/s41467-019-08877-9

ABSTRACT OF THE DISSERTATION

Transition Metal Confinement Effects on Catalysis in Two-dimensional Materials

by

Sabrina M. Younan

Doctor of Philosophy in Chemistry

University of California San Diego, 2023

San Diego State University, 2023

Professor Jing Gu, Chair

**Chapter 1.** This section introduces the research motivations driving the investigations pursued in this dissertation. Likewise, it discusses research fields of interest to the work conducted herein,

such as electrochemistry, Photoelectrochemistry, $H_2$ generation, semiconductors, 2D nanomaterials, and confinement catalysis.

**Chapter 2.** Oxide growth on the surface of semiconductors during device operation induces charge carrier recombination and photodegradation, which limit the operation lifetime of photoelectrochemical devices. Likewise, their commercialization is hindered by the use of expensive precious metal catalysts to enhance hydrogen evolution kinetics. This work demonstrates how drop casting Zn 1T-$MoS_2$ onto SiNWs generates an interface that overcomes these challenges.

**Chapter 3.** Active sites are atomic sites within catalysts that drive reactions and are essential to catalysis. Spatially confining guest metals within active site microenvironments has been predicted to improve catalytic activity by altering the electronic states of active sites. Using HER as the model reaction, we show that intercalating Zn SAs into 1T-$MoS_2$ enhances HER performance by decreasing the overpotential, charge transfer resistance, and the kinetic barrier.

**Chapter 4.** SACs have the ability to enhance reaction kinetics and the activity, stability, and selectivity of catalysts. Yet, investigations of the aspects of the SA that induce such desirable results fall short. In this work, we address this knowledge gap by comparing the performance $d^{10}$ guest metals spatially confined within layers of 1T-$MoS_2$ to the performance of $d^0$ guest metals under similar confinement using Zn and Sc SAs, respectively.

**Chapter 5.** Primary driving factors that influence interactions between the guest metal and active sites include guest metal oxidation state, local coordination geometry, and electronic occupation of valence states. Although the guest metal's spin state has the ability to alter its electronic structure, the impact it has under 1D confinement on catalysis is poorly understood. In this work,

the electrochemical HER performance of HS and LS Mn SAs confined within 1T-MoS$_2$ nanosheets are compared in acidic conditions.

**Chapter 6.** The focus of this chapter is to briefly describe the future directions of this dissertation which involve studying the catalytic effects of confining chiral molecules within the interlayer spacing of 2D materials.

CHAPTER 1: General Introduction

## 1.1 Motivation and Background

### *1.1.1 Methods of $H_2$ Generation and Renewable Alternatives*

$H_2$ is recognized as an essential green energy carrier that is widely used as a chemical feedstock in petroleum refinement, fertilizer production, and as a fuel source to produce electricity and heat. As of 2021, 95% of $H_2$ produced in the United States is generated by steam-methane reformation.[1] In addition to producing high $CO_2$ emissions, this energy-intensive process requires large scale power plants, making it expensive and inaccessible to countries that lack these resources (**Figure 1.1**).

$$1)\quad CH_{4(g)} + H_2O_{(g)} + \Delta \rightleftharpoons CO_{(g)} + 3H_{2(g)}$$
$$700\text{-}1000°C$$
$$3\text{-}25\ bar$$
$$2)\quad CO_{(g)} + H_2O_{(g)} \rightleftharpoons CO_{2(g)} + H_{2(g)}$$
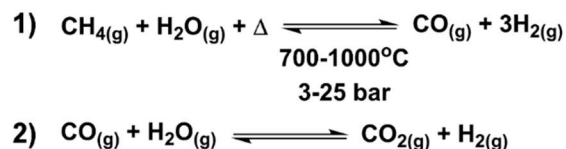
**Figure 1.1:** Steam-methane reformation reaction steps.

Luckily, alternative pathways to $H_2$ generation exist. In the electrochemical $H_2$ generation process, electricity is used to split water into $H_2$ and $O_2$ (**Figure 1.2a**). The overpotential, which is the amount of energy required to drive HER, may be lowered by using a photoelectrochemical (PEC) device that harnesses sunlight to drive water splitting (**Figure 1.2b**).[2] In the PEC process, sunlight irradiates the surface of a semiconductor and generates electron/hole charge carriers. The holes remain in the valence band and the electrons are excited to the conduction band. The electrons transfer to the semiconductor's surface, reduce adsorbed $H^+$, and generate $H_2$. Both of these two methods are sustainable, decentralized, and yield pure $H_2$, which alleviates the challenges faced by steam methane reformation.
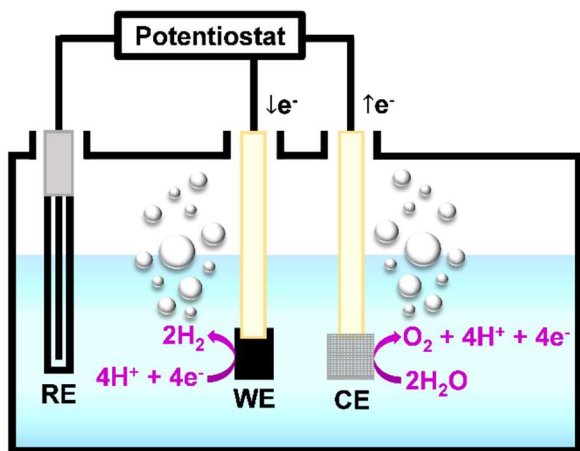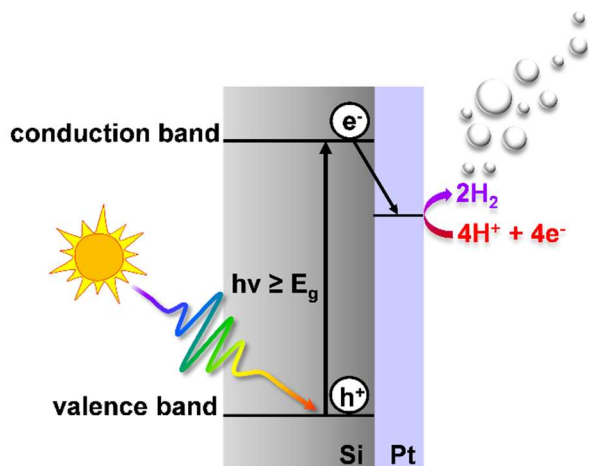
**Figure 1.2:** Schematic of **(a)** electrochemical and **(b)** PEC H$_2$ generation.

### 1.1.2   The Search for Earth-abundant, Inexpensive HER Catalysts

PEC devices face two major challenges inhibiting their commercialization potential. First, the inevitable growth of native oxides (*i.e.*, SiO$_x$) on the semiconductor surface during device operation induces charge carrier recombination, photodegradation, and limits operation lifetime.[3,4] Second, semiconductors lack efficiency in selectively catalyzing HER and must be coupled with a catalyst to facilitate HER kinetics and interfacial charge transfer processes.[5] Catalyst performance depends on the nature of their active sites, the positions at which catalytic reactions occur. The most common HER catalysts are expensive precious metals, specifically Pt, due to its thermoneutral free energy of hydrogen adsorption ($\Delta G_{H^*} \approx 0$ eV).[6-9] This implies that binding and releasing adsorbed H$^+$ on the catalyst's surface are both equally facile, which is a requirement for fast electron transport and H$_2$ generation.[10]

### 1.1.3 Earth-abundant MoS₂: a Promising Replacement for Expensive HER Catalysts

Earth-abundant MoS₂ is a transition metal dichalcogenide that was first recognized as a potential HER catalyst when theoretical calculations revealed the thermoneutral free energy of hydrogen adsorption ($\Delta G_{H^*}$ = 0.8 eV) located at S vacancies and coordinatively unsaturated Mo and S atoms exposed along the edge sites of semiconducting 2H-MoS₂.[11-14]
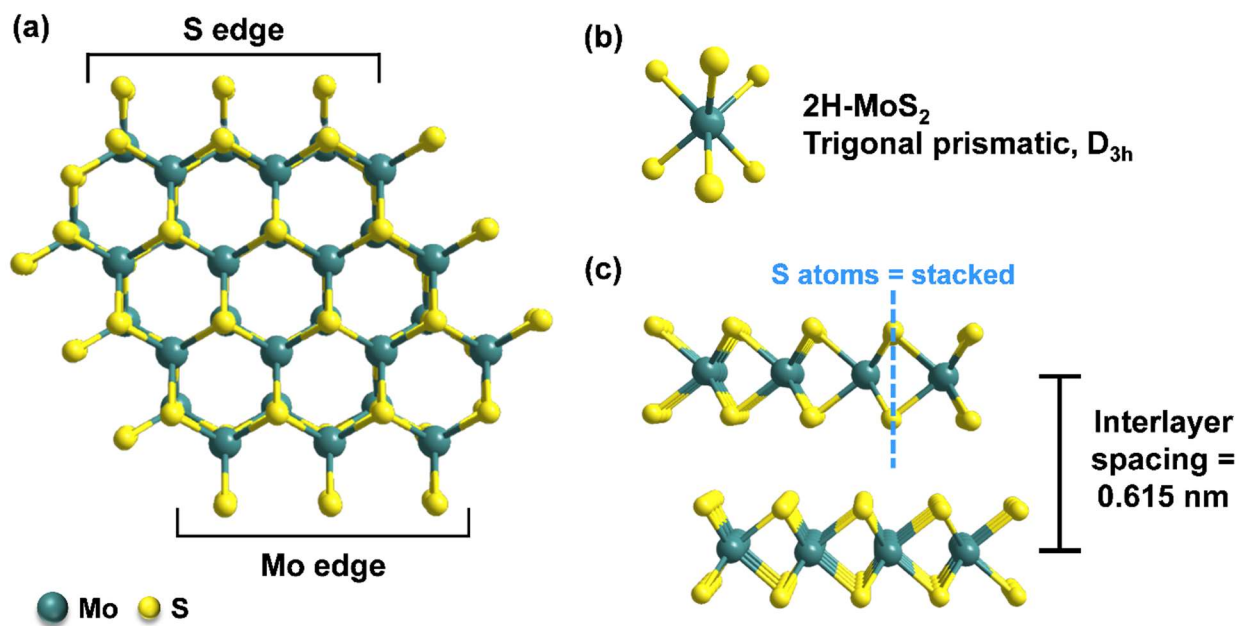


**Figure 1.3:** Geometric structure of 2H-MoS₂.
**(a)** Layer geometry. **(b)** Point group. **(c)** Side view displaying stacked S atoms and interlayer spacing.

MoS₂ is a polymorphic material where the Mo atoms are sandwiched between two layers of S atoms. The most common polymorph of MoS₂ found in nature is the semiconducting 2H phase which exhibits trigonal prismatic coordination geometry (**Figures 1.3a, 1.3b**). This coordination geometry forces the layers of S atoms to be stacked, which in turn reduces the exposure of Mo atoms to the catalyst surface and induces hydrophobicity (**Figure 1.3c**). The 2H-phase of MoS₂ also suffers from inherent layer stacking, which creates an interlayer spacing equal to 0.615 nm.

In 2007, Jaramillo *et. al.* performed a combined theoretical and experimental studying aiming to identify the locations of active sites in 2H-MoS₂.[13] Theoretically, $\Delta G_{H^*}$ values near 0 eV

predicted active sites to be limited to Mo edges and S vacancies, while high $\Delta G_{H^*}$ values calculated for active sites residing along the basal plane predicted these positions to be inert. Experimentally, the linear trend depicted in a graphical plot of the exchange current density as a function of the edge length of 2H-MoS$_2$ indicated that the rate of HER is directly proportional to the number of edge sites in 2H-MoS$_2$. As the number of vacancies in monolayer 2H-MoS$_2$ were electrochemically increased, the current density generated by the catalyst increased substantially.
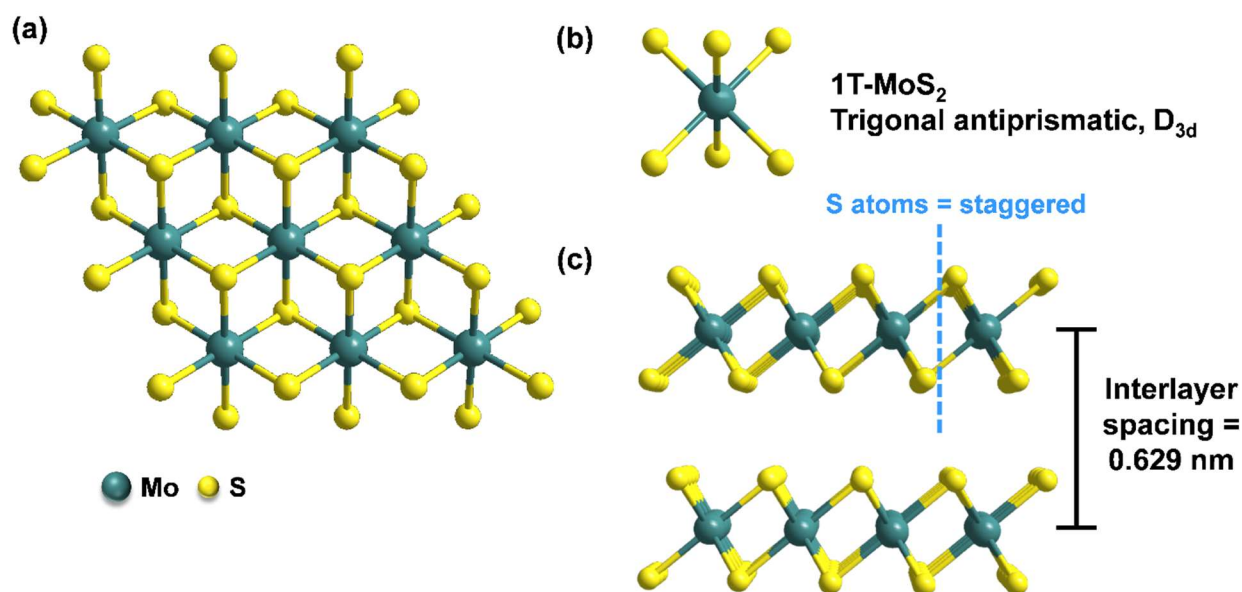


**Figure 1.4:** Geometric structure of 1T-MoS$_2$.
**(a)** Layer geometry. **(b)** Point group. **(c)** Side view displaying stacked S atoms and interlayer spacing.

Since then, strategies such as increasing S vacancies,[15, 16] incorporating transition metals,[17, 18] and tuning support interactions[19, 20] have been utilized to increase exposure of active sites in 2H-MoS$_2$. Be that as it may, the semiconducting nature of 2H-MoS$_2$ yields poor charge transport properties and limits catalytic activity.[21]

These challenges may be overcome by converting semiconducting 2H-MoS$_2$ to the metallic 1T phase of MoS$_2$ (**Figure 1.4**). In the conversion process to the 1T phase, the bottom S plane rotates by 180°, resulting with trigonal antiprismatic coordination geometry (**Figures 1.4a, 1.4b**).

In this coordination geometry, the layers of S atoms become staggered, causing 1T-MoS$_2$ to be hydrophilic (**Figure 1.4c**). Likewise, the interlayer spacing increases to 0.629 nm and the reduced layer stacking inherent to 1T-MoS$_2$ renders the basal plane active. The metallic nature and increased interlayer spacing of the 1T phase of MoS$_2$ enhances catalytic activity by facilitating charge transfer kinetics and exposing active sites located at S vacancies and undercoordinated Mo and S atoms along the basal plane.[22, 23] Intercalating transition metals within the interlayer spacing of 1T-MoS$_2$ has been shown to further improve catalytic activity of interlayer confined S atoms by altering their electronic states.[6, 24] As a result, 1T-MoS$_2$ exhibits an abundance of active sites along the basal plane, S vacancies, and lattice positions occupied by transition metal dopants. For these reasons, 1T-MoS$_2$ is considered to be an ideal candidate for replacing Pt, the best performing HER catalyst to date.

### 1.1.4   Confinement Catalysis in 2D Materials

Heterogeneous catalysis is responsible for producing nearly 90% of the chemicals we use in daily life.[25, 26] In fact, the most energy-intensive processes (i.e., N$_2$ fixation via the Haber-Bosch process, H$_2$ generation via steam-methane reforming) are driven by heterogeneous catalysis.[27] Heterogeneous catalysts play a key role in driving these chemical transformations by increasing the rate, efficiency, and selectivity of the reactions involved.[28] The performance of these catalysts depends on the nature of their active sites, which are the positions at which catalytic reactions occur.

Spatial confinement of active site microenvironments (the local coordination environment and electronic states of active sites) within catalysts has been predicted to alter the frontier orbital energies and adsorption/desorption energies of confined active sites in a manner that enhances the

catalyst's activity.[29, 30] Electronic properties of confined active sites are directly influenced by their coordination environment, which in turn alters the adsorption energetics of reaction intermediates and catalytic activity/selectivity.[31] Therefore, the relationship between active sites, local microenvironments, and confined species dictates catalytic performance. However, designing a prototype system that enables the understanding of catalytic confinement effects at the atomic level remains challenging.
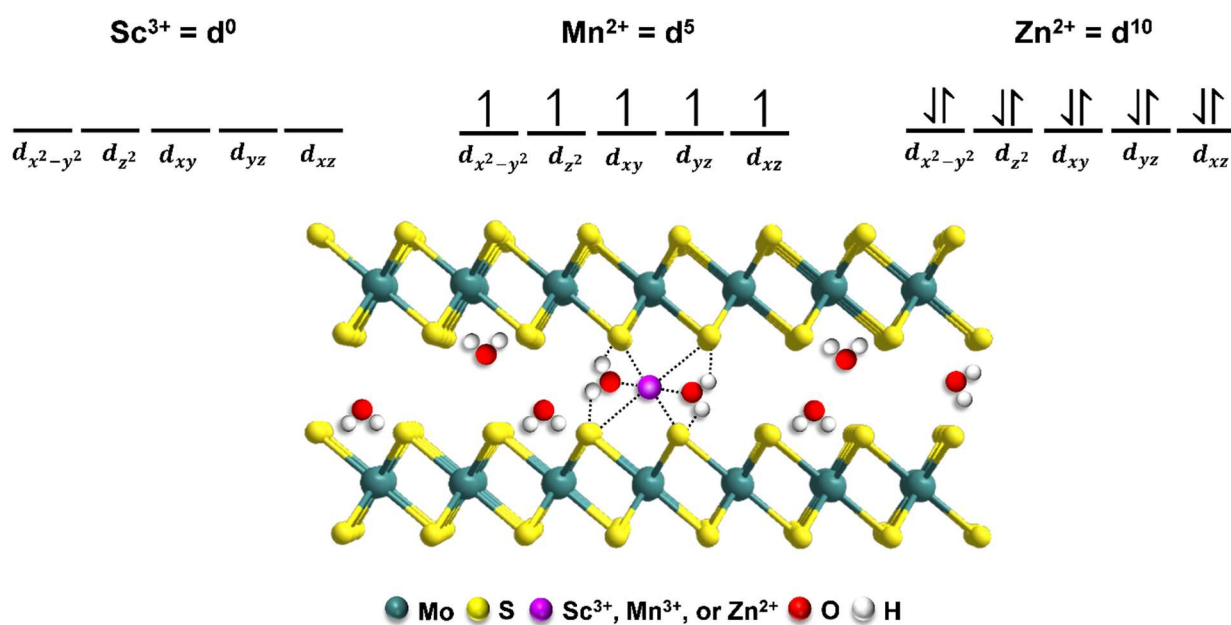


**Figure 1.5:** Schematic diagram depicting the spatial confinement of first-row transition metals Sc, Mn, and Zn within the interlayer spacing of 1T-MoS$_2$.

SACs are catalysts that exhibit SAs stabilized within supporting substrates by either adsorbing to the substrate's basal plane or substituting atoms within the substrate's lattice. As such, SACs offer an ideal prototype for the investigation of confinement catalysis. Along with demonstrating a superior catalytic performance compared to nanoparticles and nanoclusters in traditional metal catalysts, SACs exhibit flexibility with respect to crystallinity, coordination number, and electronic structures.[32] Likewise, when employing noble metal SAs, SACs require

significantly smaller quantities of noble metals to achieve competitive catalytic performances to produce solar fuels and industrial chemicals.

Suitable substrates for confinement catalysis require stable structures and a high density of exposed active sites.[31] Most investigations of confinement catalysis have been limited to porous 3D substrates (*i.e.,* zeolites, metal-organic frameworks, *etc.*).[29, 33] However, difficulty with decoupling the effects of surface area from the effects of confinement makes understanding the influence of spatial confinement on catalytic activity within these highly porous materials challenging.[34]

Compared to their 3D counterparts, 2D materials exhibit well-defined layered structures, a variety of polymorphs, and tunable geometric and electronic properties. For these reasons, *2D materials provide an ideal platform to understand how confining guest species near active sites located within their interlayer spacing influences catalytic performance*. The ability to control the electronic states of basal plane active sites and create sandwich-like structures with different types of 2D materials provides versatility in controlling chemical reactivity that is unachievable for 3D substrates.[35] Likewise, intercalating guest species into 2D materials provides a unique opportunity to understand how confinement influences catalysis by controlling the geometry and size of confined microenvironments within which active sites reside.

Computational studies have predicted the interactions between active sites and guest species confined within their local microenvironments to heavily influence catalytic activity.[36-39] Yet, experimental evidence of such outside of carbon-based 2D materials is limited.[30] Here, we seek to fill this knowledge gap by modulating the electronic states of interlayer confined S atoms in 1T-$MoS_2$ with transition metal intercalants and elucidating the effects of confining metals with varied d orbital occupancy on HER catalysis.

## 1.2 Addressing the Knowledge Gap

This dissertation's primary goal is to understand the effects of interlayer transition metal confinement on the catalytic performance of 2D materials (**Figure 1.5**). Therefore, the following specific aims were pursued.

### *1.2.1 Specific Aims of This Dissertation*

1.  Improving the stability of silicon nanowires during PEC $H_2$ generation with Zn 1T-$MoS_2$.

2.  Zn SA confinement effects on catalysis in 1T-phase $MoS_2$.

3.  Impact of metal SA d-orbital occupation on confinement catalysis: $d^0$ vs. $d^{10}$.

4.  Effects of SA spin state on confinement catalysis.

## 1.3 Characterization Techniques Employed in this Work

A diverse assortment of analytical techniques traditional to studies of intercalation chemistry were employed in this work to develop a well-rounded investigation that is both qualitative and quantitative. Identification of whether the metal SAs (Zn, Sc, HS Mn, and LS Mn) adsorb to the basal plane of 1T-$MoS_2$ or substitute Mo atoms within the substrate's crystal lattice was determined by STEM to identify the conditions of confinement each type of SA adopts. Uniform distribution of SAs, Mo, S, and O atoms, along with identification of contamination (if any), was elucidated using EDX analysis. Bulk expansion of 1T-$MoS_2$'s interlayer spacing specifically induced by adsorbed SAs was evidenced by visible peak shifts in the XRD patterns of each catalyst studied in this work. Shifts in the $2\theta$ peak at $14.07°$ corresponding to the (001) plane that bisects the interlayer spacing of 1T-$MoS_2$ to lower values of $2\theta$ confirm expansion of the

interlayer spacing. In contrast, shifts to higher $2\theta$ values correspond to a reduction in the interlayer spacing. HRTEM images were utilized to measure changes in fringe spacings along the edges of the 2D substrate induced by SA intercalation, which is the region where catalysis is most likely to take place.

Retention of the lattice structure of $1T\text{-}MoS_2$ post-intercalation was confirmed via Raman spectroscopy. Presence of the 1T phase was evidenced by additional peaks present in the 100-500 $cm^{-1}$ region that correspond to TA, LA, $J_1$, $J_2$, $J_3$, and $E_{1g}$ modes. Additionally, softening of the $A_{1g}$ mode with respect to the $E^1_{2g}$ mode, which arises from weakened interlayer coupling confirmed the dominant presence of the 1T phase and lack of the 2H phase in the bulk region of the catalyst substrate. FTIR spectroscopy was employed specifically for the LS Mn SAs case, to confirm whether or not the ligands that force Mn into a LS configuration are retained when under confinement. Oxidation states of atomic species present along the catalyst surface where HER occurs was identified using XPS analysis and was subsequently used to elucidate the bonding environment of the active sites along the catalyst surface. EPR analysis was employed to perform any magnetic studies necessary to achieve the research goals of this work.

All electrochemical studies were performed under $N_2$-saturated acidic conditions (0.5 M $H_2SO_4$, pH $\approx$ 0) within a three-probe electrochemical cell. Ag/AgCl and graphite were employed as reference and counter electrodes, respectively. Purely electrochemical studies conducted herein employed working electrodes composed of carbon fiber paper with the catalyst ink drop cast on top. Specifics for the preparation of each catalyst ink are detailed in the Materials and Methods section of each chapter. PEC studies were conducted using a visible light shortpass filter (FESH0750, Thor labs), and a steady DC-powered 150 W Xe arc lamp (New Port) light source calibrated to 100 mW/cm$^2$ using a Si photodiode providing one sun's illumination for accurate

analysis of solar collection and catalytic performance. Catalyst deposition onto working electrodes prepared for PEC studies also employed the drop cast method – specifics of their preparation steps are detailed in the Materials and Methods section in Chapter 2. HER was employed as the model reaction to evaluate changes in catalytic performance with respect to the electronic occupation of d-orbitals in SAs confined near active sites in 1T-MoS$_2$ for all investigations performed in this dissertation.

Additional techniques were employed in certain cases where necessary, including XAS to extract information related to bonding environments of SAs under confinement. Specific details of each technique employed is provided in the Materials and Methods section of every chapter following this introduction.

1.4 Expected Outcomes

This dissertation focuses on investigating the catalytic effects of confining transition metal ions with fully occupied (Zn$^{2+}$, a d$^{10}$ metal), partially occupied (Mn$^{2+}$, a d$^5$ metal), and empty (Sc$^{3+}$, a d$^0$ metal) d orbitals within the interlayer spacing of 1T-MoS$_2$. As a d$^5$ metal, Mn may adopt a high or low spin configuration depending on the ligands the metal coordinates to, we propose to investigate the effects of the guest metal's spin state on confinement catalysis in 2D materials for my final project. We hypothesize that the guest metal's coordination geometry and d orbital occupation may be altered to enhance metal-support interactions, drive charge transfer between the metals and active sites, and manipulate confinement effects on catalytic performance.

Research in the field of confinement catalysis with 2D materials is still in its infancy. Unique to this work is the potential to clarify the dynamics between reactants and metal ions spatially confined within 2D materials as they operate in catalytic processes. Intercalating

transition metal ions into layered materials enables confined microenvironments to be controlled according to the guest metal's coordination geometry and electronic states. Although this dissertation focuses on understanding how spatially confining first-row transition metal ions within the microenvironments of 1T-MoS$_2$ impacts HER activity, the basis of this work may be easily adopted to other types of catalytic reactions and layered materials. Since confinement effects have been recognized for their importance in heterogeneous, homogeneous, and enzymatic catalysis, the knowledge we gain will benefit all fields of catalysis.

## 1.5 Acknowledgements

Chapter 1 contains unpublished material introducing the research fields of interest that were pursued in this dissertation. The dissertation author was the primary author of this chapter.

## 1.6 References

1.  Finke, C. E.; Leandri, H. F.; Karumb, E. T.; Zheng, D.; Hoffmann, M. R.; Fromer, N. A., Economically Advantageous Pathways for Reducing Greenhouse Gas Emissions from Industrial Hydrogen under Common, Current Economic Conditions. *Energy &amp; Environmental Science* **2021,** *14* (3), 1517-1529.

2.  Giménez, S.; Bisquert, J., *Photoelectrochemical Solar Fuel Production*. Springer Nature: 2016.

3.  Shen, X.; Sun, B.; Yan, F.; Zhao, J.; Zhang, F.; Wang, S.; Zhu, X.; Lee, S., High-Performance Photoelectrochemical Cells from Ionic Liquid Electrolyte in Methyl-Terminated Silicon Nanowire Arrays. *ACS Nano* **2010,** *4* (10), 5869-76.

4.  Wang, X.; Peng, K. Q.; Pan, X. J.; Chen, X.; Yang, Y.; Li, L.; Meng, X. M.; Zhang, W. J.; Lee, S. T., High-Performance Silicon Nanowire Array Photoelectrochemical Solar Cells through Surface Passivation and Modification. *Angew Chem Int Ed* **2011,** *50* (42), 9861-9865.

5.  Kang, D.; Kim, T. W.; Kubota, S. R.; Cardiel, A. C.; Cha, H. G.; Choi, K. S., Electrochemical Synthesis of Photoelectrodes and Catalysts for Use in Solar Water Splitting. *Chem Rev* **2015,** *115* (23), 12839-87.

6.  Gao, G.; Sun, Q.; Du, A., Activating Catalytic Inert Basal Plane of Molybdenum Disulfide to Optimize Hydrogen Evolution Activity Via Defect Doping and Strain Engineering. *The Journal of Physical Chemistry C* **2016,** *120* (30), 16761-16766.

7.  Gao, M. R.; Chan, M. K.; Sun, Y., Edge-Terminated Molybdenum Disulfide with a 9.4-a Interlayer Spacing for Electrochemical Hydrogen Production. *Nat Commun* **2015,** *6*, 7493.

8.  Parsons, R., The Rate of Electrolytic Hydrogen Evolution and the Heat of Adsorption of Hydrogen. *Transactions of the Faraday Society* **1958,** *54*, 1053-1063.

9.  Nørskov, J. K.; Bligaard, T.; Logadottir, A.; Kitchin, J. R.; Chen, J. G.; Pandelov, S.; Stimming, U., Trends in the Exchange Current for Hydrogen Evolution. *Journal of The Electrochemical Society* **2005,** *152* (3), J23.

10.  Benck, J. D.; Hellstern, T. R.; Kibsgaard, J.; Chakthranont, P.; Jaramillo, T. F., Catalyzing the Hydrogen Evolution Reaction (Her) with Molybdenum Sulfide Nanomaterials. *ACS Catalysis* **2014,** *4* (11), 3957-3971.

11.  Li, G.; Zhang, D.; Qiao, Q.; Yu, Y.; Peterson, D.; Zafar, A.; Kumar, R.; Curtarolo, S.; Hunte, F.; Shannon, S.; Zhu, Y.; Yang, W.; Cao, L., All the Catalytic Active Sites of Mos2 for Hydrogen Evolution. 2016; Vol. 138, pp 16632-16638.

12.  Hinnemann, B.; Moses, P. G.; Bonde, J.; Jorgensen, K. P.; Nielsen, J. H.; Horch, S.; Chorkendorff, I.; Norskov, J. K., Biomimetic Hydrogen Evolution: Mos2 Nanoparticles as Catalyst for Hydrogen Evolution. **2005,** *127*, 5308-5309.

13.	Jaramillo, T. F.; Jørgensen, K. P.; Bonde, J.; Nielsen, J. H.; Horch, S.; Chorkendorff, I., Identification of Active Edge Sites for Electrochemical H2 Evolution from Mos2 Nanocatalysts. **2007,** *317*, 100-102.

14.	Li, L.; Qin, Z.; Ries, L.; Hong, S.; Michel, T.; Yang, J.; Salameh, C.; Bechelany, M.; Miele, P.; Kaplan, D.; Chhowalla, M.; Voiry, D., Role of Sulfur Vacancies and Undercoordinated Mo Regions in Mos2 Nanosheets toward the Evolution of Hydrogen. **2019,** *13*, 6824-6834.

15.	Li, H.; Tsai, C.; Koh, A. L.; Cai, L.; Contryman, A. W.; Fragapane, A. H.; Zhao, J.; Han, H. S.; Manoharan, H. C.; Abild-Pedersen, F.; Norskov, J. K.; Zheng, X., Activating and Optimizing Mos2 Basal Planes for Hydrogen Evolution through the Formation of Strained Sulphur Vacancies. *Nature Materials* **2016,** *15*, 48-53.

16.	Tsai, C.; Li, H.; Park, S.; Park, J.; Han, H. S.; Norskov, J. K.; Zheng, X.; Abild-Pedersen, F., Electrochemical Generation of Sulfur Vacancies in the Basal Plane of Mos2 for Hydrogen Evolution. **2017,** *8*, 1-8.

17.	Shi, Y.; Zhou, Y.; Yang, D. R.; Xu, W. X.; Wang, C.; Wang, F. B.; Xu, J. J.; Xia, X. H.; Chen, H. Y., Energy Level Engineering of Mos2 by Transition-Metal Doping for Accelerating Hydrogen Evolution Reaction. **2017,** *139*, 15479-15485.

18.	Lin, Y. C.; Dumcenco, D. O.; Komsa, H. P.; Niimi, Y.; Krasheninnikov, A. V.; Huang, Y. S.; Suenaga, K., Properties of Individual Dopant Atoms in Single-Layer Mos2: Atomic Structure, Migration, and Enhanced Reactivity. *Adv Mater* **2014,** *26* (18), 2857-2861.

19.	Voiry, D.; Fullon, R.; Yang, J.; de Carvalho Castro, E. S. C.; Kappera, R.; Bozkurt, I.; Kaplan, D.; Lagos, M. J.; Batson, P. E.; Gupta, G.; Mohite, A. D.; Dong, L.; Er, D.; Shenoy, V. B.; Asefa, T.; Chhowalla, M., The Role of Electronic Coupling between Substrate and 2d Mos2 Nanosheets in Electrocatalytic Production of Hydrogen. *Nat Mater* **2016,** *15* (9), 1003-9.

20.	Tsai, C.; Abild-Pedersen, F.; Norskov, J. K., Tuning the Mos(2) Edge-Site Activity for Hydrogen Evolution Via Support Interactions. *Nano Lett* **2014,** *14* (3), 1381-7.

21.	Yu, Z.; Pan, Y.; Shen, Y.; Wang, Z.; Ong, Z. Y.; Xu, T.; Xin, R.; Pan, L.; Wang, B.; Sun, L.; Wang, J.; Zhang, G.; Zhang, Y. W.; Shi, Y.; Wang, X., Towards Intrinsic Charge Transport in Monolayer Molybdenum Disulfide by Defect and Interface Engineering. *Nat Commun* **2014,** *5*, 5290.

22.	Voiry, D.; Salehi, M.; Silva, R.; Fujita, T.; Chen, M.; Asefa, T.; Shenoy, V. B.; Eda, G.; Chhowalla, M., Conducting Mos(2) Nanosheets as Catalysts for Hydrogen Evolution Reaction. *Nano Lett* **2013,** *13* (12), 6222-7.

23.	Lukowski, M. A.; Daniel, A. S.; Meng, F.; Forticaux, A.; Li, L.; Jin, S., Enhanced Hydrogen Evolution Catalysis from Chemically Exfoliated Metallic Mos2 Nanosheets. *J Am Chem Soc* **2013,** *135* (28), 10274-7.

24.	Huang, Y.; Sun, Y.; Zheng, X.; Aoki, T.; Pattengale, B.; Huang, J.; He, X.; Bian, W.; Younan, S.; Williams, N.; Hu, J.; Ge, J.; Pu, N.; Yan, X.; Pan, X.; Zhang, L.; Wei, Y.; Gu, J.,

Atomically Engineering Activation Sites onto Metallic 1t-Mos2 Catalysts for Enhanced Electrochemical Hydrogen Evolution. **2019,** *10*.

25.     Mitschke, B.;  Turberg, M.; List, B., Confinement as a Unifying Element in Selective Catalysis. *Chem-Us* **2020,** *6* (10), 2515-2532.

26.     Garlyyev, B.;  Fichtner, J.;  Pique, O.;  Schneider, O.;  Bandarenka, A. S.; Calle-Vallejo, F., Revealing the Nature of Active Sites in Electrocatalysis. *Chem Sci* **2019,** *10* (35), 8060-8075.

27.     Friend, C. M.; Xu, B., Heterogeneous Catalysis: A Central Science for a Sustainable Future. *Acc Chem Res* **2017,** *50* (3), 517-521.

28.     Seh, Z. W.;  Kibsgaard, J.;  Dickens, C. F.;  Chorkendorff, I.;  Norskov, J. K.; Jaramillo, T. F., Combining Theory and Experiment in Electrocatalysis: Insights into Materials Design. *Science* **2017,** *355* (6321).

29.     Sastre, G.; Corma, A., The Confinement Effect in Zeolites. *Journal of Molecular Catalysis A: Chemical* **2009**, 3-7.

30.     Li, X.;  Liu, L.;  Ren, X.;  Gao, J.;  Huang, Y.; Liu, B., Microenvironment Modulation of Single-Atom Catalysts and Their Roles in Electrochemical Energy Conversion. *Sci Adv* **2020,** *6* (39), 1-20.

31.     Li, H.;  Xiao, J.;  Fu, Q.; Bao, X., Confined Catalysis under Two-Dimensional Materials. *Proc Natl Acad Sci U S A* **2017,** *114* (23), 5930-5934.

32.     Wang, X.;  Zhang, Y.;  Wu, J.;  Zhang, Z.;  Liao, Q.;  Kang, Z.; Zhang, Y., Single-Atom Engineering to Ignite 2d Transition Metal Dichalcogenide Based Catalysis: Fundamentals, Progress, and Beyond. *Chemical Reviews* **2022,** *122* (1), 1273-1348.

33.     Zhang, J.;  Sun, P.;  Gao, G.;  Wang, J.;  Zhao, Z. L.;  Muhammad, Y.; Li, F. W., Enhancing Regioselectivity Via Tuning the Microenvironment in Heterogeneous Hydroformylation of Olefins. *J Catal* **2020,** *387*, 196-206.

34.     Fleischmann, S.;  Spencer, M. A.; Augustyn, V., Electrochemical Reactivity under Confinement Enabled by Molecularly Pillared 2d and Layered Materials. *Chem Mater* **2020,** *32* (8), 3325-3334.

35.     Deng, D.;  Novoselov, K. S.;  Fu, Q.;  Zheng, N.;  Tian, Z.; Bao, X., Catalysis with Two-Dimensional Materials and Their Heterostructures. *Nat Nanotechnol* **2016,** *11* (3), 218-30.

36.     Remsing, R. C.;  McKendry, I. G.;  Strongin, D. R.;  Klein, M. L.; Zdilla, M. J., Frustrated Solvation Structures Can Enhance Electron Transfer Rates. *J Phys Chem Lett* **2015,** *6* (23), 4804-8.

37.     Munoz-Santiburcio, D.;  Wittekindt, C.; Marx, D., Nanoconfinement Effects on Hydrated Excess Protons in Layered Materials. *Nat Commun* **2013,** *4*, 2349.

38.     Esfandiar, A.;  Radha, B.;  Wang, F. C.;  Yang, Q.;  Hu, S.;  Garaj, S.;  Nair, R. R.;  Geim, A. K.;  Gopinadhan, K., Size Effect in Ion Transport through Angstrom-Scale Slits. *Science* **2017,** *358* (6362), 511-513.

39.     Li, H.;  Guo, C.;  Fu, Q.; Xiao, J., Toward Fundamentals of Confined Electrocatalysis in Nanoscale Reactors. *J Phys Chem Lett* **2019,** *10* (3), 533-539.

CHAPTER 2: Improving the Stability of Silicon Nanowires During Photoelectrochemical Hydrogen Generation with Zinc 1T-phase Molybdenum Disulfide

## 2.1 Abstract

Semiconductor photoelectrodes directly convert sunlight into stored chemical energy. In photoelectrochemical devices, this photoconversion process relies on the junction between the semiconductor and catalyst to drive charge separation and generate electron/hole charge carriers. The growth of native oxides ($SiO_x$) on the surface of semiconductors during device operation induces charge carrier recombination and photodegradation, which limit the operation lifetime of PEC devices. Likewise, the commercialization of photoelectrochemical devices is hindered by the use of expensive, rare precious metal catalysts such as platinum to enhance hydrogen evolution kinetics. This work demonstrates how drop casting zinc 1T-phase molybdenum disulfide (Zn 1T-$MoS_2$) onto silicon nanowires (SiNWs) generates an interface that overcomes these challenges. This Zn 1T-$MoS_2$/SiNWs junction drives hydrogen evolution under acidic conditions (0.5 M $H_2SO_4$) comparably to platinum-modified SiNWs (Pt/SiNWs) with a positive overpotential of 164 mV at 10 mA cm$^{-2}$ and low Tafel slope of 42 mV dec$^{-1}$. Compared to the bare SiNWs, the Zn 1T-$MoS_2$/SiNWs junction retained roughly 66% more photocurrent density and reduced $SiO_x$ growth by 16% after 24 hours of continuous electrolysis. By developing a deep understanding of the catalyst-semiconductor interface, photoelectrochemical devices may be effectively designed to maintain their stability over a lifetime of operation.

## 2.2 Introduction

As unprecedented worldwide economic growth induces an upsurge in global energy demand, the need for an efficient, renewable replacement for fossil fuel-driven energy generation has never been more prevalent. Hydrogen ($H_2$) is recognized as an essential global energy carrier because it features the highest energy content per weight and can provide energy in a form that is easily stored and consumed upon demand.[2, 40] Likewise, the magnitude of available solar power striking the Earth's surface is equivalent to 130 million 500 MW power plants, making solar energy a promising alternative to coal-driven energy sources.[41] Hence, commercially employing a photoelectrochemical (PEC) platform that harvests sunlight to convert water into clean fuels such as $H_2$ is a longstanding objective of research efforts in renewable energy generation.

In the PEC $H_2$ generation process, solar irradiation strikes the surface of a semiconductor and generates electron/hole charge carriers. The holes remain in the semiconductor's valence band, while the free electrons are excited to the semiconductor's conduction band. In the conduction band, the electrons transfer to the semiconductor's surface, reduce adsorbed hydrogen ions ($H^+$), and generate $H_2$ (**Figure S2.1**).[42, 43] Although semiconductors collect solar energy proficiently, they lack efficiency in selectively catalyzing HER.[5] As a consequence, semiconductors usually need to be coupled with an $H_2$ evolution catalyst to facilitate HER kinetics and interfacial charge transfer processes. To date, the most common $H_2$ evolution catalysts are noble metals, specifically platinum (Pt), due to its thermoneutral Gibbs energy of hydrogen adsorption ($\Delta G_{H*} \approx 0$ eV).[6-9] For a heterogeneous catalyst, this implies that binding and releasing adsorbed $H^+$ on the catalyst's surface are both equally facile, which is a requirement for fast electron transport and $H_2$ generation.[10] Pt and other noble metals, however, are expensive and rare. To reduce device costs without sacrificing performance, Pt must be replaced with a cost-effective HER catalyst that

performs equivalently. One promising replacement for noble metal HER catalysts is molybdenum disulfide ($MoS_2$), an Earth-abundant catalyst that maintains a $\Delta G_{H*}$ very close to 0 eV.[28]

$MoS_2$ is a two-dimensional (2D) layered nanomaterial composed of an atomic layer of molybdenum (Mo) atoms sandwiched between two atomic layers of sulfur (S) atoms *via* strong interplanar covalent bonding.[44] Stacked layers of $MoS_2$ are held together by weak out-of-plane van der Waals forces.[45] In nature, $MoS_2$ primarily exists in its semiconducting 2H phase (2H-$MoS_2$). 2H-$MoS_2$ has trigonal prismatic crystal symmetry, hexagonal layer symmetry, and is stable and semiconducting due to the paired electrons inhabiting the 4d valence orbitals of the $Mo^{4+}$ atoms.[44, 46] Primitive unit cells of 2H-$MoS_2$ exhibit two layers of $MoS_2$ stacked atop each other. Therefore, available HER active sites that facilitate $H_2$ evolution reactions (HER) in 2H-$MoS_2$ are limited to positions along the Mo and S edges.[44, 47] One may increase the exposure of active sites in $MoS_2$ by conversion to the metallic 1T phase (1T-$MoS_2$). 1T-$MoS_2$ has octahedral crystal symmetry and distorted tetragonal layer symmetry.[46] In 2H-$MoS_2$, the trigonal prismatic crystal symmetry allows the positions of the top and bottom S atom planes to be aligned with one another. In 1T-$MoS_2$, the octahedral crystal symmetry causes the bottom plane of S atoms to be rotated by 180º with respect to the upper plane.[48] Therefore, whereas in 2H-$MoS_2$ the layer of S atoms sandwiching the Mo atomic layer are stacked, the top and bottom layers of S atoms are staggered in 1T-$MoS_2$. This change in layer symmetry increases the exposure of S atoms, which in turn increases electronic conductivity and enables fast electron transport for HER.[10, 49] This symmetric distortion, along with intercalation of transition metals, increases the interlayer spacing between adjacent layers of $MoS_2$ and exposes the large density of active sites on the basal plane that previously were unattainable.[7, 50] Furthermore, the staggered S atoms bring the Mo atoms closer to the surface of the catalyst-liquid interface, thus increasing the 2D material's hydrophilicity by increasing the

number of accessible hydrophilic surface sites.[51] Although the metastable nature of 1T-MoS$_2$ limits catalytic performance, several publications have demonstrated how modifying MoS$_2$ with various transition metals may increase HER performance and stability.[44, 46, 52-54] Liang *et al*. proposed the ability of Zn$^{2+}$ ions to increase interlayer spacing and hydrophilicity in MoS$_2$ by forming strong interactions with surrounding water molecules and diffusing through the interlayer spacing as a hydrated Zn$^{2+}$ complex.[51] In light of this, we incorporated Zn$^{2+}$ ions into 1T-MoS$_2$ to determine whether this modification enables an increase in the amount of H$_2$ generated by our PEC device.

Another major challenge to commercializing PEC H$_2$ generation is directly related to the instability of the semiconductor employed. Generally, Si is one of the most commonly used semiconductors for PEC water splitting because its conduction band straddles the overpotential required to drive HER.[42] However, the amount of H$_2$ produced by Si semiconductor materials tends to decline over time due to charge recombination and material degradation at the semiconductor-liquid junction.[3, 4, 55] A key parameter that affects the operation lifetime of Si semiconductors is the intrinsic instability of the Si surface due to oxidation.[3, 4] Here, to increase the amount of surface area available for light absorption, MACE was employed to fabricate SiNWs. Unfortunately, employing the MACE process to increase the surface area escalates the growth of native oxides (SiO$_x$), which further prevents charge transfer across the semiconductor-liquid junction.[4] Often, protection layers are deposited onto Si surfaces to limit further growth of SiO$_x$ during photoelectrolysis. Without a protective layer, photocorrosion will hasten the deterioration of the device's performance and substantially limit operation lifetime.[3]

In this work, thioacetamide was hydrothermally reacted with an Anderson-type polyoxometalate precursor ((NH$_4$)$_4$[ZnMo$_6$O$_{24}$H$_6$]·5H$_2$O) to synthesize Zn 1T-MoS$_2$. To expedite charge transfer kinetics and protect the electrode from photocorrosion, Zn 1T-MoS$_2$ was drop cast

onto SiNWs (Zn 1T-MoS$_2$/SiNWs) to form a catalyst-semiconductor interface. Results were compared to the HER performance of Pt-coated SiNWs (Pt/SiNWs) to evaluate whether Zn 1T-MoS$_2$ is an adequate HER catalyst replacement for Pt. The PEC performance was analyzed under acidic conditions (0.5 M H$_2$SO$_4$) and demonstrated a PEC performance comparable to Pt-coated SiNWs (Pt/SiNWs) under the same conditions. After 24 hours of continuous electrolysis, the Zn 1T-MoS$_2$/SiNWs retained 66% more photocurrent density than the bare SiNWs. Evidence from this work indicates that drop casting Zn 1T-MoS$_2$ along the SiNWs surface provides a layer of protection from surface oxidation, which results with a significant improvement in the SiNWs stability. Research efforts to date have demonstrated how modifying 1T-MoS$_2$ with transition metals enhances electrochemical H$_2$ generation.[17, 24, 50, 56-60] However, investigations of the PEC performance and junction formed between nanostructured Si semiconductors and 1T-MoS$_2$ catalysts modified with transition metals remain scarce. Therefore, this work seeks to not only determine the feasibility of Zn 1T-MoS$_2$ as a replacement catalyst for noble metals in PEC systems but also to understand the interfacial phenomena driving PEC performance and stability. In doing so, interfaces may be constructed to maintain their stability over a lifetime of operation. By replacing expensive precious metals with equally efficient low-cost materials, this research provides an opportunity to generate clean energy from natural resources that are abundant and decentralized.

2.3 Results and Discussion

*2.3.1 Structural Analysis of Zn 1T-MoS₂/SiNWs*
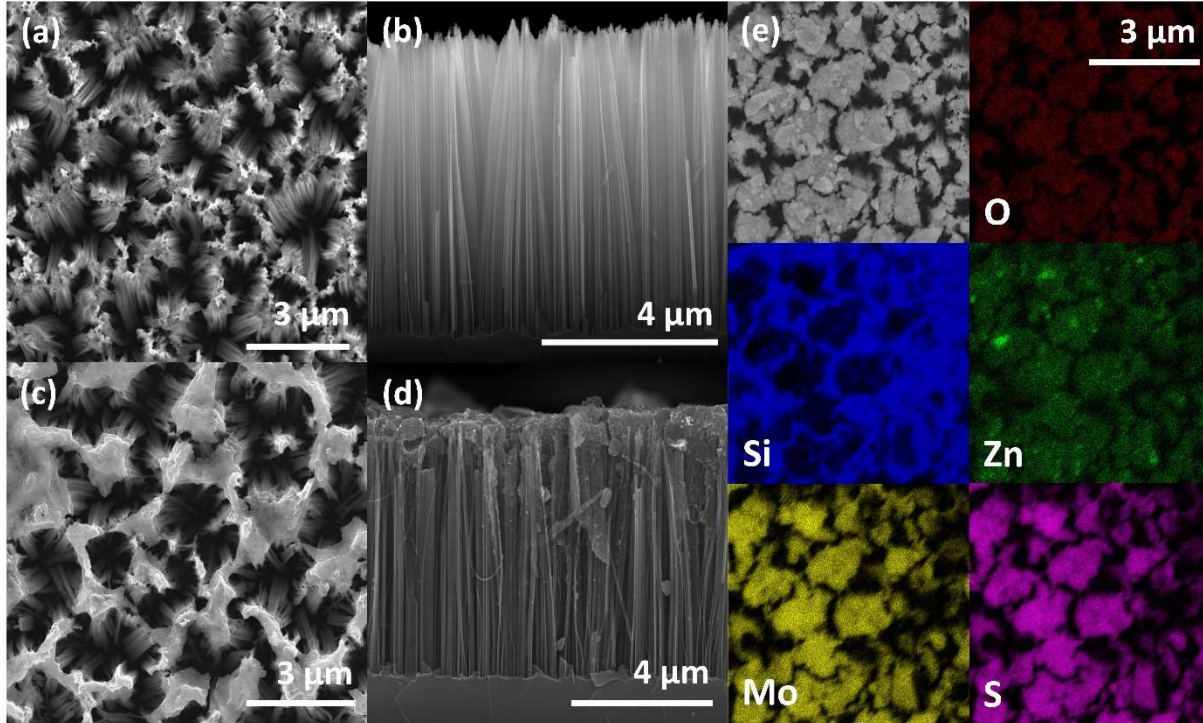


**Figure 2.1:** SEM imaging of Zn 1T-MoS₂/SiNWs.
**(a)** Surface and **(b)** cross-sectional view of bare SiNWs. **(c)** Surface and **(d)** cross-sectional view of Zn 1T-MoS₂/SiNWs. **(e)** EDX elemental mappings.

Surface and cross-sectional SEM imaging with corresponding EDX elemental mappings of both the bare SiNWs and Zn 1T-MoS₂/SiNWs indicate the following results (**Figure 2.1**). The surface and cross-sectional images of the bare SiNWs show their customary vertical alignment and uniformity in terms of density, size, and shape, with each NW between 7-9 μm in length (**Figures 2.1a, 2.1b, S2.3**). Slight agglomeration is visible near the tips of the SiNWs, which is an inherent side effect of van der Waals forces and capillary forces induced by the wet chemical etching process.[61, 62] The octahedrally coordinated atoms observed by high-angle annular dark-field scanning transmission electron microscopy confirm the successful synthesis of MoS₂ in the 1T phase (**Figure S2.4**). The surface and cross-sectional images of the Zn 1T-MoS₂/SiNWs show that Zn 1T-MoS₂ distributes uniformly across the SiNWs surface (**Figures 2.1c, 2.1d**). Further cross-sectional SEM and EDX profiling of the Zn 1T-MoS₂/SiNWs indicate that the majority of the

deposited Zn 1T-MoS$_2$ remains near the SiNWs surface (**Figure S2.5**). This may be attributed to the longitudinal direction of growth that is characteristic to 2D nanosheets. Lastly, the EDX elemental maps confirm the presence and uniform distribution of the Zn atoms, along with the other elements, throughout the catalyst material (**Figure 2.1e**).

Surface analysis of the electronic effects that arise from modifying 1T-MoS$_2$ with Zn atoms was performed by characterizing both Zn 1T-MoS$_2$ and 1T-MoS$_2$ by XPS (**Figures 2.2, S2.6, S2.7**). Experimental peak values and assignments are provided in **Table S2.1**. Peak positions identified in the Zn 2p spectrum correspond to the Zn$^{2+}$ oxidation state (**Figure S2.6**). Both samples show two sets of doublet peaks in the Mo 3d, S 2s (**Figures 2.2a, 2.2c**), and S 2p (**Figures 2.2b, 2.2d**) spectra. The purple peaks displayed in the Mo 3d spectra represent Mo$^{4+}$ and confirm the presence of stoichiometric 1T-phase MoS$_2$.[63] Presence of the minor Mo 3d peaks shown in orange indicate that an oxidized Mo$^{6+}$ species exists along the surface of both samples.[63] These results indicate that both 1T-MoS$_2$ and Zn 1T-MoS$_2$ are primarily composed of stoichiometric MoS$_2$ with a region of S depleted MoS$_x$ along the surface.[64] In both samples, associated S 2p doublets are present for both MoS$_2$ and MoS$_x$ (**Figures 2.2b, 2.2d**). While a shift is not observed for peaks present in the S 2p and O 1s spectra, the Mo 3d and S 2s peaks in Zn 1T-MoS$_2$ demonstrate an upshift of 0.1-0.3 eV compared to 1T-MoS$_2$ (**Table S2.1**). Observed upshifts up to 0.1 eV fall within the step size employed during XPS data collection (step size = 0.100 eV/step) and are therefore considered negligible. However, the Mo 3d$_{3/2}$ peak assigned to MoS$_x$ in Zn 1T-MoS$_2$ is upshifted by 0.3 eV compared to the Mo 3d$_{3/2}$ peak assigned to MoS$_x$ in 1T-MoS$_2$. This shift to a higher binding energy indicates that the incorporation of Zn increases the electron density of the d orbitals represented by the 3d$_{3/2}$ peak in MoS$_x$.[17] Fundamentally, weak interactions between atoms  do not alter electron distribution sufficiently enough to change binding energy

values significantly.[65] Thus, since binding energy shifts were not observed for stoichiometric MoS$_2$, bonding interactions between Zn and 1T-MoS$_2$ are unlikely and the structure of 1T-MoS$_2$ remains unchanged. Conversely, the binding energy shifts observed for MoS$_x$ suggests that covalent bonding interactions occur between Zn and S depleted MoS$_x$ near the catalyst surface where HER occurs.
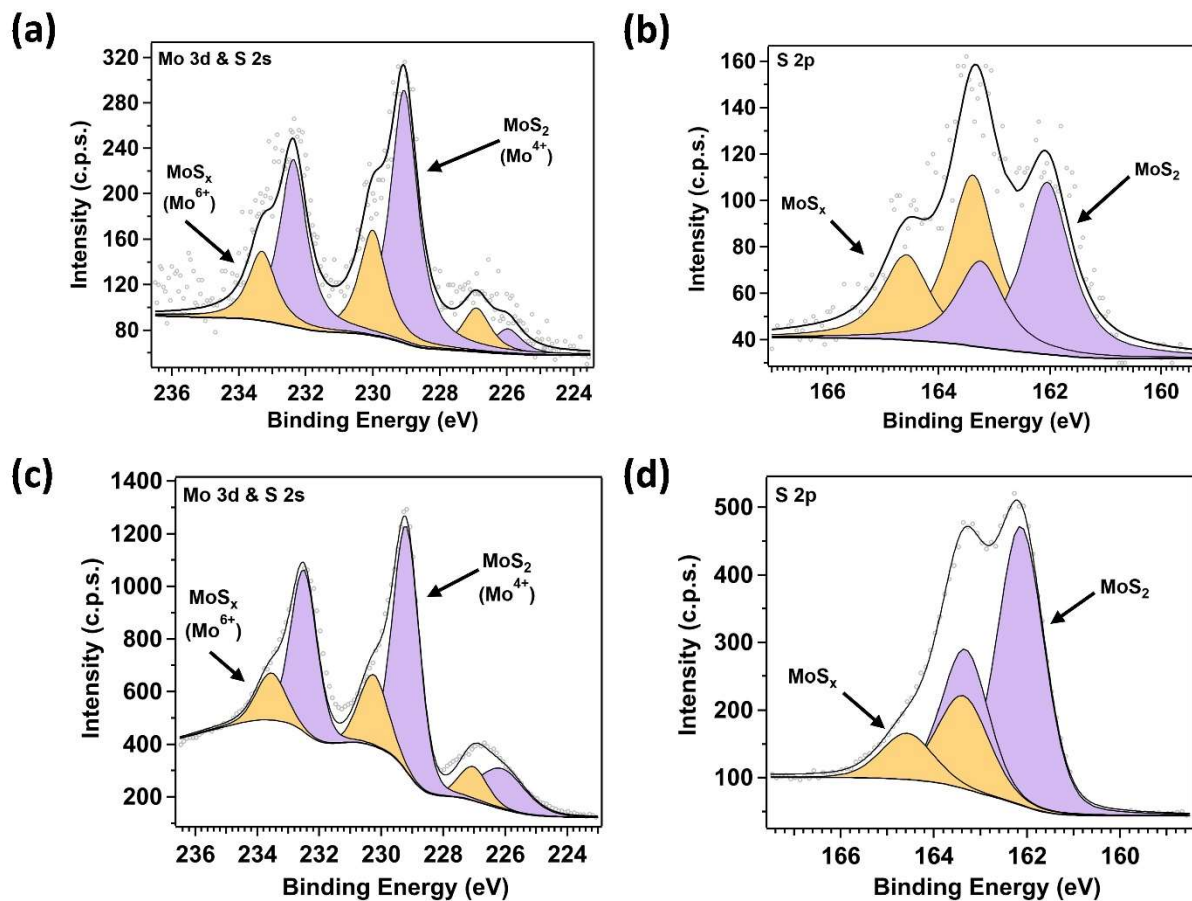


**Figure 2.2:** XPS of 1T-MoS$_2$ **(a-b)** and Zn 1T-MoS$_2$ **(c-d)**.
The purple and orange peaks are assigned to MoS$_2$ and an oxidized MoS$_x$ species, respectively. **(a, c)** Mo 3d and S 2s spectra. **(b, d)** S 2p spectra.

Raman spectra were collected for 2H-MoS$_2$, 1T-MoS$_2$, and Zn 1T-MoS$_2$ to elucidate the structural changes that arise from modifying 1T-MoS$_2$ with Zn (**Figure S2.8a**). Associated Raman peak assignments are provided in **Table S2.2**. Peaks arising from transverse acoustic phonon modes at the M point of the first Brillouin zone (TA), longitudinal acoustic phonon modes at the

M point of the Brillouin zone (LA), and the $J_1$, $J_2$, and $J_3$ phonon modes are all observed for both 1T-MoS$_2$ and Zn 1T-MoS$_2$. The $J_1$, $J_2$, and $J_3$ modes occur as a result of superlattice distortion in the basal plane.[66] The presence of these five modes arise from symmetry-induced defects, are indicative of the formation of 1T-MoS$_2$, and are not present in 2H-MoS$_2$.[45, 67, 68] $E_{1g}$ modes present in both 1T-MoS$_2$ and Zn 1T-MoS$_2$ correspond to the in- plane relative vibration of S atoms.[48] 2H-MoS$_2$ exhibits peaks assigned to the in-plane $E^1_{2g}$, out-of-plane $A_{1g}$, and 2LA phonons, respectively, customary to what is seen in literature.[48, 67] $E^1_{2g}$ modes arise from in-plane lattice vibrations of S atoms moving in the same direction, opposite of the direction of vibration experienced by the Mo atoms they are bonded to.[66] The $A_{1g}$ modes indicate out-of-plane lattice vibrations of Mo-bound S atoms moving in opposite directions.[66] Further investigation of $E^1_{2g}$ and $A_{1g}$ modes provides insight into the amount of strain and layer thickness present within the MoS$_2$ samples.[45, 67, 68] The change in intensity of the $E^1_{2g}$ peak with respect to the $A_{1g}$ peak is associated with a decrease in layer thickness and is a typical sign of structural defects in the material's crystal structure.[66, 69] Furthermore, it provides additional evidence that the bulk catalyst material is dominated by the 1T-phase of MoS$_2$. Softening of the $A_{1g}$ mode arises from the weakening of interlayer coupling and stiffening of the $E^1_{2g}$ mode increases with decrease in the number of layers.[44] Likewise, the incorporation of defects (*i.e.* vacancies or dopants) into a material will produce new defect-induced peaks and/or increase the linewidths of peaks present in the Raman spectrum.[70] Upon comparing the Raman spectrum of 1T-MoS$_2$ to Zn 1T-MoS$_2$, the negligible difference in peak positions, lack of new peak formation, and similar peak widths observed imply that the overall structural features inherent to the 1T-MoS$_2$ nanosheets are well maintained in Zn 1T-MoS$_2$.

XRD patterns are provided in **Figure S2.8b** for MoS$_2$ phase confirmation. Both diffraction patterns of bulk 1T-MoS$_2$ and Zn 1T-MoS$_2$ powder samples were successfully indexed to Powder Diffraction File (PDF) #01-075-1539 which corresponds to the signature peaks of 1T-MoS$_2$.[71] XRD peak broadening is characteristic to nanomaterials and reveals the high concentration of defects in both samples.[72] This result is in agreement with the presence of oxidized Mo$^{6+}$ in the XPS spectra (**Figure 2.2**). Minor peaks present at $2\theta = 28.7°$ and $47.6°$ in the Zn 1T-MoS$_2$ XRD spectrum are assigned to ZnS (PDF #00-001-0792). ZnS is an expected side product formed by Zn$^{2+}$ ions that react either with excess thioacetamide or the S atoms released upon S vacancy formation in the reaction chamber during hydrothermal synthesis (see Materials and Methods section for Zn 1T-MoS$_2$ synthesis). Similar results have been previously reported.[6, 15] Both XRD and Raman spectroscopy are bulk characterization techniques, whereas XPS and SEM are surface-sensitive techniques. The minor presence of ZnS in the XRD spectrum that is absent in the XPS and Raman spectra indicates that some ZnS is likely present in the bulk region of the powder sample, but not on the surface where HER occurs. Thus, the ZnS phase is not considered to catalytically contribute to Zn 1T-MoS$_2$ or facilitate HER. In summary, structural characterizations provided by the SEM, EDX, XPS, Raman, and XRD data all prove the existence of Zn$^{2+}$ atoms in 1T-MoS$_2$.

*2.3.2 Photoelectrochemical HER Performance*

Resulting PEC analysis of HER performance under acidic conditions of bare SiNWs, Pt/SiNWs, and Zn 1T-MoS$_2$/SiNWs is provided in **Figure 2.3**. To determine the best catalyst concentration for optimal PEC performance, the Zn 1T-MoS$_2$/SiNWs were investigated with the following concentrations: 1, 5, 10, and 15 mg mL$^{-1}$. Resulting onset potentials (E°$_{onset}$),

overpotentials ($\eta$), saturated potentials ($E°_{sat}$), and maximum photocurrent densities ($J_{max}$) extracted from the linear sweep voltammograms (LSVs) shown in **Figure 2.3a** are provided in **Table S2.3**. The results show that as the catalyst concentration of the Zn 1T-MoS$_2$/SiNWs samples increased, $E°_{onset}$ and $E°_{sat}$ both became more positive and $J_{max}$ decreased (see the Materials and Methods section for parameters used to define $E°_{onset}$ and $E°_{sat}$). Of the electrodes tested, the electrode with 1 mg mL$^{-1}$ catalyst concentration (Zn 1T-MoS$_2$(1mg/mL)/SiNWs) produced the most comparable $E°_{onset}$ (425 mV), $E°_{sat}$ (-302 mV), and $J_{max}$ (36.5 mA cm$^{-2}$) values to those of the Pt/SiNWs electrode (355 mV, -277 mV, and 37.2 mA/cm$^2$, respectively). When high concentrations of catalytic material are employed in a PEC device, the distance between metal centers within the catalyst decreases, and the generated electron/hole pairs suffer from charge recombination, causing the decrease in PEC efficiency observed as the catalyst concentration increased.[73] Further comparison of the Zn 1T-MoS$_2$(1mg/mL)/SiNWs electrode provided in **Table S2.4** demonstrates this electrode's performance compared to previously reported state-of-the-art MoS$_2$/SiNWs interfaces.

To understand the mechanism and rate-determining step for HER, Tafel slopes corresponding to the LSVs collected (**Figure 2.3a**) were plotted and are provided in **Figure 2.3b**. In accordance with the LSV results, the Tafel slope produced by each sample increased as the catalyst concentration increased. The Zn 1T-MoS$_2$(1mg/mL)/SiNWs produced the lowest Tafel slope (42 mV dec$^{-1}$). This slope indicates that HER at the Zn 1T-MoS$_2$ active sites follows the Volmer-Heyrovsky mechanism, where the desorption of H$_2$ is the rate-determining step (**Figure S2.4**).[74] Work published by Qian *et. al.* demonstrated the ability to lower the Tafel slope of MoSe$_2$ from 92 mV dec$^{-1}$ to 58 mV dec$^{-1}$ by doping Zn into the MoSe$_2$ lattice.[75] Liu *et. al.* reported a 35 mV dec$^{-1}$ Tafel slope for Zn-MoS$_2$ and concluded that HER follows the Volmer-Heyrovsky

mechanism, where electrochemical desorption is the rate limiting step, in agreement with our results.[76] Shi *et. al.* reported a 51 mV dec[-1] Tafel slope for Zn-doped 2H-MoS$_2$, concluding that the rate limiting step involves the recombination of two adsorbed H atoms and the presence of Zn makes HER more favorable.[17] Theoretical calculations predict 1T-MoS$_2$'s Tafel slope to be 60 mV dec[-1].[77] However, this prediction is based on the assumption that the HER-facilitating active sites are restricted to the edge sites in 1T-MoS$_2$. Voiry *et al.* reported a 41-46 mV dec[-1] Tafel slope
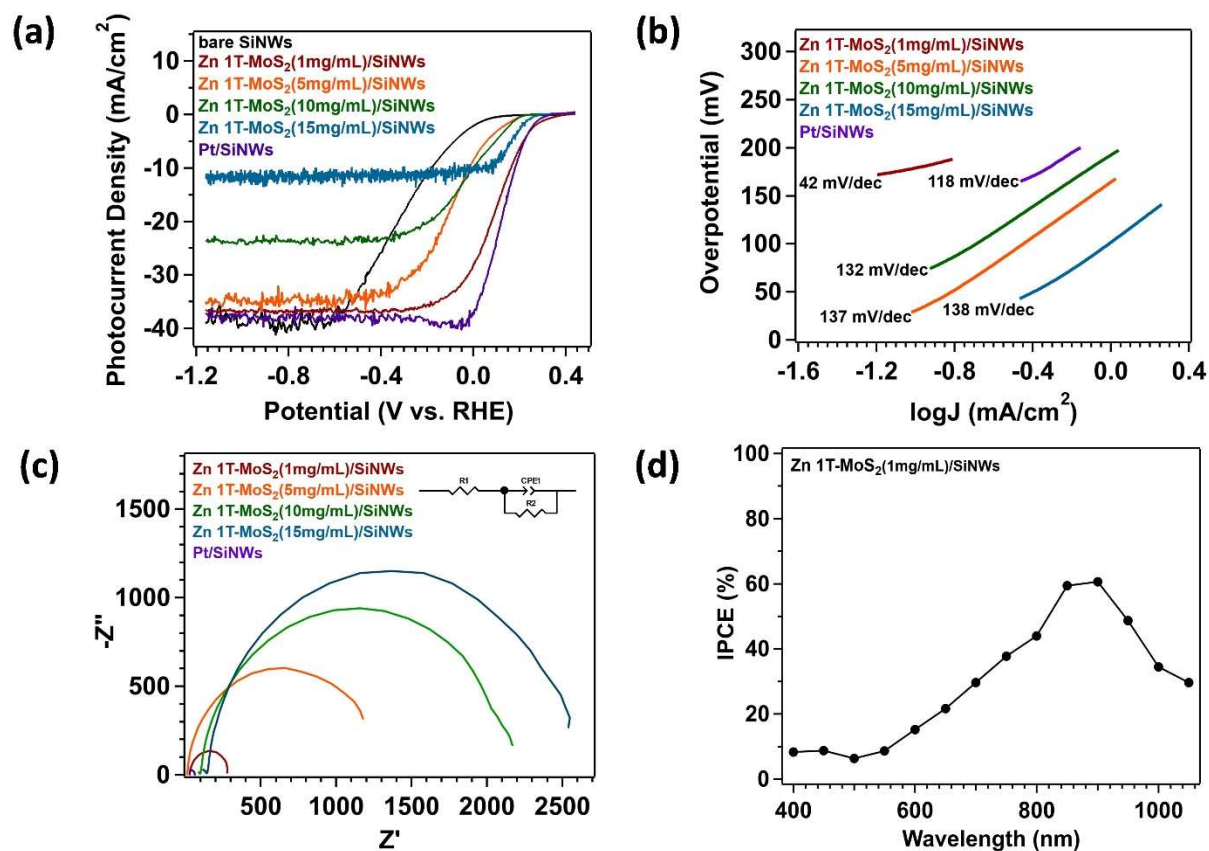


**Figure 2.3:** Electrochemical performance of the bare SiNWs, Pt/SiNWs, and Zn 1T-MoS$_2$/SiNWs at the following concentrations: 1, 5, 10, and 15 mg mL^{-1}.
All tests were performed in 0.5 M H$_2$SO$_4$. **(a)** LSVs. **(b)** Tafel plot. **(c)** Nyquist plot fitted to the equivalent circuit shown. **(d)** IPCE of the Zn 1T-MoS$_2$(1mg/mL)/SiNWs. An applied bias of -0.4 V was employed for all IPCE measurements.

before iR correction for 1T-MoS$_2$ nanosheets under acidic conditions.[22] In this work, the lower Tafel slope is attributed to the participating HER active sites located along the basal plane of 1T-MoS$_2$. To evaluate the performance of 1T-MoS$_2$ on SiNWs against that of Zn 1T-MoS$_2$, 1 mg mL[-]

[1] of 1T-MoS$_2$ was drop cast onto SiNWs (1T-MoS$_2$/SiNWs) and analyzed by LSV. Compared to the E°$_{onset}$ (303 mV) and E°$_{sat}$ (-477 mV) of 1 mg mL$^{-1}$ produced by the 1T-MoS$_2$/SiNWs, the Zn 1T-MoS$_2$(1mg/mL)/SiNWs exhibit a positive shift in E°$_{onset}$ (425 mV) and E°$_{sat}$ (-302 mV) (**Figure S2.9**). These results confirm the improvement in catalytic activity induced by the presence of Zn in 1T-MoS$_2$. The Pt/SiNWs Tafel slope reported (118 mV dec$^{-1}$) is much higher than Tafel slopes for Pt/C (~30 mV dec$^{-1}$) most commonly reported in similar studies.[17, 50, 56, 76] Deviation of experimental Tafel slopes from theoretical predictions tends to occur for reasons related to the solvent environment, surface defects, finite coverage of adsorbed H atoms, potential-induced changes in the reaction mechanism, interactions between the electrode's surface and the adsorbed species, and/or variation in experimental conditions.[78] In a previous HER kinetics study using the same electrolyte (0.5 H$_2$SO$_4$), Pt(100) was confirmed to exhibit two Tafel slopes: ~37 mV dec$^{-1}$ at low overpotentials and ~112 mV dec$^{-1}$ at high overpotentials.[79] Additionally, the Pt(100) surfaces were reported to follow the Volmer-Heyrovsky HER mechanism. Here, we postulate that the Pt deposited on the Pt/SiNWs may be similar to the (100) phase. Theoretical Pt(100) Tafel slopes are known to follow the linear relationship described in **Equation (2.1)**:[79]

$$b = 2\left(\frac{2.3RT}{F}\right) \tag{2.1}$$

where R is the gas constant, T is the temperature, and F is Faraday's constant. By this relationship (**Equation 2.1**), the theoretical Tafel slope for Pt(100) is equal to 118 mV dec$^{-1}$, which in agreement with the experimental Tafel slope reported for the Pt/SiNWs.

Nyquist plots were collected to compare limitations caused by charge and mass transport experienced by the various concentrations of Zn 1T-MoS$_2$/SiNWs and Pt/SiNWs (**Figure 2.3c**). All results were fitted to an equivalent circuit (inset of **Figure 2.3c**). The decreasing trend in the semicircle radius is proportional to the decreasing concentration of Zn 1T-MoS$_2$ and indicates a

decrease in charge and mass transport limitations. Corresponding calculated charge-transfer resistance ($R_{ct}$) results demonstrate the same trend (**Table S2.5**). The lowest $R_{ct}$ is produced by the Pt/SiNWs, as expected. Of the various catalyst concentrations studied, the Zn 1T-MoS$_2$(1mg/mL)/SiNWs experiences the least charge transport limitations and yield the most comparable results to the Pt/SiNWs, in agreement with the LSV results.

The incident photon-to-current efficiency (IPCE) of the Zn 1T-MoS$_2$(1mg/mL)/SiNWs electrode was measured to understand how efficiently this PEC device converts incident light into electrical energy across the near-ultraviolet (UV) to the near-infrared (IR) wavelength range (**Figure 2.3d** and **Table S2.6**). Maximum IPCE values of ~60% are achieved at the near-IR range (850-900 nm), which is comparable to the IPCE values of previously reported studies involving SiNWs.[80, 81] While an ideal IPCE plot will show a square curve with near 100% efficiency, most devices cannot achieve this ideal conversion performance due to carrier recombination effects. When incident photons strike a semiconductor's surface, charge carriers are generated, which consist of majority and minority carriers. Since the SiNWs in this study are fabricated from p-type Si, the minority carriers here are electrons and the majority carriers are holes. The photogenerated minority carriers must travel a distance equivalent to the absorption depth of the incident photons to reach the conduction band and react with available H$^+$ ions to generate H$_2$. If the minority carrier diffusion length and bandgap between the valence and conduction bands are shorter than the incident photon's absorption depth, the photoexcited charge carriers will recombine and the IPCE will decrease.[82] Thus, the decrease in efficiency shown in the lower wavelength region is an indication of charge recombination limiting device efficiency. Previously, a study by He *et al.* revealed the indirectly proportional relationship between SiNWs length and IPCE at lower wavelengths.[81] Therein, the enhanced aggregation experienced in longer SiNWs resulted in greater

charge recombination losses across lower wavelength regions. In this work, the fabricated SiNWs maintained lengths ranging between 7.5-9 μm (**Figure S2.3**). Light traveling at shorter wavelengths cannot reach the junction and achieve charge separation if the diffuse distance is too long. When this occurs, carriers recombine instead of reacting with $H^+$ ions. Likewise, the occurrence of bunching at the tips of the SiNWs (**Figure 2.1b**) also limits photon absorption by reducing the amount of exposed semiconductor surface area to an extent. On the other hand, current generation with wavelengths above 1100 nm is limited by Si's 1.12 eV bandgap.[83] Overall, the PEC performance and IPCE indicate that the Zn 1T-MoS$_2$(1mg/mL)/SiNWs experience some charge recombination but still provide a competitive, low-cost catalyst-semiconductor interface for effective PEC H$_2$ generation.

*2.3.3 Stability Performance*

To evaluate the stability performance over long-term operation, the bare SiNWs and Zn 1T-MoS$_2$(1mg/mL)/SiNWs were each subjected to 24 hours of continuous electrolysis in acidic media (**Figure 2.4**). Resulting 24-hour electrolysis under both light and dark conditions demonstrates the photocatalytic activity of Zn 1T-MoS$_2$(1mg/mL)/SiNWs (**Figure S2.11**). After 24-h electrolysis, the bare SiNWs and Zn 1T-MoS$_2$(1mg/mL)/SiNWs retained approximately 20% and 85% of their photocurrent densities, respectively. XPS evaluation before and after electrolysis demonstrate an 18% increase in SiO$_x$ content for the bare SiNWs (**Figures S2.12a, S2.12b**), whereas the Zn 1T-MoS$_2$(1mg/mL)/SiNWs exhibit a 2% increase in SiO$_x$ growth (**Figures S2.12c, S2.12d**). Although slight loss of catalyst is experienced during electrolysis, retention of the catalyst-semiconductor interface is evidenced by the presence of Mo and S along the SiNWs surface, as determined by post-electrolysis cross-sectional SEM and EDX analysis (**Figure S2.13**).

Based on these results, the improvement in SiNWs operation lifetime is ascribed to the reduced

growth of $SiO_x$ witnessed when Zn 1T-$MoS_2$ is drop casted along the SiNWs surface. Upon drop
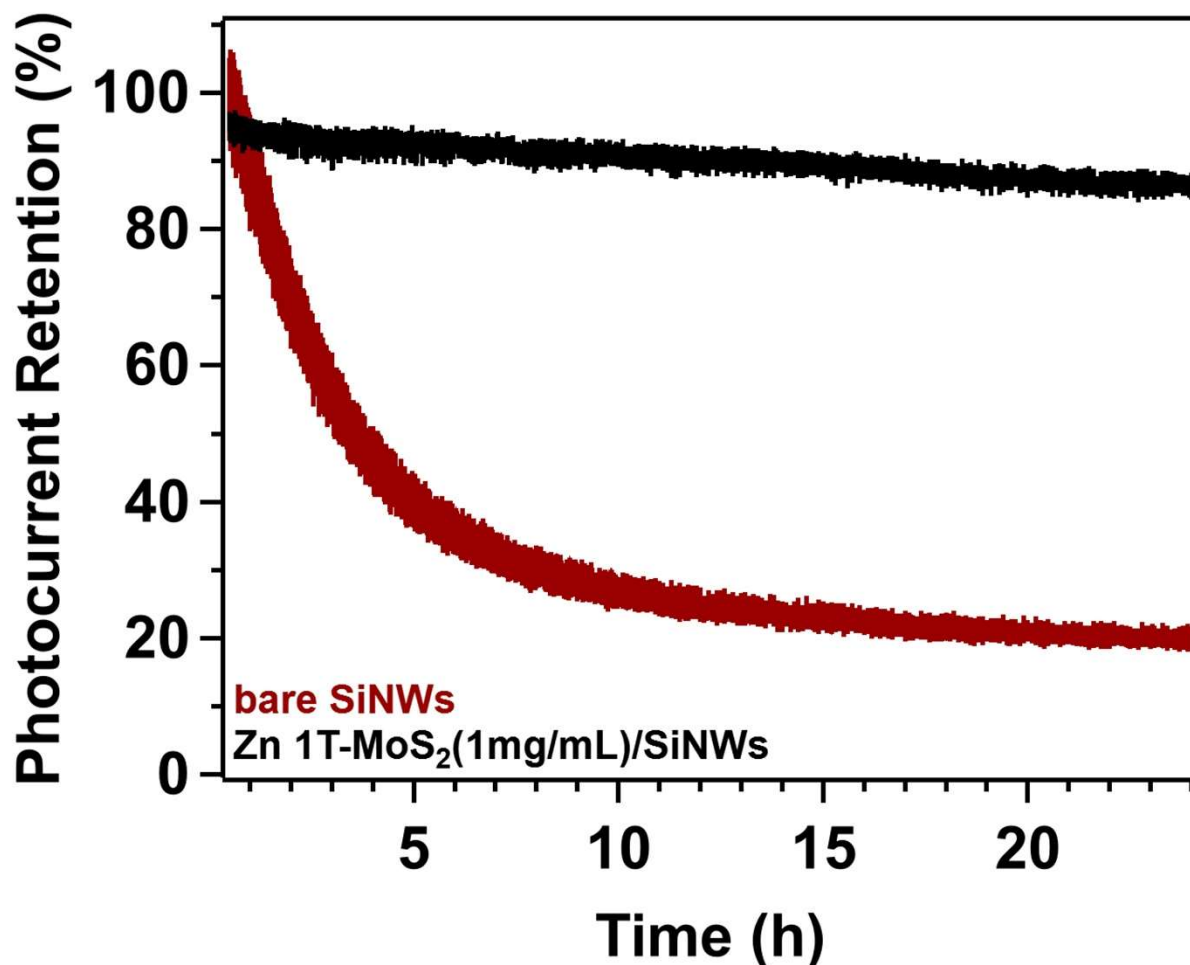


**Figure 2.4:** Photocurrent degradation over 24 h of operation.
Stability tests ran at the following saturated potentials: bare SiNWs = -0.8 V; Zn 1T-$MoS_2$(1mg/mL)/SiNWs = -0.6 V. Photocurrents retained: bare SiNWs = 20%; Zn 1T-$MoS_2$(1mg/mL)/SiNWs = 85%. The stability tests were conducted in 0.5 M $H_2SO_4$ electrolytic solution using a split electrochemical cell with three-electrode configuration. Ag/AgCl was used as the reference electrode and a graphite rod was employed as the counter electrode. The half cells were separated by a Nafion[TM] 211 semi-permeable membrane.

casting Zn 1T-$MoS_2$ onto the SiNWs, the catalyst primarily deposits across the top of the SiNWs

(**Figures 2.1d, S2.5**). Doing so allows the layer of Zn 1T-$MoS_2$ to passivate dangling bonds along

the SiNWs surface that would otherwise be oxidized into insulating $SiO_x$ when exposed to water.[3]

As a result, Zn 1T-MoS$_2$ slows oxidation of the SiNWs surface which in turn extends the photocathode's operation lifetime.

The H$_2$ evolution and Faradaic efficiency plots (**Figure S2.14**) show a 2.44 μmol min$^{-1}$ H$_2$ generation rate with high catalytic selectivity for HER. These results suggest that this catalytic system can efficiently and selectively use the supplied electrical energy for HER. Calculations of turnover frequency (TOF) and turnover number (TON) to determine the amount of H$_2$ able to be catalytically generated per active site per second are provided in the Supporting Information. Resulting values include a 0.53 s$^{-1}$ TOF and 45,792 TON for Zn 1T-MoS$_2$. These values are indicative of the high catalytic activity and selectivity Zn 1T-MoS$_2$ exhibits towards HER.

LSVs before and after 24-hour electrolysis for each sample tested were collected to unveil more insight into the changes occurring to the catalyst-semiconductor interface over time (**Figure S2.15**). Experimental values of E°$_{onset}$, E°$_{sat}$, and J$_{max}$ before and after 24-hour electrolysis for each electrode is provided in **Table S2.7**. The bare SiNWs (**Figure S2.15a**) experienced an almost complete loss in J$_{max}$ and an increase of 225 mV *vs*. RHE in E°$_{onset}$. E°$_{sat}$ after electrolysis was unable to be determined because the electrode's potential would not saturate. The major decline in photocurrent density demonstrates the instability of the liquid-semiconductor interface when the bare SiNWs surface is directly exposed to the electrolyte. In contrast, the Zn 1T-MoS$_2$/SiNWs (**Figure S2.15b**) lost ~20% of the initial J$_{max}$ measured, E°$_{onset}$ increased by 143 mV *vs*. RHE, and E°$_{sat}$ negatively shifted by 89 mV *vs*. RHE. The smaller shift in E°$_{onset}$ for the Zn 1T-MoS$_2$(1mg/mL)/SiNWs demonstrates the ability of Zn 1T-MoS$_2$ to protect Si nanostructures from HER performance degradation over extended operation lifetimes. Overall, these findings not only highlight how catalytically active, selective, and stable the Zn 1T-MoS$_2$/SiNWs interface is towards HER, but also validate its potential for successful long-term PEC H$_2$ generation.

## 2.4 Conclusions

The research presented attempts to mitigate the two major challenges experienced by PEC $H_2$ generation devices. First, the need to discover an Earth-abundant catalyst with a catalytic performance comparable to Pt. Second, developing a catalyst-semiconductor interface that reduces the growth of $SiO_x$ on SiNWs and improves PEC operation lifetimes. Resulting evaluation of PEC performance indicates that Zn 1T-MoS$_2$(1mg/mL)/SiNWs perform comparably to Pt/SiNWs in terms of onset potential and maximum photocurrent density. Furthermore, Zn 1T-MoS$_2$(1mg/mL)/SiNWs produces a smaller Tafel slope than the Pt/SiNWs (42 mV dec$^{-1}$ compared to 118 mV dec$^{-1}$). The reduction in $SiO_x$ growth when Zn 1T-MoS$_2$ is drop casted onto SiNWs was determined to enable the SiNWs to retain 66% more photocurrent after 24 hours of electrolysis. Current and future applications of semiconductor devices demand high-performance systems that prevent the accumulation of insulating oxide layers and fast charge transfer kinetics. Here, we demonstrate how modifying SiNWs interfaces with Zn 1T-MoS$_2$ provides a potential solution to simultaneously achieve the aforementioned goals.

## 2.5 Materials and Methods

### 2.5.1 Chemicals

Ammonium heptamolybdate tetrahydrate [$(NH_4)_6Mo_7O_{24}\cdot4H_2O$, 99%, Alfa Aesar] and thioacetamide ($C_2H_5NS$, 99+%, Acros Organics) were used without further purification.

## 2.5.2 1T-MoS$_2$ Synthesis

1T-MoS$_2$ nanosheets were synthesized hydrothermally according to the following procedure. First, 50 mg of $(NH_4)_6Mo_7O_{24} \cdot 4H_2O$ (Mo$_7$) and 80 mg of $C_2H_5NS$ were added together in a 25 mL autoclave, diluted with 10 mL of deionized water, and sonicated until fully dissolved. Afterwards, the autoclaves were sealed within a hydrothermal reactor and heated at 180°C for 24 hours. Once heating ceased and reactors cooled down to room temperature, the catalyst solution was transferred to 14 mL vials, washed, and centrifuged six times: twice with deionized (DI) water, twice with 200 proof ethyl alcohol, and twice with acetone. The supernatant layer was removed from the vials after each centrifugation step. Upon completion of washing, the catalyst material was dried at ~100°C for 24 hours, finely ground into a powder, and stored under ambient conditions.

## 2.5.3 $(NH_4)_4[ZnMo_6O_{24}H_6] \cdot 5H_2O$ Synthesis

$(NH_4)_4ZnMo_6O_{24}H_6 \cdot 5H_2O$ (ZnMo$_6$) was prepared in accordance with previous publications.[24, 84] In detail, 6180 mg Mo$_7$ (5 mmol) was dissolved into 80 mL of DI water under bath sonication, then heated to 100°C. 1487 mg $Zn(NO_3)_2 \cdot 6H_2O$ (5 mmol) was dissolved into 20 mL of DI water by bath sonication, then added to the Mo$_7$ solution under vigorous magnetic stirring. Heating and stirring of the mixture were maintained for 2 h until the crude product was obtained. After, the crude product was isolated by filtration and purified by recrystallizing twice in hot water maintained at 80°C. The final product was dried in a vacuum oven at 50°C for 24 hours to obtain the desired ZnMo$_6$ precursor, which was stored under ambient conditions.

*2.5.4 Zn 1T-MoS$_2$ Synthesis*

Zn 1T-MoS$_2$ nanosheets were synthesized hydrothermally according to the following procedure. First, 50 mg of ZnMo$_6$ and 80 mg of C$_2$H$_5$NS were added together in a 25 mL autoclave, diluted with 10 mL of deionized water, and sonicated until fully dissolved. Afterwards, the autoclaves were sealed within a hydrothermal reactor and heated at 180°C for 24 hours. Once heating ceased and reactors cooled down to room temperature, the catalyst solution was transferred to 14 mL vials, washed, and centrifuged six times: twice with deionized water, twice with 200 proof ethyl alcohol, and twice with acetone. The supernatant layer was removed from the vials after each centrifugation step. Upon completion of washing, the catalyst material was dried at ~100°C for 24 hours, finely ground into a powder, and stored under ambient conditions. A dopant concentration of 6.24 % Zn in Zn 1T-MoS$_2$ was confirmed by inductively coupled plasma optical emission spectrometry (ICP-OES).

*2.5.5 Silicon Nanowires Fabrication*

525 μm of (100)-oriented p-type boron-doped Si wafers with resistivity = 3-5 Ω cm (WaferPro LLC) were used. Prior to fabrication, each Si wafer was cut into quarters using a scorer for facile handling during SiNWs synthesis, followed by covering their backside with Kapton tape for protection. To clean the Si wafers, they were sonicated first in acetone for 5 min, then in DI water for 5 min. The SiNWs were prepared at room temperature, without stirring, using a modified adaption of a previously published MACE procedure.[85] Between each step during the MACE process, exposure to air was minimized as much as possible. Likewise, the wafers were laid flat in each solution to ensure vertical growth of SiNWs. First, the Si wafer was immersed in 5 wt% HF for 90 s to remove native Si oxides, followed by a quick dip in DI water. Next, the wafer was

immersed in 0.02 M AgNO$_3$/10 wt% HF solution for 60 s to grow metallic silver (Ag) nanoparticles onto the Si surface via electroless Ag deposition, followed by a quick dip in DI water. After, the wafer was transferred to a burial solution [10 wt% (5 M) HF to 30 wt% H$_2$O$_2$ to produce a volumetric ratio of 10:1] for 10 min, allowing the Ag nanoparticles to bury into the Si wafer and create the nanowires, followed by a quick dip in DI water. The wafer was then moved to a 35 wt% HNO$_3$ solution for 15 min to remove the Ag nanoparticles, followed by a quick dip in DI water. The resulting SiNWs were carefully dried with a Kimwipe and allowed to dry under air.

*2.5.6 Photoelectrode Fabrication*

After removing the Kapton tape from the SiNWs, the fabricated SiNWs were cut into appropriately sized pieces (0.1-0.3 cm$^2$). The backside of the SiNWs were washed with DI water and etched in 5 wt% HF for 30 s to remove surface oxides. Next, a thin layer of commercial Ga-In eutectic alloy was applied to the backside to create an ohmic contact. Then, the sample's backside was carefully pressed onto a spiral Cu wire coated with conductive Ag paint. Contact with the sample's surface was minimized as much as possible to avoid damaging the nanowires. Afterwards, the Cu wire's tail was passed through a glass tube to provide a mechanically stable body, leaving the spiral Cu wire holding the sample head assembly outside of the glass tube. The resulting electrode assembly was electrically insulated by covering any exposed Cu wire/Ag paint and the junction between the electrode's head and glass tube with Loctite E-120 HP epoxy adhesive. A second layer of epoxy was added after drying for 24 hours. After addition of the second layer of epoxy and prior to employment in any electrochemical experiments, the electrodes were dried for another 48 h under ambient conditions. Resulting electrodes all had exposed volumetric

areas between 0.1-0.3 cm$^2$. Surface areas were measured using Image J software (https://imagej.nih.gov/ij/).

### 2.5.7 Pt Nanoparticle Deposition

Electrodes were first etched in 5 wt% HF for 30 s, rinsed with DI water, and dried with N$_2$. Electrodes were then immersed in 5 mM K$_2$PtCl$_6$/1 wt% HF solution for 30 s, washed with DI water, then dried with N$_2$.

### 2.5.8 1T-MoS$_2$ and Zn 1T-MoS$_2$ Deposition

Electrodes were first etched in 5 wt% HF for 30 s, rinsed with DI water, and dried with N$_2$. One drop of Zn 1T-MoS$_2$ was then drop cast onto the electrode's surface using a 200 μL pipette and laid flat to dry for 5 min. This process was repeated twice for all electrodes employed herein unless otherwise stated. All electrochemical measurements were conducted immediately after the catalyst was deposited onto the electrodes.

### 2.5.9 Structural Characterization

SEM images and EDX analyses were collected using the FEI Quanta 450 FEG SEM at 20 eV. The same EDX operating conditions with the best achievable spatial and energy resolution were employed to acquire all elemental mappings reported. High-angle angular dark-filled scanning transmission electron microscopy (HAADF-STEM) images were acquired by a convergence semiangle of 22 mrad and inner and outer collection angles of 83 and 165 mrad, respectively. X-ray photoelectron spectroscopy (XPS) spectra were collected using the Kratos AXIS Supra equipped with a monochromatic Al Kα X-ray source, ran at 300 W, and operated at

37

15 kV. All XPS samples were measured within a 300 x 700 $\mu m^2$ spot size and operated at $<10^{-8}$ torr chamber pressure. The C 1s peak for aliphatic hydrocarbons at a binding energy of 284.8 eV was used as an internal binding energy reference. XPS spectra were fitted with XPSPEAK 4.1 software and the baseline was fitted to a Shirley background. 80% Lorentzian-Gaussian parameters were employed for all peak analyses and $\chi^2$ was maintained below 5.0 for all spectra analyzed.[86] Raman spectra were recorded using a Thermo Scientific DXR Raman microscope, employing an Ar-ion laser operating at 532 nm. FTIR spectra were measured using a PERKIN ELMER FTIR spectrometer. Powder XRD characterizations were performed on a Bruker D8 Advance X-ray diffractometer using Cu-Kα radiation ($\lambda = 1.5418$ Å).

### 2.5.10 Photoelectrochemical Measurements

All PEC measurements were conducted in 0.5 M $H_2SO_4$ electrolytic solution using a standard three-electrode configuration. A CHI 660E Electrochemical Workstation was used to perform all electrochemical testing, a visible light shortpass filter (FESH0750, Thor labs), and a steady DC-powered 150 W Xe arc lamp (New Port) light source calibrated to 100 mW cm$^{-2}$ using a Si photodiode provided one sun's illumination for accurate analysis. Comparative AM 1.5 and Xe Arc lamp power profiles are provided in our previously reported work.[87] Pt wire and Ag/AgCl (3 M NaCl, BASI) were employed as the counter and reference electrodes, respectively. Preparation of working electrodes employed the drop casting method to load catalyst material onto the semiconductor substrate (the SiNWs). Catalyst concentrations were prepared by diluting Zn 1T-$MoS_2$ with the volume of acetone appropriate for each desired concentration. All potentials reported were calibrated with respect to the Ag/AgCl reference electrode in acidic media (pH ≈ 0) using **Equation (2.2)**:

$$E_{RHE} = E_{Ag/AgCl} + 0.241 + 0.059pH \tag{2.2}$$

Linear sweep voltammograms (LSVs) were conducted under ambient conditions from 0.4 V to -1.4 V under the following parameters: scan rate = 0.1 V s$^{-1}$, sample interval = 0.001 V, and sensitivity = 0.001 A V$^{-1}$. Electrochemical impedance measurements for the reported Nyquist plots were performed at -0.05 V, with 0.005 V variation in the frequency range of 1-10$^5$ Hz and 12 steps per decade. Onset potentials were extracted from the LSV tests, defined as the potential at which the photocurrent began to increase (0.05 mA cm$^{-2}$). The saturation potential was defined as the potential at which the photocurrent value was saturated and ceased increasing.

*2.5.11 Stability Testing*

The stability tests were conducted in 0.5 M H$_2$SO$_4$ electrolytic solution using a split electrochemical cell with three-electrode configuration. Ag/AgCl was used as the reference electrode. To avoid the risk of Pt leaching during electrolysis, the half cells were separated by a Nafion$^{TM}$ 211 (purchased from Fuel Cell Store) semi-permeable membrane and a graphite rod was employed as the counter electrode. Stability tests were conducted at each photocathode's saturated potential (bare SiNWs = -0.8 V; Zn 1T-MoS$_2$(1mg/mL)/SiNWs = -0.6 V) using the amperometric technique and 0.001 A V$^{-1}$ sensitivity.

*2.5.12 Incident Photon-to-Current Efficiency (IPCE) Measurements*

All IPCE measurements were performed in a 0.5 M H$_2$SO$_4$ electrolytic solution using a standard three-electrode configuration. The chronoamperometric i-T technique using a CHI 660E Electrochemical Workstation and steady DC-powered 150 W Xe arc lamp (New Port) light source calibrated to 100 mW cm$^{-2}$ using a Si photodiode was employed for all IPCE measurements. Zn

1T-MoS$_2$(1mg/mL)/SiNWs was used as the working electrode, Pt wire was used as the counter electrode, and Ag/AgCl (3 M NaCl, BASI) was used as the reference electrode. An applied bias of -0.4 V was employed for all IPCE measurements. 10 nm band pass filters centered at 400, 450, 500, 550, 600, 650, 700, 750, 800, 850, 900, 950, 1000, and 1050 nm were used to limit wavelength ranges from the light source during the IPCE measurements. Photocurrent density at each irradiation intensity ($\Delta J_\lambda$) was monitored by finding the difference between the dark and irradiated photocurrent densities at a given applied voltage bias.[88] The total photon flux (I) was measured at each wavelength using an Si photodiode placed at an distance equivalent to the working electrode's position. IPCE (%) for monochromatic light at each wavelength measured was calculating using **Equation (2.3)**:

$$IPCE = \frac{1240 \times \Delta J_\lambda \left(\frac{mA}{cm^2}\right)}{\lambda(nm) \times I\left(\frac{mW}{cm^2}\right)} \times 100\% \tag{2.3}$$

All tabulated values are provided in **Table S2.4**.


### 2.5.13 Gas Chromatography and Faradaic Efficiency

H$_2$ concentrations were calibrated and measured with a Shimadzu GC-2010 Plus Tracera equipped with a Molecular Sieve 5Å capillary column and a barrier ionization discharge (BID) detector. 99.9999% He was used as the carrier gas. Split temperature was maintained at 200°C and the split ratio was set to 2.5 (split vent flow = 20.58 mL min$^{-1}$; column gas flow = 8.22 mL min$^{-1}$; purge flow = 0.5 mL min$^{-1}$). The column (0.53 mm, RT-Msieve 5A) temperature was maintained at 40°C and the BID temperature was maintained at 235°C. The BID detector gas flow rate was set to 50 mL min$^{-1}$. All calibration and sample gases were collected immediately prior to injection using a 50 μL Hamilton gas tight syringe. For H$_2$ calibrations, high purity sodium was reacted with deionized water in a septum-sealed glass vial to produce 1500 ppm of H$_2$. 5, 10, 15, 20, 25, and 30

μL samples (which correspond to 250, 500, 750, 1000, 1250, and 1500 ppm, respectively) of $H_2$ gas were injected in succession into the GC. Calibration curves were fitted by plotting the $H_2$ concentration against the $H_2$ peak are measured by GC. Calibration curve accuracy was confirmed with a standard Gasco $H_2$ calibration gas. The Faradaic efficiency (FE) for $H_2$ generation was calculated using **Equation (2.4)**:

$$FE_{H_2} = \frac{\text{number of } H_2 \text{ molecules} * 2}{\text{total current (Å)} * \text{time (s)}} * 100\% \tag{2.4}$$

### 2.5.14 ICP-OES

Sample compositions were quantified by an inductively coupled plasma optical emission spectrometer (Perkin Elmer Optima 3000 DV). Commercially available Zinc standard solutions (1000 mg/L in nitric acid, Sigma Aldrich) were used for calibration. The standards were diluted to 1000 ppb (ng/g), 500 ppb, 100 ppb, 50 ppb, and 1 ppb, respectively, by the mixed acid solutions (5 vol. % HCl + 5 vol. % $HNO_3$) to establish the calibration curves. The correction coefficient of the as-established calibration curves is 99.96% for Zn. All samples were dissolved in concentrated $HNO_3$ then diluted to a concentration of 5% with DI water, and finally Zn concentration was diluted ~25 times using the 5% $HNO_3$ for measurements.

## 2.6 Acknowledgements

## 2.7 Supplementary Information

*Turnover frequency (TOF) and turnover number (TON) calculations*

TOF and TON values were calculated as follows:

$$TOF \ (s^{-1}) = \frac{j\left(\frac{mA}{cm^2}\right) * A(cm^2)}{2 * F\left(\frac{C}{mol}\right) * n(mol)} = \frac{26.9\frac{mA}{cm^2} * \frac{1\,A}{10^3\,mA} * \frac{1\frac{C}{s}}{1\,A} * 0.209\,cm^2}{2 * 96485\frac{C}{mol} * 5.5 \times 10^{-8}\,mol} = 0.53\,s^{-1}$$

$j = current\ density;$

$A = electrode\ surface\ area;$

$F = Faraday's\ constant;$

$n = moles\ of\ H_2$

$$TON = TOF * length\ of\ stability\ test = 0.53\,s^{-1} \times \frac{60\,s}{1\,min} \times \frac{60\,min}{1\,h} \times 24\,h = 45{,}792$$
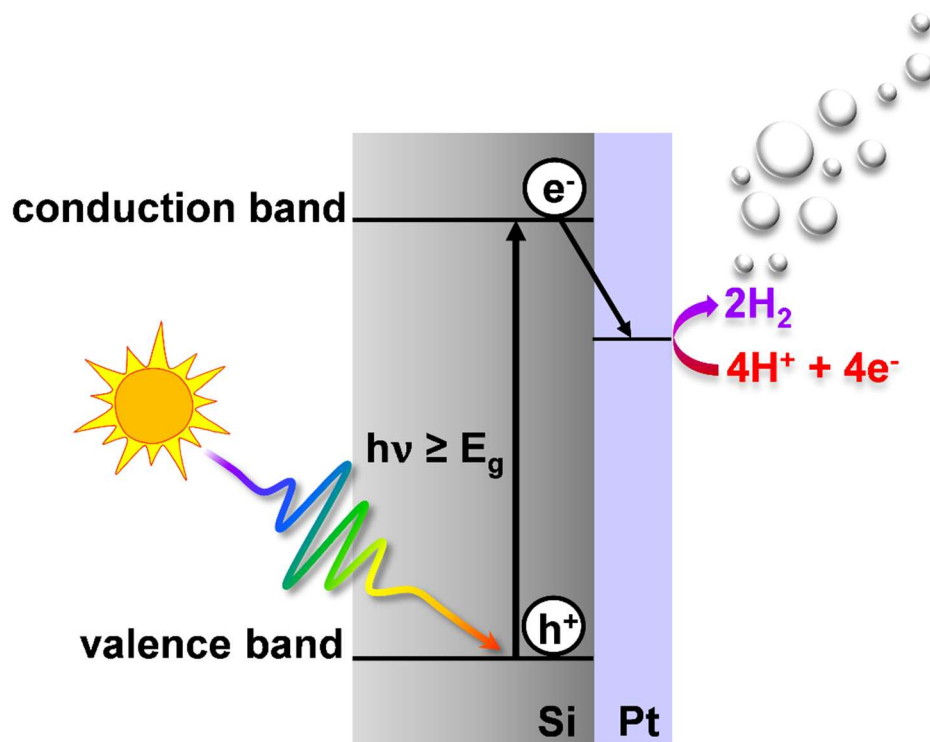
**Figure S2.1:** PEC H$_2$ generation schematic.



**STEP 1:** $H_3O^+ + e^- \rightarrow H_{ad} + H_2O$

**STEP 2:** $H_{ad} + H_3O^+ + e^- \rightarrow H_2 + H_2O$
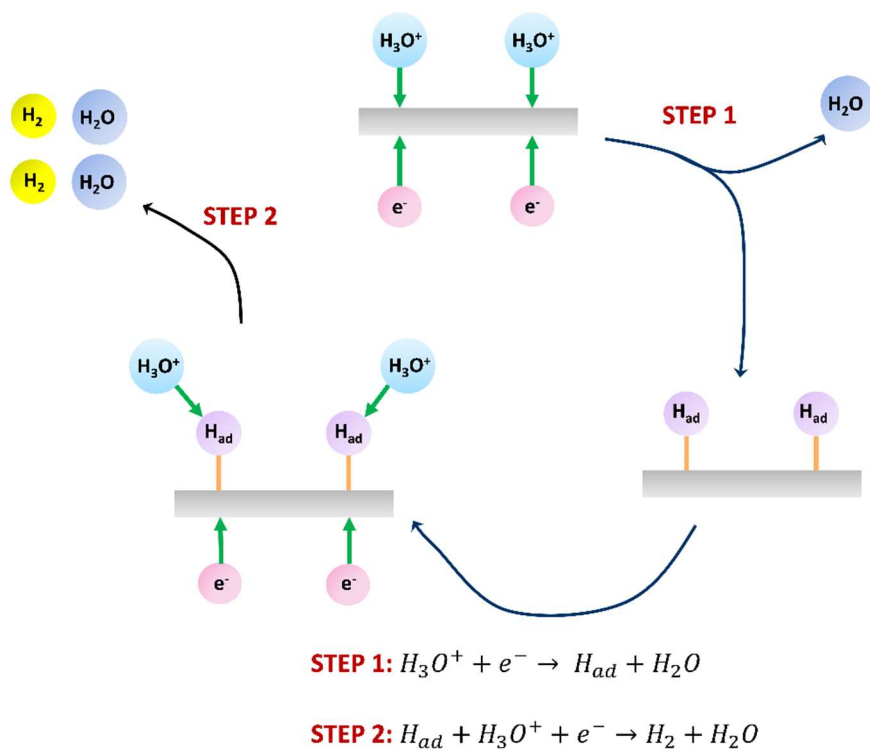
**Figure S2.2:** Schematic of Volmer-Heyrovsky HER mechanism.
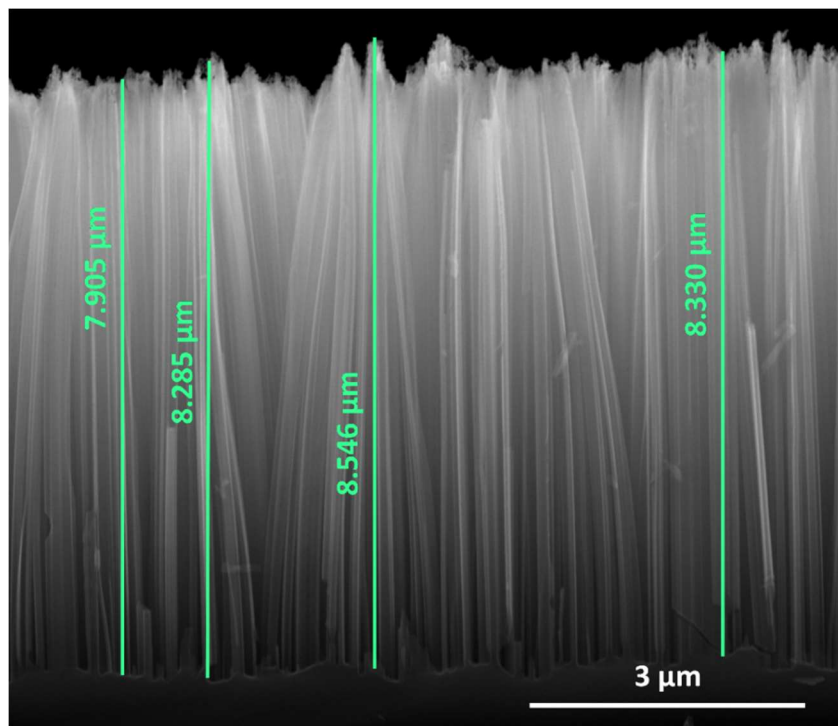
**Figure S2.3:** Cross-sectional SEM image of the bare SiNWs. Measured lengths are shown in green.
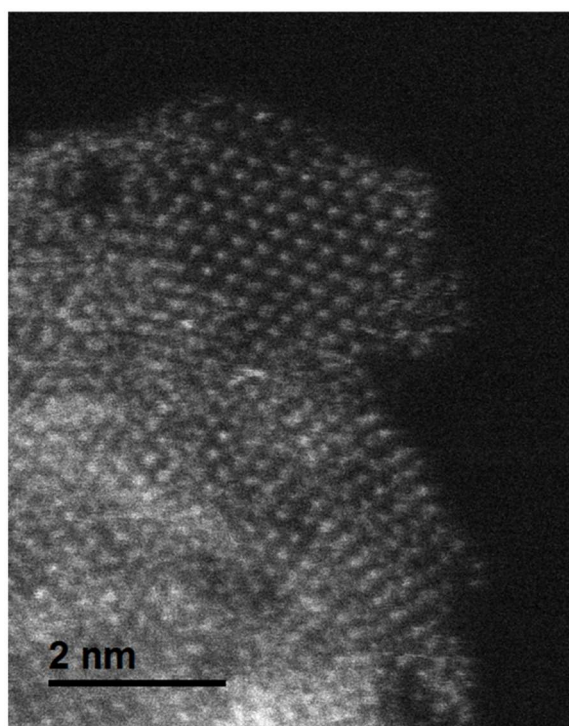


**Figure S2.4:** HADDF-STEM image confirming the successful synthesis of $MoS_2$ in the 1T phase.
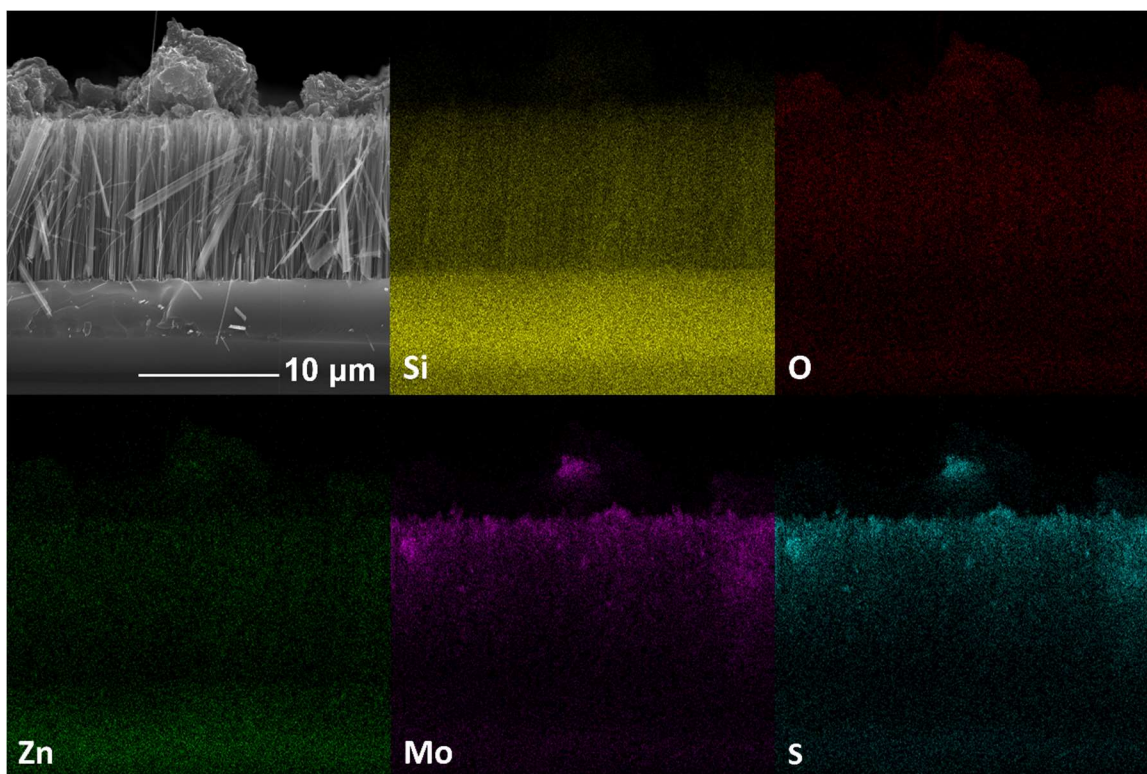
**Figure S2.5:** Zn 1T-MoS$_2$/SiNWs cross-sectional SEM images and corresponding EDX elemental mappings.
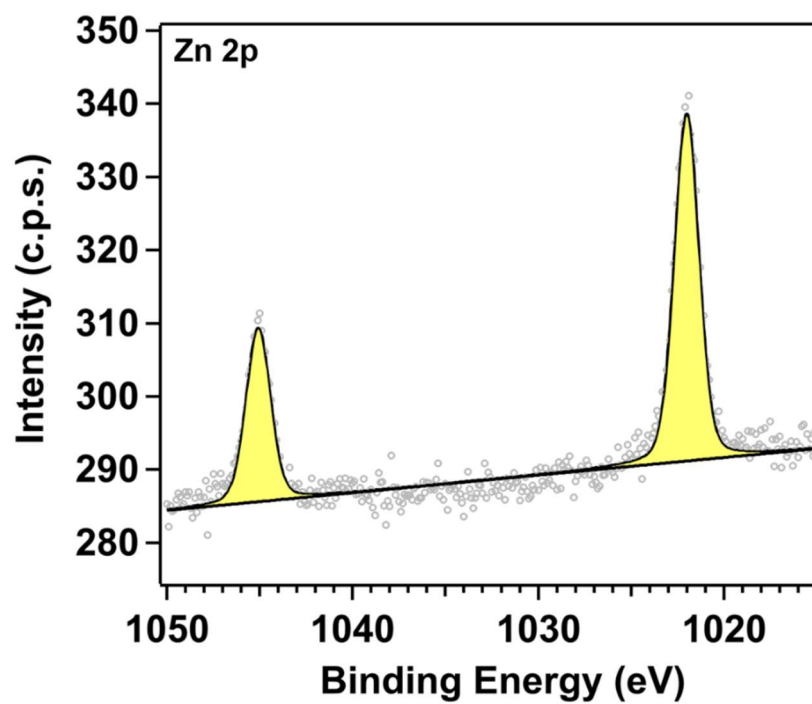


**Figure S2.6:** XPS spectra of Zn 2p peaks in Zn 1T-MoS$_2$.
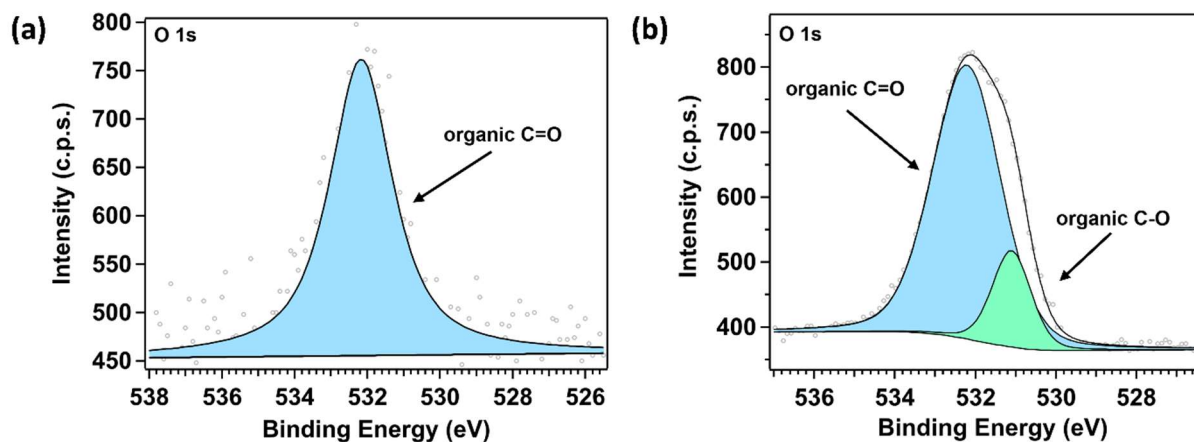
**Figure S2.7:** XPS spectra of the O 1s peak in **(a)** 1T-MoS$_2$ and **(b)** Zn 1T-MoS$_2$.
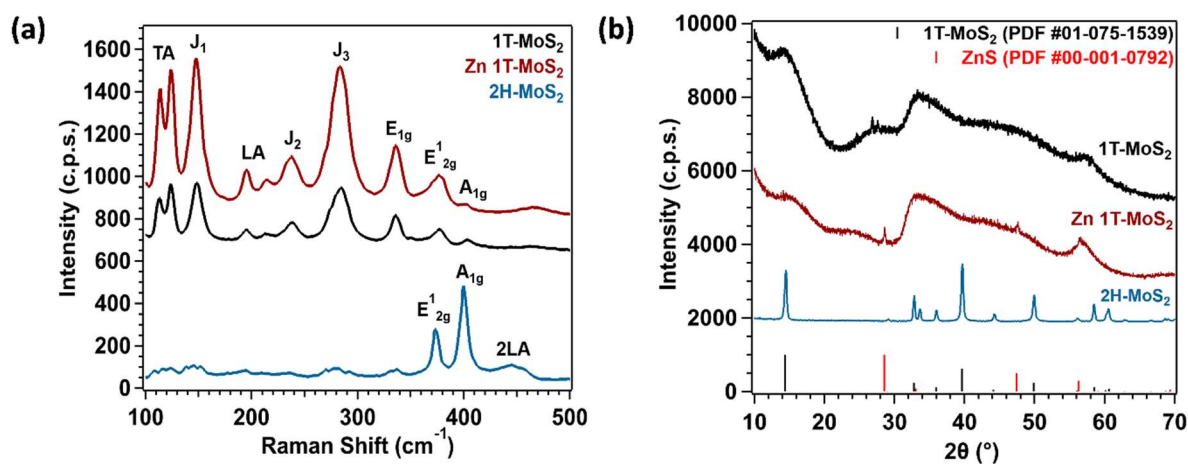


**Figure S2.8:** Structural characterization of Zn 1T-MoS$_2$ (red), 1T-MoS$_2$ (black), and 2H-MoS$_2$ (blue). **(a)** Raman spectra. **(b)** XRD spectra.
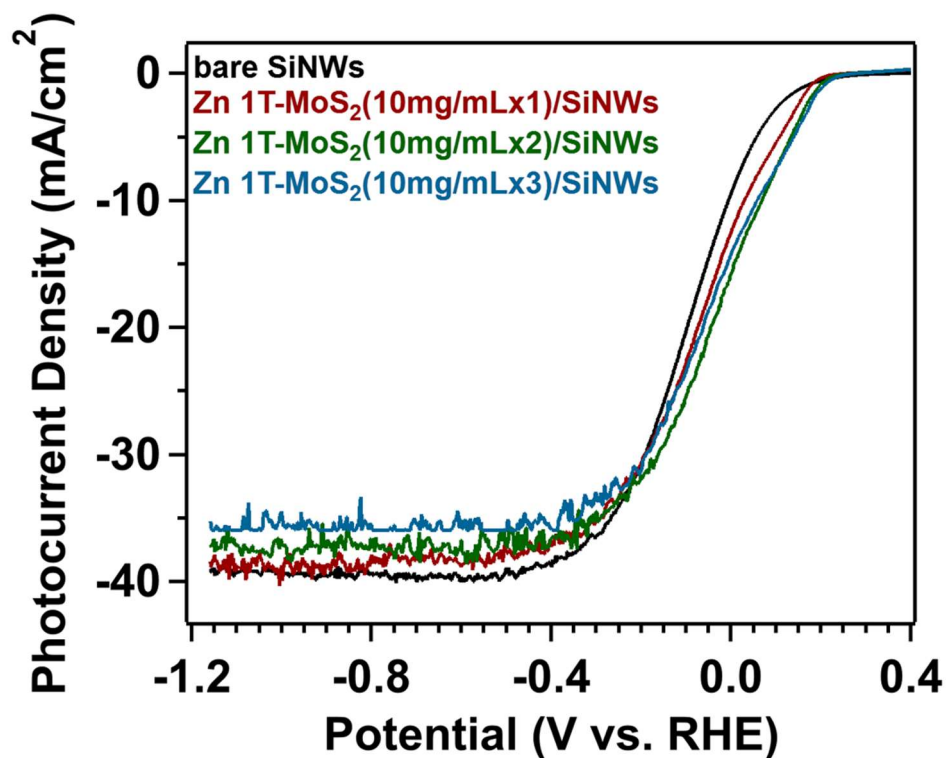
**Figure S2.9:** LSV comparison of the bare SiNWs (black), 1T-MoS$_2$/SiNWs (blue), and Zn 1T-MoS$_2$(1mg/mL)/SiNWs (red).

A 1 mg/mL concentration of 1T-MoS$_2$ was drop cast onto the SiNWs two times, similar to Zn 1T-MoS$_2$(1mg/mL)/SiNWs, to prepare the 1T-MoS$_2$/SiNWs electrodes.
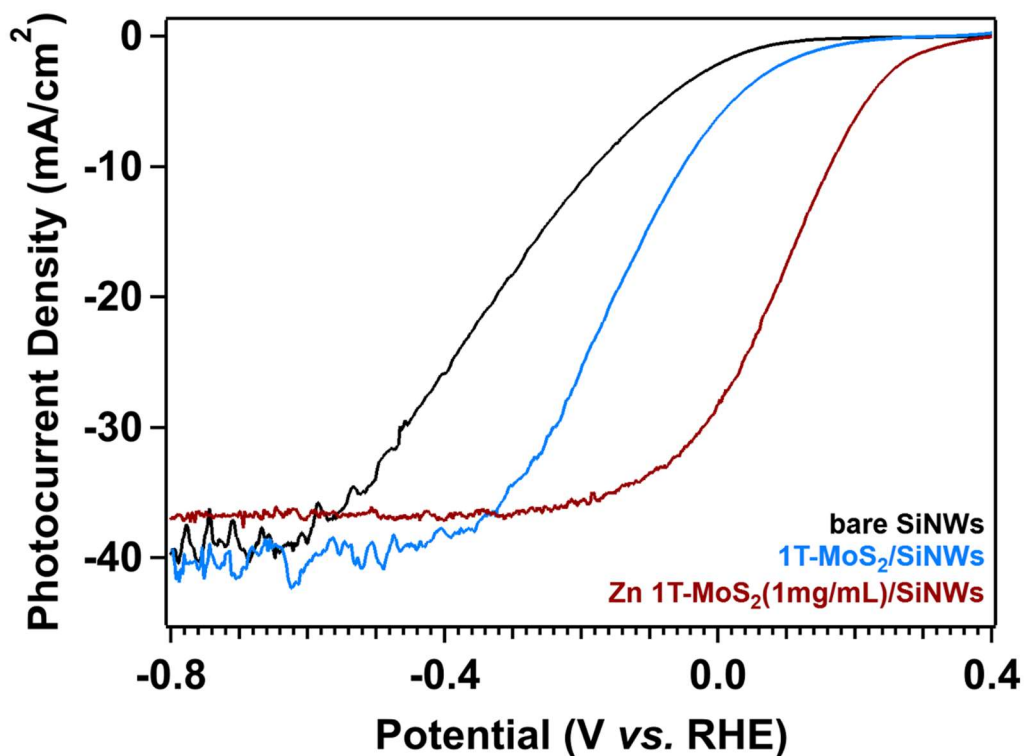
**Figure S2.10:** LSV comparison of the bare SiNWs to the Zn 1T-MoS$_2$/SiNWs with 10 mg/mL of Zn 1T-MoS$_2$ drop cast one (red), two (green), and three (blue) times.

LSV analysis of the performance of the Zn 1T-MoS$_2$/SiNWs with a constant catalyst concentration of 10 mg/mL and varied catalyst deposition was conducted. Bare SiNWs were compared against SiNWs loaded with 1, 2, and 3 drops of Zn 1T-MoS$_2$. While the difference is minor, results show that 2 drops of catalyst loaded onto the SiNWs provides the most positive onset potential. Therefore, the electrochemical analyses conducted throughout this study were performed with 2 drops of Zn 1T-MoS$_2$ loaded onto the SiNWs.
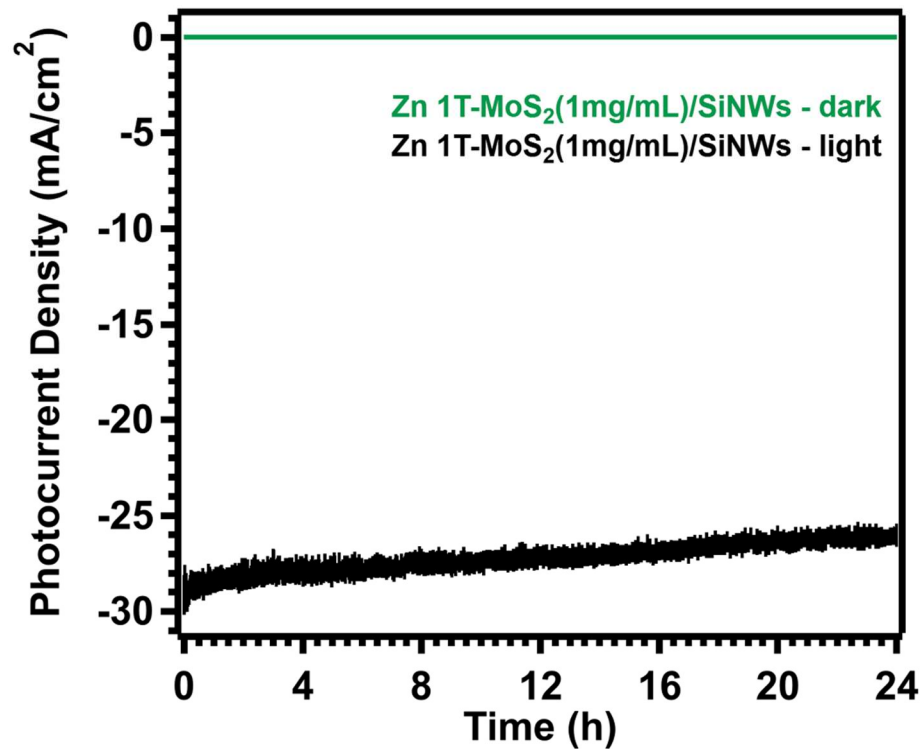
**Figure S2.11:** Comparison of Zn 1T-MoS$_2$(1mg/mL)/SiNWs undergoing 24 h electrolysis under dark (green) and light (black) conditions.
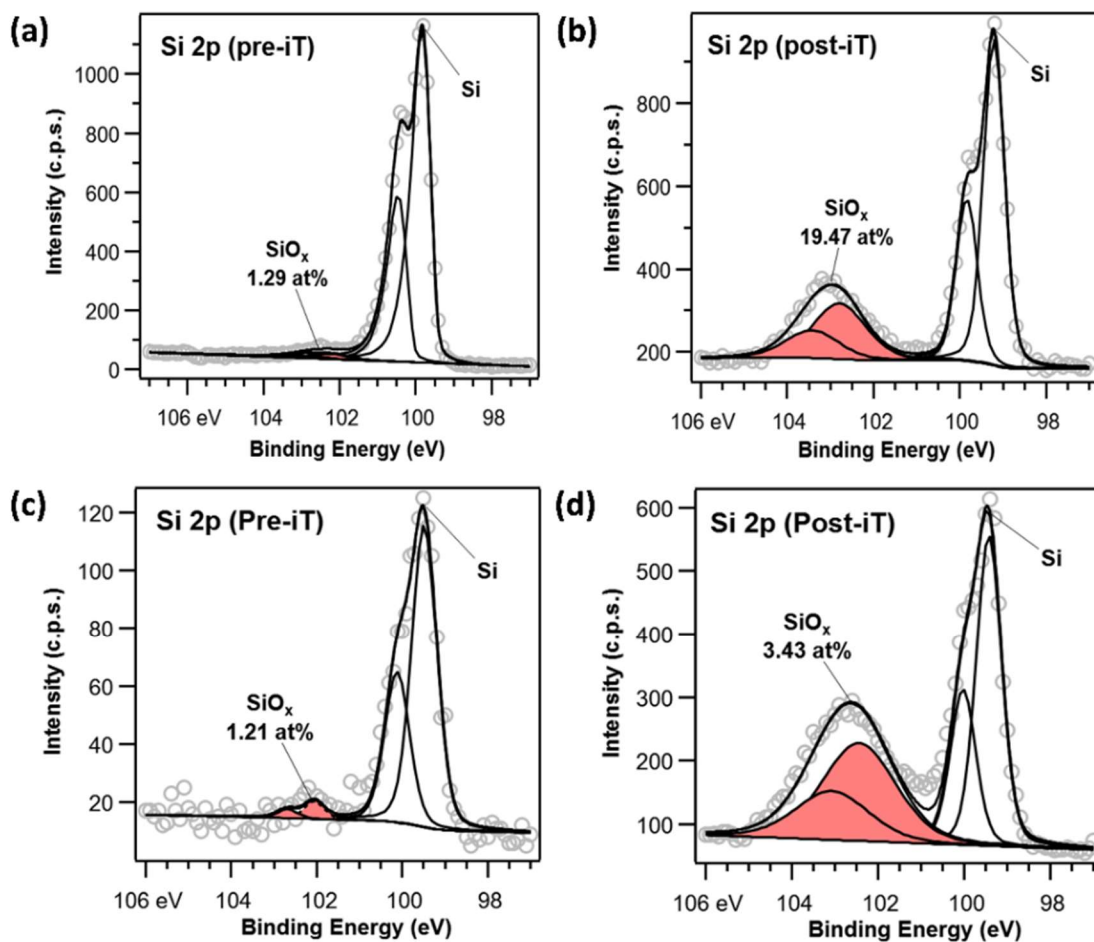
**Figure S2.12:** XPS analysis of SiO$_x$ growth in the bare SiNWs **(a-b)** compared to Zn 1T-MoS$_2$(1mg/mL)/SiNWs **(c-d)**.
The bare SiNWs **(a)** before and **(b)** after 24 h of electrolysis. Zn 1T-MoS$_2$(1mg/mL)/SiNWs **(c)** before and **(d)** after 24 h of electrolysis.
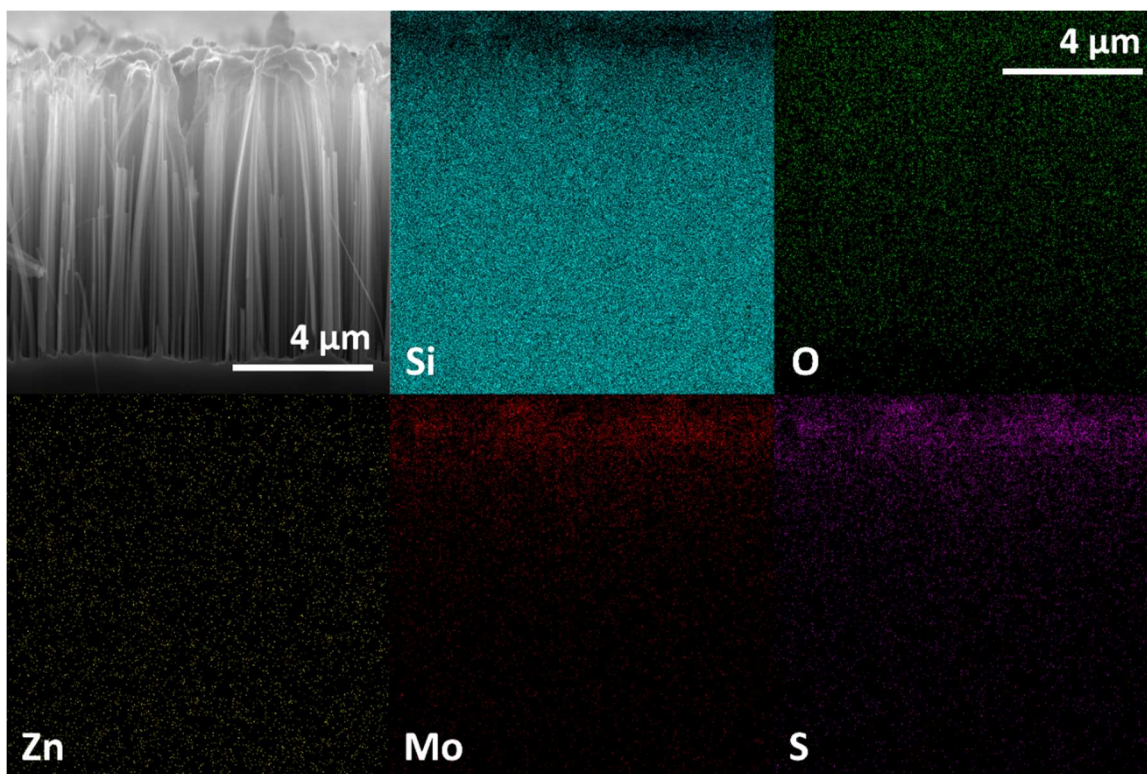
**Figure S2.13:** Cross-sectional SEM and EDX analysis of the Zn 1T-MoS$_2$(1mg/mL)/SiNWs after 24 h of electrolysis in 0.5 M H$_2$SO$_4$.
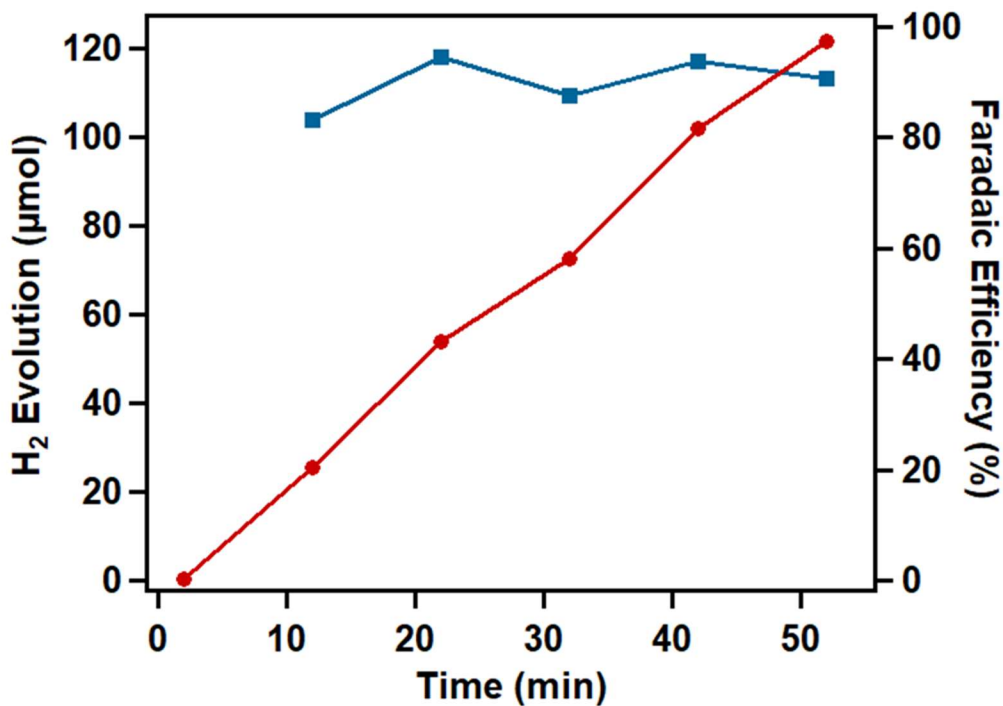
**Figure S2.14:** $H_2$ evolution (red) and Faradaic efficiency (blue) of the Zn 1T-MoS$_2$(1mg/mL)/SiNWs.
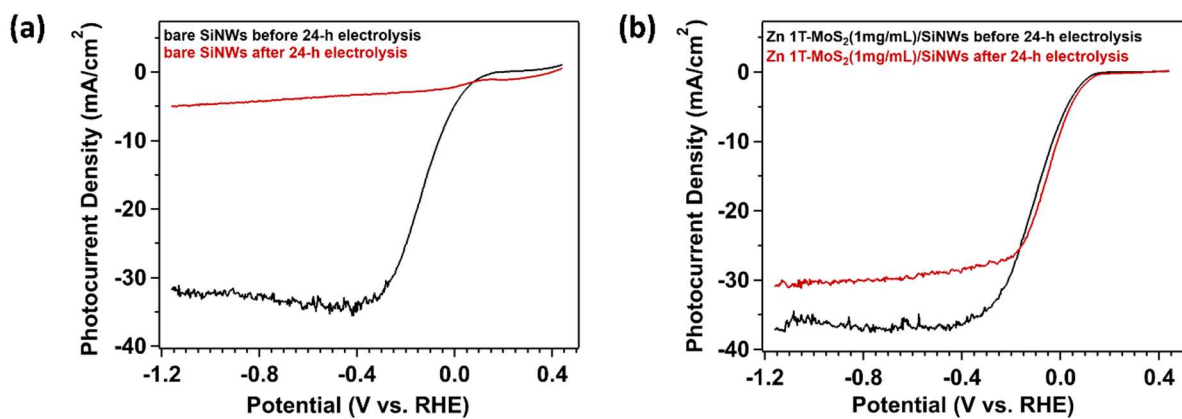


**Figure S2.15:** LSVs before and after 24-h electrolysis in 0.5 M $H_2SO_4$.
**(a)** Bare SiNWs. **(b)** Zn 1T-MoS$_2$(1mg/mL)/SiNWs.

**Table S2.1:** XPS peak assignments for 1T-MoS$_2$ and Zn 1T-MoS$_2$

| Line | Binding Energy (eV) | | Peak Assignments |
|------|---------------------|--------------------|------------------|
| | 1T-MoS$_2$ | Zn 1T-MoS$_2$ | |
| Zn 2p$_{1/2}$ | -- | 1023.5 | Zn$^{2+}$ |
| Zn 2p$_{3/2}$ | -- | 1046.6 | Zn$^{2+}$ |
| Mo 3d$_{5/2}$ | 229.1 | 229.2 | MoS$_2$, Mo$^{4+}$ |
| | 230.0 | 230.1 | MoS$_x$, Mo$^{6+}$ |
| Mo 3d$_{3/2}$ | 232.4 | 232.5 | MoS$_2$, Mo$^{4+}$ |
| | 233.3 | 233.6 | MoS$_x$, Mo$^{6+}$ |
| S 2p$_{3/2}$ | 162.1 | 162.1 | MoS$_2$, S$^{2-}$ |
| | 163.4 | 163.4 | MoS$_x$, S$^{2-}$ |
| S 2p$_{1/2}$ | 163.3 | 163.3 | MoS$_2$, S$^{2-}$ |
| | 164.6 | 164.6 | MoS$_x$, S$^{2-}$ |
| S 2s | 226.0 | 226.1 | MoS$_2$ |
| | 226.9 | 227.0 | MoS$_x$ |
| O 1s | -- | 531.1 | Organic C-O |
| | 532.2 | 532.2 | Organic C=O |

**Table S2.2:** Raman spectra peak assignments for 2H- MoS$_2$, 1T-MoS$_2$, and Zn 1T-MoS$_2$

| Peak Positions (cm$^{-1}$) | | | Peak Assignments |
|:---:|:---:|:---:|:---:|
| **2H-MoS$_2$** | **1T-MoS$_2$** | **Zn 1T-MoS$_2$** | |
| -- | 112 | 112 | TA |
| -- | 123 | 123 | TA |
| -- | 147 | 147 | J$_1$ |
| -- | 194 | 194 | LA |
| -- | 237 | 236 | J$_2$ |
| -- | 284 | 282 | E$_{1g}$ |
| -- | 335 | 335 | J$_3$ |
| 374 | 376 | 375 | E$^1_{2g}$ |
| 400 | 402 | 401 | A$_{1g}$ |
| 445 | -- | -- | 2LA |

**Table S2.3:** Resulting photoelectrochemical onset potentials ($E°_{onset}$), overpotentials ($\eta$), saturation potentials ($E°_{sat}$), and maximum current densities ($J_{max}$)

| Electrode | $E°_{onset}$ (mV *vs.* RHE) | $\eta$ (mV *vs.* RHE) | $E°_{sat}$ (mV *vs.* RHE) | $J_{max}$ (mA/cm$^2$) |
|---|---|---|---|---|
| Bare SiNWs | 370 | -182 | -655 | 37.8 |
| Pt/SiNWs | 355 | 181 | -277 | 37.2 |
| Zn 1T-MoS$_2$(1mg/mL)/SiNWs | 425 | 164 | -302 | 36.5 |
| Zn 1T-MoS$_2$(5mg/mL)/SiNWs | 321 | -17 | -360 | 34.9 |
| Zn 1T-MoS$_2$(10mg/mL)/SiNWs | 302 | -1 | -409 | 23.7 |
| Zn 1T-MoS$_2$(15mg/mL)/SiNWs | 324 | 97 | -88 | 16.5 |

$E°_{onset}$ values were defined as the potential at which the photocurrent began to increase (0.05 mA/cm$^2$). Overpotentials were measured at 10 mA/cm$^2$ photocurrent density.

**Table S2.4:** Comparison of HER performance of MoS$_2$-based catalysts in 0.5 M H$_2$SO$_4$

| Electrode Catalyst | Catalyst Deposition Method | E$^{\circ}_{onset}$ (mV vs. RHE) | η (mV vs. RHE) | Tafel Slope (mV/dec) | J$_{max}$ (mA/cm$^2$) | Stability | Reference |
|---|---|---|---|---|---|---|---|
| Zn 1T-MoS$_2$/SiNWs | drop casting | 425 | 164 | 42 | 36.5 | 24 h | This work |
| MoS$_2$/TiO$_2$/n$^+$p-SiNWs | drop casting and annealing | 225 | 75 | 84 | 25 | 75 min | [89] |
| MoS$_2$/Ag/p-SiNWs | drop casting | 62 | 330 | -- | 50 | 1.5 h | [52] |
| MoS$_2$/p-SiNWs | chemical vapor deposition | 260 | 50 | 77 | 35 | 48 h | [54] |
| MoS$_2$/TiO$_2$/n$^+$p-Si$_{NW-3\mu m}$ | atomic layer deposition | 300 | 264 | -- | 19 | -- | [53] |
| Co-doped MoS$_2$ Si microwires | drop casting | 192 | 50 | 45.7 | 30 | 8 h | [90] |
| Ni-doped MoS$_2$ Si microwires | drop casting | 192 | 50 | 50.2 | 20 | 8 h | [90] |
| Fe-doped MoS$_2$ Si microwires | drop casting | 166 | 10 | 65.6 | 30 | 8 h | [90] |

Overpotentials (η) were measured at 10 mA/cm$^2$ photocurrent density.

**Table S2.5:** Resulting Nyquist plot data equivalent circuit fittings.

| Electrode | $R_s$ ($\Omega$) | CPE-T | CPE-P | $R_{ct}$ ($\Omega$) |
|---|---|---|---|---|
| Pt/SiNWs | 28.98 | $4.4916 \times 10^{-5}$ | 0.89283 | 34.08 |
| Zn 1T-MoS$_2$(1mg/mL)/SiNWs | 28.82 | $5.5316 \times 10^{-5}$ | 0.98956 | 266.4 |
| Zn 1T-MoS$_2$(5mg/mL)/SiNWs | 13.93 | $3.4970 \times 10^{-5}$ | 0.97754 | 1255 |
| Zn 1T-MoS$_2$(10mg/mL)/SiNWs | 100.1 | $5.4912 \times 10^{-6}$ | 0.94838 | 2051 |
| Zn 1T-MoS$_2$(15mg/mL)/SiNWs | 144.4 | $7.7995 \times 10^{-6}$ | 0.96278 | 2432 |

The data reported was measured at $\eta$ = -200 mV. $R_s$, $R_{ct}$ and CPE represent the electrolyte, charge transfer resistance, and the constant phase angle element, respectively.

**Table S2.6:** Experimental IPCE values of Zn 1T-MoS$_2$(1mg/mL)/SiNWs

| Wavelength, λ (nm) | Photon Flux, φ (mW/cm²) | Photocurrent Density, J (mA/cm²) | IPCE (%) |
|---|---|---|---|
| 400 | 0.535 | 0.01433 | 8.3 |
| 450 | 0.701 | 0.02224 | 8.7 |
| 500 | 0.775 | 0.01996 | 6.4 |
| 550 | 0.828 | 0.03170 | 8.6 |
| 600 | 0.837 | 0.06156 | 15.2 |
| 650 | 0.873 | 0.09947 | 21.7 |
| 700 | 0.930 | 0.15605 | 29.7 |
| 750 | 1.338 | 0.30504 | 37.7 |
| 800 | 0.982 | 0.27889 | 44.0 |
| 850 | 0.697 | 0.28401 | 59.4 |
| 900 | 3.758 | 1.65287 | 60.6 |
| 950 | 4.166 | 1.55572 | 48.7 |
| 1000 | 1.592 | 0.44297 | 34.5 |
| 1050 | 0.768 | 0.19330 | 29.7 |

**Table S2.7:** Resulting photoelectrochemical onset potentials (E°$_{onset}$), saturation potentials (E°$_{sat}$), and maximum current densities (J$_{max}$) of electrodes before and after electrolysis

| Electrode | Bare SiNWs | | Zn 1T-MoS$_2$(1mg/mL)/SiNWs | |
|---|---|---|---|---|
| | **Pre-iT** | **Post-iT** | **Pre-iT** | **Post-iT** |
| E°$_{onset}$ (mV *vs.* RHE) | 171 | 396 | 177 | 320 |
| E°$_{sat}$ (mV *vs.* RHE) | -359 | -- | -389 | -478 |
| J$_{max}$ (mA/cm$^2$) | 32.5 | 5 | 36.3 | 28.9 |
| Photocurrent Retained (%) | | ~15% | | ~80% |

E°$_{onset}$ values were defined as the potential at which the photocurrent began to increase (0.05 mA/cm$^2$).

## 2.8 References

2.      Giménez, S.; Bisquert, J., *Photoelectrochemical Solar Fuel Production*. Springer Nature: 2016.

3.      Shen, X.; Sun, B.; Yan, F.; Zhao, J.; Zhang, F.; Wang, S.; Zhu, X.; Lee, S., High-Performance Photoelectrochemical Cells from Ionic Liquid Electrolyte in Methyl-Terminated Silicon Nanowire Arrays. *ACS Nano* **2010,** *4* (10), 5869-76.

4.      Wang, X.; Peng, K. Q.; Pan, X. J.; Chen, X.; Yang, Y.; Li, L.; Meng, X. M.; Zhang, W. J.; Lee, S. T., High-Performance Silicon Nanowire Array Photoelectrochemical Solar Cells through Surface Passivation and Modification. *Angew Chem Int Ed* **2011,** *50* (42), 9861-9865.

5.      Kang, D.; Kim, T. W.; Kubota, S. R.; Cardiel, A. C.; Cha, H. G.; Choi, K. S., Electrochemical Synthesis of Photoelectrodes and Catalysts for Use in Solar Water Splitting. *Chem Rev* **2015,** *115* (23), 12839-87.

6.      Gao, G.; Sun, Q.; Du, A., Activating Catalytic Inert Basal Plane of Molybdenum Disulfide to Optimize Hydrogen Evolution Activity Via Defect Doping and Strain Engineering. *The Journal of Physical Chemistry C* **2016,** *120* (30), 16761-16766.

7.      Gao, M. R.; Chan, M. K.; Sun, Y., Edge-Terminated Molybdenum Disulfide with a 9.4-a Interlayer Spacing for Electrochemical Hydrogen Production. *Nat Commun* **2015,** *6*, 7493.

8.      Parsons, R., The Rate of Electrolytic Hydrogen Evolution and the Heat of Adsorption of Hydrogen. *Transactions of the Faraday Society* **1958,** *54*, 1053-1063.

9.      Nørskov, J. K.; Bligaard, T.; Logadottir, A.; Kitchin, J. R.; Chen, J. G.; Pandelov, S.; Stimming, U., Trends in the Exchange Current for Hydrogen Evolution. *Journal of The Electrochemical Society* **2005,** *152* (3), J23.

10.     Benck, J. D.; Hellstern, T. R.; Kibsgaard, J.; Chakthranont, P.; Jaramillo, T. F., Catalyzing the Hydrogen Evolution Reaction (Her) with Molybdenum Sulfide Nanomaterials. *ACS Catalysis* **2014,** *4* (11), 3957-3971.

15.     Li, H.; Tsai, C.; Koh, A. L.; Cai, L.; Contryman, A. W.; Fragapane, A. H.; Zhao, J.; Han, H. S.; Manoharan, H. C.; Abild-Pedersen, F.; Norskov, J. K.; Zheng, X., Activating and Optimizing Mos2 Basal Planes for Hydrogen Evolution through the Formation of Strained Sulphur Vacancies. *Nature Materials* **2016,** *15*, 48-53.

17.     Shi, Y.; Zhou, Y.; Yang, D. R.; Xu, W. X.; Wang, C.; Wang, F. B.; Xu, J. J.; Xia, X. H.; Chen, H. Y., Energy Level Engineering of Mos2 by Transition-Metal Doping for Accelerating Hydrogen Evolution Reaction. **2017,** *139*, 15479-15485.

22.     Voiry, D.; Salehi, M.; Silva, R.; Fujita, T.; Chen, M.; Asefa, T.; Shenoy, V. B.; Eda, G.; Chhowalla, M., Conducting Mos(2) Nanosheets as Catalysts for Hydrogen Evolution Reaction. *Nano Lett* **2013,** *13* (12), 6222-7.

24.     Huang, Y.; Sun, Y.; Zheng, X.; Aoki, T.; Pattengale, B.; Huang, J.; He, X.; Bian, W.; Younan, S.; Williams, N.; Hu, J.; Ge, J.; Pu, N.; Yan, X.; Pan, X.; Zhang, L.; Wei, Y.; Gu, J., Atomically Engineering Activation Sites onto Metallic 1t-Mos2 Catalysts for Enhanced Electrochemical Hydrogen Evolution. **2019,** *10*.

28.     Seh, Z. W.; Kibsgaard, J.; Dickens, C. F.; Chorkendorff, I.; Norskov, J. K.; Jaramillo, T. F., Combining Theory and Experiment in Electrocatalysis: Insights into Materials Design. *Science* **2017,** *355* (6321).

40.     Su, T.; Shao, Q.; Qin, Z.; Guo, Z.; Wu, Z., Role of Interfaces in Two-Dimensional Photocatalyst for Water Splitting. *ACS Catalysis* **2018,** *8* (3), 2253-2276.

41.     Lewis, N. S.; Crabtree, G. *Basic Research Needs for Solar Energy Utilization*; April 21, 2005, 2005.

42.     Kudo, A.; Miseki, Y., Heterogeneous Photocatalyst Materials for Water Splitting. *Chemical Society Reviews* **2009,** *38* (1), 253-278.

43.     Li, R.; Li, C., Photocatalytic Water Splitting on Semiconductor-Based Photocatalysts. Academic Press Inc.: 2017; Vol. 60, pp 1-57.

44.     Song, I.; Park, C.; Choi, H. C., Synthesis and Properties of Molybdenum Disulphide: From Bulk to Atomic Layers. *RSC Advances* **2015,** *5* (10), 7495-7514.

45.     Jayabal, S.; Wu, J.; Chen, J.; Geng, D.; Meng, X., Metallic 1t-Mos2 Nanosheets and Their Composite Materials: Preparation, Properties and Emerging Applications. *Materials Today Energy* **2018,** *10*, 264-279.

46.     Zhao, W.; Pan, J.; Fang, Y.; Che, X.; Wang, D.; Bu, K.; Huang, F., Metastable Mos(2) : Crystal Structure, Electronic Band Structure, Synthetic Approach and Intriguing Physical Properties. *Chemistry* **2018,** *24* (60), 15942-15954.

47.     Wang, D.; Zhang, X.; Bao, S.; Zhang, Z.; Fei, H.; Wu, Z., Phase Engineering of a Multiphasic 1t/2h Mos2 Catalyst for Highly Efficient Hydrogen Evolution. *Journal of Materials Chemistry A* **2017,** *5* (6), 2681-2688.

48.     Liang, F.; Xu, H.; Wu, X.; Wang, C.; Luo, C.; Zhang, J., Raman Spectroscopy Characterization of Two-Dimensional Materials. *Chinese Physics B* **2018,** *27* (3), 269.

49.     Li, Y.; Wang, L.; Zhang, S.; Dong, X.; Song, Y.; Cai, T.; Liu, Y., Cracked Monolayer 1t Mos2with Abundant Active Sites for Enhanced Electrocatalytic Hydrogen Evolution. *Catalysis Science & Technology* **2017,** *7* (3), 718-724.

50.     Attanayake, N. H.; Thenuwara, A. C.; Patra, A.; Aulin, Y. V.; Tran, T. M.; Chakraborty, H.; Borguet, E.; Klein, M. L.; Perdew, J. P.; Strongin, D. R., Effect of Intercalated Metals on the Electrocatalytic Activity of 1t-Mos2 for the Hydrogen Evolution Reaction. *ACS Energy Letters* **2017,** *3* (1), 7-13.

51.     Liang, H.; Cao, Z.; Ming, F.; Zhang, W.; Anjum, D. H.; Cui, Y.; Cavallo, L.; Alshareef, H. N., Aqueous Zinc-Ion Storage in Mos(2) by Tuning the Intercalation Energy. *Nano Lett* **2019,** *19* (5), 3199-3206.

52.     Qiao, L.; Liao, M.; Wu, J.; Jiang, Q.; Zhang, Y.; Li, Y., Molybdenum Disulfide/Silver/P-Silicon Nanowire Heterostructure with Enhanced Photoelectrocatalytic Activity for Hydrogen Evolution. *International Journal of Hydrogen Energy* **2018,** *43* (49), 22235-22242.

53.     Hellstern, T. R.; Nielander, A. C.; Chakthranont, P.; King, L. A.; Willis, J. J.; Xu, S.; MacIsaac, C.; Hahn, C.; Bent, S. F.; Prinz, F. B.; Jaramillo, T. F., Nanostructuring Strategies to Increase the Photoelectrochemical Water Splitting Activity of Silicon Photocathodes. *ACS Applied Nano Materials* **2019,** *2* (1), 6-11.

54.     Hu, D.; Xiang, J.; Zhou, Q.; Su, S.; Zhang, Z.; Wang, X.; Jin, M.; Nian, L.; Nozel, R.; Zhou, G.; Zhang, Z.; Liu, J., One-Step Chemical Vapor Deposition of Mos(2) Nanosheets on Sinws as Photocathodes for Efficient and Stable Solar-Driven Hydrogen Production. *Nanoscale* **2018,** *10* (7), 3518-3525.

55.     Peng, K.-Q.; Wang, X.; Li, L.; Hu, Y.; Lee, S.-T., Silicon Nanowires for Advanced Energy Conversion and Storage. *Nano Today* **2013,** *8*, 75-97.

56.     Wu, W.; Niu, C.; Wei, C.; Jia, Y.; Li, C.; Xu, Q., Activation of Mos2 Basal Planes for Hydrogen Evolution by Zinc. *Angew Chem Int Ed Engl* **2019,** *58* (7), 2029-2033.

57.     Luo, R.; Luo, M.; Wang, Z.; Liu, P.; Song, S.; Wang, X.; Chen, M., The Atomic Origin of Nickel-Doping-Induced Catalytic Enhancement in Mos2 for Electrochemical Hydrogen Production. *Nanoscale* **2019,** *11* (15), 7123-7128.

58.     Qiao, W.; Xu, W.; Xu, X.; Wu, L.; Yan, S.; Wang, D., Construction of Active Orbital Via Single-Atom Cobalt Anchoring on the Surface of 1t-Mos2 Basal Plane toward Efficient Hydrogen Evolution. American Chemical Society: 2020; Vol. 3, pp 2315-2322.

59.     Qi, K.; Cui, X.; Gu, L.; Yu, S.; Fan, X.; Luo, M.; Xu, S.; Li, N.; Zheng, L.; Zhang, Q.; Ma, J.; Gong, Y.; Lv, F.; Wang, K.; Huang, H.; Zhang, W.; Guo, S.; Zheng, W.; Liu, P., Single-Atom Cobalt Array Bound to Distorted 1t Mos(2) with Ensemble Effect for Hydrogen Evolution Catalysis. *Nat Commun* **2019,** *10* (1), 5231.

60.     Lau, T. H. M.; Lu, X.; Kulhavý, J.; Wu, S.; Lu, L.; Wu, T. S.; Kato, R.; Foord, J. S.; Soo, Y. L.; Suenaga, K.; Tsang, S. C. E., Transition Metal Atom Doping of the Basal Plane of Mos2 Monolayer Nanosheets for Electrochemical Hydrogen Evolution. *Chemical Science* **2018,** *9* (21), 4769-4776.

61.     Zhao, Y. P.; Fan, J. G., Clusters of Bundled Nanorods in Nanocarpet Effect. *Applied Physics Letters* **2006,** *88*.

62.     Togonal, A. S.; He, L.; Roca i Cabarrocas, P.; Rusli, Effect of Wettability on the Agglomeration of Silicon Nanowire Arrays Fabricated by Metal-Assisted Chemical Etching. *Langmuir* **2014,** *30* (34), 10290-8.

63.     Naumkin, A. V.; Kraut-Vass, A.; Gaarenstroom, S. W.; Powell, C. J., Nist X-Ray Photoelectron Spectroscopy Database. National Institute of Science and Technology: 2012; Vol. 20899, p 20899.

64.     Baker, M. A.; Gilmore, R.; Lenardi, C.; Gissler, W., Xps Investigation of Preferential Sputtering of S from Mos2 and Determination of Mosx Stoichiometry from Mo and S Peak Positions. *Applied Surface Science* **1999,** *150* (1-4), 255-262.

65.     Vickerman, J. C.; Gilmore, I. S. I. S., Electron Spectroscopy for Chemical Analysis. In *Surface Analysis - the Principle Techniques*, 2nd ed.; Wiley: 2009; pp 47-112.

66.     Lei, Z.; Zhan, J.; Tang, L.; Zhang, Y.; Wang, Y., Recent Development of Metallic (1t) Phase of Molybdenum Disulfide for Energy Conversion and Storage. *Advanced Energy Materials* **2018,** *8* (19).

67.     Zhang, S.; Zhang, N.; Zhao, Y.; Cheng, T.; Li, X.; Feng, R.; Xu, H.; Liu, Z.; Zhang, J.; Tong, L., Spotting the Differences in Two-Dimensional Materials - the Raman Scattering Perspective. *Chem Soc Rev* **2018,** *47* (9), 3217-3240.

68.     Li, X.; Zhu, H., Two-Dimensional Mos2: Properties, Preparation, and Applications. *Journal of Materiomics* **2015,** *1* (1), 33-44.

69.     Hajiyev, P.; Cong, C.; Qiu, C.; Yu, T., Contrast and Raman Spectroscopy Study of Single- and Few-Layered Charge Density Wave Material: 2h-Tase(2). *Sci Rep* **2013,** *3*, 2593.

70.     Tan, P.-H., *Raman Spectroscopy of Two-Dimensional Materials*. Springer Singapore: 2019; p IX, 261.

71.     Gates-Rector, S.; Blanton, T., The Powder Diffraction File: A Quality Materials Characterization Database. Cambridge University Press: 2019; Vol. 34, pp 352-360.

72.     Holder, C. F.; Schaak, R. E., Tutorial on Powder X-Ray Diffraction for Characterizing Nanoscale Materials. *ACS Nano* **2019,** *13* (7), 7359-7365.

73.     Chen, Z.; Dinh, H. N.; Miller, E., *Photoelectrochemical Water Splitting Standards, Experimental Methods, and Protocols*. Springer New York, NY: 2013; p X, 126.

74.     Tang, Q.; Jiang, D.-e., Mechanism of Hydrogen Evolution Reaction on 1t-Mos2 from First Principles. *ACS Catalysis* **2016,** *6* (8), 4953-4961.

75.     Qian, J.; Wang, T.; Xia, B.; Xi, P.; Gao, D., Zn-Doped Mose2 Nanosheets as High-Performance Electrocatalysts for Hydrogen Evolution Reaction in Acid Media. *Electrochimica Acta* **2019**, 701-708.

76.     Liu, P.; Zhu, J.; Zhang, J.; Tao, K.; Gao, D.; Xi, P., Active Basal Plane Catalytic Activity and Conductivity in Zn Doped Mos2 Nanosheets for Efficient Hydrogen Evolution. *Electrochimica Acta* **2018,** *260*, 24-30.

77.     Huang, Y.; Nielsen, R. J.; Goddard, W. A., 3rd; Soriaga, M. P., The Reaction Mechanism with Free Energy Barriers for Electrochemical Dihydrogen Evolution on Mos2. *J Am Chem Soc* **2015,** *137* (20), 6692-8.

78.     Fang, Y. H.; Liu, Z.-P., Tafel Kinetics of Electrocatalytic Reactions: From Experiment to First-Principles. *ACS Catalysis* **2014,** *4* (12), 4364-4376.

79.     Marković, N. M.; Grgur, B. N.; Ross, P. N., Temperature-Dependent Hydrogen Electrochemistry on Platinum Low-Index Single-Crystal Surfaces in Acid Solutions. *The Journal of Physical Chemistry B* **1997,** *101* (27), 5405-5413.

80.     Kulakci, M.; Es, F.; Ozdemir, B.; Unalan, H. E.; Turan, R., Application of Si Nanowires Fabricated by Metal-Assisted Etching to Crystalline Si Solar Cells. *IEEE Journal of Photovoltaics* **2013,** *3* (1), 548-553.

81.     He, L.; Jiang, C.; Wang, H.; Lai, D.; Rusli, Si Nanowires Organic Semiconductor Hybrid Heterojunction Solar Cells toward 10% Efficiency. *ACS Appl Mater Interfaces* **2012,** *4* (3), 1704-8.

82.     Deng, J.; Su, Y.; Liu, D.; Yang, P.; Liu, B.; Liu, C., Nanowire Photoelectrochemistry. *Chem Rev* **2019,** *119* (15), 9221-9259.

83.     Peng, K. Q.; Lee, S. T., Silicon Nanowires for Photovoltaic Solar Energy Conversion. *Adv Mater* **2011,** *23* (2), 198-215.

84.     Nomiya, K.; Takahashi, T.; Shirai, T.; Miwa, M., Anderson-Type Heteropolyanions of Molybdenum(Vi) and Tungsten(Vi). *Polyhedron* **1987,** *6* (2), 213-218.

85.     Sivakov, V. A.; Brönstrup, G.; Pecz, B.; Berger, A.; Radnoczi, G. Z.; Krause, M.; Christiansen, S. H., Realization of Vertical and Zigzag Single Crystalline Silicon Nanowire Architectures. *The Journal of Physical Chemistry C* **2010,** *114* (9), 3798-3803.

86.     Wallart, X.; Henry de Villeneuve, C.; Allongue, P., Truly Quantitative Xps Characterization of Organic Monolayers on Silicon: Study of Alkyl and Alkoxy Monolayers on H-Si(111). *J Am Chem Soc* **2005,** *127* (21), 7871-8.

87.     Williams, N. B.; Nash, A.; Yamamoto, N.; Patrick, M.; Tran, I. C.; Gu, J., Unraveling Activity and Decomposition Pathways of [Fefe] Hydrogenase Mimics Covalently Bonded to Silicon Photoelectrodes. *Advanced Materials Interfaces* **2021,** *8* (10), 1-8.

88.     Gu, J.; Wuttig, A.; Krizan, J. W.; Hu, Y.; Detweiler, Z. M.; Cava, R. J.; Bocarsly, A. B., Mg-Doped Cufeo2 Photocathodes for Photoelectrochemical Reduction of Carbon Dioxide. *The Journal of Physical Chemistry C* **2013,** *117* (24), 12415-12422.

89.     Zhang, L.; Liu, C.; Wong, A. B.; Resasco, J.; Yang, P., Mos2-Wrapped Silicon Nanowires for Photoelectrochemical Water Reduction. *Nano Research* **2014,** *8* (1), 281-287.

90.     Chen, C.-J.; Yang, K.-C.; Liu, C.-W.; Lu, Y.-R.; Dong, C.-L.; Wei, D.-H.; Hu, S.-F.; Liu, R.-S., Silicon Microwire Arrays Decorated with Amorphous Heterometal-Doped Molybdenum Sulfide for Water Photoelectrolysis. *Nano Energy* **2017,** *32*, 422-432.

# CHAPTER 3: Zinc Single Atom Confinement Effects on Catalysis in 1T-phase Molybdenum Disulfide

## 3.1 Abstract

Active sites are atomic sites within catalysts that drive reactions and are essential to catalysis. Spatially confining guest metals within active site microenvironments has been predicted to improve catalytic activity by altering the electronic states of active sites. Using hydrogen evolution (HER) as the model reaction, we show that intercalating zinc single atoms between layers of 1T-MoS$_2$ (Zn SAs/1T-MoS$_2$) enhances HER performance by decreasing the overpotential, charge transfer resistance, and the kinetic barrier. The confined Zn atoms tetrahedrally coordinate to basal sulfur atoms and expand the interlayer spacing of 1T-MoS$_2$ by ~3.4%. Under confinement, the Zn SAs donate electrons to coordinated S atoms, which lowers the free energy barrier of H$^*$ adsorption/desorption and enhances HER kinetics. In this work, which is applicable to all types of catalytic reactions and layered materials, HER performance is enhanced by controlling the coordination geometry and electronic states of transition metals confined within active site microenvironments.

## 3.2 Introduction

H$_2$ is recognized as an essential green energy carrier that is widely used as a chemical feedstock in petroleum refinement, fertilizer production, and as a fuel source for electricity/heat generation.[91] As of 2021, 95% of H$_2$ produced in the United States is generated by steam-methane reformation.[92] In addition to being energy-intensive, this centralized process increases CO$_2$ emissions and requires large power plants that are expensive to build. Consequently, this method of H$_2$ generation is not accessible to countries that lack these resources.[93]

Luckily, alternative pathways to H$_2$ generation exist.[94] Using electrochemical methods to drive the H$_2$ evolution reaction (HER) provides a sustainable, decentralized alternative by requiring only water to yield H$_2$ with high purity.[95, 96] As such, it circumvents the challenges of steam-methane reformation and enables countries with limited resources to become more self-reliant. Before electrochemical H$_2$ generation can be implemented into society, critical obstacles still need to be overcome. Primarily, electrocatalysts that are cost-effective, highly efficient, and durable must be developed to replace precious metal electrocatalysts currently employed in commercialized electrolyzers.[97-99] Since the performance of electrocatalysts depends on the nature of their active sites, methods that maximize active site performance in the next generation of electrocatalysts need to be established.

Theoretical studies have revealed that spatially confining microenvironments (the local coordination environment and electronic states of active sites) within catalysts can enhance the catalyst's activity by modulating the frontier orbital energies and adsorption/desorption energies of active sites.[100, 101] Electronic properties of confined active sites are directly influenced by their coordination environment, which in turn alters the adsorption energetics of reaction intermediates and catalytic activity/selectivity.[102] Therefore, the relationship between active sites, local

microenvironments, and confined species dictates catalytic performance. However, designing a prototype system that enables the understanding of catalytic confinement effects at the atomic level remains challenging.

Single-atom catalysts (SACs), in which single atoms (SAs) are stabilized within supporting substrates by either adsorbing to the substrate's basal plane or substituting atoms within the substrate's lattice, offer an ideal prototype for the investigation of confinement catalysis. Along with demonstrating a superior catalytic performance compared to nanoparticles and nanoclusters in traditional metal catalysts, SACs exhibit flexibility with respect to crystallinity, coordination number, and electronic structures.[103] Likewise, when employing noble metal SAs, SACs require significantly smaller quantities of noble metals to achieve competitive catalytic performances to produce solar fuels and industrial chemicals.

To understand confinement effects between catalysts and their microenvironments, identifying a paradigmatic support material is crucial. Commonly employed scaffolds that provide spatial confinement include channels in carbon nanotubes (CNTs) and porous sites in zeolites and metal organic frameworks (MOFs).[102, 104] In these cases, methods such as doping the catalyst with nonmetals, forming bimetallic active sites, and synthetically inducing an anisotropic catalyst surface have all been shown to enhance catalytic activity.[105-107] However, both zero-dimensional (0D) nanocavities in zeolites/MOFs and one-dimensional (1D) nanocavities in CNTs suffer from major disadvantages, such as complex structural and chemical composition.[102, 104] These complexities create an uneven environment surrounding the active sites and make understanding confinement effects very difficult at the microscopic level.[102, 104]

Compared to their three-dimensional (3D) counterparts, two-dimensional (2D) materials exhibit well-defined layered structures, a variety of polymorphs, and tunable geometric and

electronic properties. Computational studies have predicted the interactions between active sites and guest species confined within their local microenvironments to heavily influence catalytic activity.[108-110] Yet, experimental evidence of 2D materials other than carbon-based 2D materials is limited.[111] For these reasons, exploring other 2D materials for confinement studies would provide an ideal platform to understand how confining guest species near active sites located within the substrate's interlayer spacing influences catalytic performance.

HER is an ideal model reaction for confinement studies due to the fast kinetics of $H^+$ diffusion that occurs between layers of 2D materials.[104] Customarily, the HER activity of HER catalysts is evaluated using hydrogen adsorption free energies ($\Delta G_{H*}$). Both non-metal and transition metal HER catalysts follow the same trend, where maximum HER activity is achieved at around $\Delta G_{H*} = 0$ Ev.[97, 112] In the continuous search for Earth-abundant catalysts, $MoS_2$ serves as a role-model in HER catalysis.[97-99] For decades, its activity has been considered limited due to the extremely high energy of proton adsorption on the basal plane of semiconducting $2H\text{-}MoS_2$ ($\Delta G_{H*} = 1.92$ eV). This changed when theoretical calculations revealed the extremely thermoneutral nature of edge sites in $2H\text{-}MoS_2$ ($\Delta G_{H*} = 0.08$ eV).[113] Volcano plots published in literature that are used to access HER activities of metal nanoparticles and other HER catalysts have demonstrated that, compared to other commonly employed non-precious HER catalysts, molybdenum dichalcogenides maintain a $\Delta G_{H*}$ nearest to zero.[97, 99, 114, 115] Therefore, $MoS_2$ is considered to be an ideal candidate because of the fast HER kinetics it sustains. The best performing HER catalysts are precious metals such as Pt, which are rare and expensive. In contrast, $MoS_2$ is comprised of Earth-abundant elements and thus is much less expensive and more feasible at scale. For these reasons, $MoS_2$ is considered to be more advantageous than other high performing HER catalysts.

Various strategies have been employed to expose more active edge sites in 2H-MoS$_2$.[116, 117] For instance, Wang *et. al.* employed a mild H$_2$O$_2$ chemical etching strategy to investigate the impact of both the concentration and distribution of S vacancies in MoS$_2$ on HER activity.[118] The results suggest that the homogeneous distribution of single S-vacancies throughout the MoS$_2$ nanosheet surface achieves optimal HER performance, as demonstrated by the 48 Mv/dec Tafel slope and 131 Mv overpotential reported. Subsequently, the direction of MoS$_2$-based HER research shifted with the discovery of the metallic 1T-phase of MoS$_2$, due to the higher density of active sites available along the basal plane of 1T-MoS$_2$.[119, 120]

Compared to the trigonal prismatic 2H-phase of MoS$_2$, 1T-MoS$_2$ layers feature well-defined octahedral symmetry which increases the exposure of surface active sites for enhanced catalytic performance.[121] Furthermore, metallic 1T-MoS$_2$ exhibits exceptional charge transport properties compared to its 2H-phase semiconducting analogue, thus enabling further exposure of active sites at which surface reactions take place.[122, 123] While 2H-MoS$_2$ is known to be the more thermodynamically stable phase in nature, intercalation of SAs between layers of MoS$_2$ enables MoS$_2$ to remain stable in the 1T-phase.[124] In addition, the distinct, local atomic environment and uniform chemical nature of SAs offer remarkable advantages of distinguished activity, selectivity, and stability studies for HER.

Thus far, only a few catalytic confinement studies have utilized MoS$_2$ as the host material. For example, Chen *et al.* intercalated platinum (Pt) nanoparticles within the van der Waals gaps of bulk MoS$_2$ and discovered that confinement not only suppressed the aggregation of Pt nanoparticles but also facilitated the transfer of H$_3$O$^+$ during HER.[125] Likewise, Luo *et al.* inserted Co(OH)$_2$ nanoparticles between layers of bulk MoS$_2$ to improve the HER performance of MoS$_2$ under alkaline media.[126] Unfortunately, previous confinement studies either suffer from utilization

of precious metals or difficulty with controlling the size and structure of intercalated species, resulting with an unsystematic study of confinement effects.

Other works have investigated the catalytic effects of modifying 1T-MoS$_2$ with first-row transition metals. Huang *et. al.* discovered that hydrothermally synthesizing 1T-MoS$_2$ with Fe, Co, and Ni enhances HER activity in alkaline media by doping the guest metals into the 1T-MoS$_2$ lattice in a 1:6 X:Mo ratio (X = Fe, Co, or Ni).[127] Li *et. al.* reported the ability to enhance the HER performance of 1T-MoS$_2$ by either substituting lattice sites with copper (Cu) SAs or adsorbing Cu SAs along the 1T-MoS$_2$ basal plane.[128] Each of these methods of stabilizing Cu SAs was achieved by employing syringe injection or hydrothermal synthetic methods, respectively. Meanwhile, in a volcano plot reported by Deng *et. al.*, Zn demonstrated a $\Delta G_{H*}$ value near 0 Ev, indicating that it is one of the few non-precious metals that may be able to modify the HER activity of MoS$_2$.[129] Therefore, Zn SAs were selected as the guest intercalants in this study to investigate the effects of non-precious metal confinement effects on HER catalysis.

In this work, Zn SAs were intercalated within the interlayer spacing of 1T-MoS$_2$ (Zn SAs/1T-MoS$_2$) via syringe injection into hydrothermally synthesized 1T-MoS$_2$ (see Supporting Information for detailed synthesis procedure). Results reported herein show that the confined SAs maintain a Zn$^{2+}$ oxidation state and expand the interlayer spacing of 1T-MoS$_2$ by ~3.4% (0.022 nm). Changes in catalytic performance during HER were monitored electrochemically under acidic conditions, where a decrease in overpotential (1T-MoS$_2$ = 265 Mv; Zn SAs/1T-MoS$_2$ = 177 Mv) and charge transport limitations (1T-MoS$_2$ = 106.4 Mv/dec; Zn SAs/1T-MoS$_2$ = 84.9 Mv/dec) were observed when Zn SAs were intercalated between 1T-MoS$_2$ layers. The experimental findings were further confirmed computationally using proton adsorption energies predicted from first principles density functional theory (DFT) and partial density of states (PDOS) plots. In

addition to facilitating HER kinetics, the spatial confinement of Zn SAs was predicted to enhance interactions between protons and the microenvironments of nearby active sites they are confined within.

## 3.3 Results and Discussion

### 3.3.1 Adsorption of Zinc Single Atoms Along the Basal Plane of 1T-MoS$_2$
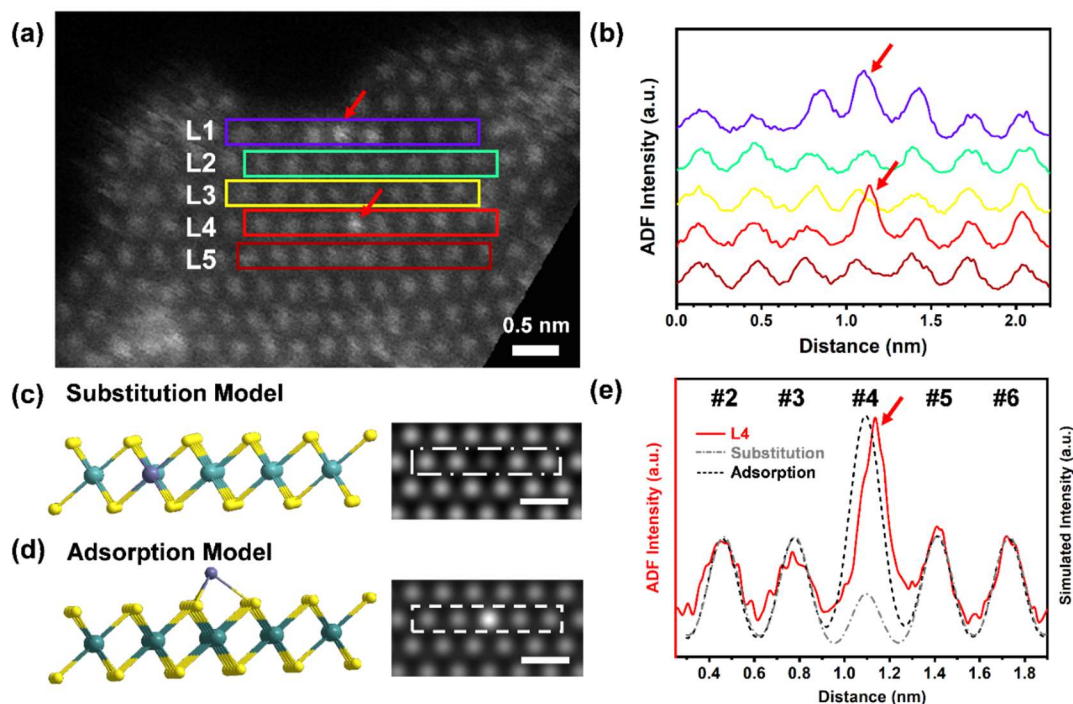


**Figure 3.1:** HAADF-STEM characterization and quantitative identification of Zn SAs adsorption to the basal plane of 1T-MoS$_2$.
**(a)** Atomically resolved HAADF-STEM image of the monolayer sample at 60 keV. **(b)** Intensity profiles taken along five adjacent lines (L1-L5) indicated by the different colored rectangles in (a). The red arrows point to the locations of Zn SAs. **(c)** Side view of the atomic structure of the Zn substitution model and the simulated HAADF-STEM image. The yellow, green, and purple atoms represent S, Mo, and Zn, respectively. **(d)** Side view of the atomic structure of the Zn adsorption model and the simulated HAADF-STEM image. **(e)** Comparison of intensity profiles from the experimental image and two simulated images of replaced and adsorbed models, respectively. All scale bars in (a, c, d) are 0.5 nm.

SAs may be stabilized on appropriate substrates by either substituting lattice vacancies or adsorbing to the substrate's basal plane. In this work, high-angle annular dark-field scanning transmission electron microscopy (HAADF-STEM) was used to identify the positions occupied

by Zn SAs in the 1T-MoS$_2$ lattice (**Figures 3.1, S3.1**). In the HAADF-STEM image shown in **Figure 3.1a**, the intensity of each lattice site is correlated to the atomic number of the element occupying the lattice site.[130] If the Zn SAs substitute Mo lattice sites, the lattice vacancies occupied by Zn SAs will appear darker since Zn ($Z_{Zn} = 30$) has a lower atomic number than Mo ($Z_{Mo} = 42$). Instead, brighter spots are observed, indicating that the Zn SAs adsorb to the basal plane and occupy sites above Mo atoms. Additional evidence that the Zn SAs adsorb to the basal plane of 1T-MoS$_2$ is shown by the HAADF-STEM images provided in **Figure S3.1** (designated with red circles).

Line profiles taken from **Figure 3.1a** (labeled L1 through L5) show an increase in annular dark field (ADF) intensity for lattice site positions with observably brighter intensities in L1 and L4 (**Figure 3.1b**). For comparison, line profiles extrapolated from the simulated models of substitution (**Figure 3.1c**) and adsorption (**Figure 3.1d**) were plotted against the experimental ADF intensity of L4 (**Figure 3.1e**). Results show that while the ADF intensity of L4 (1.95 a.u.) does not match that of the simulated substitution model (0.52 a.u.), it corresponds well with the ADF intensity of the simulated adsorption model (1.95 a.u.). These results further confirm that the Zn SAs adsorb to the basal plane of 1T-MoS$_2$.

HAADF-STEM images collected under continuous electron beam irradiation revealed the ability to trigger the migration of Zn SAs across the 1T-MoS$_2$ basal plane (**Figure S3.2**). When the electron beam was focused on the same region for 109 s, the Zn atom located in L4 (t = 0 s, designated with a red arrow in **Figure S3.2a**), jumps to L5 (t = 109 s, **Figure S3.2b**). After 203 s, only one of the four Zn atoms (designated by the yellow arrow) present remains in the same position, while the other three Zn atoms migrate out of the scope's area (**Figure S3.2c**). These observations further confirm that rather than substituting into the lattice, the Zn SAs adsorb to the

basal plane of 1T-MoS$_2$. It is worth mentioning that the dynamic movement of SAs under electron beam conditions is well known.[131-133] It would be intriguing to understand if the dynamics of SAs persists under catalytic conditions. However, a spectroscopic or microscopic technique needs to be developed that can confirm dynamics of SAs while supplying the minimum amount of external energy required to trigger their movements.

*3.3.2 Expansion of 1T-MoS$_2$ Lattice Fringe Spacing by Intercalated Zinc Single Atoms*

By convention, intercalation reactions are characterized by the expansion of a layered substrate's crystal lattice along the c axis.[134] Expansion of 1T-MoS$_2$'s interlayer spacing was evidenced by visible peak shifts in the X-ray diffraction (XRD) patterns of Zn SAs/1T-MoS$_2$ compared to that of 1T-MoS$_2$ (**Figures 3.2a, 3.2b**). Peak broadening observed in the diffraction pattern of bulk Zn SAs/1T-MoS$_2$ compared to 1T-MoS$_2$ arises from the overlap of hexagonal 1T-MoS$_2$ (P6$_3$/mmc; PDF #75-1539) and monoclinic Mo$_2$S$_3$ (P2$_1$/m; PDF #72-0821). Mo$_2$S$_3$ consists of molecular Mo-S chains intercalated between 1T'-MoS$_2$ layers (**Figure S3.3**).[135] Interestingly, the peak overlap observed in 1T-MoS$_2$ splits into two separate peaks in Zn SAs/1T-MoS$_2$: the (001) plane bisecting the interlayer spacing of 1T-MoS$_2$ and the (101) plane bisecting the Mo-S chains that intercalate the 1T'-MoS$_2$ layers in Mo$_2$S$_3$. The diffraction peak indexed to the (001) plane of 1T-MoS$_2$ shifts from 14.07° (0.629 nm) to 13.59° (0.651 nm) when Zn SAs are present, which corresponds to a ~3.4% (0.022 nm) increase in 1T-MoS$_2$'s interlayer spacing. Likewise, the peak indexed to the (101) plane of Mo$_2$S$_3$ shifts from 16.28° (0.544 nm) to 15.72° (0.563 nm) in Zn SAs/1T-MoS$_2$ and also corresponds to a ~3.4% (0.019 nm) expansion. DFT calculations reported in literature have predicted a decreased diffusion energy barrier for SA migration between

2D layers as the interlayer spacing increases.[136, 137] Here, the interlayer spacing of 1T-MoS$_2$ expands to accommodate the occupation of interlayer lattice sites by Zn SAs.
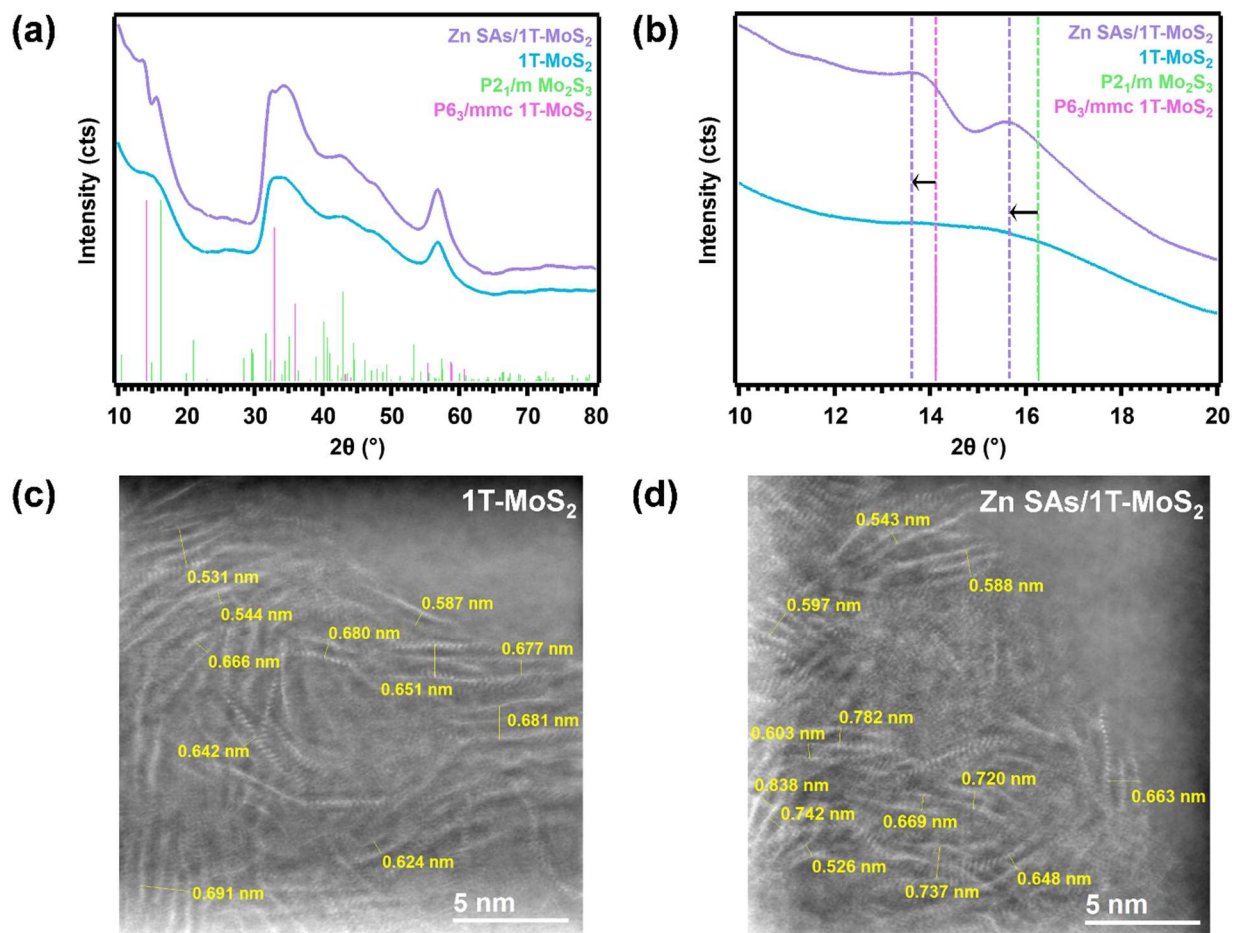


**Figure 3.2:** XRD and HRTEM analysis of 1T-MoS$_2$ lattice expansion induced by intercalated Zn SAs. **(a)** Zn SAs/1T-MoS$_2$ (purple) and 1T-MoS$_2$ (blue) XRD patterns. **(b)** Zoomed in region of XRD patterns to highlight shifts observed for the (001) and (101) planes in 1T-MoS$_2$ and Mo$_2$S$_3$, respectively. **(c)** 1T-MoS$_2$ HRTEM image. **(d)** Zn SAs/1T-MoS$_2$ HRTEM image. Experimental fringe spacings are shown in yellow.

Comparing the distance between lattice fringes in 1T-MoS$_2$ to those found in Zn SAs/1T-MoS$_2$ (**Figure 3.2d**) generates similar results. Images produced by HRTEM with the electron beam aligned in parallel to the 1T-MoS$_2$ basal plane show an average distance of 0.632 ± 0.06 nm for lattice fringes found in 1T-MoS$_2$ (**Figure 3.2c**). Lattice fringes present in Zn SAs/1T-MoS$_2$ yield an average distance of 0.661 ± 0.09 nm (**Figure 3.2d**), which is roughly 0.029 nm larger than the

1T-MoS$_2$ lattice fringes observed when Zn SAs are absent. This result corresponds to a 4.6% average increase in 1T-MoS$_2$'s interlayer spacing. Altogether, the XRD and HRTEM results both suggest that intercalating Zn SAs expands 1T-MoS$_2$'s interlayer spacing.

### 3.3.3 Structural characterization of Zn SAs/1T-MoS$_2$

The Zn SAs/1T-MoS$_2$ were analyzed by STEM and EDX spectroscopy to atomically visualize the layer geometry and confirm the elemental components present (**Figure S3.5**). The resulting elemental maps of Zn, Mo, and S confirm the presence of these atoms in Zn SAs/1T-MoS$_2$ and demonstrate the uniform distribution of Zn SAs throughout the substrate (**Figures S3.5c, S3.5e, S3.5f**). Correspondingly, the octahedral coordination of Mo and S atoms displayed throughout the Moiré patterns of Zn SAs/1T-MoS$_2$ confirms the presence of the 1T phase of MoS$_2$ (**Figures S3.5a, S3.5d**).

To understand how the confinement of Zn SAs impacts the electronic structure of 1T-MoS$_2$, XPS was employed to compare the elemental and chemical composition of Zn SAs/1T-MoS$_2$ and 1T-MoS$_2$ (**Figure S3.6, Table S3.1**). Peaks identified in the Zn 2p spectrum of Zn SAs/1T-MoS$_2$ correspond to the presence of Zn$^{2+}$ and confirm that the SAs retain their Zn$^{2+}$ oxidation state after intercalation (**Figure S3.6g**).[138] Deconvolution of peaks in the Mo 3d, S 2s (**Figures S3.6a, S3.6b**), and S 2p (**Figures S3.6c, S3.6d**) spectra produces two sets of doublet peaks, in which the set of peaks at lower binding energies (shown in purple) are assigned to Mo$^{4+}$ and S$^{2-}$ oxidation states in 1T-MoS$_2$.[138] The sets of doublet peaks at higher binding energies (shown in green) correspond to unsaturated Mo$^{5/6+}$ and S$^{2-}$ oxidation states and indicate the presence of a non-stoichiometric MoS$_x$ species along the surface of each sample.[138] Consequently, while the majority of both samples consists of stoichiometric 1T-MoS$_2$, a portion of S vacant MoS$_x$ exists near the catalyst surface.[139] Compared to 1T-MoS$_2$, Zn SAs/1T-MoS$_2$ displays downshifts in

77

binding energies up to 0.19 eV. Downshifts up to 0.10 eV fall within the step size (0.10 eV) employed during XPS analysis and as such are considered negligible. However, peak shifts exceeding the step size employed are observed for the S 2p doublet assigned to $MoS_x$ (**Figure S3.6c, S3.6d**). This shift to lower binding energies indicates that the Zn SAs donate electrons to the S atoms of $MoS_x$.[140] This electron donation likely occurs to facilitate the stabilization of Zn SAs within the substrate's interlayer spacing. Further evidence of the lack of structural changes to $1T\text{-}MoS_2$ upon intercalating Zn SAs is provided by the FTIR spectra, which also demonstrates negligible chemical and electronic structure changes (**Figure S3.4**).

Next, Raman spectroscopy was employed to explore key structural details such as lattice strain and vacancy defects. The Raman spectra for $1T\text{-}MoS_2$ and Zn SAs/$1T\text{-}MoS_2$ are displayed in **Figure S3.7** with experimental peak positions listed in **Table S3.2**. Existence of the 1T-phase in both samples is confirmed by the presence of TA and LA phonon modes at the M point of the first Brillouin zone, $J_1$, $J_2$, $E_{1g}$, and $J_3$ phonon modes. The negligible difference in $1T\text{-}MoS_2$ and Zn SAs/$1T\text{-}MoS_2$ peak positions provides further evidence that the lattice structure of $1T\text{-}MoS_2$ remains intact in the presence of Zn SAs.[141]

To compare differences in the magnetic properties and amount of S vacancies, Zn SAs/$1T\text{-}MoS_2$ and $1T\text{-}MoS_2$ were both evaluated by EPR spectroscopy. Additionally, $2H\text{-}MoS_2$ was evaluated and treated as the control during EPR analysis. The EPR spectrum of $2H\text{-}MoS_2$ displays a narrow line shape and isotropic g-value (g = 2.005) that is attributed to dangling Mo-S bonds generated by S vacancies (**Figure S3.8a**).[115, 142] In contrast, $1T\text{-}MoS_2$ (**Figure S3.8b**) and Zn SAs/$1T\text{-}MoS_2$ (**Figure S3.8c**) both produce complex EPR spectra in which more than one paramagnetic center is present. Since $1T\text{-}MoS_2$ and Zn SAs/$1T\text{-}MoS_2$ yield similar g-values, the following assignments of paramagnetic centers applies to both samples. Direct correlation of the

specific g-values each paramagnetic center is assigned to is provided in **Table S3.3**. The first paramagnetic center identified corresponds to paramagnetic S atoms in short chains (g = 2.042) and electron hole centers localized on S atoms (g $\approx$ 2.026).[143] The second paramagnetic center, which generates g-values between 1.932 to 1.959 and 2.017 to 2.019, is assigned to $Mo^{5+}$ species coordinated to S atoms.[144-146] The existence of $Mo^{5+}$ species corresponds to the presence of Mo species at higher oxidation states ($Mo^{5/6+}$) in the XPS spectra (**Figure S3.6**) and is a result of local structural defects in $1T-MoS_2$ that give rise to undercoordinated Mo atoms within the substrate.[147] The signals observed for g-values between 1.993 to 2.005 are ascribed to $S-Mo^{5+}$ defects and dangling Mo-S bonds generated by S vacancies, respectively.[142, 147] The negligible difference in signal intensity of $1T-MoS_2$ to that of Zn $SAs/1T-MoS_2$ indicates that the concentration of S vacancies is similar in both samples.[115, 142, 148] Therefore, the influence of S vacancies on the catalytic performance of Zn $SAs/1T-MoS_2$ is excluded.

### 3.3.4 Coordination Environment and Valence States of Zn SAs/1T-MoS₂

To confirm the chemical states and atomic dispersion of the Zn SAs, the electronic and coordination structures of Zn $SAs/1T-MoS_2$ were studied by XAS at both the Zn K-edge (**Figure 3.3**) and Mo K-edge (**Figure S3.9**). The XANES spectra (**Figure 3.3a**) show that the white line intensity and absorption edge of Zn $SAs/1T-MoS_2$ are closer to ZnO than Zn foil, indicating that the SAs exist in the $Zn^{2+}$ oxidation state. This is also reflected by the first derivative of the XANES spectra (**Figure 3.3b**). The $k^3$-weighted EXAFS spectra (**Figure 3.3c**) and Fourier-transformed EXAFS spectra in R-space (**Figure 3.3d**) correlate well with their best fitting lines modeled by DFT (**Figure 3.5b**), respectively, and suggest that Zn exists as SAs tetrahedrally coordinated to 4 S atoms. The coordination environment adopted by Zn SAs under confinement was first modeled
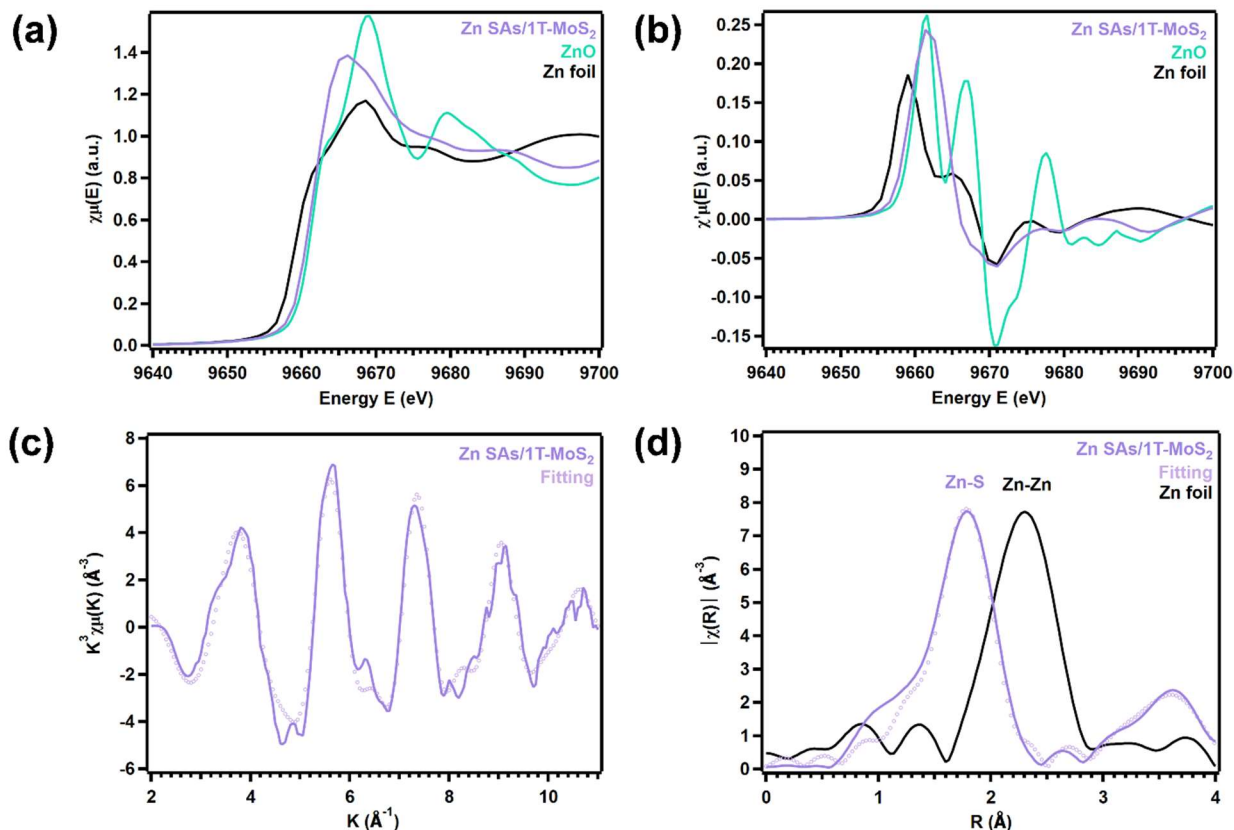
**Figure 3.3:** Zn K-edge XAS characterization of Zn SAs/1T-MoS$_2$.
**(a)** XANES spectra with Zn foil and ZnO as reference samples. **(b)** Derivative of XANES spectra. **(c)** EXAFS spectra in K space. **(d)** EXAFS spectra in R space.

as 1T-MoS$_2$ layers confining a Zn SA octahedrally coordinated to the S basal planes. After structural optimization, the SA's coordination geometry reorganized into a tetrahedral coordination with the S basal planes. Specifically, the Zn SAs formed asymmetric Zn-S1 and Zn-S3 coordination structures with the upper and lower S layers with bond lengths equal to 2.31 Å (**Table S3.4**). Typical peaks correspond to Zn-Zn bond formation (>2.50 Å) were not observed (**Figure 3.3d**), which indicates that the SAs remain atomically dispersed when under confinement.[149, 150] This tetrahedral coordination enables the Zn SAs to stabilize the expanded interlayer spacing of 1T-MoS$_2$, which in turn retains greater exposure of basal plane S active sites for enhanced HER performance.

**Figure S3.9a** shows the XANES spectra of Mo foil, 1T-MoS$_2$, and Zn SAs/1T-MoS$_2$ at the Mo K-edge corresponding to the 1s−5p transition. The edge energy of Zn SAs/1T-MoS$_2$ is visibly higher than Mo foil and very close to 1T-MoS$_2$, suggesting that the Mo atoms in Zn SAs/1T-MoS$_2$ have a similar oxidation state to that of 1T-MoS$_2$. This conclusion is further verified by the first derivative spectra of XANES (**Figure S3.9b**), where the valency of Mo atoms in Zn SAs/1T-MoS$_2$ is nearly the same as that of 1T-MoS$_2$. The Mo K-edge EXAFS spectra in K-space (**Figure S3.9c**) and Fourier-transformed EXAFS spectra in R-space (**Figure S3.9d**) coincide well with the fitting line (also based on the DFT model in **Figure 3.5b**), indicating that the Mo atoms in Zn SAs/1T-MoS$_2$ are octahedrally coordinated to 6 S atoms and an increase in S vacancies is not observed. The fitting results of the Fourier-transformed EXAFS spectra in R-space (**Table S3.5**) show that while half of the Mo-S bonds are at lengths that are expected for 1T-MoS$_2$ (2.41 Å), the other half exhibit longer bond lengths equal to 2.62 Å (**Table S3.5**). This increase in bond length may be ascribed to the slight distortion of octahedrally coordinated Mo-S centers induced by the intercalation of Zn SAs.

Altogether, these results confirm a few key findings. First, the Zn SAs adsorb between layers of 1T-MoS$_2$ and are stabilized by Zn-S bonding interactions. Second, intercalating Zn SAs between layers of 1T-MoS$_2$ expands the interlayer spacing by ~3.4%. Third, the incorporation of Zn SAs does not influence the electronic properties or concentration of S vacancies as compared to pristine 1T-MoS$_2$. Instead, the Zn SAs retain their 2+ oxidation state and d$^{10}$ electronic configuration, which inhibits their ability to perform as active sites for HER. Lastly, the Zn SAs tetrahedrally coordinate to basal S atoms and induce slight distortion of up to half of the Mo-S bonds in 1T-MoS$_2$. Based on these findings, the impact of Zn confinement on HER catalysis in 1T-MoS$_2$ is believed to solely be caused by confinement effects.

*3.3.5 HER Activity of Zn SAs/1T-MoS$_2$*

Changes in HER performance with intercalation of Zn SAs was monitored electrochemically under acidic conditions (N$_2$-saturated 0.5 M H$_2$SO$_4$) within a three-electrode configuration (detailed in the Supporting Information's Experimental Section). LSVs were collected to measure the amount of overpotential (measured at -10 mA/cm$^2$) 1T-MoS$_2$ requires to drive HER and elucidate how the overpotential changes when Zn SAs are confined near basal plane active sites in 1T-MoS$_2$. Comparison of overpotentials yielded by 1T-MoS$_2$ intercalated with 2.5, 8.5, and 16.5 mg of Zn SAs show that the overpotential peaks at 177 mV *vs.* RHE with 8.5 mg of Zn SAs intercalated into 1T-MoS$_2$ (**Figure S3.10a, Table S3.6**). The same trend is observed when analyzing the EIS of the samples to evaluate charge transport limitations (**Figure S3.10b**). The lowest charge transfer resistance (18.41 Ω) is observed when 8.5 mg of Zn SAs is intercalated into 1T-MoS$_2$ (**Table S3.7**). These results indicate that intercalating 8.5 mg of Zn SAs enhances 1T-MoS$_2$'s catalytic performance, while quantities above or below this amount exhibit worse HER activity and slow down charge transport efficiency. When 8.5 mg of Zn SAs are intercalated, 1T-MoS$_2$'s overpotential was reduced by 88 mV (**Figure 3.4a, Table S3.6**), indicating that less energy is required to drive HER when Zn SAs are spatially confined within 1T-MoS$_2$'s interlayer spacing (**Figure 3.4a**).

Tafel slopes were extracted from the onset potential region of the LSVs to identify how the presence of Zn SAs changes the rate at which HER proceeds on 1T-MoS$_2$ in acidic media (**Figure 3.4b**). In the first step of the HER mechanism, known as the Volmer step, a proton is reduced at an active site and adsorbed to the catalyst's surface. In the second step, H$_2$ is released through one of two pathways: either by a second proton/electron transfer, known as the Heyrovsky step, or the

recombination of two adsorbed protons, known as the Tafel step.[151] Since catalysts that exhibit the best HER performance yield the lowest overpotentials, these catalysts will produce the lowest Tafel slopes.[98] Comparison of Tafel slopes produced by 1T-MoS$_2$ (107.2 mV/dec) and Zn SAs/1T-MoS$_2$ (84.9 mV/dec) shows a decrease of 22.3 mV/dec when Zn SAs are intercalated between 1T-MoS$_2$ layers (**Figure 3.4b**). Spatial confinement has been predicted to increase the electrochemical potential of confined reacting species, which in turn enhances charge transfer between the catalyst surface and adsorbed protons. As a result, less applied voltage is needed to produce the same current density.[110] Here, the lowered kinetic barrier through which the HER mechanism proceeds is evidenced by the decrease in Tafel slope observed when Zn SAs are under confinement. Comparison of these results to similar cases of SACs reported in literature reveals a similar trend in overpotential and Tafel slopes for 2H and 1T MoS$_2$ supports intercalated with first row transition metals that exhibit similar electronic configurations to Zn$^{2+}$ (**Table S3.8**).

Confinement-induced changes in charge transfer properties were evaluated by EIS (**Figure 3.4c**). A reduction in charge transfer resistance when Zn SAs are spatially confined within 1T-MoS$_2$ is evidenced by the observably smaller radius of the semi-circle produced by Zn SAs/1T-MoS$_2$ compared to the radius of the semi-circle produced by 1T-MoS$_2$. Numerically, Zn confinement reduces charge transfer resistance in 1T-MoS$_2$ from 127.5 $\Omega$ to 18.41 $\Omega$. This decrease in charge transfer resistance implies that the rate of charge transfer from the active sites to the adsorbed protons is increased with interlayer confinement of Zn SAs.

In catalysis, the rate of an electrocatalytic reaction is directly proportional to the active surface area. Therefore, CV (**Figure S3.11**) was employed to derive the double-layer capacitance and calculate the ECSA of 1T-MoS$_2$ and Zn SAs/1T-MoS$_2$ (**Figure 3.4d**). Compared to the ECSA 1T-MoS$_2$ yields (7 mF/cm$^2$), Zn SAs/1T-MoS$_2$ yields an ECSA equal to 29 mF/cm$^2$, roughly four
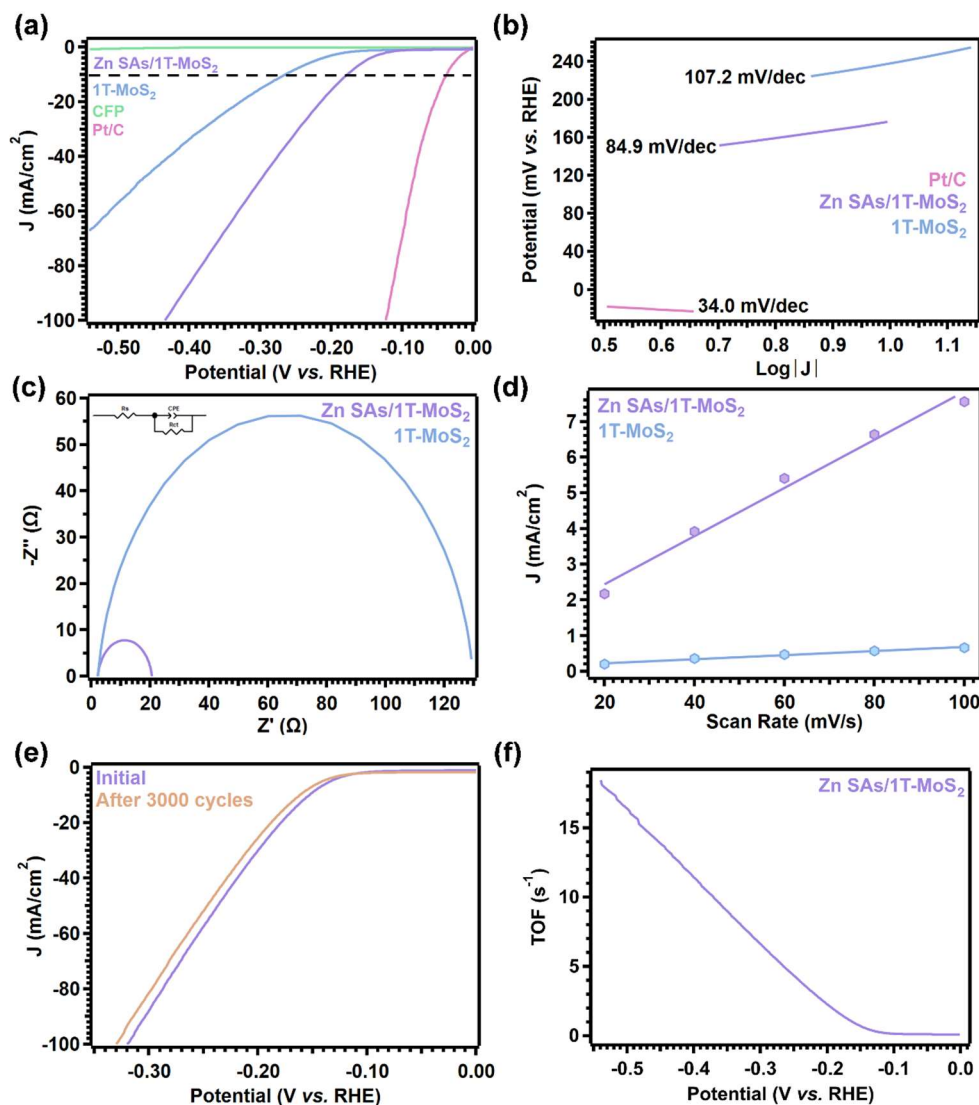
**Figure 3.4**: Electrochemical characterization of Zn SAs/1T-MoS$_2$ in N$_2$-saturated 0.5 M H$_2$SO$_4$ within a three-electrode configuration.
**(a)** Polarization curves of HER for CFP, 1T-MoS$_2$, Zn SAs/1T-MoS$_2$ and Pt/C (20%). **(b)** Tafel plots of 1T-MoS$_2$, Zn SAs/1T-MoS$_2$, and Pt/C (20%). **(c)** EIS results for 1T-MoS$_2$ and Zn SAs/1T-MoS$_2$ fitted to the equivalence circuit shown. **(d)** Scan-rate dependence of the current density at E = -300 mV *vs.* RHE. **(e)** Electrochemical stability test of Zn SAs/1T-MoS$_2$. **(f)** TOF values of Zn SAs/1T-MoS$_2$.

times greater than 1T-MoS$_2$'s ECSA. As a measure of the catalyst's surface area that is accessible

to the electrolyte, this improvement implies that there is roughly four times more area available to

facilitate charge transfer when Zn SAs are confined near basal plane active sites. This result

corresponds well with the EIS results and may be correlated to the increase in fringe spacing

induced by the Zn SAs in 1T-MoS$_2$ that was observed in the HRTEM and XRD results (**Figure 3.2**).

To test the stability of Zn SAs/1T-MoS$_2$ during catalysis, LSVs were collected both before and after the catalyst was subjected to 3,000 CV scans (**Figure 3.4e**). After 3,000 cycles, the overpotential increased by only 14 mV at 10 mA/cm$^2$. The excellent stability was further evidenced by continuous electrolysis at -0.2 V *vs.* RHE which showed nearly unchanged current generation after 24 hours (~20 mA cm$^{-2}$, **Figure S3.12**). XPS spectra of Zn SAs/1T-MoS$_2$ on CFP were collected before and after collecting 3,000 CV scans to evaluate the catalyst's structural stability (**Figure S3.13, Table S3.9**). The presence of both MoS$_2$ (Mo$^{4+}$) and MoS$_x$ (Mo$^{5/6+}$) is confirmed by the pre- (**Figures S3.13a, 3.13c, 3.13e, 3.13g**) and post-CV (**Figures S3.13b, 3.13d, 3.13f, 3.13h**) XPS spectra. While Zn$^{2+}$ SAs are observed near the catalyst surface before running CVs (**Figure S3.13a**), they are lost after the CV scans are completed (**Figure S3.13b**). Prior to stability testing, small amounts of MoO$_3$ (**Figures S3.13c, S3.13g**) and SO$_4^{2-}$ (**Figures S3.13e, S3.13g**) are observed on the sample surface. After stability testing, MoO$_3$ disappears (**Figures S3.13d, S3.13h**) and the layer of SO$_4^{2-}$ present on the sample grows (**Figures S3.13f, S3.13h**). Specifically, the sample initially starts with 4.55 at% of SO$_4^{2-}$. After CV is completed, 20.56 at% of SO$_4^{2-}$ is observed on the sample's surface. Furthermore, the Zn 2p peaks reappear after sputtering the sample for 30 s (**Figure S3.14**). Based on these results, the following observations were made. O$_2$ has been reported in literature to form Mo-oxide species by bonding to unsaturated Mo atoms at vacancy sites on defect-rich MoS$_2$ surfaces via chemical adsorption.[152, 153] Furthermore, O$_2$ adsorption has been reported to not alter the electronic properties of MoS$_2$.[153] Therefore, the complete loss of MoO$_3$ after electrolysis indicates that this species is localized along the sample surface and is likely caused by surface oxidation during working electrode preparation.

Meanwhile, interactions between the electrolyte and catalyst surface during HER drive the growth of $SO_4^{2-}$ on the catalyst surface. The significant increase of $SO_4^{2-}$ on the catalyst surface likely inhibits the ability to see the Zn 2p peaks after electrolysis, considering that the concentration of intercalated Zn SAs is so low (0.90% as determined by ICP-OES, **Table S3.10**). Since $SO_4^{2-}$ is a soluble ion, once the sample is submerged into the electrolyte, $SO_4^{2-}$ may redissolve. The reappearance of Zn 2p peaks after sputtering the sample for 30 s indicates that the Zn SAs intercalated between layers beneath the catalyst surface remain intact. The lack of significant decline (14 mV shift) in HER performance after 3,000 CVs observed further confirms that the integrity of the catalyst structure is well maintained (**Figure 3.4e**).

As previously mentioned, an average mass percent of 0.90% Zn SAs in Zn SAs/1T-MoS$_2$ quantified by ICP-OES (**Table S3.10**) was employed to determine TOF values and evaluate the catalyst's efficiency towards HER (**Figure 3.4f**). Similar to the polarization curves, the TOF values increase with higher potential. This result aligns well with reports from literature as well.[154] In our previous work, 1T-MoS$_2$ substituted with Ni SAs yielded a TOF of 0.7 s$^{-1}$ at 130 mV overpotential.[127] Here, the intercalation of Zn SAs between layers of 1T-MoS$_2$ yields a TOF equal to 1.40 s$^{-1}$ at 177 mV overpotential, when the current density is 10 mA/cm$^2$. Overall, the effects of Zn confinement within 1T-MoS$_2$ layers include decreased overpotentials, lowered kinetic barriers, faster charge transfer rates, and increased active surface area, all while retaining excellent stability.

### 3.3.6 Correlation of Confinement Effects to HER activity

First principles DFT calculations were performed to elucidate how confined Zn SAs influence 1T-MoS$_2$'s catalytic performance. Initially, two positions occupied by a Zn SA located above the basal plane of a single layer of 1T-MoS$_2$ were considered (**Figure S3.15**). In the first

structure, the Zn SA was positioned above an Mo atom (Single layer Zn SAs/1T-MoS$_2$ – Model I). In the second structure, the Zn SA is positioned above an S atom (Single layer Zn SAs/1T-MoS$_2$ – Model II). Compared to the normal length of Zn-S bonds (~2.36 Å), both coordination structures yield elongated Zn-S bond lengths that are greater than 2.95 Å.[155] Therefore, the formation of Zn SAs/1T-MoS$_2$ is predicted to be unfavorable for Models I and II with only a single layer of 1T-MoS$_2$. Instead, two or more layers of 1T-MoS$_2$ are required to stabilize intercalated Zn SAs and properly investigate the catalytic effects of spatially confining Zn SAs within the microenvironment of 1T-MoS$_2$ active sites.
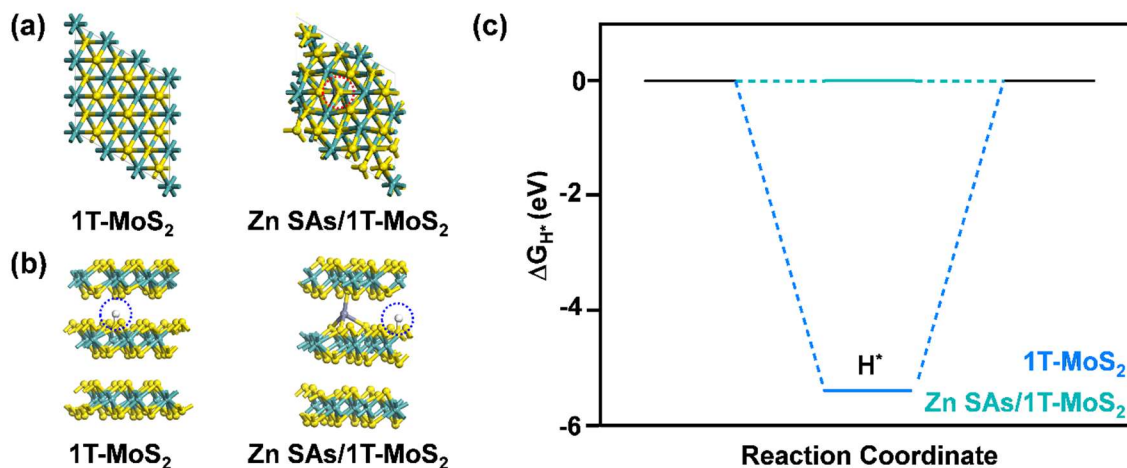


**Figure 3.5:** DFT computational analysis of 1T-MoS$_2$ and Zn SAs/1T-MoS$_2$.
**(a)** Top view. The Zn SA adsorption site between 1T-MoS$_2$ layers is circled in red. **(b)** Side view. Optimal adsorption modes of H$^*$. Proton adsorption sites are circled in blue. **(c)** Calculated $\Delta G_{H*}$ for HER at 0 V *vs.* RHE and pH = 0. The yellow, cyan, purple, and white spheres represent S, Mo, Zn, and H atoms, respectively.

In effort to understand why the Zn SAs prefer to adsorb to the basal plane on top of Mo atomic positions instead of substituting within the 1T-MoS$_2$ lattice, local active configurations demonstrating the possible atomic positions of Zn SAs on 1T-MoS$_2$ were constructed and their resulting formation energies for each configuration were compared to evaluate why the Zn SAs are prone to adsorb on top of Mo sites between layers of 1T-MoS$_2$. In total, there are four possible anchoring sites for Zn SAs on 1T-MoS$_2$ (**Figure S3.16**). The reported chemical potentials used to

calculate the formation energies discussed herein for S, Mo, and Zn were taken from the S8 molecule, Mo metal, and Zn metal, respectively. In the first model (**Figure S3.16a**), a Zn SA was tetrahedrally coordinated to 1T-MoS$_2$ with one bond formed with the top layer's basal plane and three bonds formed with the bottom layer's basal plane respectively. In this configuration, the Zn atom is adsorbed on top of an Mo atom and the formation energy is -6.06 eV. In the second model (**Figure S3.16b**), a Zn SA was tetrahedrally coordinated to form three bonds with the upper basal plane and one bond with the lower basal plane. However, the instability of this configuration caused the model to rearrange itself into a tetrahedral coordination that forms two bonds with the upper basal plane and two bonds with the lower basal plane. In this configuration, the Zn atom adsorbs on top of an S atom and the formation energy is -5.77 eV. In the third configuration (**Figure S3.16c**), an Mo atom is substituted by a Zn atom, which generates a formation energy equal to -2.14 eV. In the fourth configuration (**Figure S3.16d**), a Zn atom substitutes an S atom in the lower basal plane, which generates a formation energy equal to -4.16 eV. Comparison between the different formation energies of the four configurations shows that the first configuration with the most negative formation energy (**Figure S3.16a**, -6.06 eV) is the most likely configuration to occur due to being the most thermodynamically stable configuration. This result corresponds with the experimental STEM results (**Figure 3.1**).

To understand how confining Zn SAs within the microenvironment of 1T-MoS$_2$ active sites changes the proton adsorption/desorption kinetics of 1T-MoS$_2$, $\Delta G_{H*}$ values for a trilayer of 1T-MoS$_2$ and a trilayer 1T-MoS$_2$ intercalated with a tetrahedrally coordinated Zn SA were calculated for HER at a potential of 0 V *vs*. RHE and pH = 0 (**Figure 3.5**). Predicted models of the top view and optimal adsorption modes of H$^*$ for both cases are demonstrated in **Figures 3.5a, 3.5b**. The extremely negative $\Delta G_{H*}$ value (-5.40 eV) yielded by trilayer 1T-MoS$_2$ indicates that

adsorption of protons to the S active sites will be strong. Consequently, desorption of adsorbed protons upon producing $H_2$ will be challenging, and sluggish reaction kinetics are expected for active sites located along the basal plane. In contrast, Zn SAs/1T-MoS$_2$ yields a much more thermoneutral $\Delta G_{H*}$ (0.00294 eV), indicating that HER adsorption and desorption kinetics will be much more facile when Zn SAs are confined near the basal plane active sites in 1T-MoS$_2$. Altogether, these calculations correspond well with the experimentally observed improvement in HER performance.

Mulliken charge analysis was employed to predict the changes in the electron density of S active sites along the basal plane when Zn SAs are confined within their microenvironments (**Figure S3.17**). Here, 3D isosurface diagrams of differential charge are displayed for Zn SAs/1T-MoS$_2$. Charge clouds shown in blue represent energetically negative regions where the atom has lost electrons. Charge clouds shown in red exhibit positive charge and represent atoms that have gained electrons. The tetrahedral coordination of Zn SAs to basal S atoms yields a thermoneutral free energy value, making this coordination structure ideal for fast HER kinetics. In this coordination structure, the Zn atom donates electrons to nearby basal plane S atoms on 1T-MoS$_2$, resulting with the formation of strong ZnS bonds. This electron transfer changes the adsorption behavior of H atoms attached to neighboring S active sites. Based on these predictions, one may deduce that confining Zn SAs enhances the catalytic activity of 1T-MoS$_2$ by increasing electron density surrounding the S active sites around SAs. As a result, the catalytic activity of 1T-MoS$_2$ is enhanced accordingly.

To reveal the influence of Zn intercalation on the band structure of 1T-MoS$_2$, the PDOS spectra of the Zn 4s (black), Zn 3d (blue), S 3s (green), and S 3p (purple) orbitals were evaluated (**Figure S3.18**). Results show a strong electronic overlap between the Zn 4s and S 3p orbitals.

Together with the Mulliken charge population analysis of the atomic orbitals (**Figure S3.17**), one may deduce that the electrons transfer from the Zn 4s orbital to the S 3p orbital during Zn-S bond formation, which in turn causes the Zn atom to lose electrons and exhibit a positive valence state. Consequently, the S atoms coordinated to the adsorbed Zn atom gain electrons and exhibit a more negative valence state than they would in bare 1T-MoS$_2$. These results match well with the experimental XPS results reported herein (**Figure S3.6**). In regard to the effects of electronic accumulation at S sites on H* adsorption, near the Fermi level the density of states mainly come from S atoms, while the contribution from Zn is close to 0 eV. Therefore, the Zn atoms exhibit weak adsorption capacity for H$^*$ and are thus inactive, which is consistent with the H$^*$ adsorption configuration. In contrast, the S atoms have available p orbitals that can form bonds with H$^*$. The observed electron transfer from Zn to neighboring S atoms (**Figures S3.17, S3.18**) leads to an increase in electron filling and decrease in empty orbitals near the Fermi level, which weakens the electron accepting ability of S sites and thus H$^*$ adsorption.

To further elucidate the influence of Zn intercalation on the electronic structure and resulting HER activity of 1T-MoS$_2$, the PDOS spectra of the s and p orbitals in 1T-MoS$_2$ and Zn SAs/1T-MoS$_2$ were compared (**Figure S3.19**). As elucidated from **Figure S3.18**, electron transfer from Zn to neighboring S atoms results in a higher electron filling extent of neighboring S atoms. As shown by **Figure S3.19a**, this leads to a negative shift in the p band center of S atoms in Zn SAs/1T-MoS$_2$ from -3.78 (red dashed line) to -4.0 eV (green dashed line) and a decrease in the intensity of state density compared to 1T-MoS$_2$ near the Fermi level (shown in the black dashed box). Since the electronegativity of the S atom is stronger than a proton's electronegativity, the protons will donate electrons to active S sites in the adsorption process. However, the increase in electronic occupation of the S 3p orbitals and decrease in empty orbitals near the Fermi level

caused by Zn intercalation will cause a reduction in the electron accepting ability of the S atoms. Although the adsorption of protons is not strictly linear with the atomic electron density of S, it is negatively correlated. Thus, the number of electrons transferred to 1T-MoS$_2$ induced by proton adsorption is reduced after Zn intercalation. Proton adsorption capacity reduces from -5.40 eV to 0.5819 eV after Zn intercalation, which in turn sharply increases the catalyst's HER activity.

Since Zn intercalation influences the electronic structure of the catalyst's entire surface, we also calculated the H$^*$ adsorption behavior of some typical sites (**Figure S3.20**). The results suggest that Zn intercalation causes the HER activity of the catalyst's entire surface to improve, as shown by the resulting $\Delta G_{H*}$ values being closer to 0 eV for all of the H$^*$ adsorption sites considered. Meanwhile, compared to the neighboring S atoms in the first coordination sphere, the adsorption capacity of neighboring S atoms in the second coordination sphere is also weakened and yields better HER activity than the S atoms in the first coordination sphere (0.00294 eV).

To explore the influence of interlayer spacing expansion on HER activity of 1T-MoS$_2$, we manually set the lattice parameters of the supercell to increase by 3.4% along the Z axis before structural optimization (**Figure S3.21a**). By fixing the lattice parameters, only the structure of the ion step can be changed during structural optimization (**Figure S3.21b**). Calculation results show a $\Delta G_{H*}$ of -4.8081 eV, far worse than Zn SAs/1T-MoS$_2$ (0.00294 eV). In this regard, the electronic regulation of neighboring S atoms is believed to be the root cause of the observed improvement in HER activity upon intercalating Zn SAs between layers of 1T-MoS$_2$. By comparison, the lattice spacing expansion is only a secondary factor.

3.4 Conclusions

In this work, the catalytic effects of confining Zn SAs within the interlayer spacing of 1T-MoS$_2$ was investigated and several key findings were revealed. First, the Zn SAs adsorb to the basal plane of 1T-MoS$_2$. Second, this adsorption behavior allows the Zn intercalants to expand the interlayer spacing of 1T-MoS$_2$ by ~3.4%. Third, as SAs existing in the Zn$^{2+}$ oxidation state, the Zn intercalants tetrahedrally coordinate to nearby S atoms and donate electrons to basal S atoms. While they do induce a slight distortion in the 1T-MoS$_2$ lattice, the octahedral coordination surrounding Mo atoms remains unchanged. Zn confinement does not alter the amount of S vacancies or magnetic properties significantly. Catalytically, spatial confinement of Zn SAs within 1T-MoS$_2$ causes an 88 mV decrease in overpotential, 22.3 mV/dec decrease in Tafel slope, 109.09 $\Omega$ drop in charge transfer resistance, and excellent stability. Based on the in-depth structural analysis reported herein, the significant improvement in catalytic performance observed is attributed to the effects of confining Zn SAs within the microenvironments of basal plane active sites in 1T-MoS$_2$. DFT and PDOS calculations predict Zn SAs/1T-MoS$_2$ to yield a much more thermoneutral $\Delta G_{H*}$ (0.00294 eV) compared to 1T-MoS$_2$ (-5.40 eV), suggesting that HER adsorption and desorption kinetics will be much more facile when Zn SAs are under confinement.

This work reveals that intercalating transition metal ions such as Zn$^{2+}$ into catalytic layered materials such as 1T-MoS$_2$ enables the electronic states of confined microenvironments to be controlled according to the guest metal's coordination geometry and electronic states. In turn, the catalytic activity of 2D supports may be enhanced accordingly. Although this work investigates the confinement of Zn SAs within the microenvironments of 1T-MoS$_2$'s basal plane active sites and its influence on HER performance, the basis of this work may easily be adopted to other types of catalytic reactions and layered materials. Since confinement effects have been recognized for

their importance in heterogeneous, homogeneous, and enzymatic catalysis, the knowledge gained from this work may be appropriately applied to all fields of catalysis.

## 3.5 Materials and Methods

### 3.5.1 Chemicals

Ammonium heptamolybdate tetrahydrate [$(NH_4)_6Mo_7O_{24} \cdot 6H_2O$, 99% Alfa Aesar] and thioacetamide ($CH_3CSNH_2$, 99+% Acros Organics) were used without further purification.

### 3.5.2 Synthesis of 1T-MoS₂ nanosheets

First, 50 mg of $(NH_4)_6Mo_7O_{24} \cdot 6H_2O$, 80 mg of $CH_3CSNH_2$, and 10 mL of deionized (DI) water were combined in a 25 mL autoclave and sonicated until fully dissolved. Once dissolved, the autoclave was sealed within a hydrothermal reactor and heated at 180°C for 24 h. Once the reactor cooled to room temperature, the solution of crude product was transferred to 15 mL Conical Centrifuge Tubes. The crude product was washed and centrifuged three times: once with DI water, once with ethyl alcohol, and once with acetone. The solutions were centrifuged for 10 min. at ~4,000 rpm in between each washing step and the supernatant layer was removed after each centrifugation step. After washing, the purified product was dried in a vacuum oven at ~80°C and ~25 inHg for 24 h. The dried and purified product was finely ground with a mortar and pestle and stored under ambient conditions.

### 3.5.3 Synthesis of Zn SAs/1T-MoS₂

First, 50 mg of 1T-MoS₂, 15 mL DI water, and 35 mL ethanol were combined and continuously stirred at room temperature during the entire synthesis. Next, 2.5, 8.5, and 16.5 mg

of $ZnCl_2$ was dissolved in 6 mL of DI water to prepare Zn SAs (2.5 mg)/1T-MoS$_2$, Zn SAs (8.5 mg)/1T-MoS$_2$, and Zn SAs (16.5 mg)/1T-MoS$_2$, respectively. A syringe pump apparatus was employed to inject the Zn solution into the 1T-MoS$_2$ solution. To do this, the entire solution of $ZnCl_2$ was injected into the 1T-MoS$_2$ solution at a 10 µL/min flow rate. The solution stirred continuously at room temperature for 24 h after the injection was complete. Afterwards, the solution was transferred to 15 mL Conical Centrifuge Tubes, centrifuged for 10 min. at ~4,000 rpm, washed with DI water, and centrifuged again for the same amount of time. The supernatant layer was removed after each centrifugation step. The purified product was dried in a vacuum oven at ~80°C and ~25 inHg for 24 h, then finely ground with a mortar and pestle and stored under ambient conditions.

### 3.5.4 Characterization

XRD patterns were measured using a Panalytical X'Pert multipurpose XRD with Cu-Kα radiation ($\lambda = 1.5418$ Å) at 45 kV and 40 mA, with step size = 0.02° and scan step time = 17.75 s. The measurement range was from 10° to 80° in terms of 2θ. XPS measurements were collected with a PHI 5600 XPS system equipped with a monochromatic Al Kα X-ray source and Omni Focus III lens, operating at 250 W, 14 kV, 600 µm$^2$ spot size, and a maximum base pressure of $5 \times 10^{-9}$ torr. A 90° angle was maintained between the X-ray source and analyzer. Survey spectra were collected with 117.4 eV pass energy, 1.0 eV/step, and 50 µs dwell time. Multiplexes were collected using 11.75 eV pass energy, 0.100 eV/step, and 50 µs dwell time. The instrument was calibrated to Au 4f$_{7/2}$ = 84.00 eV and Cu 2p$_{3/2}$ = 932.67 eV immediately prior to collecting data. All spectra were calibrated to C 1s = 284.8 eV.[156] Multiplexes were fitted using IgorPro XPS Tools Software. A Shirley background and 80% Lorentzian-Gaussian was employed for all peak analyses. FTIR

spectra were collected using a PERKIN ELMER CE-440. Raman spectra were recorded using a Thermo Scientific DXR Raman Spectrometer employing an Ar-ion laser operating at 532 nm, 50 μm pinhole, and 3.0 mW laser power. EPR characterization was carried out on a Bruker EMX spectrometer (X-band) operating at a frequency of ~9.46 GHz. Field frequency modulation, modulation amplitude, and microwave power were set to 100 kHz, 0.4 mT, and 2.0 mW, respectively in every case to avoid saturation effects. All EPR measurements were recorded at room temperature.

AC-STEM was performed using the JEOL Grand ARM equipped with two spherical aberration correctors at 300 kV. HAADF-STEM images were acquired by a convergence semiangle of 22 mrad and inner and outer collection angles of 83 and 165 mrad, respectively. EDX spectroscopy was conducted using JEOL dual EDX detectors and a specific high count analytical TEM holder. Sample compositions were analyzed by a Perkin Elmer Optima 3000 DV ICP-OES. Commercially available Copper standard solutions (1000 mg $L^{-1}$ in nitric acid, Sigma Aldrich) were used for calibration. The standards were diluted to 1000 ppb (ng $g^{-1}$), 500 ppb, 100 ppb, 50 ppb, and 1 ppb, respectively, by mixing acid solutions (5 v/v% HCl + 5 v/v% $HNO_3$) to establish the calibration curves. All samples were dissolved in concentrated $HNO_3$ and then diluted to a concentration of 5% with DI water. Zn SAs/1T-$MoS_2$ were diluted 100 times using 5% $HNO_3$ for measurements.

Mo K-edge XAS spectra were collected at beamline 4-1 from the Stanford Synchrotron Radiation Lightsource (SSRL). The X-ray fluorescence was detected by a Lytle-type fluorescence-yield ion chamber detector. To reduce background noise from elastic scattering, the Soller slits were aligned and fitted with suitable Z-1 filters. Mo K-edge XAS data was measured within the range 19.778–20.887 keV in fluorescence mode with a step size of 0.25 eV at the near edge. The

Zn K-edge XAS was run within the 9.46-10.50 keV range in fluorescence mode with a step size of 0.25 eV at the near edge. All samples were prepared by placing a small amount of homogenized powder mixed with boron nitride (via agate mortar and pestle) on 3M Kapton Polyimide tape, which was purchased from 3M (https://www.3m.com/).

*3.5.5 Electrochemical Measurements*

All electrochemical measurements were conducted in $N_2$-saturated 0.5 M $H_2SO_4$ electrolytic solution within a three-electrode configuration. A CHI 660E electrochemical workstation was used for all electrochemical measurements. Graphite was employed as the counter electrode and Ag/AgCl (3 M NaCl, BASI) as the reference electrode. Electrodes were prepared by drop casting 200 μL of catalyst ink (50 μL each time, repeated 4 times) onto a 1×2 $cm^2$ piece of CFP. The loading of catalysts on CFP is 1 mg/$cm^2$. All potentials reported were calibrated with respect to the Ag/AgCl reference electrode in acidic media (0.5 M $H_2SO_4$) using **Equation (2.2)**.

LSVs were conducted under ambient conditions from 0 to -0.8 V with 5 mV/s scan rate, 1 mV step size, and 0.001 A/V sensitivity. Onset potentials were extracted from the LSVs and defined as the potential at which the current began to increase (0.05 mA/$cm^2$). Overpotentials were measured at -10 mA/$cm^2$. EIS measurements were performed at -0.4 V with 0.005 V variation in the frequency range of 1-$10^5$ Hz and 12 steps per decade. The electrochemical active surface area (ECSA) was derived from cyclic voltammograms (CV) measured with varying scanning rates of 20, 40, 60, 80 and 100 mV $s^{-1}$. The stability of Zn SAs/1T-MoS$_2$ was evaluated by running CV for 3,000 cycles from 0 to -0.8 V, followed by comparison of the initial and final LSV curves. The turnover frequency (TOF) was reported as the TOF corresponding to the overpotential reported (177 mV *vs.* RHE).

*3.5.6 Computational Methods*

Density functional theory (DFT) calculations were performed using CASTEP coding. The electronic exchange-correlation potential was conducted using the Perdew-Burke-Ernzerhof (PBE) functional of generalized gradient approximation (GGA) and the ultrasoft pseudopotentials were used. The kinetic energy cutoff was set to 400 eV for the plane-wave basis set. Brillouin zone integration was sampled with the $3\times3\times1$ MonkhorstPack mesh K-point for bulk and surface calculations, respectively. The DFT dispersion correction (DFT-D) method was used to correct the van der Walls interactions. A three-layer repeating unit supercell with the formula $Mo_{27}S_{54}$ and $Mo_{27}S_{54}Zn$ were constructed for bulk calculations. Monolayered 1T-$MoS_2$ ($Mo_9S_{18}$), Zn SAs/1T-$MoS_2$ ($Mo_9S_{18}Zn$), with a vacuum region of 15 Å along the Z axis, were constructed based on the HAADF-STEM imaging. The convergence tolerances were set to $1\times10^{-5}$ eV per atom for energy, $1\times10{-3}$ Å for maximum displacement, and 0.03 eV $Å^{-1}$ for maximum force. The thermodynamic energies and Gibbs free energies $\Delta G_{H*}$ were calculated using **Equation (3.2)**:

$$\Delta G_{H*} = E_{surf+} - E_{surf} - \frac{1}{2}E_{H_2} + \Delta E_{ZPE} - T\Delta S \qquad (3.2)$$

where $\Delta E_{ZPE}$ and $\Delta S$ are the difference in the zero-point energy and entropy between the adsorbed H atom and the gaseous phase $H_2$. At T=300 K, $\Delta G_{H*}$ may be calculated using **Equation (3.3)**:

$$\Delta G_{H*} = E_{surf+H} - E_{surf} - \frac{1}{2}E_{H_2} + 0.24 \ eV \qquad (3.3)$$

3.6 Acknowledgements

Chapter 3, in full, is a reprint of the material as it appears in "Zinc Single Atom Confinement Effects on Catalysis in 1T-phase Molybdenum Disulfide." *ACS Nano* 2023, 17, 2, 1414-1426. Younan, S., Li, Z., Yan, X., He, D., Hu, W., Demetrashvili, N., Trulson, G., Washington, A., Xiao, X., Pan, X., Huang, J., Gu, J. The dissertation author was the primary investigator and author of this paper.

## 3.7 Supplementary Information
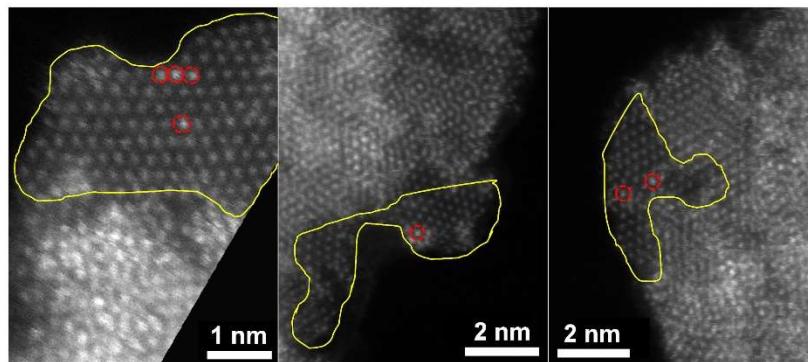


**Figure S3.1:** Identification of the adsorption model of Zn SAs/1T-MoS$_2$ by STEM.
Monolayer regions of 1T-MoS$_2$ sheets are outlined in yellow. The red circles highlight brighter atomic positions where Zn atoms are located on top of Mo atoms.
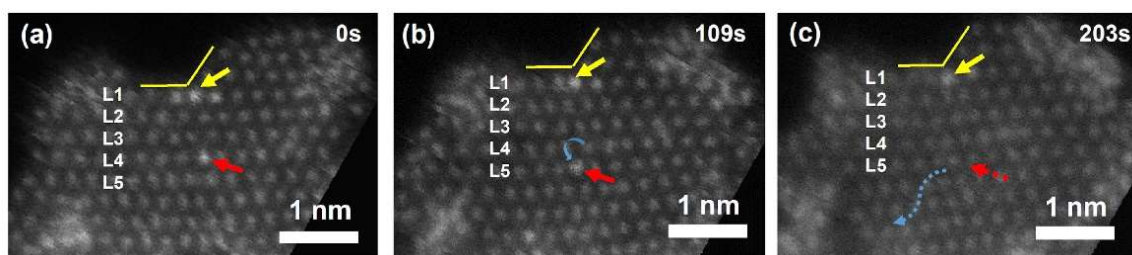


**Figure S3.2:** Migration of Zn SAs on 1T-MoS$_2$. STEM images of continued electron beam irradiation for: **(a)** 0 s, **(b)** 109 s, and **(c)** 203 s.
Scale bars are all 1 nm. Yellow lines and arrows indicate the edge of this region, while the Zn SA acts as a reference to align the images. The Zn SA indicated by the red arrow moves from the L4 to L5 at 109 s, then disappears after 203 s.

The maximum energy $E_m$ transferred from a high energy electron with an accelerating voltage of $E$ to the atomic nucleus may be calculated using the following equation:[132, 157]

$$E_m = 2.1477 \times 10^{-9} \times E(E + 1.022 \times 10^6) / A$$

where $A$ is the atomic mass and the energies are in unit of eV. For the 60-keV electron beam used in our experiments, the $E_m$ for Zn atoms is 4.65 eV. Such energy is larger than the bonding energy of Zn-S (1.06-2.63 eV).[158] Therefore, the electron beam is expected to be able to drive the migration of Zn SAs adsorbed along the 1T-MoS$_2$ basal plane.
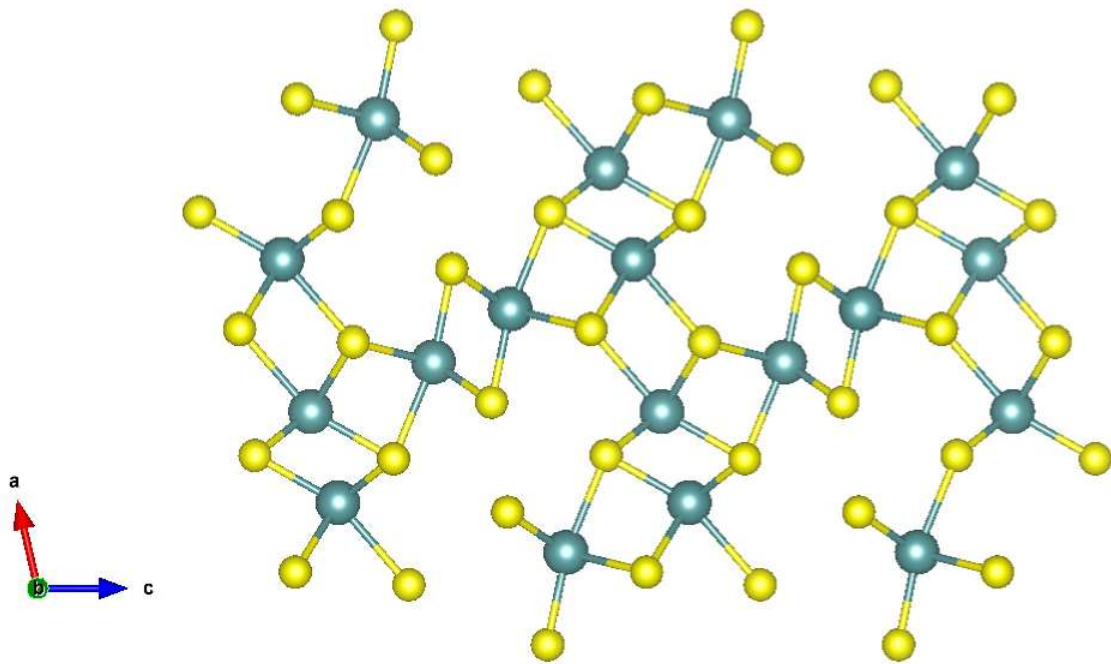
**Figure S3.3:** Lattice structure of monoclinic $Mo_2S_3$.
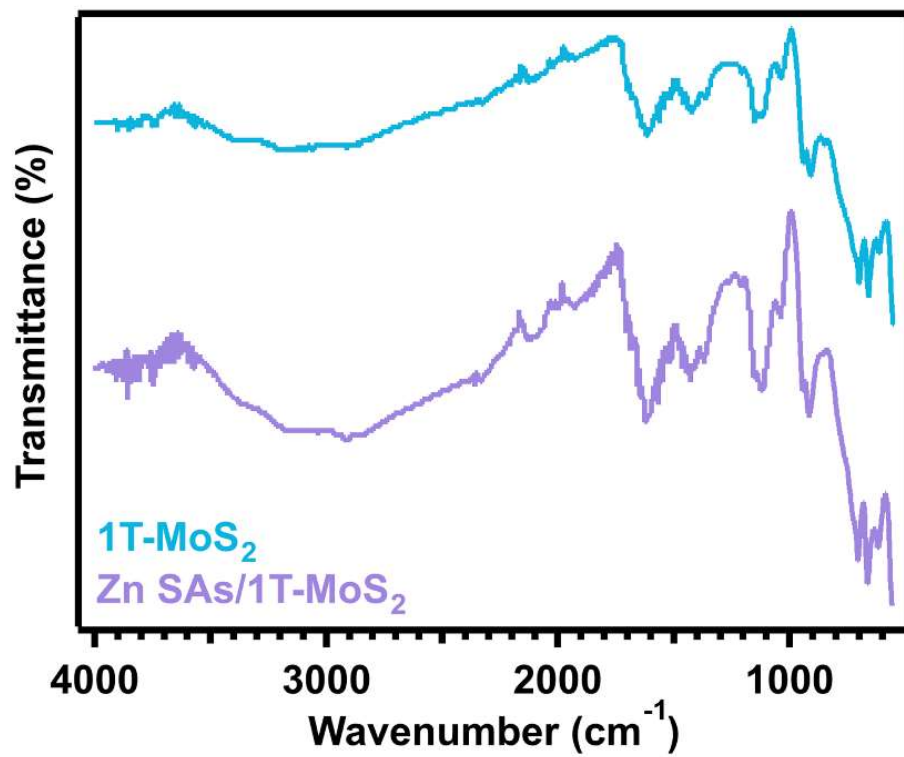
**Figure S3.4:** FTIR spectra of Zn SAs/1T-MoS$_2$ (purple) and 1T-MoS$_2$ (blue).
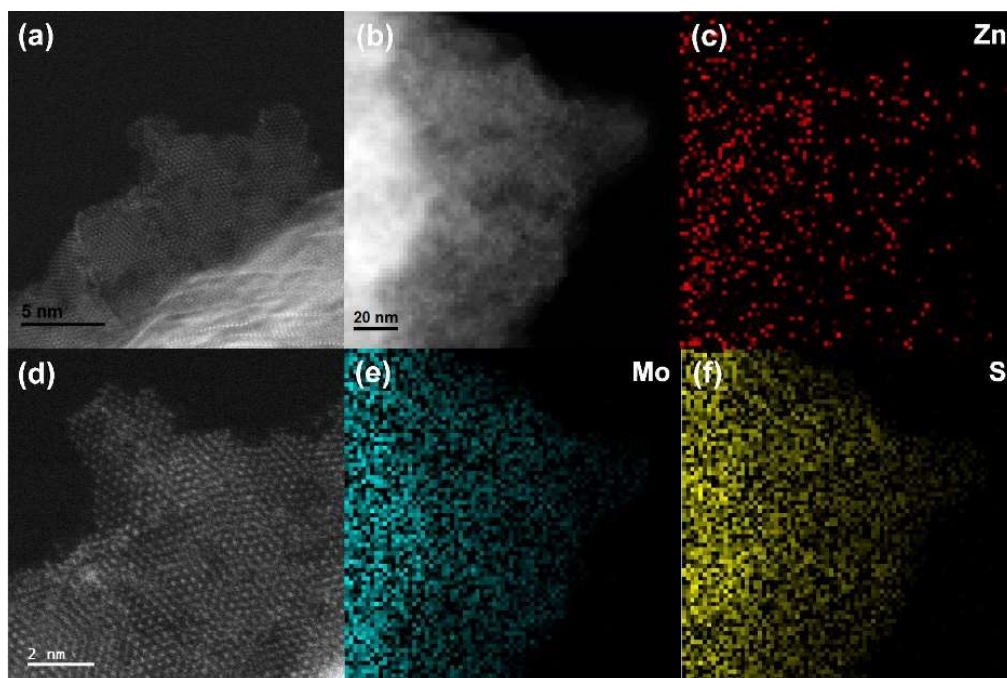


**Figure S3.5:** STEM and EDX mapping of Zn SAs/1T-MoS$_2$.
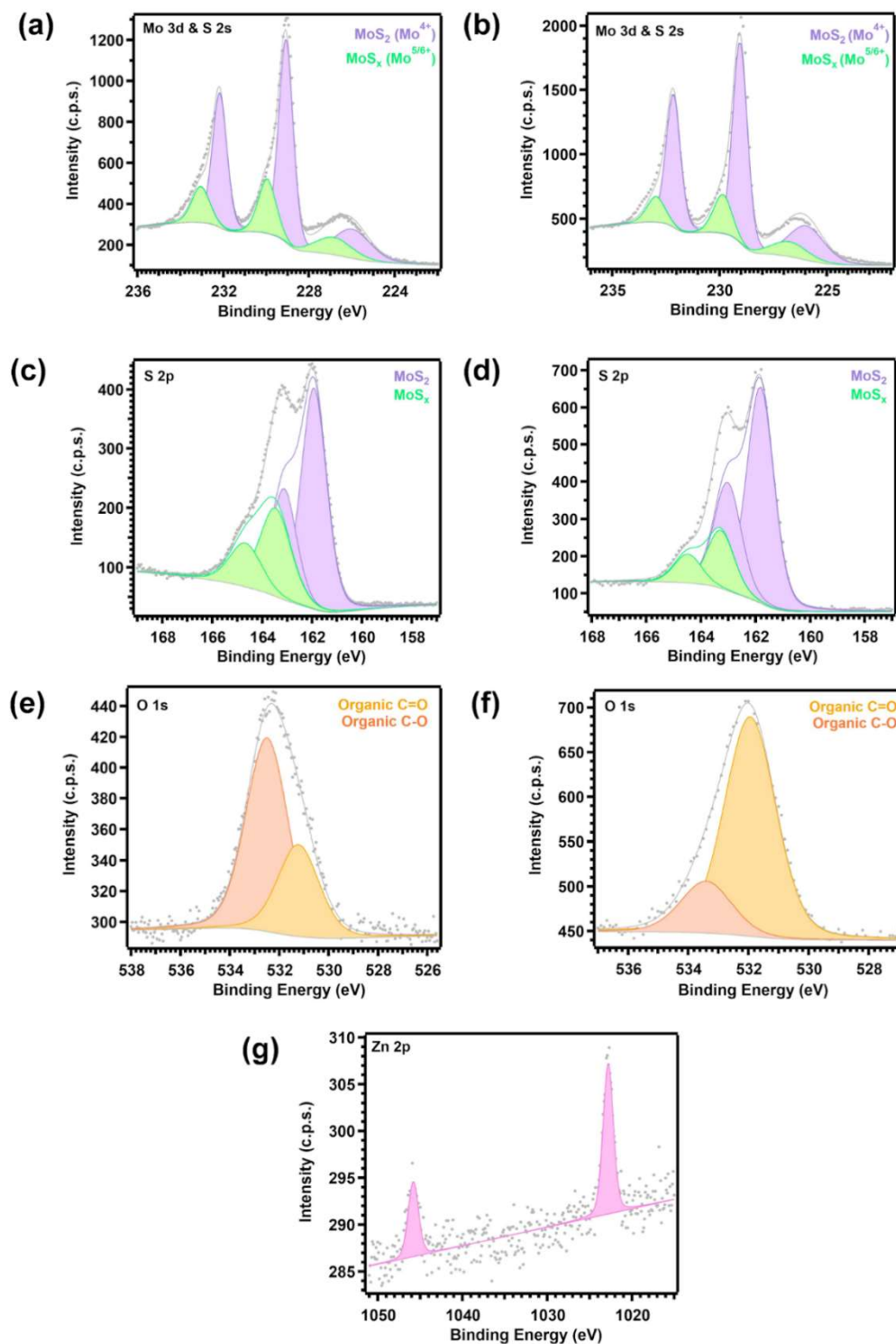
**Figure S3.6:** XPS characterization of 1T-MoS$_2$ **(a, c, e)** and Zn SAs/1T-MoS$_2$ **(b, d, f, g)**. **(a-b)** Mo 3d and S 2s spectra. **(c-d)** S 2p spectra. **(e-f)** O 1s spectra. **(g)** Zn 2p spectrum.
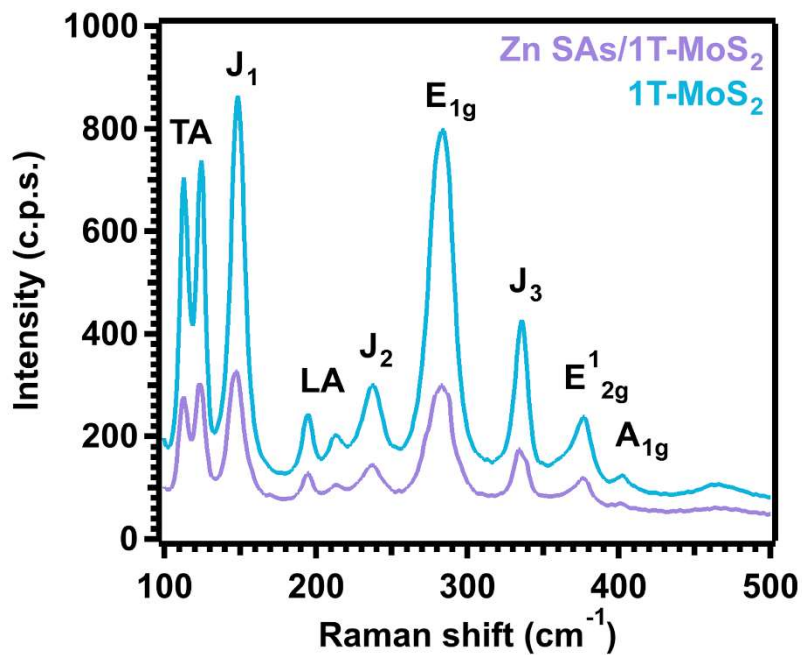
**Figure S3.7:** Raman spectra of Zn SAs/1T-MoS$_2$ (purple) and 1T-MoS$_2$ (blue).
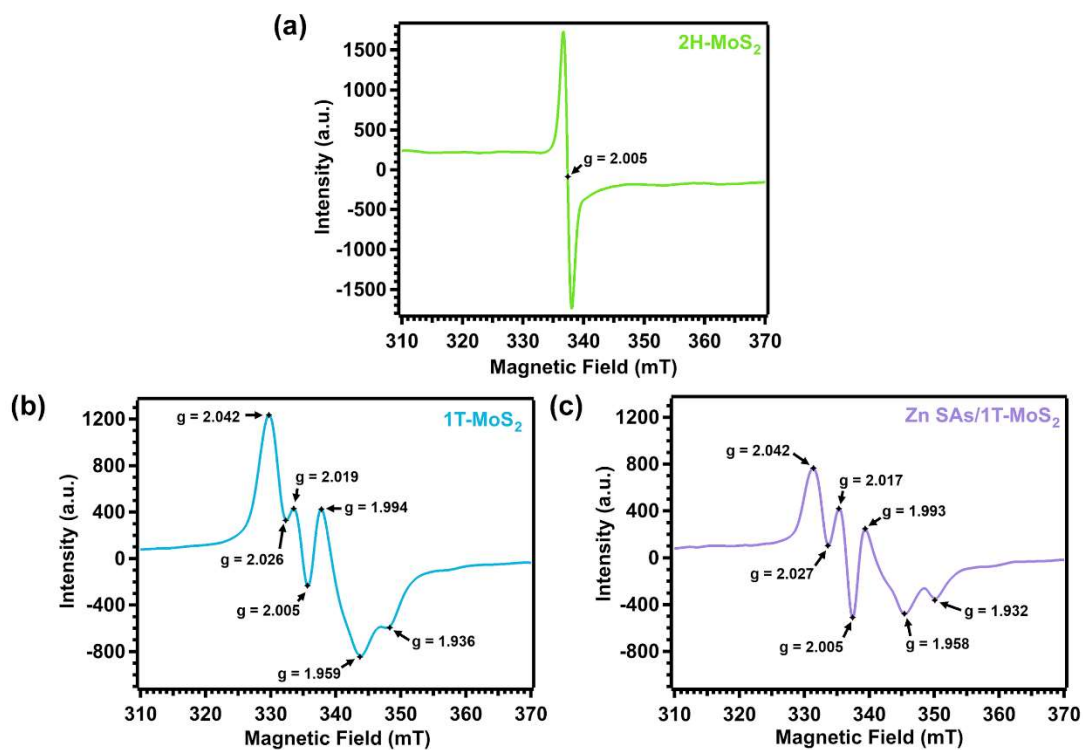


**Figure S3.8:** EPR spectra of **(a)** 2H-MoS$_2$, **(b)** 1T-MoS$_2$, and **(c)** Zn SAs/1T-MoS$_2$.
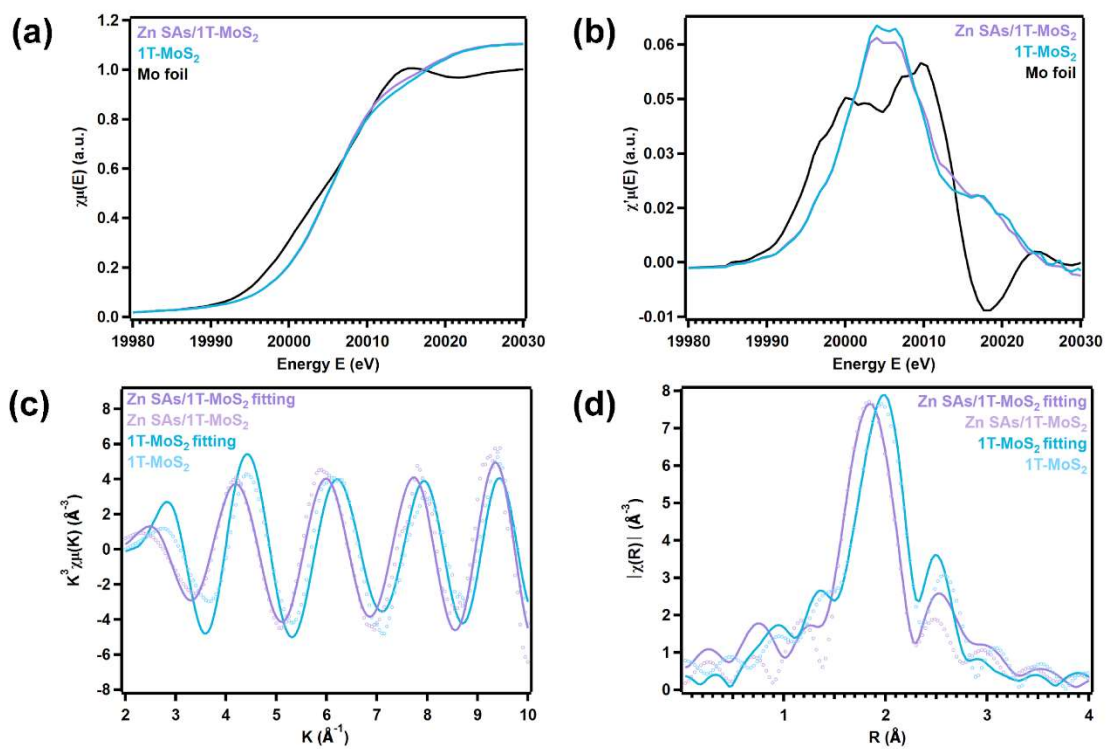
**Figure S3.9:** Mo K-edge XAS characterization of Zn SAs/1T-MoS$_2$.
**(a)** XANES spectra with Mo foil and 1T-MoS$_2$ as reference samples. **(b)** Derivative of XANES spectra. **(c)** EXAFS spectra in k space. **(d)** Fourier-transformed EXAFS spectra in R space.
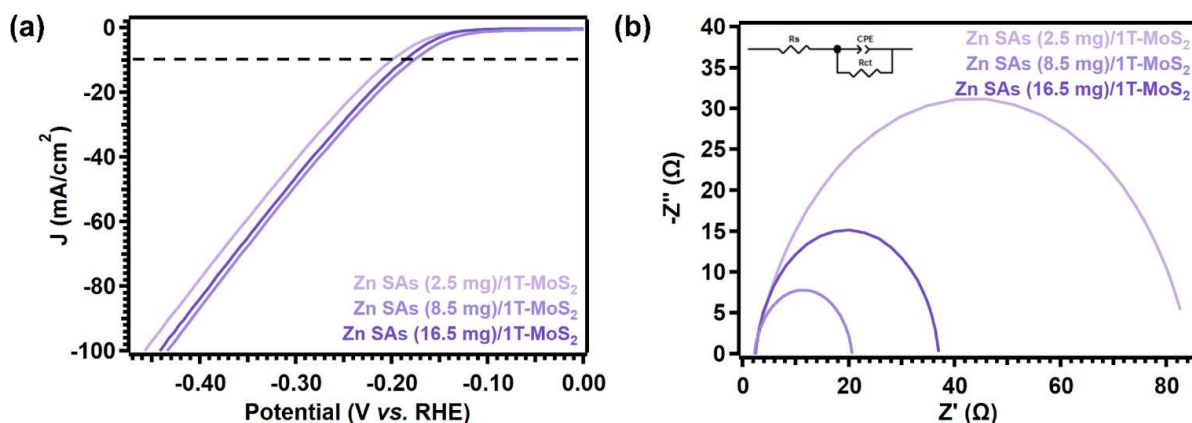
**Figure S3.10:** Electrochemical analysis of how the HER performance of 1T-MoS$_2$ changes as the quantity of Zn SAs increases.
These measurements were performed within a standard three-electrode configuration, with N$_2$-saturated 0.5 M H$_2$SO$_4$ as the electrolyte. **(a)** LSVs. **(b)** EIS fitted to the equivalent circuit shown.
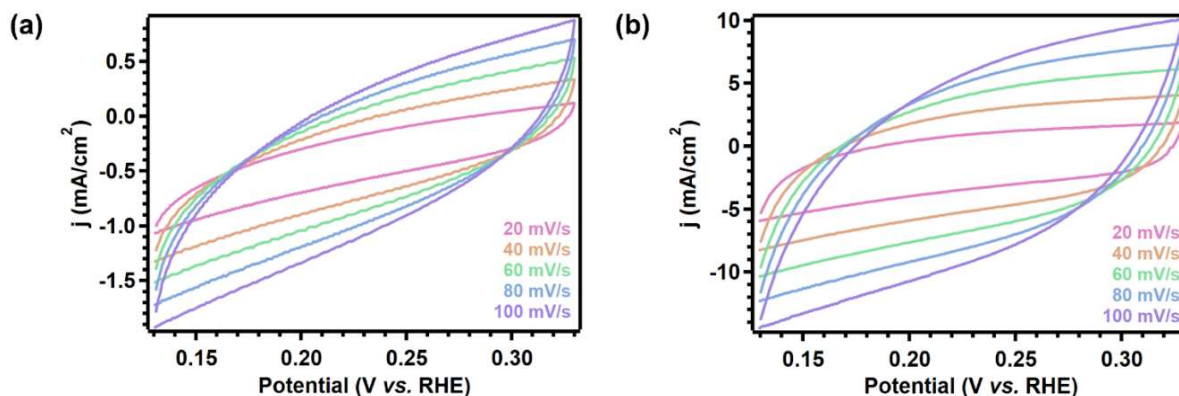


**Figure S3.11:** CV measurements of **(a)** 1T-MoS$_2$ and **(b)** Zn SAs/1T-MoS$_2$.
Measurements were performed within a standard three-electrode configuration 0.5 M H$_2$SO$_4$ saturated with N$_2$ was used as the electrolyte. The scanning rates are 20, 40, 60, 80, and 100 mV s$^{-1}$ respectively.
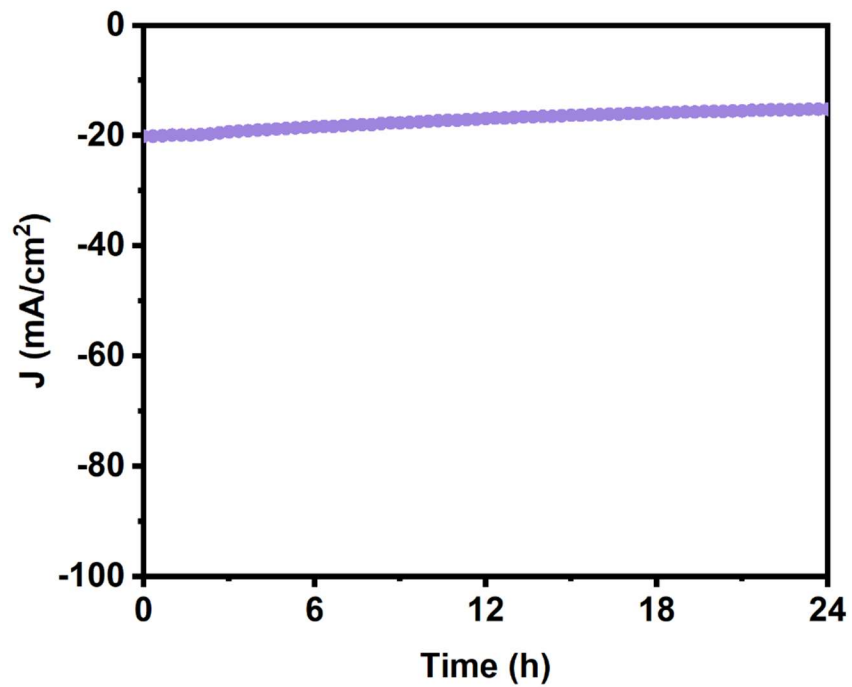
**Figure S3.12:** Recorded current generation during 24 hours of continuous electrolysis at -0.2 V vs. RHE with Zn SAs/1T-MoS$_2$ used as the working electrode.
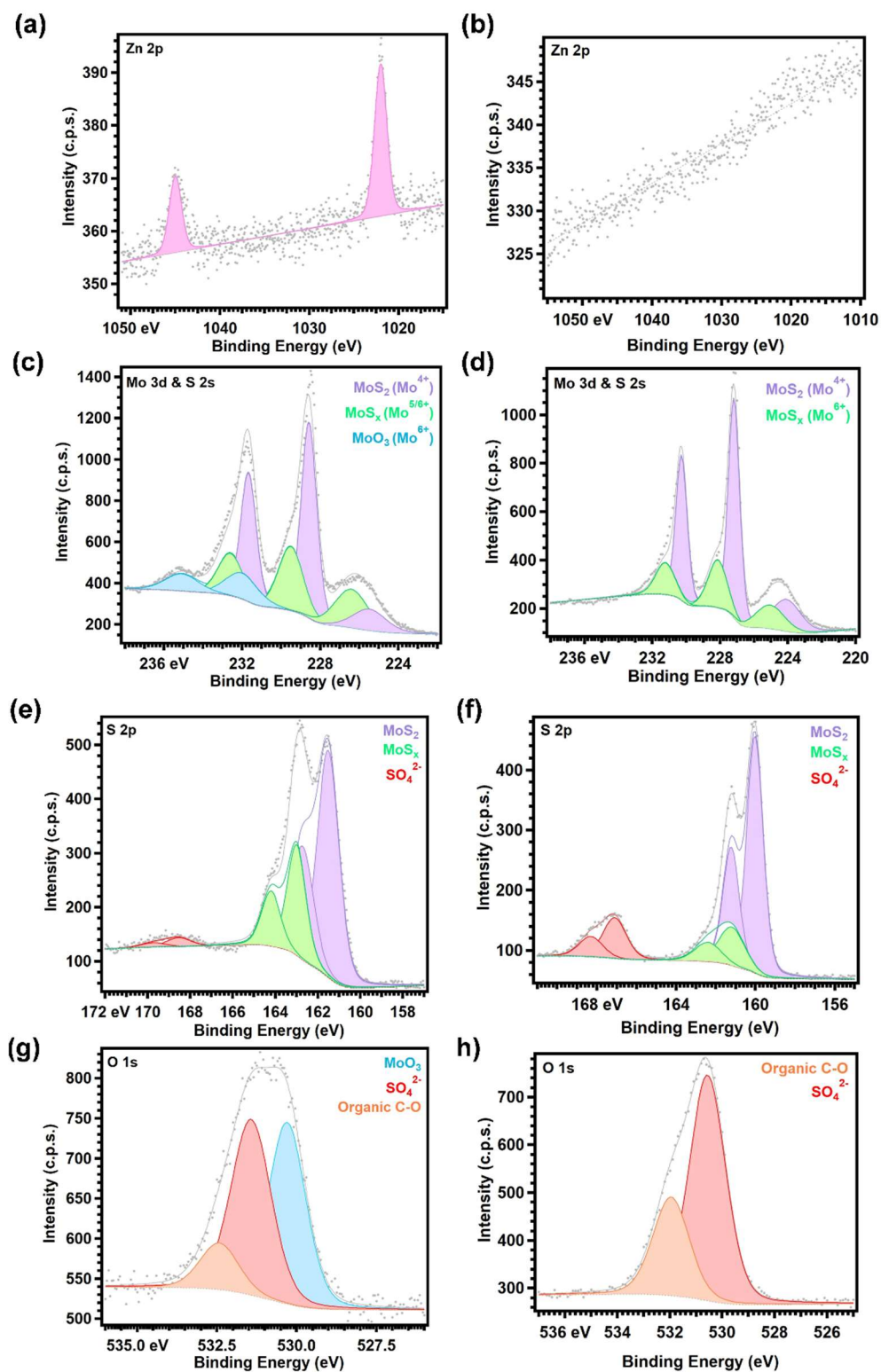
**Figure S3.13:** XPS data and peak assignments for Zn SAs/1T-MoS$_2$ **(a, c, e, g)** before and **(b, d, f, h)** after collecting 3,000 CV scans.
**(a, b)** Zn 2p. **(c, d)** Mo 3d and S 2s. **(e, f)** S 2p. **(g, h)** O 1s.
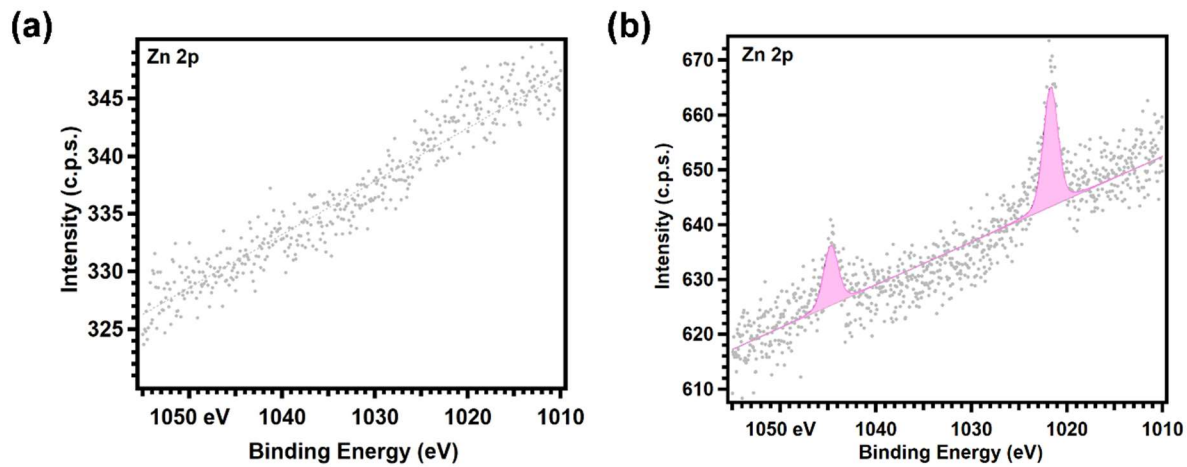
**Figure S3.14:** XPS analysis of Zn 2p **(a)** before and **(b)** after sputtering the sample for 30 s.



Bond Lengths:
1) 3.038 Å
2) 3.378 Å
3) 3.376 Å

Monolayer Zn SAs/1T-MoS$_2$ – Model I

Bond Lengths:
1) 3.271 Å
2) 2.949 Å
3) 3.270 Å

Monolayer Zn SAs/1T-MoS$_2$ – Model II
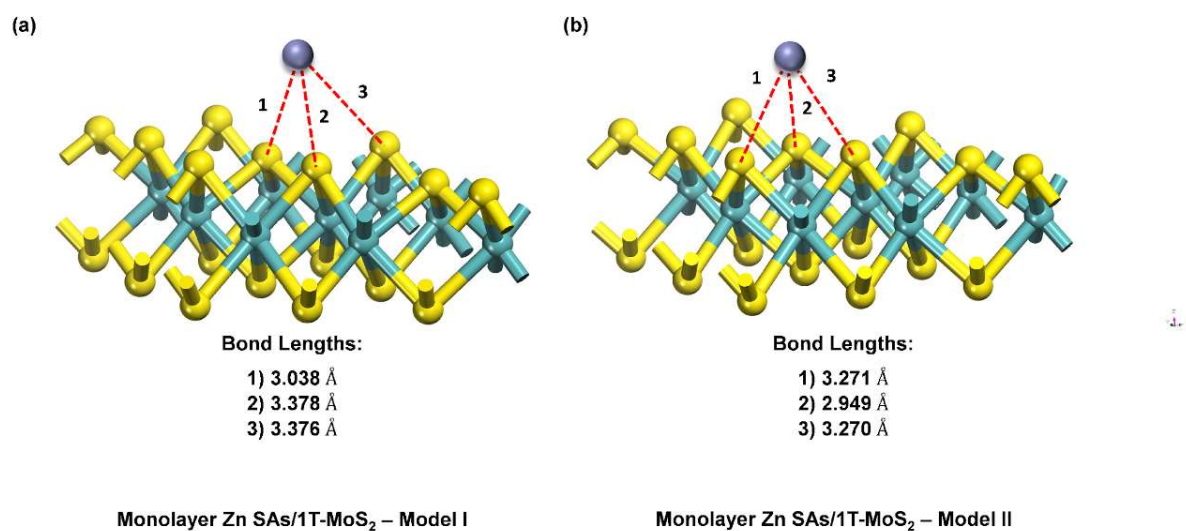
**Figure S3.15:** DFT models of the single layer Zn SAs/1T-MoS$_2$.
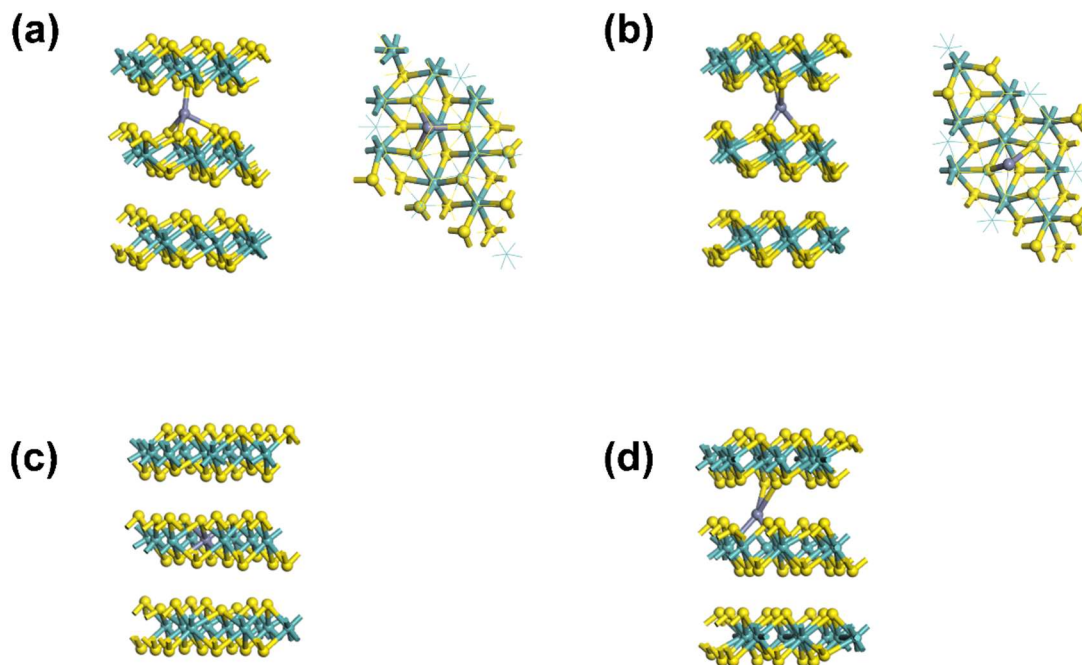
**Figure S3.16:** Possible configurations of Zn SA anchoring sites on 1T-MoS$_2$.
**(a)** Tetrahedral coordination forming one bond with the upper basal plane and three bonds with the lower basal plane. **(b)** Tetrahedral coordination forming two bonds each with the upper and lower basal planes. **(c)** Zn substituting an Mo atom within the 1T-MoS$_2$ lattice. **(d)** Zn substituting an S atom in the bottom basal plane.
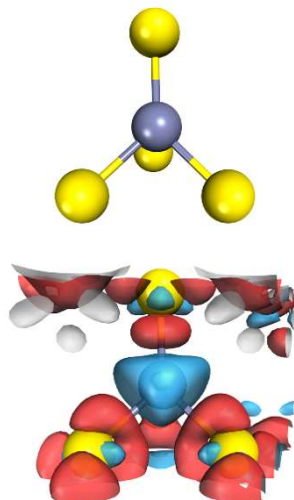
**Figure S3.17:** Mulliken charge analysis and 3D isosurface diagrams of a tetrahedrally coordinated Zn SA coordinated to S atoms along the basal plane of 1T-MoS$_2$.

The purple and yellow atoms represent Zn and S, respectively. Charge clouds shown in blue represent energetically negative regions where electrons have been lost. Charge clouds shown in red exhibit positive charge and represent regions where electrons have been gained.
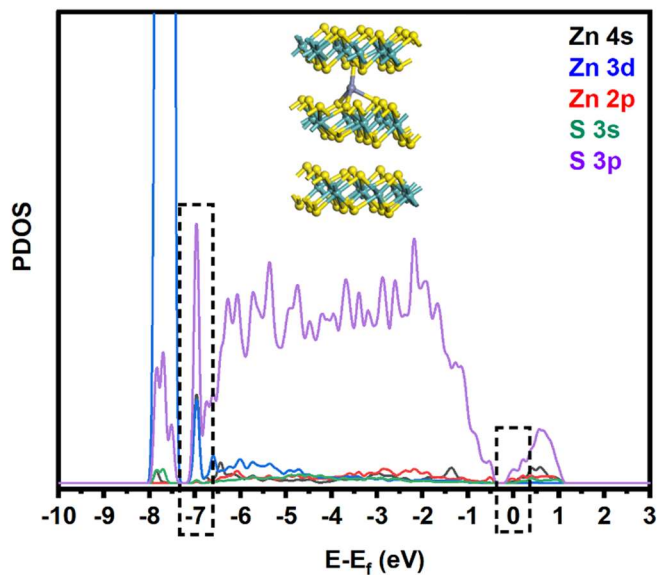


**Figure S3.18:** PDOS spectra of the Zn 4s (black), Zn 3d (blue), Zn 2p (red), S 3s (green), and S 3p (purple) orbitals.
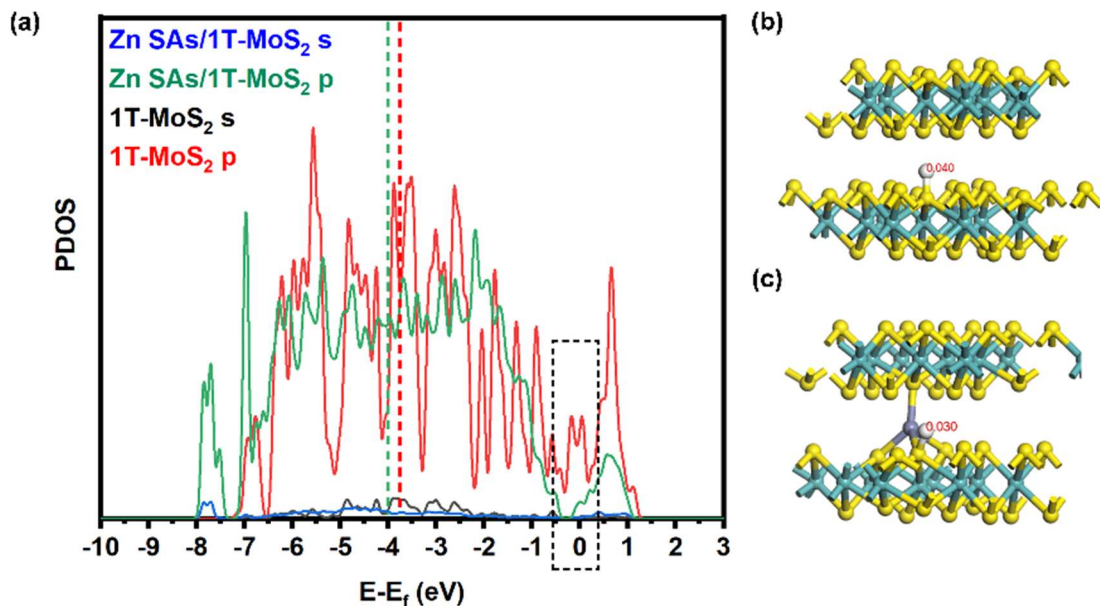
**Figure S3.19:** 1T-MoS$_2$ and Zn SAs/1T-MoS$_2$ PDOS spectra of s and p orbitals and H$^*$ adsorption models.

**(a)** PDOS spectra of the s and p orbitals in 1T-MoS$_2$ and Zn SAs/1T-MoS$_2$. **(b)** H$^*$ adsorption model on 1T-MoS$_2$. **(c)** H$^*$ adsorption model on Zn SAs/1T-MoS$_2$.
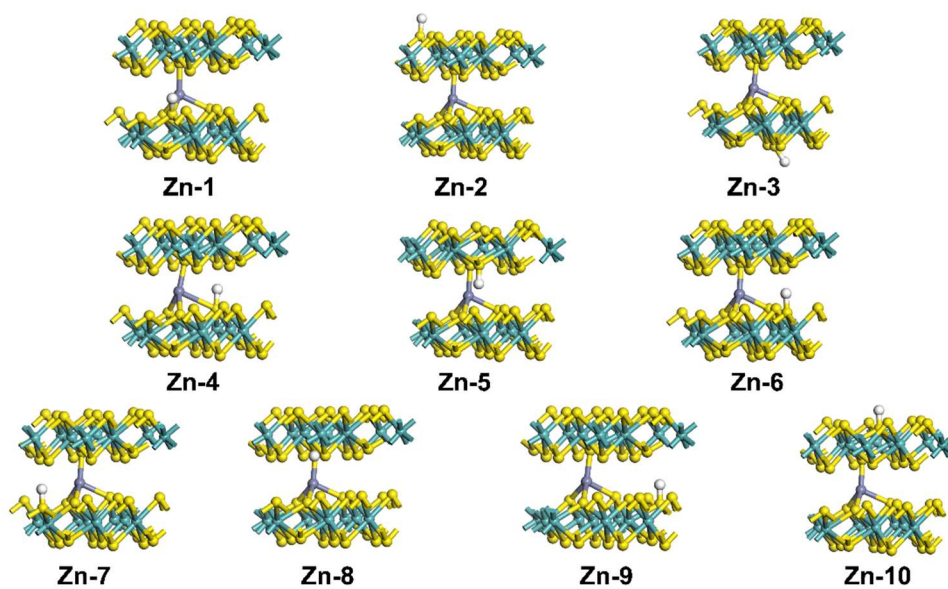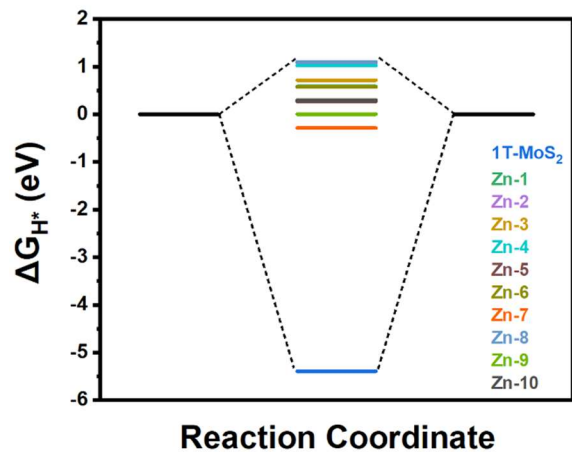
**Figure S3.20:** Calculated $\Delta G_{H*}$ for HER at typical H* adsorption sites (at 0 V vs. RHE and pH = 0) with models of the H* adsorption sites Zn-1 through Zn-10.
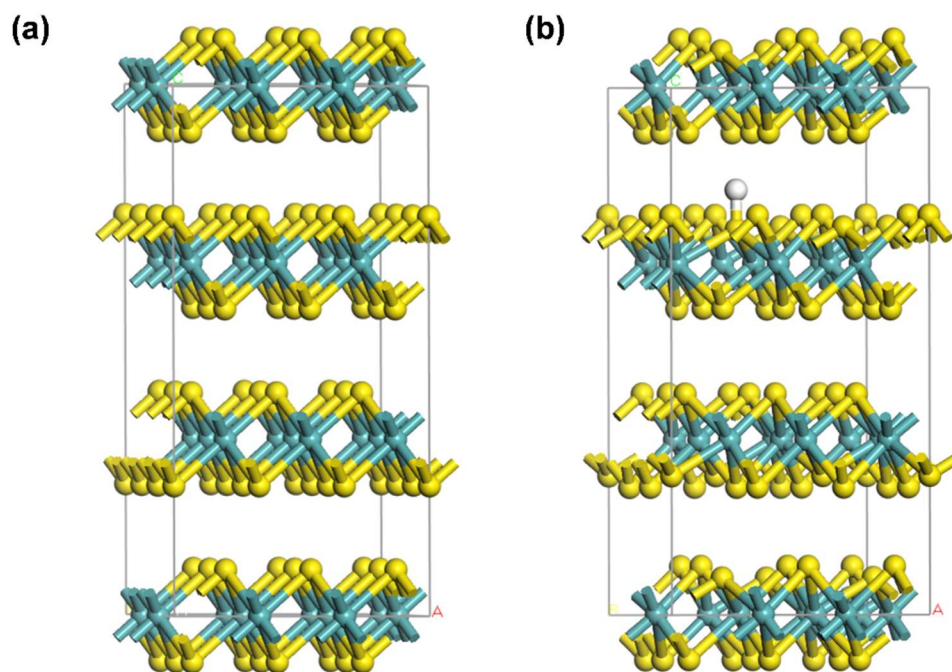
**Figure S3. 21:** Supercell modeling of H* adsorption on 1T-MoS$_2$ with the Z axis increased by 3.4% **(a)** before and **(b)** after structural optimization.

**Table S3.1:** XPS data and peak assignments for 1T-MoS$_2$ and Zn SAs/1T-MoS$_2$

| Peak | Binding Energy (eV) | | Peak Assignment |
|---|---|---|---|
| | **1T-MoS$_2$** | **Zn SAs/1T-MoS$_2$** | |
| Zn 2p$_{3/2}$ | -- | 1022.80 | Zn$^{2+}$ |
| Zn 2p$_{1/2}$ | -- | 1045.80 | Zn$^{2+}$ |
| Mo 3d$_{5/2}$ | 229.05 | 229.03 | MoS$_2$, Mo$^{4+}$ |
| | 229.93 | 229.84 | MoS$_x$, Mo$^{5/6+}$ |
| Mo 3d$_{3/2}$ | 232.15 | 232.13 | MoS$_2$, Mo$^{4+}$ |
| | 233.03 | 232.94 | MoS$_x$, Mo$^{5/6+}$ |
| S 2p$_{3/2}$ | 161.90 | 161.81 | MoS$_2$, S$^{2-}$ |
| | 163.45 | 163.26 | MoS$_x$, S$^{2-}$ |
| S 2p$_{1/2}$ | 163.10 | 163.01 | MoS$_2$, S$^{2-}$ |
| | 164.65 | 164.46 | MoS$_x$, S$^{2-}$ |
| S 2s | 225.95 | 225.93 | MoS$_2$ |
| | 226.83 | 226.74 | MoS$_x$ |
| O 1s | 531.20 | 531.93 | Organic C=O |
| | 532.48 | 533.39 | Organic C-O |

**Table S3.2:** Raman peak assignments for 1T-MoS$_2$ and Zn SAs/1T-MoS$_2$

| Peak Positions (cm$^{-1}$) | | Peak Assignments |
|---|---|---|
| **1T-MoS$_2$** | **Zn SAs/1T-MoS$_2$** | |
| 113 | 113 | TA |
| 125 | 124 | TA |
| 149 | 148 | J$_1$ |
| 195 | 195 | LA |
| 213 | 213 | LA |
| 237 | 237 | J$_2$ |
| 284 | 283 | E$_{1g}$ |
| 336 | 334 | J$_3$ |
| 377 | 376 | E$^1_{2g}$ |
| 402 | 400 | A$_{1g}$ |

**Table S3.3:** Assignments of experimental g-values for 2H-MoS$_2$, 1T-MoS$_2$, and Zn SAs/1T-MoS$_2$

| | g-values | | Assignment |
|---|---|---|---|
| **2H-MoS$_2$** | **1T-MoS$_2$** | **Zn SAs/1T-MoS$_2$** | |
| | 2.042 | 2.042 | Paramagnetic S in short chains |
| | 2.026 | 2.027 | Electron hole center localized on S atoms |
| | 2.019 | 2.017 | Mo$^{5+}$ species coordinated to S atoms |
| 2.005 | 2.005 | 2.005 | Dangling Mo-S bonds generated by S vacancies |
| | 1.994 | 1.993 | S-Mo$^{5+}$ defects |
| | 1.959 | 1.958 | Paramagnetic Mo$^{5+}$ coordinated to S atoms |
| | 1.936 | 1.932 | Mo$^{5+}$ species coordinated to S atoms |

**Table S3.4:** Local structure parameters of Zn SAs/1T-MoS$_2$ fitted from the Zn K-edge EXAFS spectra

| Sample | Path | CN | $\Delta E$ (eV) | R (Å) | $\sigma^2$ (Å$^2$) |
|---|---|---|---|---|---|
| Zn SAs/1T-MoS$_2$ | Zn-S | 4 | -9.6 | 2.31 | 0.009 |

**Table S3.5:** Local structure parameters in Zn SAs/1T-MoS$_2$ fitted from Mo K-edge EXAFS spectra

| Sample | Path | CN | $\Delta E$ (eV) | R (Å) | $\sigma^2$ (Å$^2$) |
|---|---|---|---|---|---|
| 1T-MoS$_2$ [a] | Mo-S | 6 | 3.910 | 2.44 | 0.010 |
| Zn SAs/1T-MoS$_2$ | Mo-S1 | 3 | -1.4 | 2.41 | 0.001 |
| | Mo-S2 | 3 | -1.4 | 2.62 | 0.0089 |

[a] Control sample taken from reference.[127]

**Table S3.6:** Comparison of the overpotentials and Tafel slopes observed for each sample evaluated in this work

| Sample | Overpotential (mV *vs.* RHE) | Tafel slope (mV/dec) |
|---|---|---|
| CFP | -- | -- |
| Pt/C | 37 | 34.0 |
| 1T-MoS$_2$ | 265 | 107.2 |
| Zn SAs (2.5 mg)/1T-MoS$_2$ | 199 | -- |
| Zn SAs (8.5 mg)/1T-MoS$_2$ | 177 | 84.9 |
| Zn SAs (16.5 mg)/1T-MoS$_2$ | 187 | -- |

Overpotentials are defined as the potential (mV *vs.* RHE) measured at -10 mA/cm$^2$.

**Table S3.7:** Equivalent circuit fittings for EIS data

| Sample | $R_s$ (Ω) | $R_{ct}$ (Ω) | CPE-T | CPE-P |
|---|---|---|---|---|
| 1T-MoS$_2$ | 2.289 | 127.5 | 0.0247 | 0.923 |
| Zn SAs (2.5 mg)/1T-MoS$_2$ | 2.302 | 82.13 | 0.0573 | 0.828 |
| Zn SAs (8.5 mg)/1T-MoS$_2$ | 2.191 | 18.41 | 0.00410 | 0.897 |
| Zn SAs (16.5 mg)/1T-MoS$_2$ | 2.371 | 34.59 | 0.0209 | 0.915 |

The data was measured at overpotentials of -200 mV. $R_s$, $R_{ct}$, and CPE represent the electrolyte, charge transfer resistance, and the constant phase element, respectively.

**Table S3.8:** HER performance comparison with similar 1T-MoS$_2$ single atom catalysts

| Catalyst | Intercalation Method | Electrolyte | Overpotential (mV *vs.* RHE) | Tafel Slope (mV/dec) | Reference |
|---|---|---|---|---|---|
| Zn SAs/1T-MoS$_2$ | Adsorption | 0.5 M H$_2$SO$_4$ | 177 | 84.9 | This work |
| Zn 2H-MoS$_2$ | Substitution | 0.5 M H$_2$SO$_4$ | 300 | 51 | [140] |
| Zn 2H-MoS$_2$ | Substitution | 0.5 M H$_2$SO$_4$ | 194 | 78 | [56] |
| Ni(OH)$_2$ 2H-MoS$_2$ | Adsorption | 0.5 M H$_2$SO$_4$ | 139 | 45 | [159] |
| Cu$_{ads}$ 1T-MoS$_2$ | Adsorption | 0.5 M H$_2$SO$_4$ | 173 | 91 | [160] |
| Cu$_{sub}$ 1T-MoS$_2$ | Substitution | 0.5 M H$_2$SO$_4$ | 160 | 86 | [160] |
| Co 1T-MoS$_2$ | Adsorption | 0.5 M H$_2$SO$_4$ | 84 | 47 | [58] |
| Mn 2H-MoSe$_2$ | Substitution | 0.5 M H$_2$SO$_4$ | 167 | 60 | [161] |
| V 1T/2H-MoS$_2$ | Substitution (V$^{4+}$) and Adsorption (V$^{2+}$) | 0.5 M H$_2$SO$_4$ | 146 | 48 | [162] |

Overpotentials were measured at -10 mA/cm$^2$.

**Table S3.9:** XPS data and peak assignments for Zn SAs/1T-MoS$_2$ before and after collecting 3,000 CV scans

| Peak | Zn SAs/1T-MoS$_2$ | | Peak Assignment |
|---|---|---|---|
| | **Pre-CV** | **Post-CV** | |
| Zn 2p$_{3/2}$ | 1022.41 | -- | Zn$^{2+}$ |
| Zn 2p$_{1/2}$ | 1045.41 | -- | Zn$^{2+}$ |
| Mo 3d$_{5/2}$ | 229.03 | 228.98 | MoS$_2$, Mo$^{4+}$ |
| | 229.96 | 229.94 | MoS$_x$, Mo$^{5/6+}$ |
| | 232.45 | -- | MoO$_3$, Mo$^{6+}$ |
| Mo 3d$_{3/2}$ | 232.13 | 232.08 | MoS$_2$, Mo$^{4+}$ |
| | 233.06 | 233.04 | MoS$_x$, Mo$^{5/6+}$ |
| | 235.55 | -- | MoO$_3$, Mo$^{6+}$ |
| S 2p$_{3/2}$ | 161.96 | 161.82 | MoS$_2$, S$^{2-}$ |
| | 163.45 | 162.99 | MoS$_x$, S$^{2-}$ |
| | 168.99 | 168.90 | SO$_4^{2-}$ |
| S 2p$_{1/2}$ | 163.16 | 163.02 | MoS$_2$, S$^{2-}$ |
| | 164.65 | 164.19 | MoS$_x$, S$^{2-}$ |
| | 170.19 | 170.10 | SO$_4^{2-}$ |
| S 2s | 225.93 | 225.88 | MoS$_2$ |
| | 226.86 | 226.84 | MoS$_x$ |
| O 1s | 530.75 | -- | MoO$_3$, O$^{2-}$ |
| | 531.88 | 532.35 | SO$_4^{2-}$ |
| | 532.88 | 533.75 | Organic C-O |

**Table S3.10:** ICP-OES analysis of $1T$-$MoS_2$ intercalated with the various amounts of Zn SAs studied in this work

| Sample | Zn (wt%) | Mo (wt%) | Zn:Mo (mol) |
|---|---|---|---|
| Zn SAs (2.5 mg)/1T-MoS$_2$ | 0.634 | 29.286 | 0.032 |
| Zn SAs (8.5 mg)/1T-MoS$_2$ | 1.016 | 27.465 | 0.054 |
| Zn SAs (16.5 mg)/1T-MoS$_2$ | 1.125 | 24.596 | 0.067 |

## 3.8 References

56.     Wu, W.; Niu, C.; Wei, C.; Jia, Y.; Li, C.; Xu, Q., Activation of Mos2 Basal Planes for Hydrogen Evolution by Zinc. *Angew Chem Int Ed Engl* **2019,** *58* (7), 2029-2033.

58.     Qiao, W.; Xu, W.; Xu, X.; Wu, L.; Yan, S.; Wang, D., Construction of Active Orbital Via Single-Atom Cobalt Anchoring on the Surface of 1t-Mos2 Basal Plane toward Efficient Hydrogen Evolution. American Chemical Society: 2020; Vol. 3, pp 2315-2322.

91.     Turner, J., Sustainable Hydrogen Production. *Science* **2004,** *305*, 972-974.

92.     Finke, C. E.; Leandri, H. F.; Karumb, E. T.; Zheng, D.; Hoffmann, M. R.; Fromer, N. A., Economically Advantageous Pathways for Reducing Greenhouse Gas Emissions from Industrial Hydrogen under Common, Current Economic Conditions. *Energ. Environ. Sci.* **2021,** *14* (3), 1517-1529.

93.     LeValley, T. L.; Richard, A. R.; Fan, M., The Progress in Water Gas Shift and Steam Reforming Hydrogen Production Technologies–a Review. *Int. J. Hydrogen Energy* **2014,** *39* (30), 16983-17000.

94.     Dinçer, İ.; Zamfirescu, C., *Sustainable Hydrogen Production*. Elsevier: 2016.

95.     Anantharaj, S.; Ede, S. R.; Sakthikumar, K.; Karthick, K.; Mishra, S.; Kundu, S., Recent Trends and Perspectives in Electrochemical Water Splitting with an Emphasis on Sulfide, Selenide, and Phosphide Catalysts of Fe, Co, and Ni: A Review. *ACS Catal.* **2016,** *6* (12), 8069-8097.

96.     Yan, Y.; Xia, B. Y.; Zhao, B.; Wang, X., A Review on Noble-Metal-Free Bifunctional Heterogeneous Catalysts for Overall Electrochemical Water Splitting. *J. Mater. Chem. A* **2016,** *4* (45), 17587-17603.

97.     Jaramillo, T. F.; Jorgensen, K. P.; Bonde, J.; Nielsen, J. H.; Horch, S.; Chorkendorff, I., Identification of Active Edge Sites for Electrochemical $H_2$ Evolution from Mos2 Nanocatalysts. *Science* **2007,** *317* (5834), 100-102.

98.     Laursen, A. B.; Kegnaes, S.; Dahl, S.; Chorkendorff, I., Molybdenum Sulfides-Efficient and Viable Materials for Electro - and Photoelectrocatalytic Hydrogen Evolution. *Energ. Environ. Sci.* **2012,** *5* (2), 5577-5591.

99.     Li, G. Q.; Zhang, D.; Qiao, Q.; Yu, Y. F.; Peterson, D.; Zafar, A.; Kumar, R.; Curtarolo, S.; Hunte, F.; Shannon, S.; Zhu, Y. M.; Yang, W. T.; Cao, L. Y., All the Catalytic Active Sites of Mos2 for Hydrogen Evolution. *J Am Chem Soc* **2016,** *138* (51), 16632-16638.

100.    Sastre, G.; Corma, A., The Confinement Effect in Zeolites. *J. Mol. Catal. A-Chem.* **2009,** *305* (1-2), 3-7.

101.    Leenders, S. H.; Gramage-Doria, R.; de Bruin, B.; Reek, J. N., Transition Metal Catalysis in Confined Spaces. *Chem. Soc. Rev.* **2015,** *44* (2), 433-448.

102. Li, H.; Xiao, J.; Fu, Q.; Bao, X., Confined Catalysis under Two-Dimensional Materials. *P. Natl. Acad. Sci. USA* **2017,** *114* (23), 5930-5934.

103. Wang, X.; Zhang, Y.; Wu, J.; Zhang, Z.; Liao, Q.; Kang, Z.; Zhang, Y., Single-Atom Engineering to Ignite 2d Transition Metal Dichalcogenide Based Catalysis: Fundamentals, Progress, and Beyond. *Chem. Rev.* **2022,** *122* (1), 1273-1348.

104. Shifa, T. A.; Vomiero, A., Confined Catalysis: Progress and Prospects in Energy Conversion. *Adv. Energy Mater.* **2019,** *9* (40), 1902307.

105. Zhang, Z.; Bian, L.; Tian, H.; Liu, Y.; Bando, Y.; Yamauchi, Y.; Wang, Z.-L., Tailoring the Surface and Interface Structures of Copper-Based Catalysts for Electrochemical Reduction of Co2 to Ethylene and Ethanol. *Small* **2022,** *18* (18), 2107450.

106. Wang, Z.-L.; Choi, J.; Xu, M.; Hao, X.; Zhang, H.; Jiang, Z.; Zuo, M.; Kim, J.; Zhou, W.; Meng, X.; Yu, Q.; Sun, Z.; Wei, S.; Ye, J.; Wallace, G. G.; Officer, D. L.; Yamauchi, Y., Optimizing Electron Densities of Ni-N-C Complexes by Hybrid Coordination for Efficient Electrocatalytic Co2 Reduction. *ChemSusChem* **2020,** *13* (5), 929-937.

107. Cai, Z.-X.; Wang, Z.-L.; Xia, Y.-J.; Lim, H.; Zhou, W.; Taniguchi, A.; Ohtani, M.; Kobiro, K.; Fujita, T.; Yamauchi, Y., Tailored Catalytic Nanoframes from Metal–Organic Frameworks by Anisotropic Surface Modification and Etching for the Hydrogen Evolution Reaction. *Angew. Chem. Int. Ed.* **2021,** *60* (9), 4747-4755.

108. Esfandiar, A.; Radha, B.; Wang, F.; Yang, Q.; Hu, S.; Garaj, S.; Nair, R. R.; Geim, A.; Gopinadhan, K., Size Effect in Ion Transport through Angstrom-Scale Slits. *Science* **2017,** *358* (6362), 511-513.

109. Remsing, R. C.; McKendry, I. G.; Strongin, D. R.; Klein, M. L.; Zdilla, M. J., Frustrated Solvation Structures Can Enhance Electron Transfer Rates. *J. Phys. Chem. Lett.* **2015,** *6* (23), 4804-4808.

110. Li, H.; Guo, C.; Fu, Q.; Xiao, J., Toward Fundamentals of Confined Electrocatalysis in Nanoscale Reactors. *J. Phys. Chem. Lett.* **2019,** *10* (3), 533-539.

111. Li, X.; Liu, L.; Ren, X.; Gao, J.; Huang, Y.; Liu, B., Microenvironment Modulation of Single-Atom Catalysts and Their Roles in Electrochemical Energy Conversion. *Sci. Adv.* **2020,** *6* (39), eabb6833.

112. Tsai, C.; Abild-Pedersen, F.; Nørskov, J. K., Tuning the Mos2 Edge-Site Activity for Hydrogen Evolution Via Support Interactions. *Nano Lett.* **2014,** *14* (3), 1381-1387.

113. Raybaud, P.; Hafner, J.; Kresse, G.; Kasztelan, S.; Toulhoat, H., Ab Initio Study of the H2–H2s/Mos2 Gas–Solid Interface: The Nature of the Catalytically Active Sites. *J. Catal.* **2000,** *189* (1), 129-146.

114.	Hinnemann, B.; Moses, P. G.; Bonde, J.; Jørgensen, K. P.; Nielsen, J. H.; Horch, S.; Chorkendorff, I.; Nørskov, J. K., Biomimetic Hydrogen Evolution: Mos2 Nanoparticles as Catalyst for Hydrogen Evolution. *J Am Chem Soc* **2005**, *127* (15), 5308-5309.

115.	Li, L.; Qin, Z.; Ries, L.; Hong, S.; Michel, T.; Yang, J.; Salameh, C.; Bechelany, M.; Miele, P.; Kaplan, D., Role of Sulfur Vacancies and Undercoordinated Mo Regions in Mos2 Nanosheets toward the Evolution of Hydrogen. *ACS Nano* **2019**, *13* (6), 6824-6834.

116.	Li, Y.; Wang, H.; Xie, L.; Liang, Y.; Hong, G.; Dai, H., Mos2 Nanoparticles Grown on Graphene: An Advanced Catalyst for the Hydrogen Evolution Reaction. *J Am Chem Soc* **2011**, *133* (19), 7296-7299.

117.	Kibsgaard, J.; Chen, Z.; Reinecke, B. N.; Jaramillo, T. F., Engineering the Surface Structure of Mos 2 to Preferentially Expose Active Edge Sites for Electrocatalysis. *Nat. Mater.* **2012**, *11* (11), 963.

118.	Wang, X.; Zhang, Y.; Si, H.; Zhang, Q.; Wu, J.; Gao, L.; Wei, X.; Sun, Y.; Liao, Q.; Zhang, Z.; Ammarah, K.; Gu, L.; Kang, Z.; Zhang, Y., Single-Atom Vacancy Defect to Trigger High-Efficiency Hydrogen Evolution of Mos2. *J Am Chem Soc* **2020**, *142* (9), 4298-4308.

119.	Shi, Y.; Zhang, B., Identifying the High Activity of the Basal Plane in 1t′-Phase Mos 2 Towards Electrochemical Hydrogen Evolution. *Inorg. Chem. Front.* **2018**, *5* (7), 1490-1492.

120.	Tang, Q.; Jiang, D.-e., Mechanism of Hydrogen Evolution Reaction on 1t-Mos2 from First Principles. *ACS Catal.* **2016**, *6* (8), 4953-4961.

121.	Maitra, U.; Gupta, U.; De, M.; Datta, R.; Govindaraj, A.; Rao, C., Highly Effective Visible-Light-Induced H2 Generation by Single-Layer 1t-Mos2 and a Nanocomposite of Few-Layer 2h-Mos2 with Heavily Nitrogenated Graphene. *Angew. Chem. Int. Ed.* **2013**, *52* (49), 13057-13061.

122.	Lukowski, M. A.; Daniel, A. S.; Meng, F.; Forticaux, A.; Li, L.; Jin, S., Enhanced Hydrogen Evolution Catalysis from Chemically Exfoliated Metallic Mos2 Nanosheets. *J Am Chem Soc* **2013**, *135* (28), 10274-10277.

123.	Liu, Q.; Li, X.; He, Q.; Khalil, A.; Liu, D.; Xiang, T.; Wu, X.; Song, L., Gram-Scale Aqueous Synthesis of Stable Few-Layered 1t-Mos2: Applications for Visible-Light-Driven Photocatalytic Hydrogen Evolution. *Small* **2015**, *11* (41), 5556-5564.

124.	Lei, Z.; Zhan, J.; Tang, L.; Zhang, Y.; Wang, Y., Recent Development of Metallic (1t) Phase of Molybdenum Disulfide for Energy Conversion and Storage. *Adv. Energy Mater.* **2018**, *8* (19), 1703482.

125.	Chen, Z.; Leng, K.; Zhao, X.; Malkhandi, S.; Tang, W.; Tian, B.; Dong, L.; Zheng, L.; Lin, M.; Yeo, B. S., Interface Confined Hydrogen Evolution Reaction in Zero Valent Metal Nanoparticles-Intercalated Molybdenum Disulfide. *Nat. Commun.* **2017**, *8* (1), 1-9.

126. Luo, Y.; Li, X.; Cai, X.; Zou, X.; Kang, F.; Cheng, H.-M.; Liu, B., Two-Dimensional Mos2 Confined Co (Oh) 2 Electrocatalysts for Hydrogen Evolution in Alkaline Electrolytes. *ACS Nano* **2018,** *12* (5), 4565-4573.

127. Huang, Y.; Sun, Y.; Zheng, X.; Aoki, T.; Pattengale, B.; Huang, J.; He, X.; Bian, W.; Younan, S.; Williams, N., Atomically Engineering Activation Sites onto Metallic 1t-Mos2 Catalysts for Enhanced Electrochemical Hydrogen Evolution. *Nat. Commun.* **2019,** *10* (1), 1-11.

128. Li, Z.; Yan, X.; He, D.; Hu, W.; Younan, S.; Ke, Z.; Patrick, M.; Xiao, X.; Huang, J.; Wu, H.; Pan, X.; Gu, J., Manipulating Coordination Structures of Mixed-Valence Copper Single Atoms on 1t-Mos2 for Efficient Hydrogen Evolution. *ACS Catal.* **2022,** *12* (13), 7687-7695.

129. Deng, J.; Li, H.; Xiao, J.; Tu, Y.; Deng, D.; Yang, H.; Tian, H.; Li, J.; Ren, P.; Bao, X., Triggering the Electrocatalytic Hydrogen Evolution Activity of the Inert Two-Dimensional Mos2 Surface Via Single-Atom Metal Doping. *Energ. Environ. Sci.* **2015,** *8* (5), 1594-1601.

130. Krivanek, O. L.; Chisholm, M. F.; Nicolosi, V.; Pennycook, T. J.; Corbin, G. J.; Dellby, N.; Murfitt, M. F.; Own, C. S.; Szilagyi, Z. S.; Oxley, M. P., Atom-by-Atom Structural and Chemical Analysis by Annular Dark-Field Electron Microscopy. *Nature* **2010,** *464* (7288), 571-574.

131. Robertson, A. W.; Montanari, B.; He, K.; Kim, J.; Allen, C. S.; Wu, Y. A.; Olivier, J.; Neethling, J.; Harrison, N.; Kirkland, A. I.; Warner, J. H., Dynamics of Single Fe Atoms in Graphene Vacancies. *Nano Letters* **2013,** *13* (4), 1468-1475.

132. Su, C.; Tripathi, M.; Yan, Q.-B.; Wang, Z.; Zhang, Z.; Hofer, C.; Wang, H.; Basile, L.; Su, G.; Dong, M.; Meyer, J. C.; Kotakoski, J.; Kong, J.; Idrobo, J.-C.; Susi, T.; Li, J., Engineering Single-Atom Dynamics with Electron Irradiation. *Sci. Adv.* **2019,** *5* (5), eaav2252.

133. Yang, X.; Liu, Y.; Ta, H. Q.; Rezvani, E.; Zhang, Y.; Zeng, M.; Fu, L.; Bachmatiuk, A.; Luo, J.; Liu, L.; Rümmeli, M. H., Single-Atom Catalytic Growth of Crystals Using Graphene as a Case Study. *npj 2D Materials and Applications* **2021,** *5* (1), 91.

134. Whittingham, M. S., Intercalation Chemistry: An Introduction. In *Intercalation Chemistry*, Academic Press New York: 1982; pp 1-18.

135. Gates-Rector, S.; Blanton, T., The Powder Diffraction File: A Quality Materials Characterization Database. *Powder Diffr.* **2019,** *34* (4), 352-360.

136. Zhang, K.; Li, P.; Guo, S.; Jeong, J. Y.; Jin, B.; Li, X.; Zhang, S.; Zeng, H.; Park, J. H., An Ångström-Level D-Spacing Controlling Synthetic Route for Mos 2 Towards Stable Intercalation of Sodium Ions. *J. Mater. Chem. A* **2018,** *6* (45), 22513-22518.

137. Shuai, J.; Yoo, H. D.; Liang, Y.; Li, Y.; Yao, Y.; Grabow, L. C., Density Functional Theory Study of Li, Na, and Mg Intercalation and Diffusion in Mos2 with Controlled Interlayer Spacing. *Mater. Res. Express* **2016,** *3* (6), 064001.

138.    Powell, C., X-Ray Photoelectron Spectroscopy Database Xps, Version 4.1, Nist Standard Reference Database 20. *National Institute of Standards and Technology* **1989**.

139.    Baker, M.;  Gilmore, R.;  Lenardi, C.; Gissler, W., Xps Investigation of Preferential Sputtering of S from Mos2 and Determination of Mosx Stoichiometry from Mo and S Peak Positions. *Appl. Surf. Sci.* **1999**, *150* (1-4), 255-262.

140.    Shi, Y.;  Zhou, Y.;  Yang, D.-R.;  Xu, W.-X.;  Wang, C.;  Wang, F.-B.;  Xu, J.-J.;  Xia, X.-H.; Chen, H.-Y., Energy Level Engineering of Mos2 by Transition-Metal Doping for Accelerating Hydrogen Evolution Reaction. *J Am Chem Soc* **2017**, *139* (43), 15479-15485.

141.    Lei, S.;  Wang, X.;  Li, B.;  Kang, J.;  He, Y.;  George, A.;  Ge, L.;  Gong, Y.;  Dong, P.;  Jin, Z., Surface Functionalization of Two-Dimensional Metal Chalcogenides by Lewis Acid–Base Chemistry. *Nat. Nanotech.* **2016**, *11* (5), 465.

142.    Hu, J.;  Yu, L.;  Deng, J.;  Wang, Y.;  Cheng, K.;  Ma, C.;  Zhang, Q.;  Wen, W.;  Yu, S.;  Pan, Y., Sulfur Vacancy-Rich Mos 2 as a Catalyst for the Hydrogenation of Co 2 to Methanol. *Nat. Catal.* **2021**, *4* (3), 242-250.

143.    Berger, R.;  Haddad, M., Computer Simulations of Esr Spectra of Amorphous Thiomolybdates. *Physica Status Solidi B* **1991**, *163* (2), 463-471.

144.    Tran, P. D.;  Tran, T. V.;  Orio, M.;  Torelli, S.;  Truong, Q. D.;  Nayuki, K.;  Sasaki, Y.;  Chiam, S. Y.;  Yi, R.;  Honma, I., Coordination Polymer Structure and Revisited Hydrogen Evolution Catalytic Mechanism for Amorphous Molybdenum Sulfide. *Nat. Mater.* **2016**, *15* (6), 640-646.

145.    Busetto, L.;  Vaccari, A.; Martini, G., Electron Spin Resonance of Paramagnetic Species as a Tool for Studying the Thermal Decomposition of Molybdenum Trisulfide. *J. Phys. Chem.* **1981**, *85* (13), 1927-1930.

146.    Bensimon, Y.;  Belougne, P.;  Giuntini, J.; Zanchetta, J., Electron Spin Resonance of Water Adsorption on Amorphous Molybdenum Sulfide. *J. Phys. Chem.* **1984**, *88* (13), 2754-2757.

147.    González, J. R.;  Alcántara, R.;  Tirado, J. L.;  Fielding, A. J.; Dryfe, R. A., Electrochemical Interaction of Few-Layer Molybdenum Disulfide Composites Vs Sodium: New Insights on the Reaction Mechanism. *Chem. Mater.* **2017**, *29* (14), 5886-5895.

148.    Liu, G.;  Robertson, A. W.;  Li, M. M.-J.;  Kuo, W. C.;  Darby, M. T.;  Muhieddine, M. H.;  Lin, Y.-C.;  Suenaga, K.;  Stamatakis, M.; Warner, J. H., Mos 2 Monolayer Catalyst Doped with Isolated Co Atoms for the Hydrodeoxygenation Reaction. *Nat. Chem.* **2017**, *9* (8), 810-816.

149.    Tanaka, K.;  Kozai, N.;  Yamasaki, S.;  Ohnuki, T.;  Kaplan, D. I.; Grambow, B., Adsorption Mechanism of Reo4− on Ni–Zn Layered Hydroxide Salt and Its Application to Removal of Reo4− as a Surrogate of Tco4−. *Appl. Clay Sci.* **2019**, *182*, 105282.

150. Yang, F.; Song, P.; Liu, X.; Mei, B.; Xing, W.; Jiang, Z.; Gu, L.; Xu, W., Highly Efficient Co2 Electroreduction on Znn4-Based Single-Atom Catalyst. *Angew. Chem. Int. Ed.* **2018,** *57* (38), 12303-12307.

151. Shinagawa, T.; Garcia-Esparza, A. T.; Takanabe, K., Insight on Tafel Slopes from a Microkinetic Analysis of Aqueous Electrocatalysis for Energy Conversion. *Sci. Rep.* **2015,** *5* (1), 1-21.

152. Yi, H.; Zhang, X.; Jia, F.; Wei, Z.; Zhao, Y.; Song, S., Competition of Hg2+ Adsorption and Surface Oxidation on Mos2 Surface as Affected by Sulfur Vacancy Defects. *Appl. Surf. Sci.* **2019,** *483*, 521-528.

153. Liu, H.; Han, N.; Zhao, J., Atomistic Insight into the Oxidation of Monolayer Transition Metal Dichalcogenides: From Structures to Electronic Properties. *RSC Adv.* **2015,** *5* (23), 17572-17581.

154. Ji, L.; Yan, P.; Zhu, C.; Ma, C.; Wu, W.; Wei, C.; Shen, Y.; Chu, S.; Wang, J.; Du, Y., One-Pot Synthesis of Porous 1t-Phase Mos2 Integrated with Single-Atom Cu Doping for Enhancing Electrocatalytic Hydrogen Evolution Reaction. *Appl. Catal. B-Environ.* **2019,** *251*, 87-93.

155. Sun, Y.; Xie, S.-Y.; Meng, X., A First-Principles Study on Hydrogen in Zns: Structure, Stability and Diffusion. *Phys. Lett. A* **2015,** *379* (5), 487-490.

156. Yang, D.-Q.; Sacher, E., S-P Hybridization in Highly Oriented Pyrolitic Graphite and Its Change on Surface Modification, as Studied by X-Ray Photoelectron and Raman Spectroscopies. *Surf. Sci.* **2002,** *504*, 125-137.

157. Ghatak, J.; Guan, W.; Möbus, G., In Situ Tem Observation of Lithium Nanoparticle Growth and Morphological Cycling. *Nanoscale* **2012,** *4* (5), 1754-1759.

158. Zack, L. N.; Ziurys, L. M., The Pure Rotational Spectrum of Zns (X1σ+). *Journal of Molecular Spectroscopy* **2009,** *257* (2), 213-216.

159. He, Z.; Liu, Q.; Zhu, Y.; Tan, T.; Cao, L.; Zhao, S.; Chen, Y., Defect-Mediated Adsorption of Metal Ions for Constructing Ni Hydroxide/Mos2 Heterostructures as High-Performance Water-Splitting Electrocatalysts. *ACS Applied Energy Materials* **2020,** *3* (7), 7039-7047.

160. Li, Z.; Yan, X.; He, D.; Hu, W.; Younan, S.; Ke, Z.; Patrick, M.; Xiao, X.; Huang, J.; Wu, H.; Pan, X.; Gu, J., Manipulating Coordination Structures of Mixed-Valence Copper Single Atoms on 1t-Mos2 for Efficient Hydrogen Evolution. *ACS Catalysis* **2022,** *12* (13), 7687-7695.

161. Kuraganti, V.; Jain, A.; Bar-Ziv, R.; Ramasubramaniam, A.; Bar-Sadan, M., Manganese Doping of Mose2 Promotes Active Defect Sites for Hydrogen Evolution. *ACS Appl Mater Interfaces* **2019,** *11* (28), 25155-25162.

162.    Liu, T.; Fang, C.; Yu, B.; You, Y.; Niu, H.; Zhou, R.; Zhang, J.; Xu, J., Vanadium-Doping in Interlayer-Expanded Mos2 Nanosheets for the Efficient Electrocatalytic Hydrogen Evolution Reaction. *Inorganic Chemistry Frontiers* **2020,** *7* (13), 2497-2505.

# CHAPTER 4: Impact of Metal Single Atom d-Orbital Occupation on Confinement Catalysis: $d^0$ vs. $d^{10}$

## 4.1 Abstract

SACs have the ability to enhance reaction kinetics and the activity, stability, and selectivity of catalysts. Yet, investigations of the aspects of the SA that induce such desirable results fall short. Much research has investigated the impact of the guest metal's oxidation state and coordination geometry on confinement catalysis. Likewise, theoretical calculations have predicted the electronic structures of guest metals to be driving the enhanced catalytic performance of the catalyst materials they are confined within. Experimentally, it seems that in the never-ending search for synthetic methods that enhance confinement catalysis, published investigations of the impact of the metal intercalant's d-orbital occupation on confinement catalysis are nonexistent. In this work, we address this knowledge gap by comparing the performance $d^{10}$ guest metals spatially confined within layers of 1T-MoS$_2$ to the performance of $d^0$ guest metals under similar confinement using Zn and Sc SAs, respectively. Electrochemically, the Zn SAs reduce the HER overpotential of 1T-MoS$_2$ by 88 mV, while the Sc SAs only reduce 1T-MoS$_2$'s overpotential by 3 mV. Electronically, the Zn SAs donate electrons to nearby S active sites which in turn promotes HER kinetics. In contrast, electronic donation between the Sc SAs and S active sites is not observed. Altogether, this work demonstrates that the electron occupation of d orbitals belonging to intercalated SAs is necessary to enhance catalysis in 2D materials.

## 4.2 Introduction

Spatial orientation of d orbitals in TMDs has been shown to generate a variety of electronic phases that give rise to a wide range of macroscopic properties.[163] These changes in electronic,

physical, or structural properties may in turn impact catalytic performance. Since active sites are the locations at which catalytic reactions occur, the geometry, coordination, and electronic structure of their microenvironments is critical to optimizing the physical and chemical properties of SACs employed in catalytic reactions.[30] Several synthetic strategies have been demonstrated to optimize desired properties in SACs. Intentional construction of surface defects on layered substrates, known as defect engineering, creates traps that in turn may capture guest metal dopants or intercalants to synthesize SACs that exhibit a well-defined microenvironment. Depending on the type of layered substrate employed, defect sites may be generated through the formation of atomic vacancies within the substrate's lattice. For instance, Qiao $et. al.$ employed defect engineering to anchor Pt SAs to $FeO_x$ through the formation of O vacancies in the substrate.[164] The resulting $Pt/FeO_x$ catalyst demonstrated high stability and activity towards CO oxidation to $H_2$. The observed improvement in catalytic activity was attributed to reduction in CO adsorption energy and activation barriers for CO oxidation induced by the partial occupation of 5d orbitals in the Pt SAs. Fine-tuning metal-support interactions provides another valuable method to modify the electronic structure of SAs by forming covalent/ionic bonds with their substrates.[30] Qu $et. al.$ employed this strategy to capture transition metal ions (such as Fe, Co, Ni, and Cu) on GO.[165] By employing a facile dangling bond strategy under ambient conditions, they synthesized SACs in which the $M^0$ species (M = Fe, Co, Ni, Cu) were oxidized to $M^{\delta+}$ ($0 < \delta < 3$) species by transferring electrons to the dangling O groups in GO. The resulting SACs exhibited enhanced ORR activity and stability accordingly. Another promising route to synthesizing SACs with desired catalytic properties involves heteroatom tethering, where metal-support interactions are manipulated to form anchoring sites on a substrate that attach to metal SAs.[30] Wang $et. al.$ employed this strategy to load atomically dispersed metals (such as Ru, Rh, Pd, Ir, and Pt) on mesoporous S-doped carbon

substrates.[166] Specifically, the S-doped Pt/C and Ir/C catalysts exhibited 30- and 20-fold higher activity compared to commercial Pt/C and Ir/C catalysts employed in formic acid oxidation and quinoline hydrogenation, respectively.

Spatial confinement is both an effective and versatile method to construct SACs with well-defined microenvironments for enhanced catalytic activity.[30] Most important to maximizing the results of this strategy are the selection of substrates that exhibit uniform cavities and mononuclear metal precursors that possess suitable charge states and molecular size with respect to the substrate they form SACs with. In this strategy, microporous diffusion limitations ensure the uniform dispersion of guest metal precursors throughout the substrate material. Acceleration of reactions may be achieved via spatial confinement by increasing the local concentration of reagents/catalysts within the active site's microenvironment, as well as by pre-organizing reagents into a conformation that exhibits favorable reactivity.[167] In a similar manner, catalytic selectivity may be enhanced by restricting the region of space housing active site microenvironments in a manner that enables only the reagents that possess an appropriate size or shape to fit within the confined cavity.[167]

Since SACs have demonstrated their ability to enhance reaction kinetics and the activity, stability, and selectivity of catalysts, one must inquire about the aspects of the SA that induce such desirable results. For example, how do factors such as the SA's ionic radius, coordination geometry/bonding environment, and oxidation state influence catalysis? Examples of such questions that scientists have sought to address are discussed here. In order to understand the role of undercoordinated sites in 2D substrates in CO dissociation under confinement, Zhang *et. al.* sandwiched Rh(111) and a monolayer of *h*-BN to create a 2D confined region within which CO dissociation/activation was investigated.[168] DFT results predicted that CO dissociation restricted

between layers of *h*-BN and Ru(111) does not occur. Undercoordinated B atoms were determined to be responsible for *h*-BN-assisted CO activation due to having substantially stronger CO affinity than pristine *h*-BN or undercoordinated N atoms. Additionally, undercoordinated B atoms at large vacancy or edge sites demonstrated greater stability and higher resistance towards CO and O poisoning. Based on these results, undercoordinated active sites were shown to facilitate CO dissociation more readily than what could be achieved by the *h*-BN overlayer on Ru(111) that maintained a pristine lattice structure. Tang *et. al.* tailored the selectivity of ORR on SACs in acidic media by modifying the atomic structure of the catalyst's first and second coordination spheres.[169] To do this, the authors first doped graphene with active sites such as Co, Fe, Ni, Mo, Pt, *etc.* Lattice sites within the metal dopant's first coordination sphere were substituted with nonmetal dopants (N, S, O, P) and vacancies. The second coordination sphere was modified by incorporating various functional groups into the C matrix. Results showed that applying modifications to the active site's first and second coordination spheres tailors ORR selectivity from a four-electron pathway to a two-electron pathway. Calculations performed predicted these changes to alter the *OOH adsorption behavior of active sites in a manner that yields >95% selectivity for acidic $H_2O_2$ electrosynthesis. An example of how coordination environment impacts catalytic activity is provided by Zhang *et. al.*, which reports the enhancement of ORR by tuning the coordination environment of Fe, Co, and Ni SAs anchored on a porous N,S co-doped carbon (NSC) matrix.[170] During synthesis, the authors noted that the Fe SAs coordinated strictly to four N atoms in the NSC matrix with two of the N atoms bonded to S atoms in the second coordination sphere. In contrast, Co and Ni formed a single bond with an S atom within the first coordination sphere in addition to bonding to three N atoms. While all three cases showed enhanced ORR activity, the $FeN_4S_2$ center site yielded the highest ORR activity due to exhibiting higher charge density and

lower energy barriers for the intermediate species and products formed. *Altogether, it seems that in the never-ending search for synthetic methods that enhance confinement catalysis, published investigations of the impact of the metal intercalant's d-orbital occupation on confinement catalysis are nonexistent.* Thus, we seek to address this knowledge gap in both this chapter and the next.

In this work, 1T-MoS$_2$ intercalated with Sc SAs is synthesized by hydrothermally reacting ScCl$_3$, (NH$_4$)$_6$Mo$_7$O$_{24}$·4H$_2$O, thioacetamide, and urea together in water (detailed in the Materials and Methods section). Changes in HER performance were measured in acidic conditions (0.5 M H$_2$SO$_4$) using a three-electrode configuration with Ag/AgCl and graphite as the reference and counter electrodes, respectively. Results showed that spatial confinement of Sc SAs within 1T-MoS$_2$ basal active site microenvironments causes a negligible difference in overpotential (1T-MoS$_2$ = 265 mV; Sc SAs/1T-MoS$_2$ = 262 mV) and HER kinetics (1T-MoS$_2$ = 107.2 mV/dec; Sc SAs/1T-MoS$_2$ = 108.7 mV/dec), as well as a significant decrease in charge transport limitations (1T-MoS$_2$ = 127.5 Ω; Sc SAs/1T-MoS$_2$ = 14.23 Ω). In this chapter, we analyze the changes in 1T-MoS$_2$'s structural properties induced by the spatial confinement of Sc SAs and employ the results to elucidate the driving forces behind the catalyst's observed activity and stability towards HER. Afterwards, the results are compared to the performance of Zn SAs/1T-MoS$_2$ to identify a relationship between 1T-MoS$_2$'s HER performance and the d-orbital occupation of metal intercalants.

## 4.3 Results and Discussion

### 4.3.1 Structural Characterization of Sc SAs/1T-MoS₂

Evidence of whether the Sc SAs adsorb to the 1T-MoS$_2$ basal plane or substitute Mo atoms within 1T-MoS$_2$'s crystal lattice was collected using HAADF-STEM imaging (**Figure 4.1**). Visibly brighter spots scattered across the Moiré pattern of 1T-MoS$_2$ confirm the adsorption of Sc SAs to the 1T-MoS$_2$ basal plane (**Figure 4.1a**). A simulated model of the adsorption process is provided in **Figure 4.1b**. The intensity profile shown in **Figure 4.1c** is extracted from the row of atoms highlighted in yellow in **Figure 4.1a**. The visibly greater ADF intensity of the peak corresponding to the brightest atom in the row selected experimentally confirms the adsorption of an Sc atom on top of an Mo atom. EDX mappings evidence the uniform distribution of Sc, Mo, and S atoms throughout Sc SAs/1T-MoS$_2$ (**Figure S4.1**).

Intercalation of metal SAs in the formation of SACs has the potential to induce various structural defects into 2D materials. Raman spectroscopy is well-known as a fast, convenient, and nondestructive technique commonly employed to investigate the fundamental properties of 2D materials, including atomic displacement of lattice vibrations and defect-induced phase transitions.[171] Therefore, Raman spectroscopy was employed to explore structural changes to 1T-MoS$_2$ induced by the intercalation of Sc SAs. Raman

spectra for 1T-MoS$_2$ and Sc SAs/1T-MoS$_2$ are provided in **Figure 4.2a** with experimental peak positions given in **Table S4.1** The presence of $J_1$, $J_2$, $E_{1g}$, $J_3$, TA, and LA phonon modes at the M point of the first Brillouin zone confirm that both samples are predominantly in the 1T-phase. An in-depth description of each phonon mode present is provided in Chapter 2. The higher intensity of the $E^1_{2g}$ peak compared to the $A_{1g}$ peak further confirms the majority presence of 1T-MoS$_2$. Evidence of 2H-phase contributions is characterized by the dominant intensity of the $A_{1g}$ peak

compared to the $E^1_{2g}$ peak and is unobservable in both samples. The negligible difference in peak positions between 1T-MoS$_2$ and Sc SAs/1T-MoS$_2$ suggests the lack of changes in the bulk lattice structure of 1T-MoS$_2$ upon Sc SA intercalation.[172]
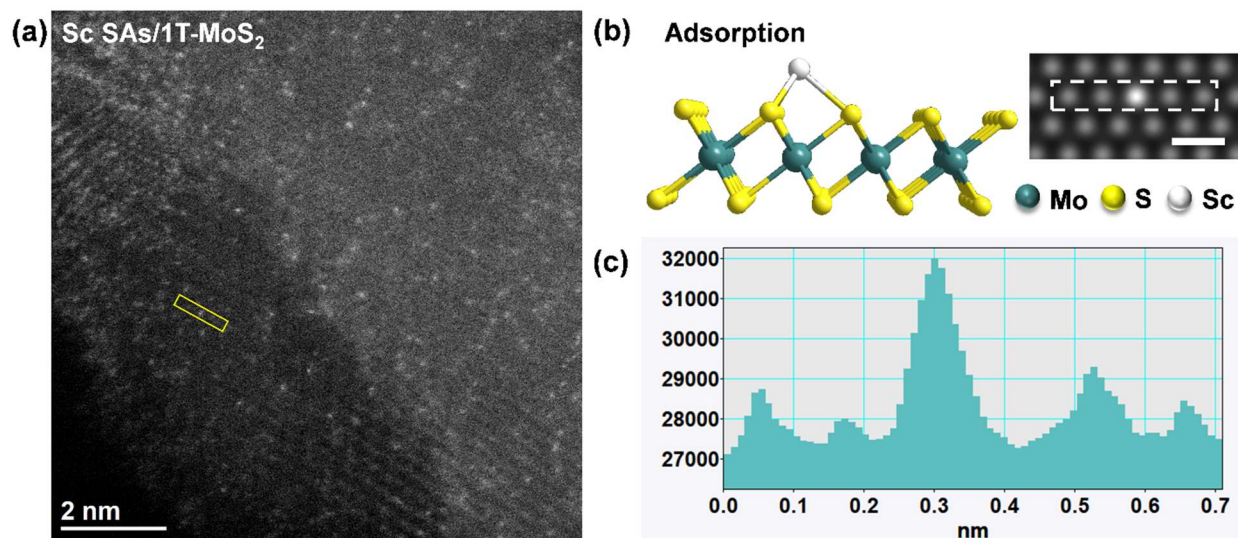


**Figure 4.1:** HAADF-STEM characterization and quantitative identification of Sc SAs adsorption to the 1T-MoS$_2$ basal plane.
**(a)** Atomically-resolved HAADF-STEM image of the sample. **(b)** Side view of the atomic structure of the Sc SAs/1T-MoS$_2$ adsorption model and simulated HAADF-STEM image. Scale bar is 0.5 nm. **(c)** Intensity profile taken along the row of atoms highlighted in the yellow box in (a).

A shift in the peak corresponding to the (001) plane in 1T-MoS$_2$ observed in the XRD pattern of Sc SAs/1T-MoS$_2$ confirms the intercalation of Sc SAs within the interlayer spacing of 1T-MoS$_2$ (**Figure 4.2b**). XRD patterns for 1T-MoS$_2$ and Zn SAs/1T-MoS$_2$ are included for comparison. Peak broadening observed in the diffraction pattern of Sc SAs/1T-MoS$_2$ indicates that the same overlap of hexagonal 1T-MoS$_2$ and monoclinic Mo$_2$S$_3$ occurs in Sc SAs/1T-MoS$_2$ as was observed for Zn SAs/1T-MoS$_2$ and 1T-MoS$_2$. Additional peaks present in Sc SAs/1T-MoS$_2$ correspond to hexagonal MoO$_3$ (P6$_3$/m).[173, 174] In contrast to Zn SAs/1T-MoS$_2$, planes corresponding to Mo$_2$S$_3$ in Sc SAs/1T-MoS$_2$ do not experience changes in d-spacing. In Sc SAs/1T-MoS$_2$, the (001) plane bisecting the interlayer spacing of 1T-MoS$_2$ shifts from 14.07° (0.629 nm) to 13.26° (0.665 nm), which corresponds to a 5.7% (0.036 nm) expansion of 1T-MoS$_2$'s

interlayer spacing. Greater expansion of 1T-MoS$_2$'s d-spacing to accommodate Sc SAs than what is required to accommodate Zn SAs is expected due to Sc's larger ionic radius ($r_{Sc} = 75\ pm$, $r_{Zn} = 60\ pm$).[175] Similar to the results observed for Zn SAs/1T-MoS$_2$, the interlayer spacing of 1T-MoS$_2$ expands to accommodate the occupation of interlayer lattice sites by Sc SAs.
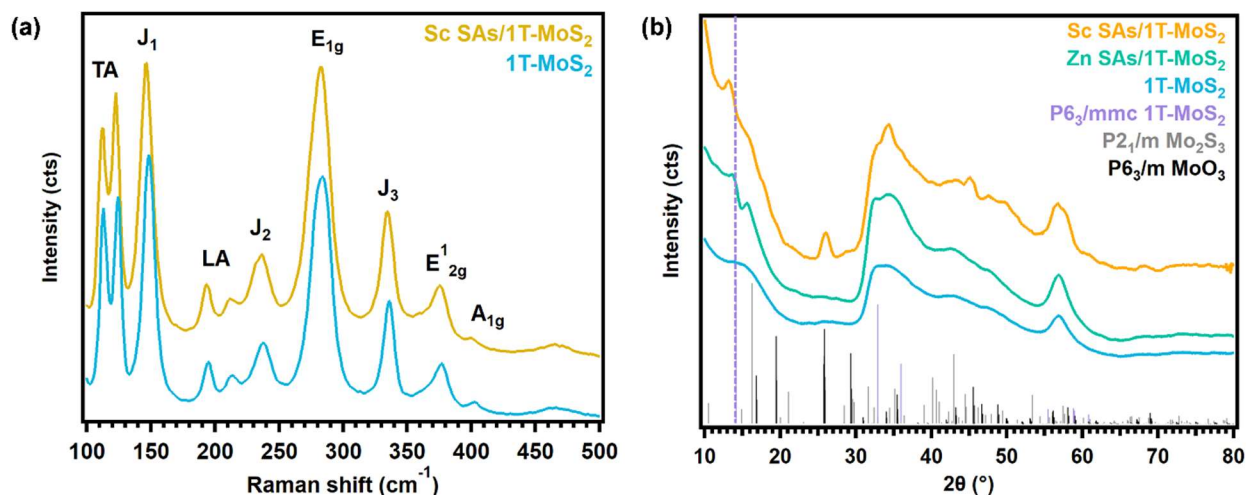


**Figure 4.2:** Structural characterization of Sc SAs/1T-MoS$_2$.
**(a)** Raman spectra of 1T-MoS$_2$ (blue) and Sc SAs/1T-MoS$_2$ (orange). **(b)** XRD patterns of 1T-MoS$_2$ (blue), Zn SAs/1T-MoS$_2$ (green). and Sc SAs/1T-MoS$_2$ (orange). The purple dashed line marks the 2θ value that corresponds to the (001) plane in 1T-MoS$_2$.

Changes in the electronic structure of 1T-MoS$_2$ induced by the intercalation of Sc SAs was evaluated by XPS. Resulting XPS spectra of 1T-MoS$_2$ and Sc SAs/1T-MoS$_2$ were compared to evaluate changes in oxidation states and chemical compositions induced by the intercalation of Sc SAs (**Figure 4.3**). Peak values and assignments are provided in **Table S4.2** (along with XPS data for Zn SAs/1T-MoS$_2$ for comparison). The Mo 3d, S 2s, and S 2p spectra demonstrate two sets of doublet peaks assigned to two different Mo species (**Figures 4.3a, 4.3b**). The purple doublets observed correspond to Mo$^{4+}$ and S$^{2-}$ oxidation states in 1T-MoS$_2$.[63] The green doublets are assigned to unsaturated Mo$^{5/6+}$ and S$^{2-}$ oxidation states and indicate the presence of a nonstoichiometric MoS$_x$ species along the surface of each sample.[63] The XPS spectra of 1T-MoS$_2$

and Zn SAs/1T-MoS$_2$ also demonstrate the same set of 1T-MoS$_2$ and MoS$_2$ species, as discussed in detail in Chapter 3 (**Figure S3.6**). Thus, we conclude that although the majority of Sc SAs/1T-MoS$_2$ consists of stoichiometric 1T-MoS$_2$, a portion of MoS$_x$ exists near the catalyst surface.[64] Compared to 1T-MoS$_2$'s Mo 3d spectrum, the Mo 3d, S 2p, and S 2s peaks attributed to 1T-MoS$_2$ and MoS$_x$ in Sc SAs/1T-MoS$_2$ exhibit downshifts up to 0.10 eV. Downshifts of up to 0.10 eV fall
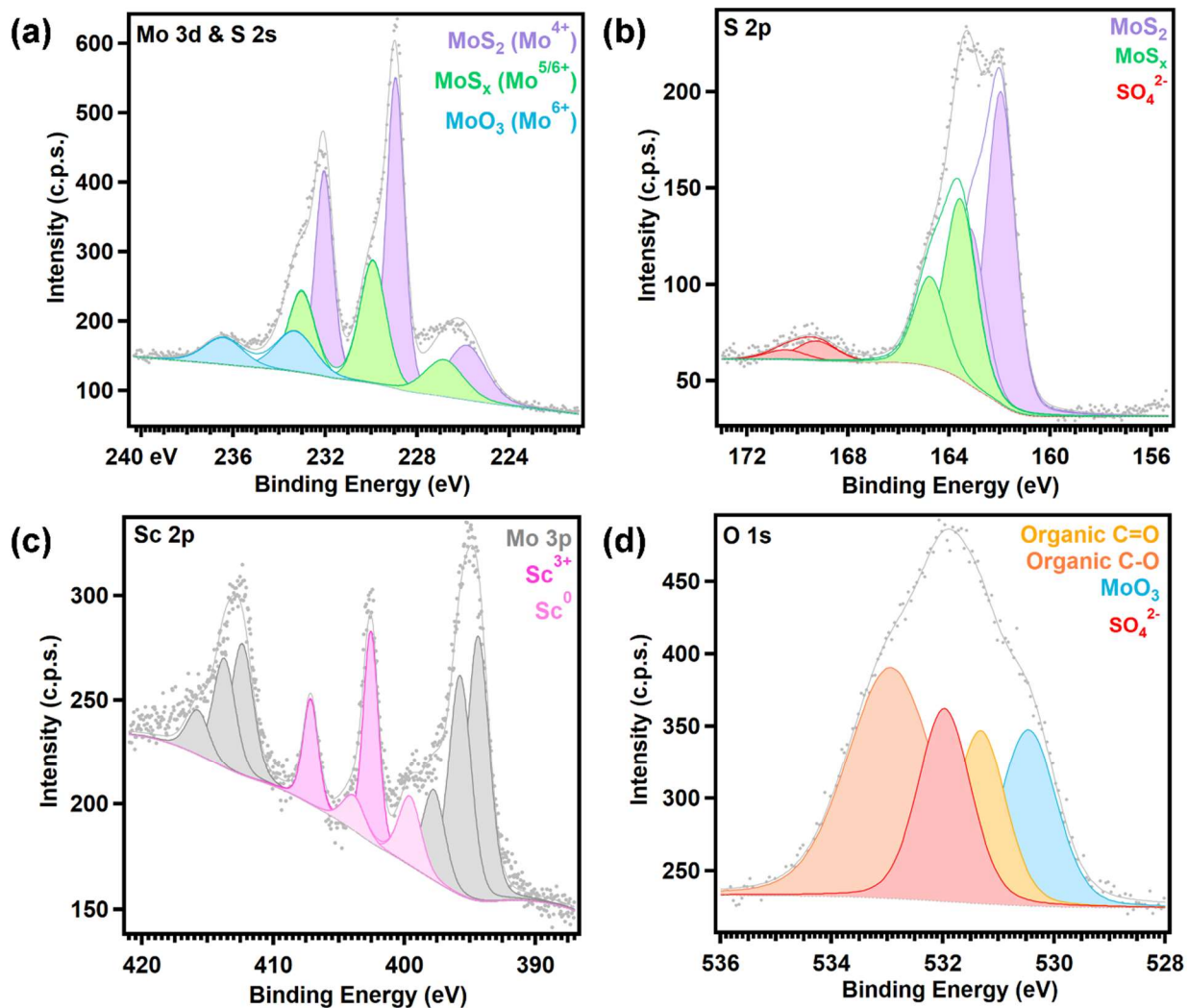


**Figure 4.3:** XPS data and peak assignments of Sc SAs/1T-MoS$_2$.
**(a)** Mo 3d and S 2s spectra. **(b)** S 2p spectrum. **(c)** Sc 2p spectrum. **(d)** O 1s spectrum.

within the step size (0.10 eV) employed during XPS analysis and thus are considered negligible.

An additional set of doublets in the Mo 3d spectrum (shown in blue) indicates the presence of

$MoO_3$ ($Mo^{6+}$).[63] The presence of $MoO_3$ in Sc SAs/1T-$MoS_2$ likely arises from $O_2$ bonding to unsaturated Mo atoms via chemical adsorption at vacancy sites within the catalyst.[176, 177] A small amount of physically-adsorbed $SO_4^{2-}$ is observed in the S 2p spectrum of Sc SAs/1T-$MoS_2$ that may be removed from the substrate by washing with DI $H_2O$.[24] The O 1s peaks located at 530.37 eV and 532.08 eV confirm the presence of $MoO_3$ and $SO_4^{2-}$, respectively (**Figure 4.3d**).[63] Since the Sc 2p region overlaps with the Mo 3p region, peaks attributed to the three Mo species present in Sc SAs/1T-$MoS_2$ are shown in gray (**Figure 4.3c**). Two doublets assigned to Sc species are observed in this region and are colored in various shades of pink. The observed Sc 2p doublet shown in pink (Sc $2p_{3/2}$ = 403.87 eV) is attributed to $Sc^{3+}$.[63] This results confirms that the intercalated Sc SAs exist in the $d^0$ electronic state. Biesinger *et. al.* reported the Sc 2p peak binding energies for various Sc species, including $Sc^0$ metal and Sc-oxides.[178] According to Biesinger, the binding energy of $Sc_2O_3$ occurs at 401.7 eV with a corresponding O 1s peak at 529.7 eV indicative of a lattice oxide. Likewise, the Sc $2p_{3/2}$ peak corresponding to ScOOH is observed at 402.9 eV with a broad O 1s peak at 531.8 eV indicative of an oxyhydroxide species. The absence of these peaks in the Sc 2p and O 1s spectra of **Figures 4.3c, 4.3d** confirm the absence of Sc-oxides in Sc SAs/1T-$MoS_2$. Thus, the $Sc^{3+}$ ions exist as SAs confined within the local microenvironments of active sites located along the basal plane of 1T-$MoS_2$.

### 4.3.2 Catalytic Comparison of Sc SAs/1T-MoS₂ (d⁰ Case) with Zn SAs/1T-MoS₂ (d¹⁰ Case)

Changes in HER performance induced by the intercalation of Sc SAs was measured electrochemically under acidic conditions ($N_2$-saturated 0.5 M $H_2SO_4$) within a three-electrode configuration. LSVs were collected to quantify how 1T-$MoS_2$'s overpotential (measured at -10 mA/cm$^2$) changes when various concentrations of Sc SAs (5 mg, 10 mg, 15 mg, and 20 mg) are

intercalated between layers of 1T-MoS$_2$ (**Figure S4.2a**). Upon comparison of the overpotentials produced by 1T-MoS$_2$ samples intercalated with 5, 10, 15 and 20 mg of Sc SAs, results showed that 1T-MoS$_2$ intercalated with 15 mg of Sc SAs (Sc (15 mg) SAs/1T-MoS$_2$) yields the best overpotential (262 mV *vs.* RHE) of the four cases (**Table S4.3**). Spatially confining 5, 10, and 20 mg of Sc SAs within 1T-MoS$_2$ produced significantly higher overpotentials equal to 340, 293, and 311 mV *vs.* RHE, respectively.
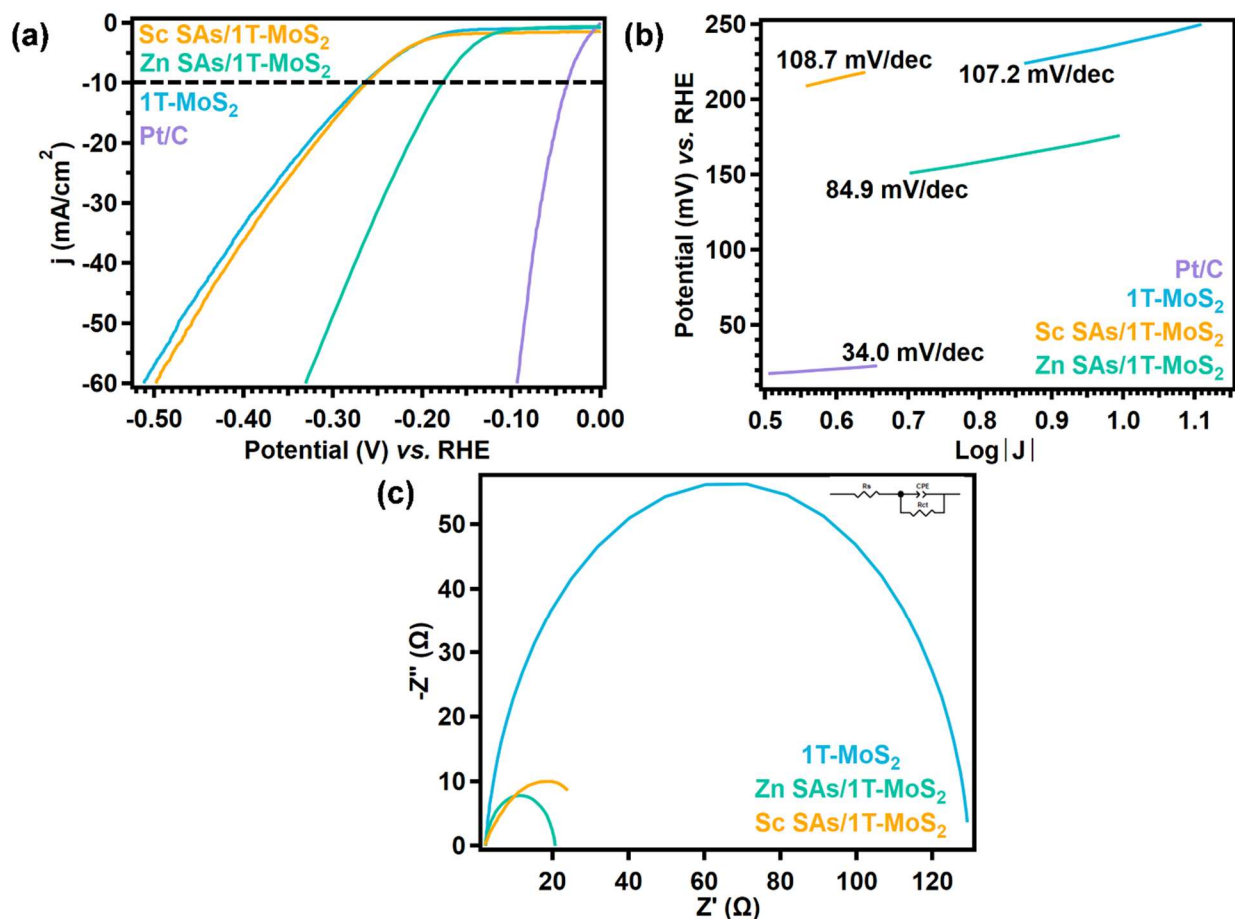


**Figure 4.4:** Electrochemical characterization of Sc SAs/1T-MoS$_2$, Zn SAs/1T-MoS$_2$, 1T-MoS$_2$, and Pt/C (20%).
Data was collected in N$_2$-saturated 0.5 M H$_2$SO$_4$ within a three-electrode configuration. **(a)** HER polarization curves. **(b)** Tafel plots. **(c)** EIS results fitted to the equivalent circuit shown.

EIS was employed to evaluate charge transfer resistance and mass transport limitations for each electrode (**Figure S4.2b, Table S4.4**). Analysis of the high frequency (low Z') region is

shown in **Figure 4.2b**'s inset. The lowest charge transfer resistance was achieved by Sc (20 mg) SAs/1T-MoS$_2$ (16.77 $\Omega$), followed by Sc (15 mg) SAs/1T-MoS$_2$ (42.87 $\Omega$), Sc (10 mg) SAs/1T-MoS$_2$ (7.005×10$^7$ $\Omega$), and Sc (5 mg) SAs/1T-MoS$_2$ (1.025×10$^9$ $\Omega$). Sc (5 mg) SAs/1T-MoS$_2$ displays mass transport limitations, indicated by the linear portion of the curve in the low frequency (high Z') range. Sc (5 mg) SAs/1T-MoS$_2$, and Sc (15 mg) SAs/1T-MoS$_2$ produce two semi-circles, indicating that these two electrodes experience minor ion conduction resistance in addition to charge transfer resistance. Thus, Sc (20 mg) SAs/1T-MoS$_2$ is believed to yield the lowest charge transfer resistance due to the lack of ion conduction resistance experienced by the electrode, which in turn allows H$^+$ ions to flow more easily to the electrode surface where they may be reduced to form H$_2$. Although Sc (20 mg) SAs/1T-MoS$_2$ yields the lowest charge transfer resistance, Sc (15 mg) SAs/1T-MoS$_2$ was selected for HER activity comparison with Zn SAs/1T-MoS$_2$ because it produced the lowest overpotential of the various Sc SA concentrations studied.

After identifying the optimal concentration of Sc SAs intercalated within 1T-MoS$_2$, the HER performance of Sc (15 mg) SAs/1T-MoS$_2$ was compared to 1T-MoS$_2$ and Zn SAs/1T-MoS$_2$ to evaluate differences in catalytic performance between the d$^0$ (Sc SAs/1T-MoS$_2$) and d$^{10}$ (Zn SAs/1T-MoS$_2$) cases (**Figure 4.4**). First, the overpotentials yielded by each case clearly demonstrates that that the d$^{10}$ case, Zn SAs/1T-MoS$_2$, yields a significantly lower overpotential compared to the d$^0$ case, Sc SAs/1T-MoS$_2$ (**Figure 4.4a**). Numerically, Zn SAs/1T-MoS$_2$ reduce the overpotential of 1T-MoS$_2$ by 88 mV *vs*. RHE, whereas Sc SAs/1T-MoS$_2$ only lower 1T-MoS$_2$'s overpotential by 3 mV *vs*. RHE (**Table S4.3**). With respect to Tafel slopes, Zn SAs/1T-MoS$_2$ yields the lowest Tafel slope (84.9 mV/dec), while Sc SAs/1T-MoS$_2$ (108.7 mV/dec) produces a Tafel slope very similar to that of 1T-MoS$_2$ (107.2 mV/dec) (**Figure 4.4b**). Customarily, SACs are predicted to lower the kinetic barrier through which HER proceeds.[39] In Chapter 3, the lower Tafel

slope produced by Zn SAs/1T-MoS$_2$ compared to 1T-MoS$_2$ indicated that spatial confinement of Zn SAs does lower the kinetic barrier through which HER proceeds (**Figure 3.4b** and **Table S3.6**). As a result, a lower overpotential is observed when Zn SAs are under confinement. Since the difference in Tafel slope between Sc SAs/1T-MoS$_2$ and 1T-MoS$_2$ is negligible, we conclude that the Sc SAs do not change the kinetic barrier and facilitate HER kinetics when confined within the local microenvironment of basal plane active sites in 1T-MoS$_2$. This result is further demonstrated by the negligible change in overpotential observed by Sc SAs intercalation within 1T-MoS$_2$. Comparison of the charge transfer resistance shows that Zn SAs/1T-MoS$_2$ (34.59 Ω) yields a lower value for charge transfer resistance than Sc SAs/1T-MoS$_2$ (42.87 Ω). The difference in charge transfer for the two cases arises from the ion conduction limitations and slightly greater charge transfer resistance Sc SAs/1T-MoS$_2$ experiences. Resistance to ion conduction is not observed for Zn SAs/1T-MoS$_2$. These results tell us that, compared to d$^0$ guest metals, spatially confining d$^{10}$ metals within active site microenvironments in 1T-MoS$_2$ enhances HER performance by not only lowering the amount of energy required to drive HER but also reducing resistance towards ion conduction and charge transfer experienced by the electrode.

In attempt to understand the reasons driving Sc SAs/1T-MoS$_2$'s lack of improvement in catalytic performance compared to 1T-MoS$_2$, a few experimental findings from Chapter 3 must be revisited. As discussed in detail in Chapter 3, evidence of electron donation from confined Zn SAs to basal S active sites was experimentally identified from the downshift in the binding energies of the S 2p doublet assigned to MoS$_x$ (**Figure S3.6d, Table S3.1**). Additionally, DFT analysis discussed in Chapter 3 theorizes that this electronic interaction between Zn SAs and their neighboring S atoms causes $\Delta G_{H*}$ to decrease from -4.30 eV to 0.00294 eV, which in turn enables HER adsorption and desorption kinetics to be much more facile (**Figure 3.5**). In contrast, XPS

analysis of Sc SAs/1T-MoS$_2$ does not induce any electronic donation from the Sc SAs to the S atoms in either 1T-MoS$_2$ or MoS$_x$ (**Table S4.2**). Catalytically, Sc SAs/1T-MoS$_2$ exhibit an overpotential and Tafel slope that is almost identical to 1T-MoS$_2$ (**Table S4.3**). These results lead us to believe that spatial confinement of d$^0$ metals such as Sc SAs is unable to improve the HER performance of 2D materials such as 1T-MoS$_2$ because they do not electronically alter the local environments of active sites in the substrate. Surprisingly, confinement of d$^0$ guest metals does lower charge transfer resistance. However, this change is not effective enough to significantly improve 1T-MoS$_2$'s HER performance comparably to the improvement induced by d$^{10}$ guest metals.

In a similar manner to how the stability of Zn SAs/1T-MoS$_2$ during HER catalysis was tested, LSVs were collected before and after subjecting Sc SAs/1T-MoS$_2$ to 3,000 CV scans (**Figure S4.3**). After 3,000 CV scans, the overpotential increased by 104 mV *vs.* RHE, ~7x more than the overpotential shift observed for Zn SAs/1T-MoS$_2$ (14 mV increase observed, **Figure 3.4e**). This major shift in overpotential indicates that Sc SAs/1T-MoS$_2$ does not exhibit optimal stability for HER catalysis in acidic media. These results clearly demonstrate that the d$^{10}$ case outperforms the d$^0$ case in terms of catalytic stability. In Chapter 3, the Zn SAs/1T-MoS$_2$ surface was evaluated by XPS before and after being subjected to CV cycles (**Figure S3.13** and **Table S3.9**). Based on the results, the high stability of Zn SAs/1T-MoS$_2$ was attributed to the structural retention of the catalyst material after 3,000 cycles. Results for the Sc SAs/1T-MoS$_2$ catalyst surface before (**Figure S4.4**) and after (**Figure S4.5**) running 3,000 CV cycles differed tremendously. Numerical comparison of the results is provided in **Table S3.5**. After running 3,000 CV cycles, significant loss of both MoS$_2$ and S atoms is observed (**Figures S4.5a, S4.5b**). The Mo 3d doublets belonging to MoS$_2$ upshift by 0.26 eV, whereas those belonging to undercoordinated

MoS$_x$ upshift by 1.73 eV. This major upshift in binding energy indicates that electrons are withdrawn from Mo centers during catalysis. The at% of Sc SAs in Sc SAs/1T-MoS$_2$ decreases from 1.65 at% pre-CV (**Figure S4.4c**) to 0.07 at% post-CV (**Figure S4.5c**), which tells us that almost all of the Sc SAs are lost during catalysis. This result further evidences the instability of this d$^0$ guest metal when under confinement. Lastly, major growth of MoO$_3$ occurs, which has the potential to block many active sites in the remaining portion of the catalyst material (**Figures S4.5a, S4.5d**). As a result, a major decline in the HER performance of Sc SAs/1T-MoS$_2$ is observed after long-term electrolysis, which is attributed to the poor retention of the catalyst structure observed with d$^0$ metal intercalation.

An interesting observation when comparing the catalytic performance of the d$^0$ and d$^{10}$ cases involves the increase in 1T-MoS$_2$'s interlayer spacing that occurs when Sc SAs are under confinement compared to when Zn SAs are under confinement. Customarily, one would assume that the increase in interlayer spacing would allow a greater density of active sites along the basal plane of 1T-MoS$_2$ to be exposed.[7, 179] In turn, the catalytic activity would be expected to improve. Instead, we observe that, although Sc SAs increase the interlayer spacing of 1T-MoS$_2$ 2.3% more than Zn SAs do, an improvement in the HER activity is not observed. This observation indicates that increasing the interlayer spacing of 1T-MoS$_2$ does not necessarily guarantee an improvement in the catalyst's activity. Instead, this work demonstrates a trend between electron donation from guest metal SAs to S active sites and changes in HER overpotential. This electron donation was observed for the Zn SAs case, along with an 88 mV decrease in HER overpotential. In contrast, the lack of electron donation from the Sc SAs to nearby S active sites resulted with a negligible (3 mV) decrease in 1T-MoS$_2$'s overpotential. These results suggest that changes in HER activity are

more heavily influenced by electronic effects than changes in the catalytic substrate's interlayer spacing.

4.4 Conclusions

In this work, $d^0$ Sc SAs were spatially confined within the microenvironments of basal plane active sites in 1T-MoS$_2$. The structure and HER performance of Sc SAs/1T-MoS$_2$ was assessed in detail. The resulting catalytic performance of Sc SAs/1T-MoS$_2$ was compared to the catalytic performance of Zn SAs/1T-MoS$_2$ to establish a trend between the d-orbital occupancy of metal single atoms confined near basal plane active sites in 1T-MoS$_2$. The oxidation state of the intercalated Sc$^{3+}$ ions was confirmed by XPS and XRD. While structural changes to the bulk 1T-MoS$_2$ material was not observed, a 5.7% increase in 1T-MoS$_2$'s interlayer spacing was observed. This increase in interlayer spacing, however, does not correspond to an increase in catalytic activity. Experimentally, the spatial confinement of Sc SAs reduced the overpotential of 1T-MoS$_2$ by only 3 mV. XPS analysis of Sc SAs/1T-MoS$_2$ did not show any significant change in the binding energies measured for Mo and S species in 1T-MoS$_2$ or the undercoordinated MoS$_x$ species present within the sample. This lack of change in binding energies indicates that the electronic environment of basal S atoms remains unchanged when Sc SAs are confined within their local microenvironments. As a result, the activation barrier that drives HER and the corresponding catalytic activity remains unchanged. These results are found to be in contrast to those discovered for Zn SAs/1T-MoS$_2$ (reported in detail in Chapter 3). Altogether, these results suggest that electronic occupation of d orbitals belonging to SAs spatially confined within active site microenvironments is required to enable the adsorption and desorption kinetics to be altered in a manner that enhances HER performance.

## 4.5 Materials and Methods

### 4.5.1 Chemicals

Ammonium heptamolybdate tetrahydrate [$(NH_4)_6Mo_7O_{24} \cdot 6H_2O$, 99% Alfa Aesar], thioacetamide ($CH_3CSNH_2$, 99$^+$% Acros Organics), urea ($H_2NCONH_2$, Sigma-Aldrich), and scandium(III) chloride hexahydrate ($ScCl_3 \cdot 6H_2O$, 99.9% STREM Chemicals) were used without further purification.

### 4.5.2 Synthesis of Sc SAs/1T-MoS$_2$

First, 50 mg of $(NH_4)_6Mo_7O_{24} \cdot 6H_2O$, 80 mg of $CH_3CSNH_2$, 40 mg of $H_2NCONH_2$, either 5, 10, 15, or 20 mg of $ScCl_3 \cdot 6H_2O$, and 10 mL of deionized (DI) water were combined in a 25 mL autoclave and sonicated until they were fully dissolved. Once dissolved, the autoclave was sealed within a hydrothermal reactor and heated at 180°C for 24 h. Once the reactor cooled to room temperature, the solution of crude product was transferred to 15 mL conical centrifuge tubes. The crude product was washed and centrifuged three times: once with DI water, once with ethyl alcohol, and once with acetone. The solutions were centrifuged for 10 min at ~4,000 rpm in between each washing step and the supernatant layer was removed after each centrifugation step. After washing, the purified product was dried in a vacuum oven at ~80°C and ~25 mmHg for 24 h. The dried and purified product was finely ground with a mortar and pestle and stored under ambient conditions.

*4.5.3 Characterization*

HAADF-STEM images were acquired using JEOL Grand ARM equipped with two spherical aberration correctors at 300 kV by a convergence semiangle of 22 mrad and inner and outer collection angles of 83 and 165 mrad, respectively. Energy dispersive X-ray spectroscopy (EDX) was conducted by using JEOL dual EDX detectors and a specific high count analytical TEM holder. XPS measurements were collected with a PHI 5600 XPS system equipped with a monochromatic Al Kα X-ray source and Omni Focus III lens operating at 250 W, 14 kV, 600 $\mu m^2$ spot size, and a maximum base pressure of $5 \times 10^{-9}$ Torr. A 90° angle was maintained between the X-ray source and analyzer. Survey spectra were collected with 117.4 eV pass energy, 1.0 eV/step, and 50 μs dwell time. Multiplexes were collected using 11.75 eV pass energy, 0.100 eV/step, and 50 μs dwell time. The instrument was calibrated to Au $4f_{7/2}$ = 84.00 eV and Cu $2p_{3/2}$ = 932.67 eV immediately prior to collecting the data. All spectra were calibrated to C 1s = 284.8 eV.[180] Multiplexes were fitted using IgorPro XPS Tools Software. A Shirley background and 80% Lorentzian–Gaussian were employed for all peak analyses. Raman spectra were recorded using a Thermo Scientific DXR Raman Spectrometer employing an Ar-ion laser operating at 532 nm, a 50 μm pinhole, and 3.0 mW laser power. XRD patterns were measured using the Bruker D2 PHASER XE-T benchtop XRD with Cu–Kα radiation (λ = 1.5406 Å) at 30 kV and 10 mA, step size = 0.02˚, and scan step time = 1.0 s/step. The measurement range was from 6° to 80° in terms of 2θ.

*4.5.4 Electrochemical Measurements*

All electrochemical measurements were conducted in $N_2$-saturated 0.5 M $H_2SO_4$ electrolytic solution within a three-electrode configuration. A CHI 660E electrochemical workstation was used for all electrochemical measurements. Graphite was employed as the counter

electrode and Ag/AgCl (3 M NaCl, BASI) as the reference electrode. Electrodes were prepared by drop casting 100 µL of catalyst ink (20 µL each time, repeated 5 times) onto a 1×2 cm$^2$ piece of carbon fiber paper (CFP). The loading of catalysts on CFP is ~1 mg/cm$^2$. All potentials reported were calibrated with respect to the Ag/AgCl reference electrode in acidic media (0.5 M H$_2$SO$_4$) using **Equation (2.2)**.

LSVs were conducted under ambient conditions from 0 to -0.8 V with 5 mV/s scan rate, 1 mV step size, and 0.001 A/V sensitivity. Onset potentials were extracted from the LSVs and defined as the potential at which the current began to increase (0.05 mA/cm$^2$). Overpotentials were measured at 10 mA/cm$^2$. EIS measurements were performed at -0.45 V with 0.005 V variation in the frequency range of 1-10$^5$ Hz and 12 steps per decade. The stability of Sc SAs/1T-MoS$_2$ was evaluated by running CV at a 0.01 V/s scan rate for 375 cycles from 0 to -0.43 V, followed by comparison of the initial and final LSV curves.

## 4.6 Acknowledgements

## 4.7 Supplementary Information



**Figure S4. 1:** EDX mappings of Sc SAs/1T-MoS$_2$.



**Figure S4.2:** Electrochemical analysis of how the HER performance of 1T-MoS$_2$ changes as the quantity of Sc SAs increases.

These measurements were performed within a standard three-electrode configuration with N$_2$-saturated 0.5 M H$_2$SO$_4$ as the electrolyte. **(a)** LSVs. **(b)** EIS fitted to the equivalent circuit shown. The inset zooms into the low Z' *vs.* -Z" region for clarity.
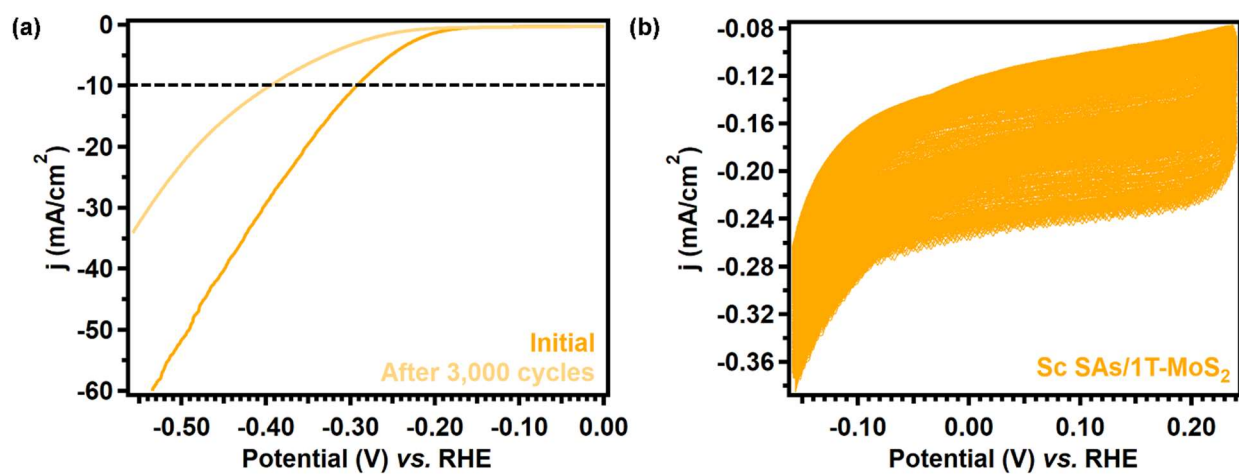
**Figure S4.3:** Stability evaluation of Sc SAs/1T-MoS$_2$.
**(a)** LSVs measured before and after running 3,000 CV cycles. **(b)** Corresponding CV.
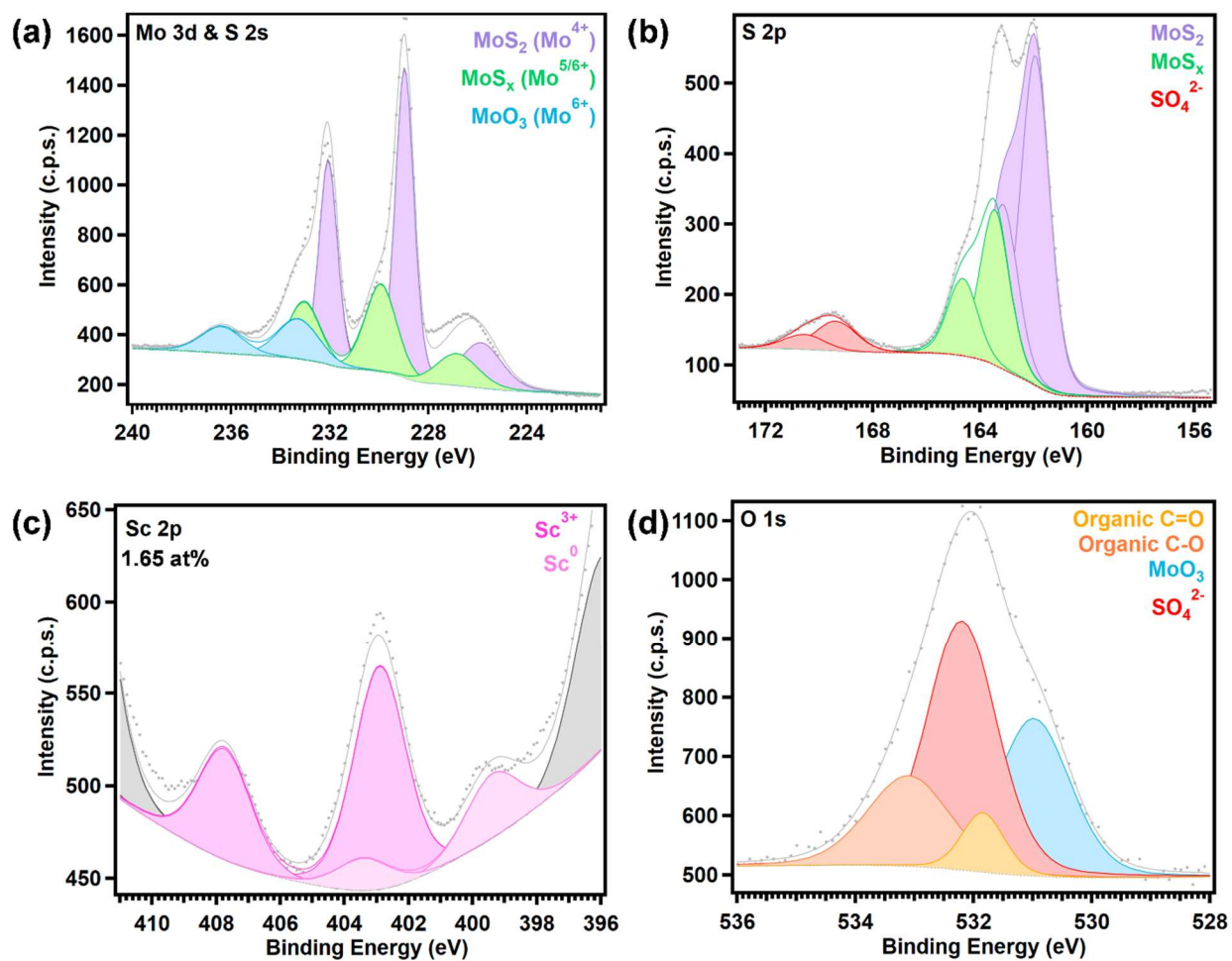
**Figure S4.4:** XPS data and peak assignments for Sc SAs/1T-$MoS_2$ on CFP before running 3,000 CV cycles.
**(a)** Mo 3d and S 2s spectra. **(b)** S 2p spectrum. **(c)** Sc 2p spectrum. **(d)** O 1s spectrum.
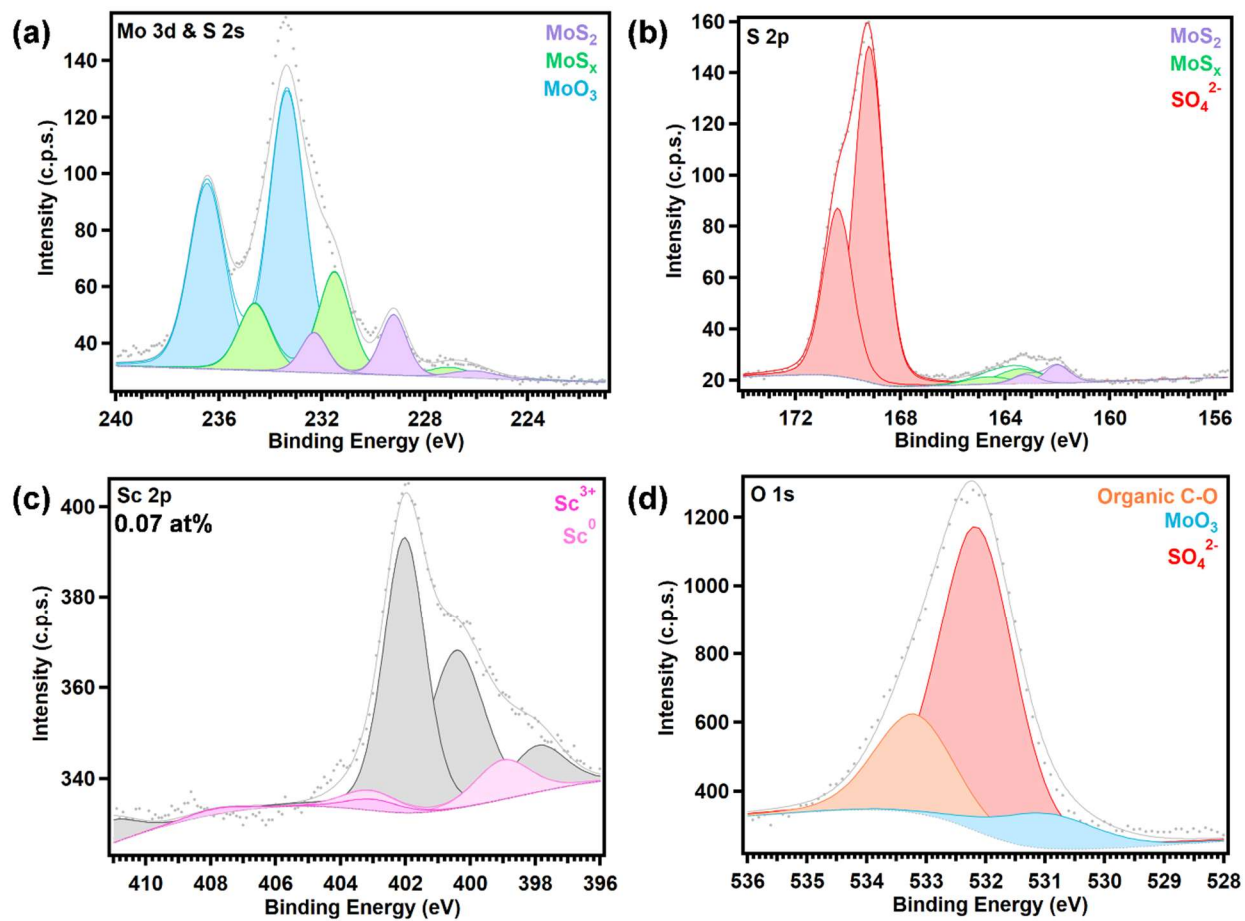
**Figure S4.5:** XPS data and peak assignments for Sc SAs/1T-MoS$_2$ on CFP after running 3,000 CV cycles.
**(a)** Mo 3d and S 2s spectra. **(b)** S 2p spectrum. **(c)** Sc 2p spectrum. **(d)** O 1s spectrum.

**Table S4.1:** Raman peak assignments for Sc SAs/1T-MoS$_2$

| Peak Positions (cm$^{-1}$) | | Peak Assignments |
|---|---|---|
| 1T-MoS$_2$ | Sc SAs/1T-MoS$_2$ | |
| 113 | 113 | TA |
| 125 | 123 | TA |
| 149 | 146 | J$_1$ |
| 195 | 193 | LA |
| 213 | 212 | LA |
| 237 | 237 | J$_2$ |
| 284 | 283 | E$_{1g}$ |
| 336 | 335 | J$_3$ |
| 377 | 376 | E$^1_{2g}$ |
| 402 | 400 | A$_{1g}$ |

**Table S4.2:** XPS data and peak assignments for Sc SAs/1T-MoS$_2$

| Peak | Binding Energy (eV) | | | Peak Assignment |
|---|---|---|---|---|
| | 1T-MoS$_2$ | Sc SAs/1T-MoS$_2$ | Zn SAs/1T-MoS$_2$ | |
| Zn 2p$_{3/2}$ | -- | 1022.80 | -- | Zn$^{2+}$ |
| Zn 2p$_{1/2}$ | -- | 1045.80 | -- | Zn$^{2+}$ |
| Sc 2p$_{3/2}$ | -- | -- | 399.57 | Sc$^0$ |
| | -- | -- | 402.55 | Sc$^{3+}$ |
| Sc 2p$_{1/2}$ | -- | -- | 403.87 | Sc$^0$ |
| | -- | -- | 407.14 | Sc$^{3+}$ |
| Mo 3d$_{5/2}$ | 229.05 | 228.98 | 229.05 | MoS$_2$, Mo$^{4+}$ |
| | 229.93 | 229.93 | 229.94 | MoS$_x$, Mo$^{5/6+}$ |
| | -- | -- | -- | MoO$_3$, Mo$^{6+}$ |
| Mo 3d$_{3/2}$ | 232.15 | 232.08 | 232.15 | MoS$_2$, Mo$^{4+}$ |
| | 233.03 | 233.03 | 232.94 | MoS$_x$, Mo$^{5/6+}$ |
| | -- | -- | -- | MoO$_3$, Mo$^{6+}$ |
| S 2p$_{3/2}$ | 161.90 | 161.80 | 161.98 | MoS$_2$, S$^{2-}$ |
| | 163.45 | 163.28 | 163.33 | MoS$_x$, S$^{2-}$ |
| | -- | -- | -- | SO$_4$$^{2-}$ |
| S 2p$_{1/2}$ | 163.10 | 163.00 | 163.18 | MoS$_2$, S$^{2-}$ |
| | 164.65 | 164.48 | 164.53 | MoS$_x$, S$^{2-}$ |
| | -- | -- | -- | SO$_4$$^{2-}$ |
| S 2s | 225.95 | 225.88 | 225.95 | MoS$_2$ |
| | 226.83 | 226.83 | 226.84 | MoS$_x$ |
| O 1s | -- | -- | -- | MoO$_3$ |
| | 531.20 | 531.56 | 531.24 | Organic C=O |
| | -- | -- | -- | SO$_4$$^{2-}$ |
| | 532.48 | 533.18 | 532.73 | Organic C-O |

**Table S4.3:** Comparison of the overpotentials and Tafel slopes observed for Sc (5 mg) SAs/1T-MoS$_2$, Sc (10 mg) SAs/1T-MoS$_2$, Sc (15 mg) SAs/1T-MoS$_2$, and Sc (20 mg) SAs/1T-MoS$_2$

| Sample | Overpotential (mV *vs.* RHE) | Tafel slope (mV/dec) |
| --- | --- | --- |
| Carbon fiber paper (CFP) | -- | -- |
| Pt/C | 37 | 34.0 |
| 1T-MoS$_2$ | 265 | 107.2 |
| Zn SAs/1T-MoS$_2$ | 177 | 84.9 |
| Sc SAs (5 mg)/1T-MoS$_2$ | 340 | -- |
| Sc SAs (10 mg)/1T-MoS$_2$ | 293 | -- |
| Sc SAs (15 mg)/1T-MoS$_2$ | 262 | 108.7 |
| Sc SAs (20 mg)/1T-MoS$_2$ | 311 | -- |

Overpotentials are defined as the potential (mV *vs.* RHE) measured at -10 mA/cm$^2$.

**Table S4.4:** Equivalent circuit fittings for EIS data reported for Sc (5 mg) SAs/1T-MoS$_2$, Sc (10 mg) SAs/1T-MoS$_2$, Sc (15 mg) SAs/1T-MoS$_2$, and Sc (20 mg) SAs/1T-MoS$_2$

| Sample | R$_s$ ($\Omega$) | R$_{ct}$ ($\Omega$) | CPE-T | CPE-P |
| --- | --- | --- | --- | --- |
| 1T-MoS$_2$ | 2.289 | 127.5 | 0.0247 | 0.923 |
| Zn SAs/1T-MoS$_2$ | 2.191 | 18.41 | 0.00410 | 0.897 |
| Sc SAs (5 mg)/1T-MoS$_2$ | 1.948 | $1.025 \times 10^9$ | 0.0261 | 0.557 |
| Sc SAs (10 mg)/1T-MoS$_2$ | 2.034 | $7.005 \times 10^7$ | 0.00985 | 0.543 |
| Sc SAs (15 mg)/1T-MoS$_2$ | 1.728 | 42.87 | 0.00830 | 0.611 |
| Sc SAs (20 mg)/1T-MoS$_2$ | 1.199 | 16.77 | 0.00391 | 0.738 |

**Table S4.5:** XPS data and peak assignments for Sc SAs/1T-MoS$_2$ before and after collecting 3,000 CV scans

| Peak | Sc SAs/1T-MoS$_2$ | | Peak Assignment |
| --- | --- | --- | --- |
| | Pre-CV | Post-CV | |
| Sc 2p$_{3/2}$ | 399.39 | 399.01 | Sc$^0$ |
| | 402.90 | 403.00 | Sc$^{3+}$ |
| Sc 2p$_{1/2}$ | 403.39 | 403.11 | Sc$^0$ |
| | 407.75 | 407.85 | Sc$^{3+}$ |
| Mo 3d$_{5/2}$ | 228.96 | 229.21 | MoS$_2$, Mo$^{4+}$ |
| | 229.93 | 231.66 | MoS$_x$, Mo$^{5/6+}$ |
| | 233.28 | 233.43 | MoO$_3$, Mo$^{6+}$ |
| Mo 3d$_{3/2}$ | 232.06 | 232.31 | MoS$_2$, Mo$^{4+}$ |
| | 233.03 | 234.76 | MoS$_x$, Mo$^{5/6+}$ |
| | 236.38 | 236.53 | MoO$_3$, Mo$^{6+}$ |
| S 2p$_{3/2}$ | 161.94 | 162.01 | MoS$_2$, S$^{2-}$ |
| | 163.45 | 163.43 | MoS$_x$, S$^{2-}$ |
| | 169.38 | 169.19 | SO$_4^{2-}$ |
| S 2p$_{1/2}$ | 163.14 | 163.21 | MoS$_2$, S$^{2-}$ |
| | 164.65 | 164.63 | MoS$_x$, S$^{2-}$ |
| | 170.58 | 170.39 | SO$_4^{2-}$ |
| S 2s | 225.86 | 226.11 | MoS$_2$ |
| | 226.83 | 227.04 | MoS$_x$ |
| O 1s | 530.98 | 531.01 | MoO$_3$, O$^{2-}$ |
| | 531.84 | -- | Organic C=O |
| | 532.20 | 532.15 | SO$_4^{2-}$ |
| | 533.10 | 533.20 | Organic C-O |

## 4.8 References

7.      Gao, M. R.;  Chan, M. K.; Sun, Y., Edge-Terminated Molybdenum Disulfide with a 9.4-a Interlayer Spacing for Electrochemical Hydrogen Production. *Nat Commun* **2015,** *6*, 7493.

24.      Huang, Y.;  Sun, Y.;  Zheng, X.;  Aoki, T.;  Pattengale, B.;  Huang, J.;  He, X.;  Bian, W.;  Younan, S.;  Williams, N.;  Hu, J.;  Ge, J.;  Pu, N.;  Yan, X.;  Pan, X.;  Zhang, L.;  Wei, Y.;  Gu, J., Atomically Engineering Activation Sites onto Metallic 1t-Mos2 Catalysts for Enhanced Electrochemical Hydrogen Evolution. **2019,** *10*.

30.      Li, X.;  Liu, L.;  Ren, X.;  Gao, J.;  Huang, Y.;  Liu, B., Microenvironment Modulation of Single-Atom Catalysts and Their Roles in Electrochemical Energy Conversion. *Sci Adv* **2020,** *6* (39), 1-20.

39.      Li, H.;  Guo, C.;  Fu, Q.; Xiao, J., Toward Fundamentals of Confined Electrocatalysis in Nanoscale Reactors. *J Phys Chem Lett* **2019,** *10* (3), 533-539.

63.      Naumkin, A. V.;  Kraut-Vass, A.;  Gaarenstroom, S. W.;  Powell, C. J., Nist X-Ray Photoelectron Spectroscopy Database. National Institute of Science and Technology: 2012; Vol. 20899, p 20899.

64.      Baker, M. A.;  Gilmore, R.;  Lenardi, C.; Gissler, W., Xps Investigation of Preferential Sputtering of S from Mos2 and Determination of Mosx Stoichiometry from Mo and S Peak Positions. *Applied Surface Science* **1999,** *150* (1-4), 255-262.

163.      Wilson, J. A.; Yoffe, A. D., The Transition Metal Dichalcogenides Discussion and Interpretation of the Observed Optical, Electrical and Structural Properties. *Advances in Physics* **1969,** *18* (73), 193-335.

164.      Qiao, B.;  Wang, A.;  Yang, X.;  Allard, L. F.;  Jiang, Z.;  Cui, Y.;  Liu, J.;  Li, J.; Zhang, T., Single-Atom Catalysis of Co Oxidation Using Pt1/Feox. *Nature Chemistry* **2011,** *3* (8), 634-641.

165.      Qu, Y.;  Wang, L.;  Li, Z.;  Li, P.;  Zhang, Q.;  Lin, Y.;  Zhou, F.;  Wang, H.;  Yang, Z.;  Hu, Y.;  Zhu, M.;  Zhao, X.;  Han, X.;  Wang, C.;  Xu, Q.;  Gu, L.;  Luo, J.;  Zheng, L.; Wu, Y., Ambient Synthesis of Single‑Atom Catalysts from Bulk Metal Via Trapping of Atoms by Surface Dangling Bonds. *Advanced Materials* **2019,** *31* (44), 1904496.

166.      Wang, L.;  Chen, M.-X.;  Yan, Q.-Q.;  Xu, S.-L.;  Chu, S.-Q.;  Chen, P.;  Lin, Y.;  Liang, H.-W., A Sulfur-Tethering Synthesis Strategy Towardhigh-Loading Atomically Dispersed Noble Metal Catalysts. *Sci Adv* **2019,** *5* (10).

167.      Grommet, A. B.;  Feller, M.; Klajn, R., Chemical Reactivity under Nanoconfinement. *Nature Nanotechnology* **2020,** *15* (4), 256-271.

168.      Zhang, L.;  Ng, M. L.; Vojvodic, A., Role of Undercoordinated Sites for the Catalysis in Confined Spaces Formed by Two-Dimensional Material Overlayers. *The Journal of Physical Chemistry Letters* **2020,** *11* (21), 9400-9407.

169.    Tang, C.; Chen, L.; Li, H.; Li, L.; Jiao, Y.; Zheng, Y.; Xu, H.; Davey, K.; Qiao, S.-Z., Tailoring Acidic Oxygen Reduction Selectivity on Single-Atom Catalysts Via Modification of First and Second Coordination Spheres. *Journal of the American Chemical Society* **2021,** *143* (20), 7819-7827.

170.    Zhang, J.; Zhao, Y.; Chen, C.; Huang, Y.-C.; Dong, C.-L.; Chen, C.-J.; Liu, R.-S.; Wang, C.; Yan, K.; Li, Y.; Wang, G., Tuning the Coordination Environment in Single-Atom Catalysts to Achieve Highly Efficient Oxygen Reduction Reactions. *Journal of the American Chemical Society* **2019,** *141* (51), 20118-20126.

171.    Cong, X.; Liu, X. L.; Lin, M. L.; Tan, P. H., Application of Raman Spectroscopy to Probe Fundamental Properties of Two-Dimensional Materials. *Npj 2d Mater Appl* **2020,** *4* (1), 1-12.

172.    Lei, S.; Wang, X.; Li, B.; Kang, J.; He, Y.; George, A.; Ge, L.; Gong, Y.; Dong, P.; Jin, Z.; Brunetto, G.; Chen, W.; Lin, Z.-T.; Baines, R.; Galvão, D. S.; Lou, J.; Barrera, E.; Banerjee, K.; Vajtai, R.; Ajayan, P., Surface Functionalization of Two-Dimensional Metal Chalcogenides by Lewis Acid–Base Chemistry. *Nature Nanotechnology* **2016,** *11* (5), 465-471.

173.    Lou, X. W.; Zeng, H. C., Hydrothermal Synthesis of A-Moo<Sub>3</Sub> Nanorods Via Acidification of Ammonium Heptamolybdate Tetrahydrate. *Chem Mater* **2002,** *14* (11), 4781-4789.

174.    Guo, J.; Zavalij, P.; Whittingham, S. M., Metastable Hexagonal Molybdates: Hydrothermal Preparation, Structure, and Reactivity. *Journal of Solid State Chemistry* **1994,** *117* (2), 323-332.

175.    Housecroft, C.; Sharpe, A. G., Appendix 6: Van Der Walls, Metallic, Covalent and Ionic Radii. In *Inorganic Chemistry*, 4th Ed ed.; Pearson Education Limited: 2012; pp 1126-1127.

176.    Liu, H.; Han, N.; Zhao, J., Atomistic Insight into the Oxidation of Monolayer Transition Metal Dichalcogenides: From Structures to Electronic Properties. *RSC Advances* **2015,** *5* (23), 17572-17581.

177.    Yi, H.; Zhang, X.; Jia, F.; Wei, Z.; Zhao, Y.; Song, S., Competition of Hg2+ Adsorption and Surface Oxidation on Mos2 Surface as Affected by Sulfur Vacancy Defects. *Applied Surface Science* **2019,** *483*, 521-528.

178.    Biesinger, M. C.; Lau, L. W. M.; Gerson, A. R.; Smart, R. S. C., Resolving Surface Chemical States in Xps Analysis of First Row Transition Metals, Oxides and Hydroxides: Sc, Ti, V, Cu and Zn. *Applied Surface Science* **2010,** *257* (3), 887-898.

179.    Kang, Q.; Vernisse, L.; Remsing, R. C.; Thenuwara, A. C.; Shumlas, S. L.; McKendry, I. G.; Klein, M. L.; Borguet, E.; Zdilla, M. J.; Strongin, D. R., Effect of Interlayer Spacing on the Activity of Layered Manganese Oxide Bilayer Catalysts for the Oxygen Evolution Reaction. *Journal of the American Chemical Society* **2017,** *139* (5), 1863-1870.

180. Yang, D.-Q.; Sacher, E., S-P Hybridization in Highly Oriented Pyrolitic Graphite and Its Change on Surface Modification, as Studied by X-Ray Photoelectron and Raman Spectroscopies. *Surface Science* **2002,** *504*, 125-137.

# CHAPTER 5: Effects of Single Atom Spin State on Confinement Catalysis

## 5.1 Abstract

Spatial confinement of metal SAs within local microenvironments of active sites enhance catalytic activity by electronically manipulating active site frontier orbitals in a manner that alters the adsorption/desorption energies which drive reaction kinetics. Primary driving factors that influence interactions between the guest metal and active sites include guest metal oxidation state, local coordination geometry, and electronic occupation of valence states. Although the guest metal's spin state has the ability to alter its electronic structure, the impact it has under 1D confinement on catalysis is poorly understood. In this work, the electrochemical HER performance of HS and LS Mn SAs confined within $1T$-$MoS_2$ nanosheets are compared in acidic conditions (0.5 M $H_2SO_4$). In the HS case, the Mn SAs substitute Mo atoms within the $1T$-$MoS_2$ crystal lattice, adopt $d^5$ electron configuration and octahedral coordination geometry, and decrease $1T$-$MoS_2$'s overpotential by 64 mV. In the LS case, the Mn SAs adsorb to the basal plane of $1T$-$MoS_2$, octahedrally coordinate to their LS inducing ligands and basal S atoms, and reduce $1T$-$MoS_2$'s overpotential by 24 mV. This smaller reduction in HER overpotential is attributed to the smaller extent of electron donation provided by the LS Mn SAs to nearby S active sites compared to the HS Mn SAs. Elucidating the effects of the confined metal's spin state enhances the ability to control the manner in which confined single atoms influence the catalytic performance of 2D substrates in all fields of catalysis.

## 5.2 Introduction

Unique to complexes formed with first-row transition metals that have electron configurations between $d^4$ through $d^7$ is the ability to rearrange their valence electrons. This

158

rearrangement occurs to reduces electron-electron repulsion that arises when the electrons are paired in the same orbital. According to Hund's Rule, pairing electrons in the same orbital requires energy. When electrons are added to an orbital, it occurs in a manner that minimizes the orbital's total energy, known as the pairing energy. When two electrons occupy the same orbital, the two electrons repel each other. As a consequence, the energy and stability of the orbital they occupy increases. Whether the electrons pair up or occupy higher energy orbitals depends on the crystal field splitting energy ($\Delta$). If the crystal field splitting energy is greater than the pairing energy, greater stability will be achieved by pairing electrons in lower level degenerate orbitals. Metal complexes with this type of electron configuration are considered LS. If the crystal field splitting energy is less than the pairing energy, greater stability will be achieved by keeping electrons in the lower level degenerate orbitals unpaired and allowing additional electrons to singly occupy higher level degenerate orbitals. Metal complexes with this type of electron configuration are considered HS.

In the LS configuration, the crystal field splitting energy between the metal complex's HOMO and LUMO frontier orbitals is greater compared to the crystal field splitting energy exhibited by the HS configuration. As an example, a schematic diagram of the HS and LS $d^5$ orbital configurations using octahedral coordination as an example is provided in **Figure S5.1**. Although the example provided is of an octahedral complex, it is important to note that these configurations may occur for any type of coordination geometry. The one exception involves tetrahedrally coordinated 3d (first row) transition metals, which always adopt HS configurations due to the rarity of the complex's pairing energy to exceed its crystal field splitting energy.[181] In addition to the number of valence electrons that occupy a 3d metal's d orbitals, the types of ligands that bond to the metal center will influence the crystal field splitting energy and resulting spin configuration of

the metal complex formed. Metal complexes formed with strong $\pi$-donating ligands (*i.e.,* halides, $S^{2-}$, $O^{2-}$, $NR_2^-$, $RO^-$) favor HS configurations, whereas those formed with $\pi$-accepting (*i.e.,* CO, $NO^+$, bipy, $CN^-$, CNR) or $\sigma$-donating ligands (*i.e.,* $OH_2$, $NH_3$, $CH_3^-$, $H^-$) favor LS configurations. Likewise, complexes formed with first-row transition metals in low valence states tend to prefer low crystal field splitting energies (HS configuration) whereas those formed with first-row transition metals in high valence states prefer larger crystal field splitting energies (LS configuration). Due to the fact that the crystal field splitting energy increases down a group in the periodic table, the majority of second and third row transition metal complexes are LS regardless of the ligands they bond to.

The catalytic performance of SACs is strongly dictated by their electronic structure. The electronic structure of SACs is regulated by their local atomic structure, including the coordination geometry and oxidation state of the guest metal.[182] These factors control the local arrangement of orbitals belonging to active sites within the SAC which in turn influence the reaction kinetics that drive catalysis.[31] Therefore, once the guest metal is confined within an active site's local microenvironment, the energies of the active site's frontier orbitals will be affected by the guest metal's electronic configuration. As an intrinsic property of SACs, the spin configuration of confined guest metals will influence the electronic properties of the SAC's active sites.[182] Gong *et. al.* reported the ability to control the spin states of Co SAs to be LS or HS by regulating the oxidation states of single Co atoms such as $Co^{2+}$-TAP and $Co^{3+}$-TAP, respectively.[183] Based on experimental findings and theoretical simulations, $Co^{3+}$-TAP with HS configuration demonstrated greater activity and selectivity towards electroreduction of $CO_2$ to HCOOH via the COOH pathway compared to the LS configurated $Co^{2+}$-TAP. In contrast, $Co^{2+}$-TAP demonstrated greater selectivity towards converting HCOOH into CO and $CH_4$. DFT calculations predicted lower

energy barriers for the two hydrogenation steps that facilitate $CO_2$ reduction to HCOOH to be the primary factors driving the improvement in selectivity and activity. Li *et. al.* enhanced the performance of electrochemical NRR by anchoring Fe SAs on a S and N co-doped C matrix (Fe$_{SA}$-NSC).[184] Based on their findings, doping S atoms generated an FeN$_3$S coordination that pushed the Fe$^+$ SAs to adopt a medium spin state ($t_{2g}^6e_g^1$). Theoretical analysis of the NRR mechanism showed that the energy barrier of the reaction's rate determining step, reductive protonation of the adsorbed $^*$N$_2$ intermediate, was lowered when the Fe SAs coordinate to three N atoms and one S atom (FeN$_3$S) compared to when they are coordinated to four N atoms (FeN$_4$), which in turn improved catalytic activity.

In this chapter, we investigated the catalytic effects of spatially confining octahedrally-coordinated Mn SAs, a d$^5$ first-row transition metal, in HS and LS configurations near basal plane active sites in 1T-MoS$_2$. In the HS case, all five d orbitals are singly occupied ($t_{2g}^{*3}e_g^{*2}$). In the LS case, two of the t$_{2g}$ orbitals are doubly occupied, one is singly occupied, and both e$_g$ orbitals are empty ($t_{2g}^{*5}e_g^{*0}$). To synthesize the HS case, MnCl$_2$ was syringe injected into a 1T-MoS$_2$ dispersion (HS Mn SAs/1T-MoS$_2$). For the LS case, Mn(bpy)(CO)$_3$Br was syringe injected into a dispersion of 1T-MoS$_2$ (LS Mn SAs/1T-MoS$_2$). Detailed synthetic steps are provided in the Methods section and schematic diagrams of each SAC is provided in **Figure S5.2**. We hypothesized that the orbitals that overlap well with $p_z$ orbitals belonging to basal S atoms in 1T-MoS$_2$ will promote bond formation. This bond formation, in turn, will enhance charge transfer effects between the guest metal and catalytic substrate. As demonstrated by the results for Zn SAs/1T-MoS$_2$ discussed in detail in Chapter 2, enhancement of charge transfer from the metal intercalant to 1T-MoS$_2$ will alter its H$^*$ adsorption and H$_2$ desorption energies and promote HER kinetics. Since the $d_{z^2}$ orbital overlaps best with the $p_z$ orbital, and the $d_{z^2}$ orbital is partially

occupied in the HS case and empty in the LS case, we hypothesized that the HS case will outperform the LS case. Based on our experimental findings, HS Mn SAs spatially confined near the catalyst surface exhibited $d^5$ electron configuration, greater electron donation from the HS Mn SAs to nearby S active sites, and lowered 1T-$MoS_2$'s overpotential by 64 mV. In contrast, LS Mn SAs residing near the catalyst surface exhibited $d^4$ electron configuration under confinement, less electron donation from LS Mn SAs to S active sites compared to the HS case, and reduced 1T-$MoS_2$'s overpotential by 24 mV. The greater improvement in HER performance demonstrated by HS Mn SAs/1T-$MoS_2$ is ascribed to the HS Mn SAs ability to donate more electrons to nearby S active sites compared to the extent of electron donation exhibited by the LS Mn SAs. This chapter concludes with an overall comparison of the catalytic performance of all four cases of d-orbital occupations investigated herein and identifies trends between the confined SA's d-orbital occupation, electronic modulation of S active sites, and resulting impact on 1T-$MoS_2$'s HER activity.

## 5.3 Results and Discussion

### 5.3.1 Structural Characterization of HS Mn SAs/1T-MoS₂

HAADF-STEM images produced by HS Mn SAs/1T-$MoS_2$ demonstrated surprising results compared to the $d^0$ and $d^{10}$ cases investigated (**Figure 5.1**). Whereas both Sc and Zn SAs adsorb to the basal plane of 1T-$MoS_2$ (see **Figure 3.1** in Chapter 3 and **Figure 4.1** in Chapter 4),
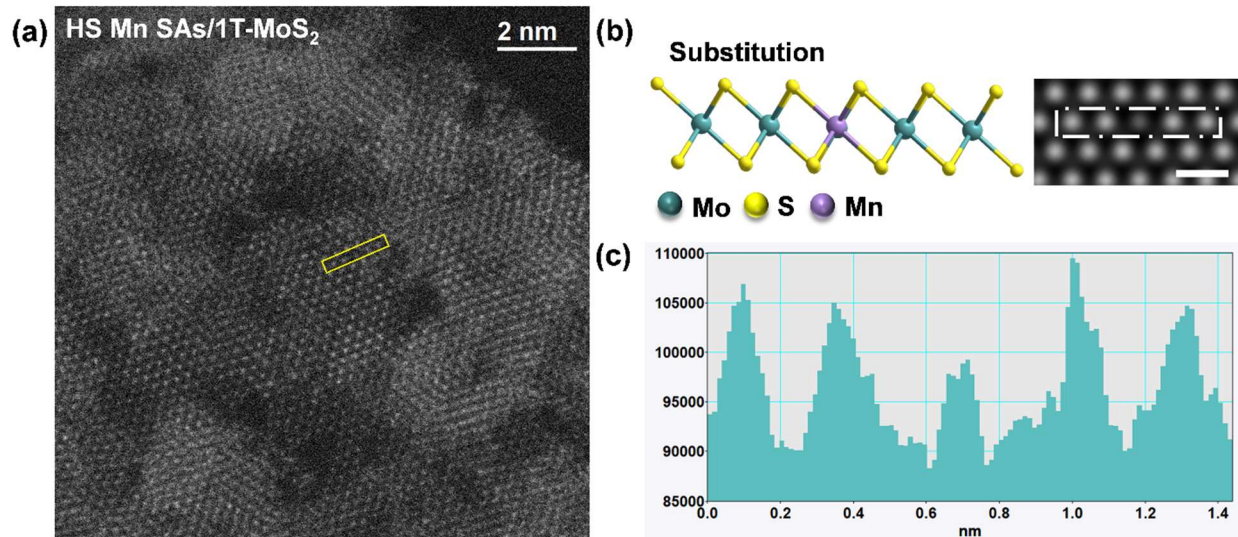
**Figure 5. 1:** HAADF-STEM characterization and quantitative identification of HS Mn SAs substitution into the 1T-MoS$_2$ lattice.
**(a)** Atomically-resolved HAADF-STEM image of the sample. **(b)** Side view of the atomic structure of the HS Mn SAs/1T-MoS$_2$ substitution model and simulated HAADF-STEM image. Scale bar is 0.5 nm. **(c)** Intensity profile taken along the row of atoms highlighted in the yellow box in (a).

the HS Mn SAs in fact substitute lattice sites occupied by Mo atoms in 1T-MoS$_2$'s crystal structure

(**Figure 5.1a**). Since the Mo atoms exhibit octahedral coordination in the 1T-MoS$_2$ lattice, we

conclude that the HS Mn SAs that substitute Mo atoms in 1T-MoS$_2$ also adopt octahedral

coordination geometries. A simulated model of the substitution process provided in **Figure 5.1b**

matches the atomic sites boxed in yellow in **Figure 5.1a**. In **Figure 5.1c,** intensity profiles

extracted from the highlighted atomic sites in **Figure 5.1a** demonstrate a decreased ADF intensity

for the Mo lattice site that has been replaced by a HS Mn SA. EDX mappings shown in **Figure

S5.3** confirm the uniform distribution of Mn, Mo, and S atoms throughout HS Mn SAs/1T-MoS$_2$.

As a liquid phase intercalation process, the syringe injection method used to synthesize HS Mn

SAs/1T-MoS$_2$ is governed by the kinetic and thermodynamic nature of the liquid-intercalant

source and host.[185] Similar to vapor phase synthetic methods, liquid phase intercalation methods

lack control over the composition of the final product. In other words, syringe injection synthesis

does not force the SAs into the lattice sites desired to be occupied. Regardless, since substitution

of Mo sites still allows the HS Mn SAs to reside within the local microenvironment of S active sites along the basal plane, this result is not believed to conflict with the investigation conducted herein.
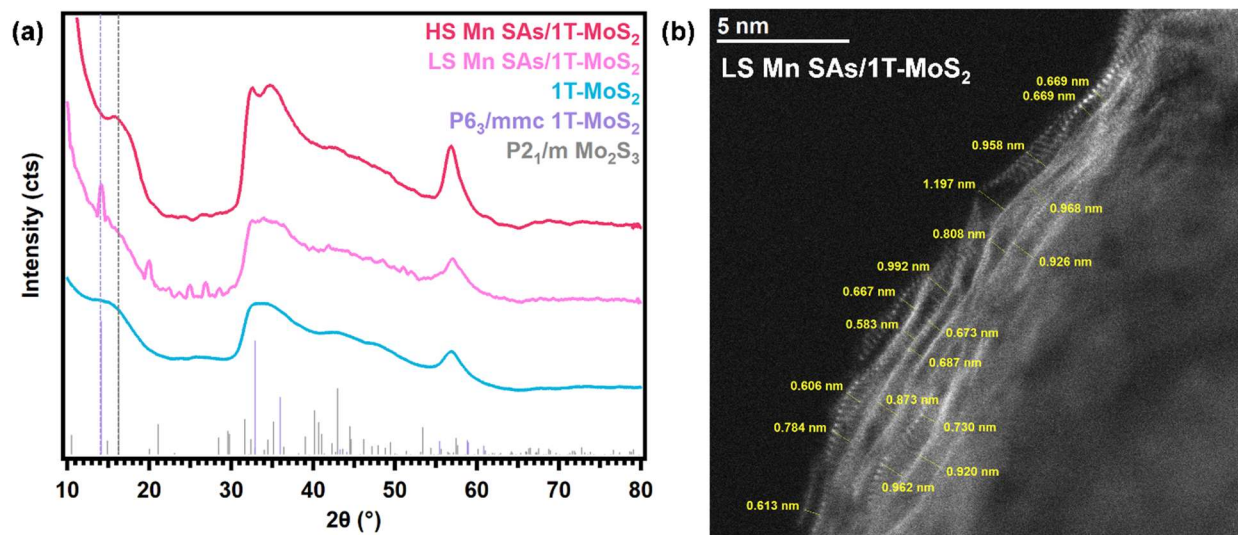


**Figure 5.2:** XRD and HAADF-STEM analysis of changes to 1T-MoS$_2$ interlayer spacing induced by HS Mn SAs and LS Mn SAs.
**(a)** HS Mn SAs/1T-MoS$_2$ (red), LS Mn SAs/1T-MoS$_2$ (pink), and 1T-MoS$_2$ (blue) XRD patterns. The purple and grey dashed lines highlight the (001) plane in 1T-MoS$_2$ and (10$\bar{1}$) plane in Mo$_2$S$_3$, respectively.
**(b)** HAADF-STEM image of fringe spacing along the edge of LS Mn SAs/1T-MoS$_2$. Experimental fringe spacings are shown in yellow.

Changes in d-spacing with substitution of HS Mn SAs into 1T-MoS$_2$ lattice sites were evaluated using the XRD pattern produced by HS Mn SAs/1T-MoS$_2$ (**Figure 5.2a**, shown in red). Peak shifts corresponding to the (001) plane of 1T-MoS$_2$ are not observed. However, a slight shift from 16.28° (0.544 nm) to 15.87° (0.558 nm) in the (10$\bar{1}$) plane that bisects Mo-S chains that intercalate the 1T'-MoS$_2$ layers in Mo$_2$S$_3$ is observed. Customarily, if the HS Mn SAs adsorbed to the basal plane of 1T-MoS$_2$, an increase in d-spacing would be expected, as was observed for Zn SAs/1T-MoS$_2$ and Sc SAs/1T-MoS$_2$ (see **Figure 3.2a** in Chapter 3 and **Figure 4.2b** in Chapter 4, respectively). The absence of this peak shift further confirms the substitution of HS Mn SAs into 1T-MoS$_2$'s crystal structure.

One of the primary synthetic goals of the intercalation strategies employed in this work is to ensure that 1T-MoS$_2$ remains structurally intact after intercalation of each type of guest metal studied herein. Raman spectroscopy was employed to evaluate the resulting structure of the catalyst post intercalation of HS Mn SAs. Resulting spectra of HS Mn SAs/1T-MoS$_2$ compared to 1T-MoS$_2$ and LS Mn SAs/1T-MoS$_2$ is shown in **Figure S5.4a**. Corresponding peak positions and assignments are provided in **Table S5.1**. Existence of the 1T phase in the bulk region of HS Mn SAs/1T-MoS$_2$ is confirmed by the presence of J$_1$, J$_2$, E$_{1g}$, J$_3$, TA, and LA phonon modes at the M point of the first Brillouin zone. If desired, an in depth discussion of these types of phonon modes is provided in Chapter 1. Likewise, the greater intensity of the E$^1_{2g}$ peak with respect to the A$_{1g}$ peak further confirms the majority presence of 1T-MoS$_2$ and indicates that the 2H-phase of MoS$_2$ does not exist within the sample. As shown in **Table S5.1**, a slight variation in peak positions between 1-3 cm$^{-1}$ occurs with the presence of HS Mn SAs. However, these shifts are not significant enough to indicate that the HS Mn SAs induce a structural change in the bulk region of 1T-MoS$_2$.[172]

As a fundamental aspect of this chapter, confirmation of the SA's spin state is crucial. Probing the paramagnetic properties of a metal species with EPR spectroscopy is a valuable technique that may be used to elucidate the geometric and electronic structure of the guest metal being studied.[186] Customarily, the EPR spectrum of HS Mn$^{2+}$ (S = 5/2) shows six characteristic hyperfine lines with axially anisotropic g-values.[187] However, upon substituting into 1T-MoS$_2$'s crystal lattice, a single broad isotropic signal (g = 2.031) is observed at both room temperature (**Figure S5.5a**) and 40 K (**Figure S5.5c**) which likely corresponds to electron hole centers localized on S atoms.[187] Assignments of g-values are also provided in **Table S5.2**. The lack of signal induced by the HS Mn SAs may be due to the very low quantity of HS Mn SAs that are intercalated within 1T-MoS$_2$. It is important to note that the magnetic studies conducted on HS Mn

SAs/1T-MoS$_2$ are still preliminary. Since evidence that the Mn SAs adopt HS configurations in the bulk region of the catalyst material is still unclear, further in-depth magnetic studies are necessary to develop a thorough understanding of the catalyst's magnetic structure.

Electronic modulations of active sites were measured by XPS. Resulting XPS spectra of HS Mn SAs/1T-MoS$_2$ was compared to 1T-MoS$_2$ to identify changes in oxidation states and chemical compositions that arise when HS SAs are under spatial confinement (**Figure S5.6**). Peak values and assignments are provided in **Table S5.3**. Two sets of doublet peaks are present in the Mo 3d, S 2s, and S 2p spectra, similar to the results observed for 1T-MoS$_2$, Zn SAs/1T-MoS$_2$, and Sc SAs/1T-MoS$_2$ in previous chapters. The purple doublet peaks correspond to Mo$^{4+}$ and S$^{2-}$ oxidation states in 1T-MoS$_2$ (**Figure S5.6c**).[63] The green doublet peaks correspond to unsaturated Mo$^{5/6+}$ and S$^{2-}$ oxidation states and indicate the presence of a nonstoichiometric MoS$_x$ species along the surface of each sample.[63] Similar to conclusions made in previous chapters, while a portion of MoS$_x$ that exists near the catalyst surface, the bulk region of the catalyst consists of stoichiometric 1T-MoS$_2$.[64] A downshift in the Mo 3d peaks equal to 0.07 eV is observed for MoS$_2$, with no shift in binding energy observed for the MoS$_x$ species. Since this shift is within the step size (0.10 eV) employed when the data was collected, this shift is considered negligible. The S 2p peaks assigned to MoS$_2$ experience a negligible downshift equal to 0.10 eV as well (**Figure S5.6d**). In contrast, the S 2p peaks belonging to MoS$_x$ downshift by 0.17 eV, slightly less than what was observed for Zn SAs/1T-MoS$_2$ (0.19 eV downshift, see **Figure S3.6** and **Table S3.1** in Chapter 3). This result implies that under spatial confinement the HS Mn SAs donate electrons to nearby S atoms in MoS$_x$.[17] The O 1s spectra confirms the presence of organic C-O and C=O, which is associated with adventitious carbon present in the sample (**Figure S5.6b**).[63] MoO$_3$ and SO$_4^{2-}$ species were not observed. Likewise, lacking evidence of any type of oxide or oxyhydroxide peaks

in the O 1s spectrum confirms the absence of any Mn-oxide or Mn-oxyhydroxide species near the catalyst surface. The Mn 2p spectrum displays doublet peaks which correspond to the $Mn^{2+}$ oxidation state (**Figure S5.6a**).[188] The multiplet splitting observed for Mn 2p arises in atoms that contain unpaired electrons. When unpaired electrons are present, photoionization may form a core electron vacancy which in turn may induce coupling between an unpaired core electron and an unpaired outer shell electron. As a result, multiple final states may be created, which in the photoelectron spectrum of Mn 2p are displayed as multiple doublet peaks.[188] This confirmation of the HS Mn SAs existing in the $Mn^{2+}$ oxidation state indicates that the HS Mn SAs retain their $d^5$ electron configuration when spatially confined between layers of $1T\text{-}MoS_2$.

### 5.3.2 Structural Characterization of LS Mn SAs/1T-MoS₂

Due to the molecular nature of the LS Mn SAs, it is reasonable to assume that their ability to substitute Mo atoms in the $1T\text{-}MoS_2$ crystal lattice may be limited. To verify the truth behind this hypothesis, HAADF-STEM imaging and EDX mappings were collected (**Figures 5.3, S5.7**). Adsorption of the LS Mn SAs was confirmed by the presence of brighter lattice sites at positions occupied (**Figure 5.3a**). A simulated sketch of the expected STEM results for adsorption behavior is shown in **Figure 5.3b**. Due to the low atomic number of the C, N, O, and H atoms that make up the bpy and CO ligands, their presence cannot be verified via STEM analysis. The experimental ADF intensity extracted from the section of **Figure 5.3a** highlighted in a yellow box was plotted in the line profile shown in **Figure 5.3c**. The higher intensity of the peak corresponding to the brightest lattice site in the section of atoms analyzed experimentally supports the adsorption behavior of the LS Mn SAs. EDX mappings of a section of the catalyst material show the uniform distribution of the Mn, Mo, and S elements in LS Mn SAs/$1T\text{-}MoS_2$ (**Figure S5.7**).
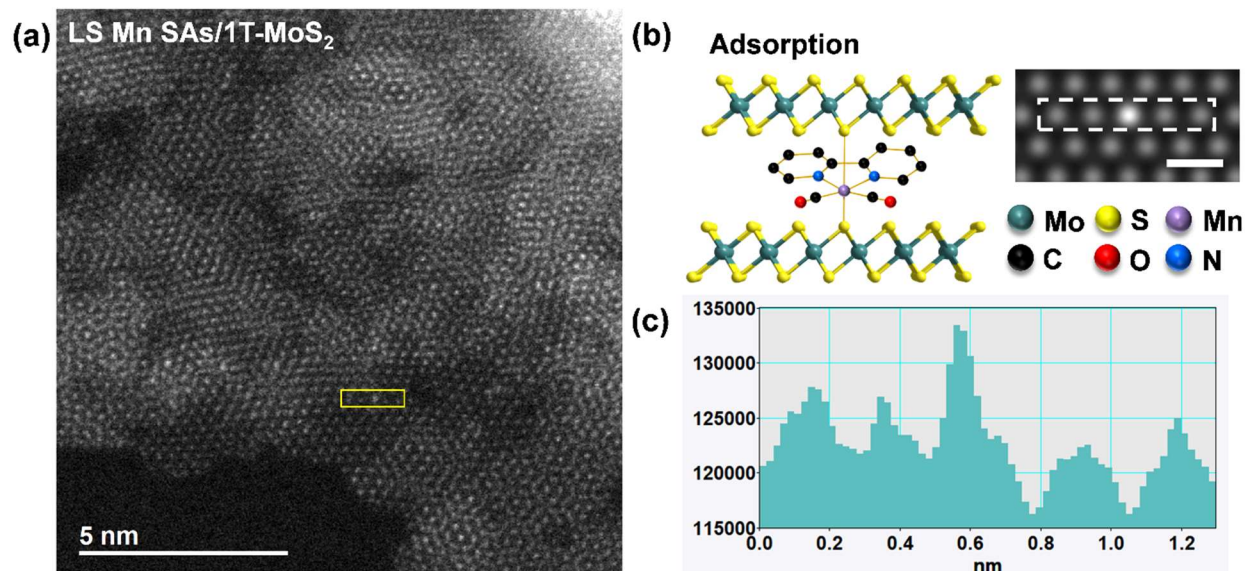
**Figure 5.3:** HAADF-STEM characterization and quantitative identification of LS Mn SAs adsorption to the 1T-MoS₂ basal plane.
**(a)** Atomically-resolved HAADF-STEM image of the sample. **(b)** Side view of the atomic structure of the LS Mn SAs/1T-MoS₂ adsorption model and simulated HAADF-STEM image. Scale bar is 0.5 nm. **(c)** Intensity profile taken along the row of atoms highlighted in the yellow box in (a).

The resulting XRD pattern produced by LS Mn SAs/1T-MoS$_2$ shows an overall structure similar to 1T-MoS$_2$ and the results observed for the d$^0$, d$^{10}$, and HS d$^5$ cases (**Figure 5.2a**, shown in pink). Slight formation of narrow peak structures present in the spectrum indicates the existence of a more crystalline catalyst structure, in contrast to the highly amorphous crystal structure observed in of the other cases studied in this work. The peak corresponding to the (001) plane of 1T-MoS$_2$ is highlighted with a purple dashed line in **Figure 5.2a**. The lack of a shift in that peak to a higher or lower 2θ value suggests that the average d-spacing in the bulk material remains unchanged when LS Mn SAs are intercalated within layers of 1T-MoS$_2$. Customarily, energy must be expended by the 2D host to generate larger interlayer sites for larger guest species to occupy.[189] This results suggests that the parameters of the synthetic method employed was not sufficient enough to intercalate the LS Mn SAs deep within the bulk material. However, confirmation of this

hypothesis is unable to be achieved due to the inherent layer stacking that makes it impossible to reliably identify LS Mn SAs in the bulk region of 1T-MoS$_2$.

HAADF-STEM images displaying fringes near the edge of LS Mn SAs/1T-MoS$_2$ were also analyzed to investigate the change in fringe spacing near the edge of the catalyst material where the likelihood of HER occurring is greatest (**Figure 5.2b**). Compared to the average d-spacing of 1T-MoS$_2$ (0.632 $\pm$ 0.06 nm, **Figure 3.2c**, discussed in Chapter 3), lattice fringes in LS Mn SAs/1T-MoS$_2$ show an average distance equal to 0.804 $\pm$ 0.2 nm. This result hints that the LS Mn SAs may primarily reside near the edge regions of the catalyst material, since observation of lattice regions further from the catalyst's edge show crystalline, uniform lattice structure (**Figure S5.8**). This result corresponds well with the XRD results, which lack evidence of a peak shift of the (001) that would indicate an increase or decrease in d-spacing in the bulk material. Altogether, these results suggest that the intercalation of LS Mn SAs is restricted to edge regions of the catalyst material.

To verify the structural retention of 1T-MoS$_2$ after spatially confining the LS Mn SAs within the interlayer spacing of 1T-MoS$_2$, Raman spectroscopy was again utilized. Results are demonstrated in **Figure S5.4a** with peak positions and assignments provided in **Table S5.1**. Similar to previous results, the presence of J$_1$, J$_2$, E$_{1g}$, J$_3$, TA, and LA phonon modes at the M point of the first Brillouin zone and higher intensity of the E$^1_{2g}$ peak compared to the A$_{1g}$ peak validate the fact that the bulk catalyst material exists in the 1T phase and the absence of the 2H phase. Negligible shifts in peak positions corresponding to each phonon mode conclude the structure of 1T-MoS$_2$ is in fact retained after intercalating LS Mn SAs.[172] Retention of the bpy and CO ligands post intercalation of LS Mn SAs into 1T-MoS$_2$ is critical to ensure that the Mn centers retain their LS character when under spatial confinement. Spectral fingerprints unique to each type of ligand

may be readily identified by FTIR analysis. Therefore, this technique was employed to confirm the presence of bpy and CO ligands in LS Mn SAs/1T-MoS$_2$ (**Figure S5.4b**). Vibrational modes corresponding to sp$^2$ CH stretching, C=C stretching, and CN stretching confirm the presence of bpy ligands in the sample. Likewise, peaks corresponding to CO stretching confirm the presence of CO ligands. Altogether, these results confirm that the Mn centers retain the ligands necessary to force them into a LS configuration all while retaining the overall lattice structure of 1T-MoS$_2$ and suggest that the LS Mn centers maintain octahedral coordination geometry under spatial confinement.

Next, EPR spectroscopy was employed to evaluate the paramagnetic nature of the LS Mn SAs under spatial confinement. Again, we observe a single broad isotropic signal (g = 2.017) at both 293 K (**Figure S5.5b**) and 40 K (**Figure S5.5d**) which likely corresponds to unsaturated Mo$^{5+}$ species coordinated to S atoms.[190-192] Similar to the HS Mn SAs case, it is important to note that the magnetic studies conducted on LS Mn SAs/1T-MoS$_2$ are still preliminary. Although the EPR spectra for LS Mn SAs/1T-MoS2 demonstrate the broad isotropic signal expected that would be expected for LS Mn SAs, the results are still unclear and further in-depth magnetic studies are necessary to develop a thorough understanding of the catalyst's magnetic structure.

Electronic modulations to the 1T-MoS$_2$ substrate were evaluated by XPS. The results, including oxidation states and chemical composition, are provided in **Figure S5.9**. Corresponding peak positions and assignments are available in **Table S5.3**. Two sets of doublet peaks observed in the Mo 3d, S 2s, and S 2p spectra correspond to Mo$^{4+}$ and S$^{2-}$ oxidation states in 1T-MoS$_2$ (shown in purple) as expected (**Figure S5.9c**).[63] The second set of doublet peaks located at higher binding energies correspond to unsaturated Mo$^{5/6+}$ and S$^{2-}$ oxidation states and confirm the presence of nonstoichiometric MoS$_x$ along the surface of the sample, similar to previous

conclusions made for all other SACs studied in this work.[63] Compared to 1T-MoS$_2$, the LS Mn

SAs downshift S 2p peaks belonging to nonstoichiometric MoS$_x$ by 0.12 eV (**Figure S5.9d**). All

other peaks in the Mo 3d and S 2p spectra either display negligible downshifts within the step size

limit or do not shift at all. Based on these results, we conclude that while some electronic donation

from the LS Mn SAs to the S atoms in MoS$_x$ is observed, it is less than what is contributed by the

HS Mn SAs. Similar to HS Mn SAs/1T-MoS$_2$, the O 1s spectrum displays peaks corresponding to

organic C-O and organic C=O, whose presence may be attributed to the existence of adventitious

carbon on the sample (**Figure S5.9b**).[63] The Mn 2p spectrum displays sets of doublet peaks which

are assigned to the Mn$^{3+}$ oxidation state (**Figure S5.9a**).[188] Multiplet peak splitting is observed for

the LS Mn SAs case in a manner similar to what was observed for the HS Mn SAs. In addition to

having oxidation states which exhibit significant multiplet splitting, the oxidation states for Mn

also exhibit overlapping binding energy ranges for the multiplet splitting structures.[188] These

results indicate that although the LS Mn center exists in the Mn$^+$ oxidation state when syringe

injection synthesis begins, the LS Mn centers near the catalyst surface oxidize to a higher oxidation

state when under spatial confinement. Confirmation of the LS Mn SAs existing in the Mn$^{3+}$

oxidation state tells us that the LS Mn centers have d$^4$ electronic configurations near the catalyst

surface, in contrast to the d$^5$ electron configuration maintained by the HS Mn SAs.


*5.3.3 Catalytic Performance of the High Spin vs. Low Spin Cases of Mn SAs/1T-MoS$_2$*

Electrochemical analyses were performed in acidic conditions (N$_2$-saturated 0.5 M H$_2$SO$_4$)

using a three-electrode configuration. Graphite and Ag/AgCl were employed as the counter and

reference electrodes, respectively. LSV (**Figure S5.10a**) and EIS (**Figure S5.10b**) analyses were

performed on 1T-MoS$_2$ substrates hosting 5, 10, and 15 mg of HS Mn SAs. The results indicate

that loading 10 mg of HS Mn SAs yields the best overpotential and lowest charge transfer resistance. Therefore, the HS and LS cases of intercalated Mn SAs were compared by injecting 10 mg of each precursor (MnCl$_2$ for HS Mn SAs, Mn(bpy)(CO)$_3$Br for LS Mn SAs) into 1T-MoS$_2$ (synthesis details are provided in the Methods section). Catalytic performances of the two spin cases were compared to 1T-MoS$_2$ and Pt/C to evaluate changes in 1T-MoS$_2$'s HER performance and compare the results to a well-known high performing HER catalyst (**Figure 5.4a**). Numerical results for LSVs and EIS results collected are available in **Tables S5.5 and S5.6**, respectively. As demonstrated in **Figure 5.4a**, both spin cases reduce the overpotential of 1T-MoS$_2$. The HS Mn SAs reduce 1T-MoS$_2$'s overpotential by 64 mV, whereas the LS Mn SAs reduce 1T-MoS$_2$'s overpotential by 21 mV. The difference in overpotential between HS Mn SAs/1T-MoS$_2$ and LS Mn SAs/1T-MoS$_2$ is large enough (40 mV difference) to conclude that changing the spin configuration of the SA influences HER performance. In support of our preliminary hypothesis, these results indicate that the HS Mn SAs are able to lower the amount of energy required to drive HER at 1T-MoS$_2$ active sites more than the LS Mn SAs can.

Tafel slopes extracted from the LSV onset potential region shown in **Figure 5.4b** further verify these results. While LS Mn SAs/1T-MoS$_2$ slightly lower's 1T-MoS$_2$'s Tafel slope, a greater decrease is observed for the HS Mn SAs/1T-MoS$_2$. As a method employed to measure changes in the rate at which the HER mechanism proceeds, the catalyst that exhibits lower Tafel slopes is expected to require the lowest overpotential to drive HER.[193] The lower Tafel slope produced by HS Mn SAs/1T-MoS$_2$ compared to LS Mn SAs/1T-MoS$_2$ suggests that the kinetic barrier through which HER proceeds is lowered when the Mn SAs exhibit high spin characteristics.

**Figure 5.4c** shows the EIS results produced by 1T-MoS$_2$, HS Mn SAs/1T-MoS$_2$, and LS Mn SAs/1T-MoS$_2$, with quantitative results provided in **Table S5.6**. Clearly, the semi-circle radius
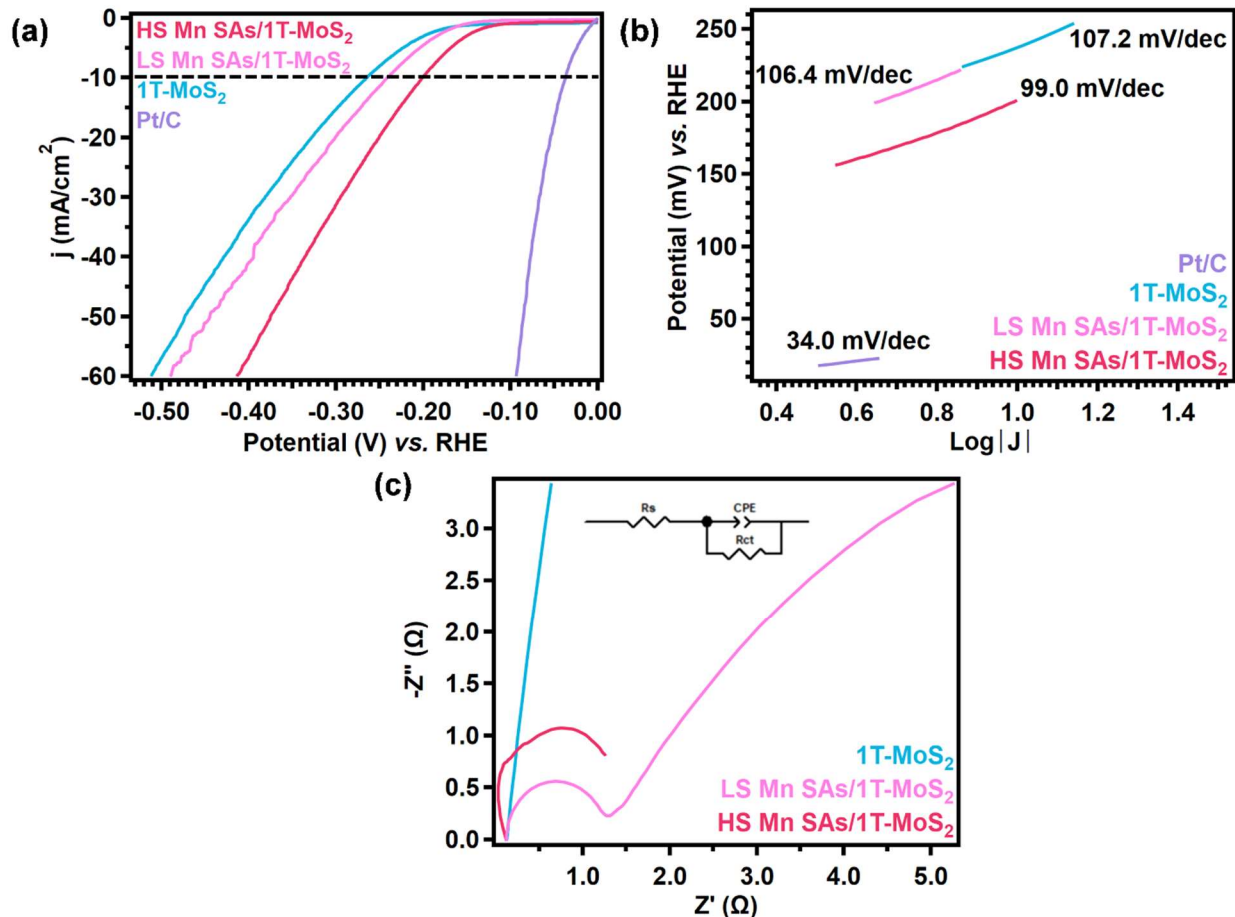
**Figure 5.4:** Electrochemical characterization of HS Mn SAs/1T-MoS$_2$, LS Mn SAs/1T-MoS$_2$, 1T-MoS$_2$, and Pt/C (20%).

Measurements were collected in N$_2$-saturated 0.5 M H$_2$SO$_4$ using a three-electrode configuration. **(a)** HER polarization curves. **(b)** Tafel plots. **(c)** EIS results fitted to the equivalent circuit shown.

of both HS and LS cases are significantly smaller than 1T-MoS$_2$'s semi-circle radius. Fundamentally, a decrease in the semi-circle's radius corresponds to a decrease in charge transport limitations experienced by the electrode during device operation. The observed results therefore suggest that both spin configurations lower charge transport resistance in 1T-MoS$_2$. Deeper analysis of the curve produced by LS Mn SAs/1T-MoS$_2$ identifies a non-vertical line following the semi-circle curve present. This straight line indicates that the electrode is subject to diffuse layer resistance.[194] Numerically, this diffuse layer resistance is represented by the Warburg constant (A$_w$) shown in **Table S5.6**. The experimentally confirmed presence of diffuse layer resistance in the LS case indicates that ion transport is limited in either the diffuse layer region or

bulk electrolyte. As a result, transport of $H^+$ ions through the electrolyte to the electrode surface, where they may subsequently be reduced to $H_2$, is inhibited, along with the electrochemical performance.

Similar to the $d^0$ and $d^{10}$ cases respectively discussed in Chapters 2 and 3, the stability of both spin cases was evaluated by subjecting each catalyst to 3,000 CV cycles. Pre- and post-CV XPS analysis of HS Mn SAs/1T-MoS$_2$'s is provided in **Figure S5.12** and **Figure S5.13**, respectively. A numerical comparison of the results is provided in **Table S5.6**. LSVs collected before and after CV was performed are provided in **Figures S5.11a, S5.11b**. Both spin configurations exhibit high stability after 3,000 cycles. Surprisingly, while HS Mn SAs/1T-MoS$_2$'s overpotential increases by a mere 12 mV (**Figure S5.11a**), LS Mn SAs/1T-MoS$_2$'s overpotential decreases by 5 mV, indicating that the overpotential improved after running 3,000 CV cycles (**Figure S5.11b**). To gain a better understanding of these intriguing results, surface analysis of each electrode was performed before and after running CVs. After 3,000 cycles, shifts in binding energies of peaks belonging to MoS$_2$ and MoS$_x$ present in HS Mn SAs/1T-MoS$_2$ are negligible (**Figures S5.12, S5.13**). Slight growth of MoO$_3$ (**Figures S5.13b, S5.13c**) and SO$_4^{2-}$ (**Figures S5.13b, S5.13d**) are both observed. Analysis of the Mn 2p spectra of HS Mn SAs/1T-MoS$_2$ shows that 0.40 at% of Mn SAs near the catalyst surface is lost during catalysis and oxidation of the Mn SAs retained from Mn$^{2+}$ to Mn$^{3+}$ is observed (**Figures S5.12a, S5.13a**). Oxidation of the Mn SAs near the catalyst surface provides further support of the observed donation of electrons from the HS Mn SAs to the basal S atoms in 1T-MoS$_2$. Overall, the high stability observed for the HS case is attributed to structural retention of the catalyst material during catalysis.

XPS analysis of LS Mn SAs/1T-MoS$_2$'s is provided in **Figure S5.14** and **Figure S5.15**, respectively. A numerical comparison of the results is provided in **Table S5.7**. Prior to running

CV cycles, surface oxidation of LS Mn SAs/1T-MoS$_2$ is evidenced by the presence of MoO$_3$ in the Mo 3d and O 1s spectra (**Figures S5.14b, S5.14c**). Post-CV XPS analysis confirm that this layer of surface oxidation is removed during catalysis (**Figures S5.15b, S5.15c**). SO$_4^{2-}$ growth is observed in the same manner as it was for the HS case (**Figures S5.15b, S5.15d**). Negligible changes in Mo 3d and S 2p binding energies belonging to MoS$_2$ and MoS$_x$ in LS Mn SAs/1T-MoS$_2$ confirms structural retention of the catalyst material in a similar manner to what was observed for the HS case. Therefore, the same conclusion relating the high stability during catalysis to the retention of the catalyst's structure is made. However, Mn 2p peaks could not be identified after LS Mn SAs/1T-MoS$_2$ was subjected to 3,000 cycles (**Figure S5.15a**). Even after sputtering the catalyst surface for 30 s, the peaks remained absent (**Figure S5.16b**). STEM results previously demonstrated in **Figure 5.2b** suggested that the LS Mn complexes only intercalate near the edges of 1T-MoS$_2$'s nanosheets. Therefore, loss of LS Mn SAs is hypothesized to occur easily during catalysis. Since the bulky ligands attached to the LS Mn SAs may potentially block basal plane active sites, the loss of these species may be the culprit driving the slight improvement in overpotential observed after running 3,000 cycles.

### 5.3.4 Resulting Trend and Factors Driving the Catalytic Activity Observed for the $d^0$, Low Spin $d^4$, High Spin $d^5$, and $d^{10}$ Cases

In order to fully conclude the work completed herein, an analysis of the electrochemical performance of each SA case studied and correspondence with the electronic factors driving these results is necessary. A full comparison of the electrochemical performance of all four SACs studied in this work is provided in **Figure 5.5**. Numerical results are reported altogether in **Table S5.8**.

Altogether, comparison of the LSVs (**Figure 5.5a**), Tafel slopes (**Figure 5.5b**), and EIS (**Figures 5.5c, 5.5d**) demonstrate a consistent trend between HER performance and electronic occupation
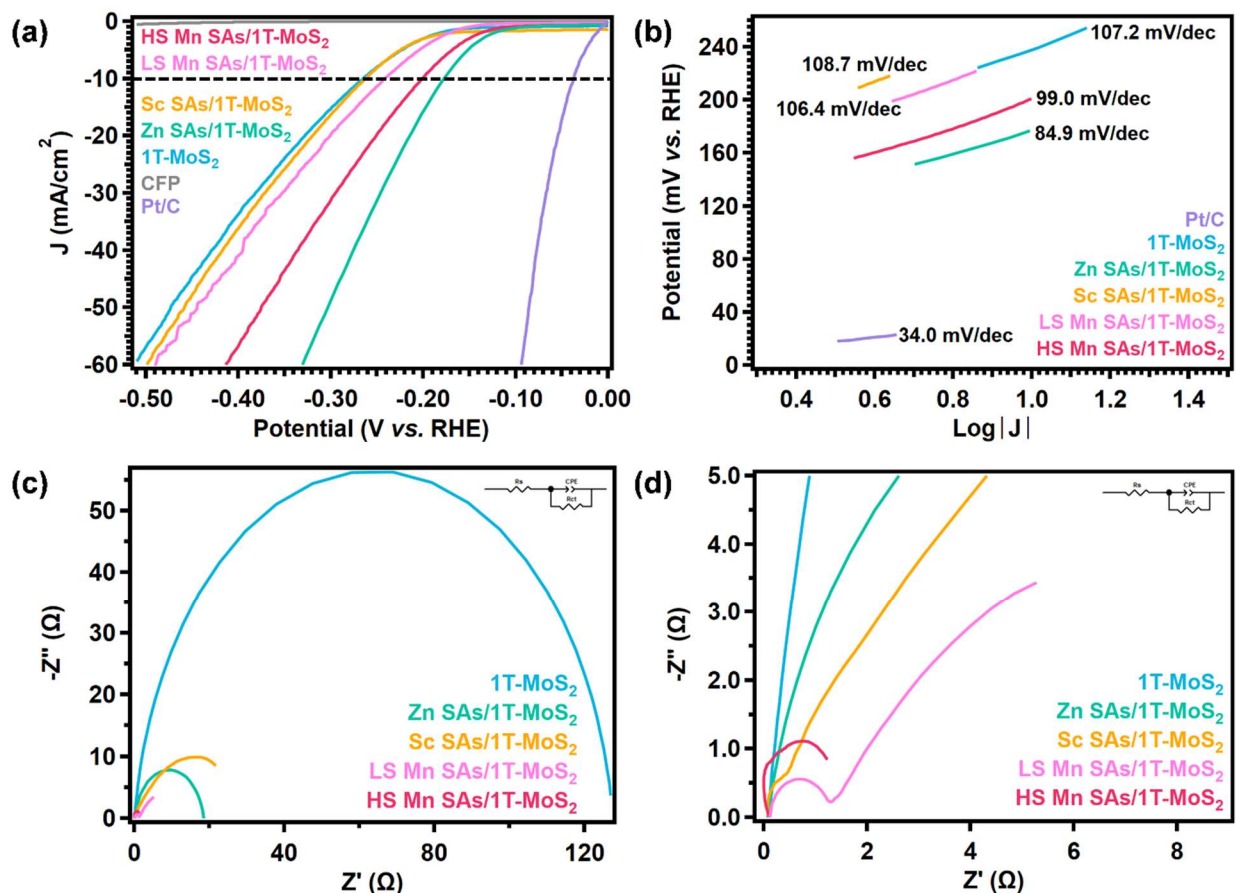


**Figure 5.5:** Electrochemical comparison of HS Mn SAs/1T-MoS$_2$, LS Mn SAs/1T-MoS$_2$, Sc SAs/1T-MoS$_2$, Zn SAs/1T-MoS$_2$, 1T-MoS$_2$, and Pt/C (20%).
Measurements were collected in N$_2$-saturated 0.5 M H$_2$SO$_4$ within a three-electrode configuration. **(a)** HER polarization curves. **(b)** Tafel plots. **(c)** EIS results fitted to the equivalent circuit shown. **(d)** Zoomed in region of EIS data to visualize results for HS Mn SAs/1T-MoS$_2$, LS Mn SAs/1T-MoS$_2$, and Sc SAs/1T-MoS$_2$ more clearly.

of d-orbitals belonging to guest metals spatially confined near basal plane active sites in 1T-MoS$_2$.

In 2018, Benson *et. al.* employed covalent chemical functionalization to modify the electronic properties of 1T-MoS$_2$.[195] By functionalizing 1T-MoS$_2$ with a series of organic phenyl rings ranging from electron withdrawing to electron donating character, the authors discovered that the electronic nature of these functional groups can influence HER kinetics on the 1T-MoS$_2$ substrate. According to their results, 1T-MoS$_2$ covalently bonded to the most electron donating functional

group ($p$-(CH$_3$CH$_2$)$_2$NPh-MoS$_2$) studied yielded the best HER performance of the various cases studied. These results correspond well with the trend in electron donating character observed with the four guest metal cases studied in this work.

As the electronic occupation of d-orbitals belonging to guest metals confined within active site microenvironments increases, the catalyst's HER performance increases. The d$^0$ case, Sc SAs/1T-MoS$_2$, yielded the worst catalytic performance, in which 1T-MoS$_2$'s overpotential decreased by only 3 mV. The detailed investigation of the d$^0$ case described in Chapter 3 brought us to conclude that the lack of electron donation from the Sc SAs to S atoms in 1T-MoS$_2$ and its unsaturated MoS$_x$ component led us to this lack of change in HER performance. The LS Mn SAs residing near the catalyst surface exhibited a d$^4$ electron configuration, induced a 0.12 eV downshift in MoS$_x$'s S 2p doublet, and decreased 1T-MoS$_2$'s overpotential by 21 mV. The HS Mn SAs located near the catalyst surface retained their d$^5$ electron configuration, downshifted MoS$_x$'s S 2p doublet by 0.17 eV, and decreased 1T-MoS$_2$'s overpotential by 64 mV.

Lastly, our d$^{10}$ case, Zn SAs/1T-MoS$_2$, downshift the S 2p doublet belonging to unsaturated MoS$_x$ by 0.19 eV, and reduced the overpotential of 1T-MoS$_2$ by 88 mV, which was the greatest reduction in overpotential of all the cases studied. DFT calculations employed to analyze changes in HER kinetics induced by the intercalated Zn SAs demonstrated that the spatial confinement of the Zn SAs yields a thermoneutral $\Delta G_{H^*}$ value (0.00294 eV compared to -5.40308 eV generated by a trilayer of 1T-MoS$_2$, see **Figure 3.5b** in Chapter 3). As a result, HER kinetics are predicted to be much more facile when this d$^{10}$ guest metal is confined within 1T-MoS$_2$ active site microenvironments. Based on these results, we draw the following conclusions. Electronic donation from the SAs to S active sites increases as the electronic occupation of d-orbitals belonging to SAs increases. This electron donation facilitates HER kinetics and improves catalytic

performance. Thus, we conclude that intercalated SAs that maintain higher d-orbital occupations are required to drive electron donation to S active sites and enhance HER performance accordingly (**Figure 5.6**).

## 5.4 Conclusions

$Sc^{3+} = d^0$  $\qquad$  LS $Mn^{3+} = d^4$  $\qquad$  HS $Mn^{2+} = d^5$  $\qquad$  $Zn^{2+} = d^{10}$

$d_{x^2-y^2}$ $d_{z^2}$ $d_{xy}$ $d_{yz}$ $d_{xz}$  $\qquad$  $d_{x^2-y^2}$ $d_{z^2}$ $d_{xy}$ $d_{yz}$ $d_{xz}$  $\qquad$  $d_{x^2-y^2}$ $d_{z^2}$ $d_{xy}$ $d_{yz}$ $d_{xz}$  $\qquad$  $d_{x^2-y^2}$ $d_{z^2}$ $d_{xy}$ $d_{yz}$ $d_{xz}$

**Increased d-orbital occupation of confined metals linked to enhanced catalytic performance**

**Figure 5.6:** Observed trend between d-orbital occupation of confined SAs and HER performance.

Comparing all four cases of SA d-orbital occupations, we observe the following. Electrochemically, a decrease in overpotential is observed as electronic occupation of d-orbitals increases. Electronically, as the d-orbital occupation of SAs increases, the number of electrons donated to nearby active sites increases. This electron donation facilitates HER kinetics by making the $H^*$ adsorption/$H_2$ desorption process easier to occur. As a result, lower overpotentials are required to drive HER. Altogether, this work addresses a major knowledge gap in confinement catalysis by identifying the relationship between the guest metal's valence electrons and catalytic performance. Since quantum confinement is a phenomenon present in all nanomaterials, intercalation strategies and metal confinement effects may be used to enhance electronic and structural properties in all types of nanomaterials. It is well known that current efforts to develop novel materials with enhanced properties requires the incorporation of nanomaterials to achieve these goals. Properties of 2D materials can be synthetically controlled by inducing atomic modifications such as defects and dopants. Therefore, the insight gained from this work reveals synthetic methods that enable precise control over properties in nanomaterials, which in turn can

maximize the performance of novel materials, devices, and applications sought after by the sci-tech industry today.

## 5.5 Materials and Methods

### 5.5.1 Chemicals

Ammonium heptamolybdate tetrahydrate [$(NH_4)_6Mo_7O_{24}\cdot6H_2O$, 99% Alfa Aesar], thioacetamide ($CH_3CSNH_2$, 99$^+$% Acros Organics), urea ($H_2NCONH_2$, Sigma-Aldrich), manganese(II) chloride tetrahydrate ($MnCl_2\cdot4H_2O$, 99$^+$% Acros Organics), bromopentacarbonylmanganese(I) ($Mn(CO)_5Br$, 98% Alfa Aesar), 2,2'-dipyridyl (Oakwood Chemicals), and diethyl ether (Fisher Scientific) were used without further purification.

### 5.5.2 Synthesis of HS Mn SAs/1T-MoS$_2$

First, 50 mg of $(NH_4)_6Mo_7O_{24}\cdot6H_2O$, 80 mg of $CH_3CSNH_2$, 40 mg of $H_2NCONH_2$, either 5, 10, or 15 mg of $ScCl_3\cdot6H_2O$, and 10 mL of deionized (DI) water were combined in a 25 mL autoclave and sonicated until they were fully dissolved. Once dissolved, the autoclave was sealed within a hydrothermal reactor and heated at 180°C for 24 h. Once the reactor cooled to room temperature, the solution of crude product was transferred to 15 mL conical centrifuge tubes. The crude product was washed and centrifuged three times: once with DI water, once with ethyl alcohol, and once with acetone. The solutions were centrifuged for 10 min at ~4,000 rpm in between each washing step and the supernatant layer was removed after each centrifugation step. After washing, the purified product was dried in a vacuum oven at ~80°C and ~25 mmHg for 24 h. The dried and purified product was finely ground with a mortar and pestle and stored under ambient conditions.

### 5.5.3 Synthesis of Mn(bpy)(CO)₃Br

First, 2 mmol of Mn(CO)$_5$Br and 2 mmol 2,2'-dipyridyl (which same compound as 2,2'-bypridine) were added to a 100 mL three-prong round bottom flask. The flask was filled halfway with diethyl ether and attached to a reflux apparatus and heating mantle. The reagents were refluxed in ether for 30 mins (while stirring to prevent bumping). The product precipitates immediately as fine orange crystals. The mother liquor was then cooled to -80°C using liquid N$_2$ to complete precipitation. The product was vacuum filtered, washed twice with 30 mL of ice cold diethyl ether, and dried under vacuum. The final product was wrapped in aluminum foil to protect it from light and stored in a refrigerator when not in use.

### 5.5.4 Synthesis of LS Mn SAs/1T-MoS₂

To start, 50 mg of 1T-MoS$_2$, 15 mL DI water, and 35 mL ethanol were combined and vigorously stirred at room temperature throughout the entire synthesis. Next, a solution of LS Mn SAs was prepared by adding 6.0 mL of acetonitrile to 10 mg of Mn(bpy)(CO)$_3$Br and sonicating the solution until completely dissolved. This solution was transferred to a syringe and attached to a syringe pump apparatus which was utilized to inject the LS Mn SAs solution into the 1T-MoS$_2$ dispersion. During this step, the entire solution of Mn(bpy)(CO)$_3$Br was injected into the 1T-MoS$_2$ dispersion at a 10 µL/min flow rate. After the injection was complete, the solution continued to be vigorously stirred at room temperature for seven days. Afterwards, the solution was transferred to 15 mL Conical Centrifuge Tubes, centrifuged for 10 min. at ~4,000 rpm, washed with DI water, and centrifuged again for the same amount of time. The supernatant layer was removed after each

centrifugation step. The purified product was dried in a vacuum oven at ~80˚C and ~25 inHg for 24 h, then finely ground with a mortar and pestle and stored under ambient conditions.

*5.5.5 Characterization*

HAADF-STEM images were acquired using JEOL Grand ARM equipped with two spherical aberration correctors at 300 kV by a convergence semiangle of 22 mrad and inner and outer collection angles of 83 and 165 mrad, respectively. Energy dispersive X-ray spectroscopy (EDX) was conducted by using JEOL dual EDX detectors and a specific high count analytical TEM holder. XPS measurements were collected with a PHI 5600 XPS system equipped with a monochromatic Al Kα X-ray source and Omni Focus III lens operating at 250 W, 14 kV, 600 $\mu m^2$ spot size, and a maximum base pressure of $5 \times 10^{-9}$ Torr. A 90° angle was maintained between the X-ray source and analyzer. Survey spectra were collected with 117.4 eV pass energy, 1.0 eV/step, and 50 μs dwell time. Multiplexes were collected using 11.75 eV pass energy, 0.100 eV/step, and 50 μs dwell time. The instrument was calibrated to Au $4f_{7/2}$ = 84.00 eV and Cu $2p_{3/2}$ = 932.67 eV immediately prior to collecting the data. All spectra were calibrated to C 1s = 284.8 eV.[180] Multiplexes were fitted by using IgorPro XPS Tools Software. A Shirley background and 80% Lorentzian–Gaussian were employed for all peak analyses. Raman spectra were recorded using a Thermo Scientific DXR Raman Spectrometer employing an Ar-ion laser operating at 532 nm, a 50 μm pinhole, and 3.0 mW laser power. XRD patterns were measured using the Bruker D2 PHASER XE-T benchtop XRD with Cu–Kα radiation (λ = 1.5406 Å) at 30 kV and 10 mA, step size = 0.02˚, and scan step time = 1.0 s/step. The measurement range was from 6° to 80° in terms of 2θ. FTIR spectra were collected using a PERKIN ELMER CE-440. EPR spectra were analyzed with the Bruker EMXplus X-band CW EPR spectrometer system operating at a frequency of 9.36

GHz. Field frequency modulation, modulation amplitude, and microwave power were set to 100 kHz, 0.6 mT, and  0.02 mW, respectively, in every case to avoid saturation effects. EPR measurements were recorded at 293 K and 40 K.

*5.5.6 Electrochemical Measurements*

All electrochemical measurements were conducted in $N_2$-saturated 0.5 M $H_2SO_4$ electrolytic solution within a three-electrode configuration. A CHI 660E electrochemical workstation was used for all electrochemical measurements. Graphite was employed as the counter electrode and Ag/AgCl (3 M NaCl, BASI) as the reference electrode. Electrodes were prepared by drop casting 100 µL of catalyst ink (20 µL each time, repeated 5 times) onto a 1×2 $cm^2$ piece of CFP. The loading of catalysts on CFP is ~1 $mg/cm^2$. All potentials reported were calibrated with respect to the Ag/AgCl reference electrode in acidic media (0.5 M $H_2SO_4$) using **Equation (2.2)**.

LSVs were conducted under ambient conditions from 0 to -0.8 V with 5 mV/s scan rate, 1 mV step size, and 0.001 A/V sensitivity. Onset potentials were extracted from the LSVs and defined as the potential at which the current began to increase (0.05 $mA/cm^2$). Overpotentials were measured at -10 $mA/cm^2$. EIS measurements were performed at -0.45 V with 0.005 V variation in the frequency range of 1-$10^5$ Hz and 12 steps per decade. The stability of Sc SAs/1T-$MoS_2$ was evaluated by running CV at a 0.01 V/s scan rate for 375 cycles from 0 to -0.43 V, followed by comparison of the initial and final LSV curves.

## 5.6 Acknowledgements

**Figure S5.1:** HS and LS $d^5$ orbital configurations under octahedral coordination geometry.



**Figure S5.2:** Molecular models of HS Mn SAs/1T-MoS$_2$ and LS Mn SAs/1T-MoS$_2$.

**Figure S5.3:** EDX mappings of HS Mn SAs/1T-MoS$_2$.



**Figure S5.4:** Structural characterization and peak assignments of HS Mn SAs/1T-MoS$_2$ and LS Mn SAs/1T-MoS$_2$.
**(a)** Raman spectra. **(b)** FTIR spectrum.
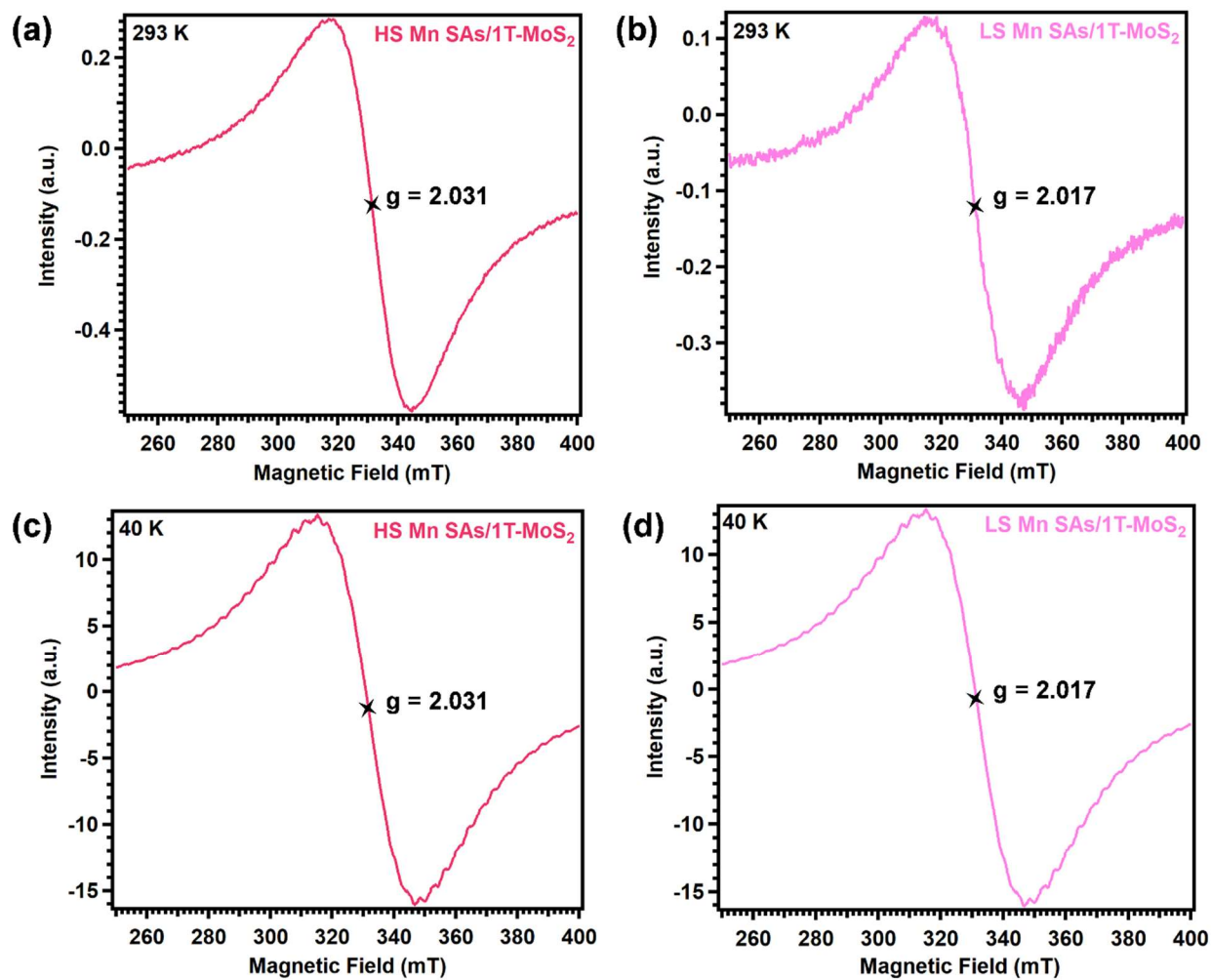
**Figure S5.5:** EPR analysis of HS Mn SAs/1T-MoS$_2$ and LS Mn SAs/1T-MoS$_2$ at **(a-b)** 293 K and **(c-d)** 40 K.
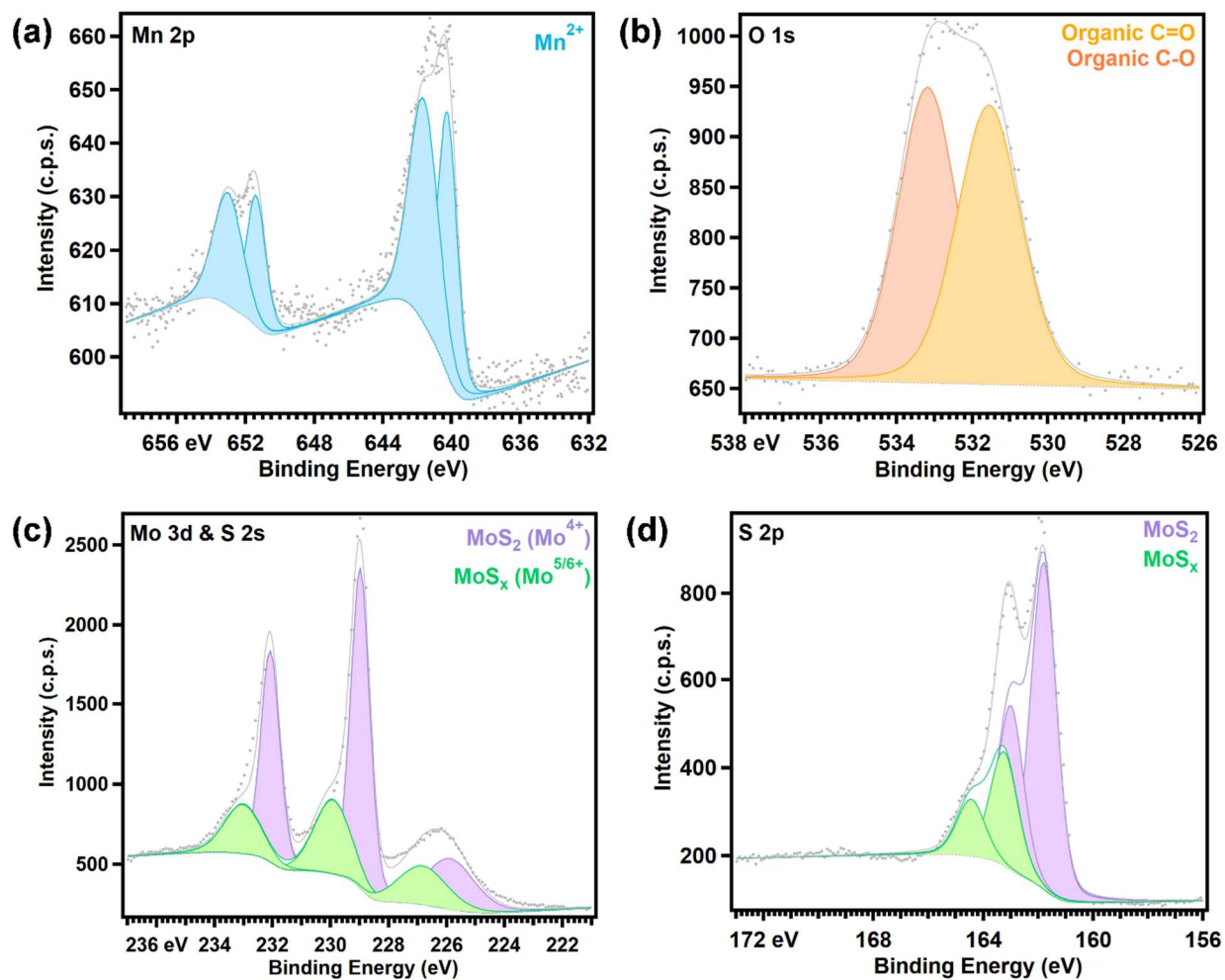
**Figure S5.6:** XPS data and peak assignments of HS Mn SAs/1T-MoS$_2$.
**(a)** Mn 2p spectrum. **(b)** O 1s spectrum. **(c)** Mo 3d and S 2s spectra. **(d)** S 2p spectrum.
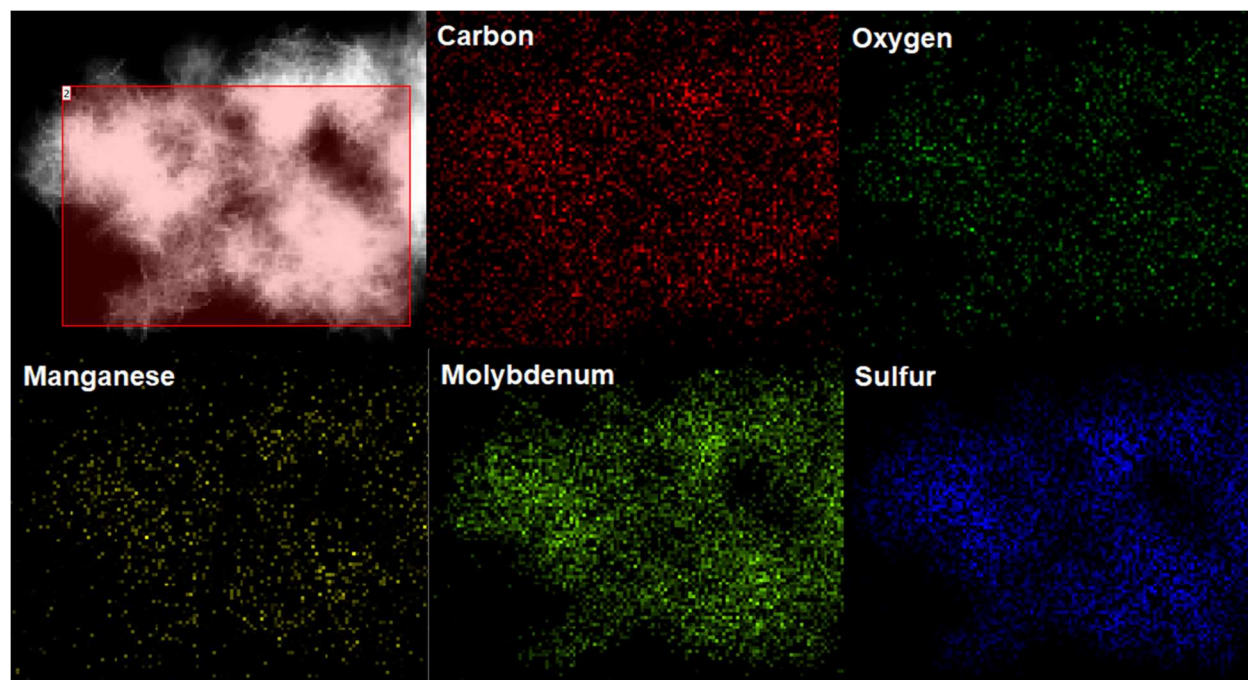
**Figure S5.7:** EDX mappings of LS Mn SAs/1T-MoS$_2$.
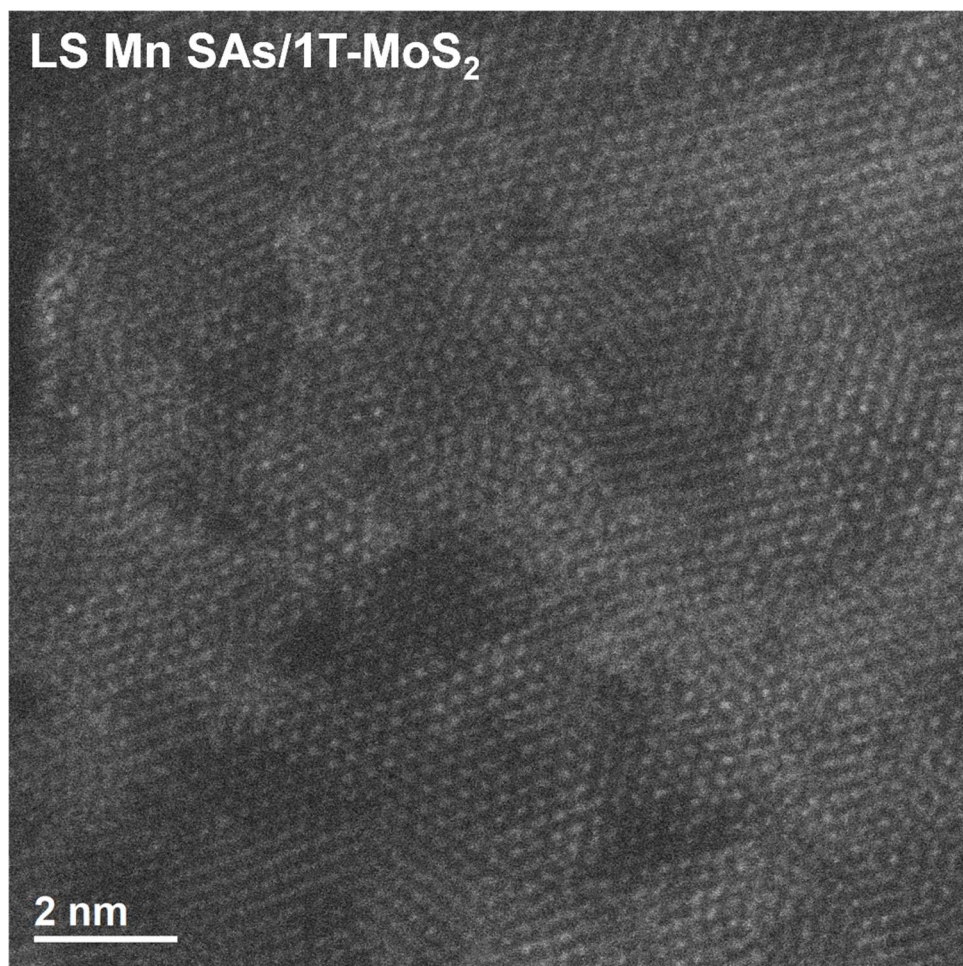
**Figure S5.8:** Additional HAADF-STEM image of LS Mn SAs/1T-MoS$_2$ demonstrating uniform lattice structure in the bulk region of the catalyst material.
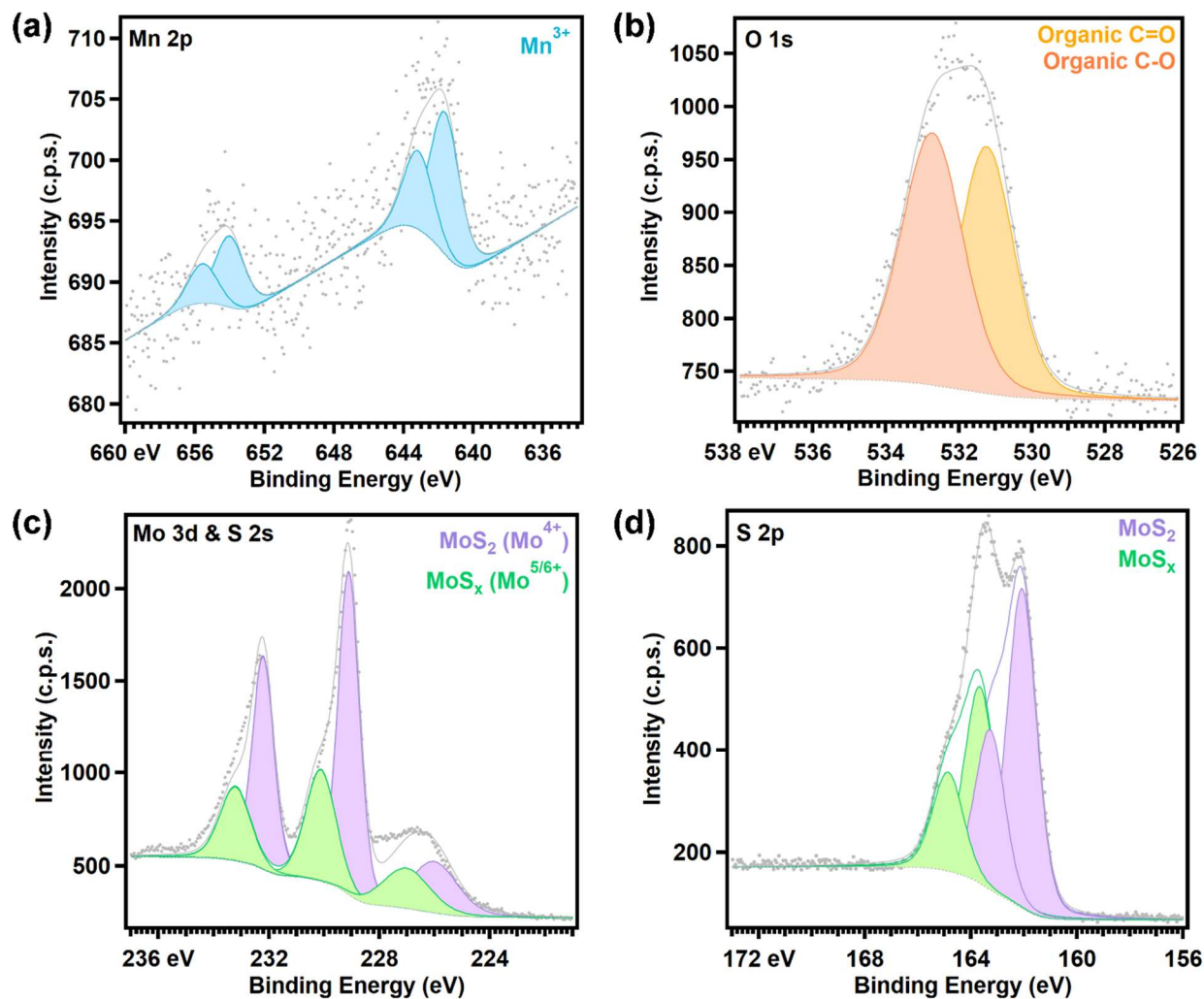
**Figure S5.9:** XPS data and peak assignments for LS Mn SAs/1T-MoS$_2$.
**(a)** Mn 2p spectrum. **(b)** O 1s spectrum. **(c)** Mo 3d and S 2s spectra. **(d)** S 2p spectrum.
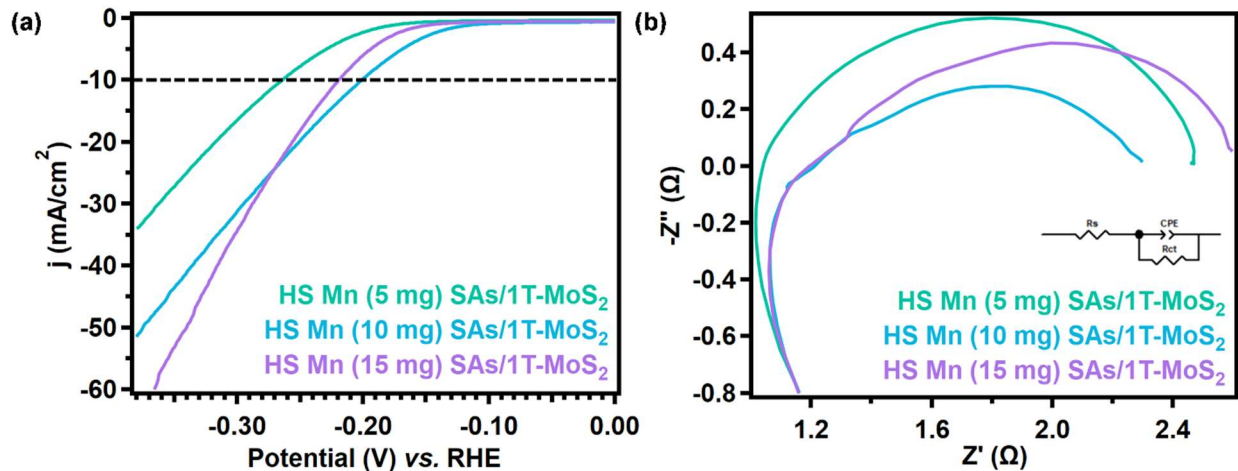
**Figure S5.10:** Electrochemical analysis of how the HER performance of 1T-MoS$_2$ changes as the quantity of HS Mn SAs increases.
These measurements were performed within a standard three-electrode configuration with N$_2$-saturated 0.5 M H$_2$SO$_4$ as the electrolyte. **(a)** LSVs. **(b)** EIS fitted to the equivalent circuit shown.
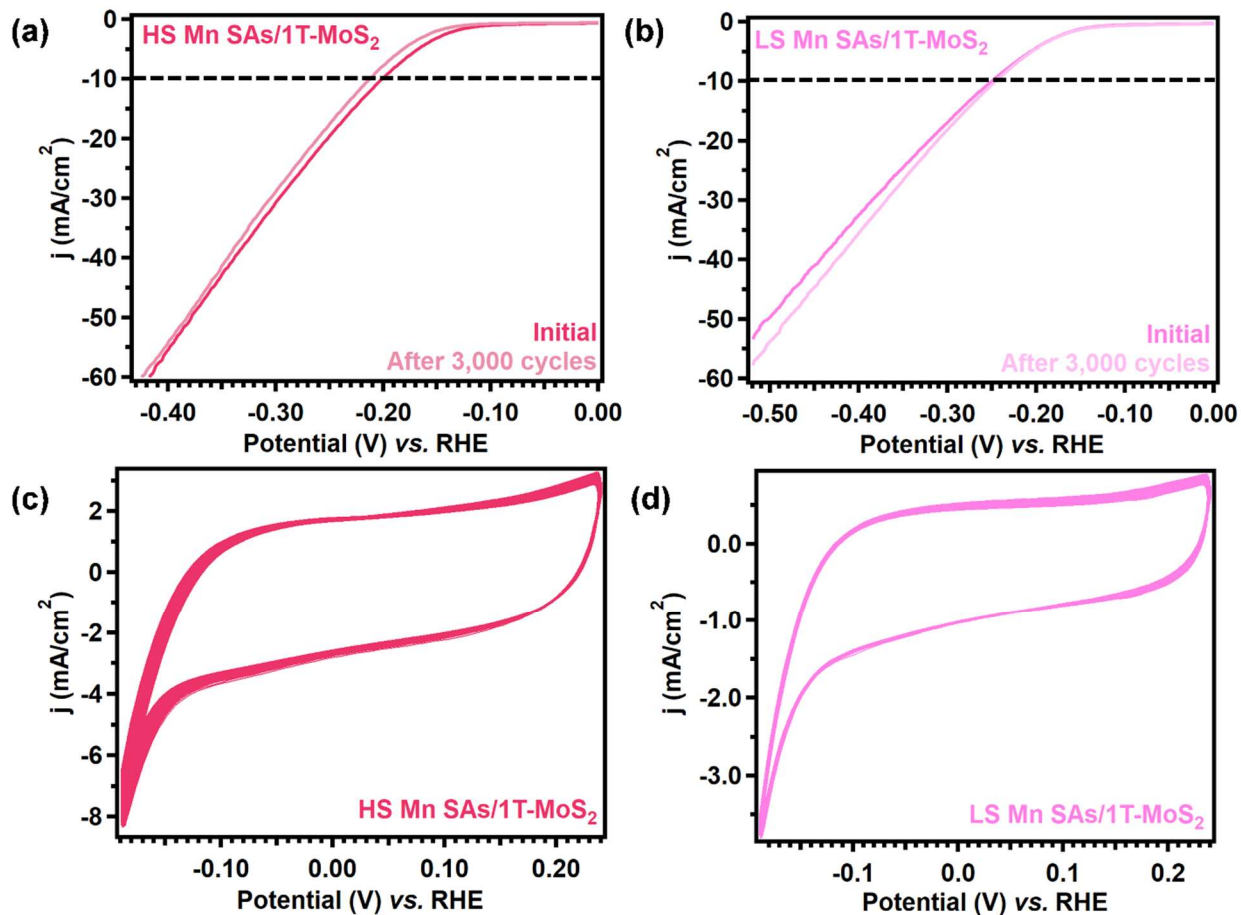
**Figure S5.11:** Stability evaluation of **(a,c)** HS Mn SAs/1T-MoS$_2$ and **(b,d)** LS Mn SAs/1T-MoS$_2$. **(a-b)** LSVs for each catalyst measured before and after running 3,000 CV cycles. **(c-d)** Corresponding CVs.
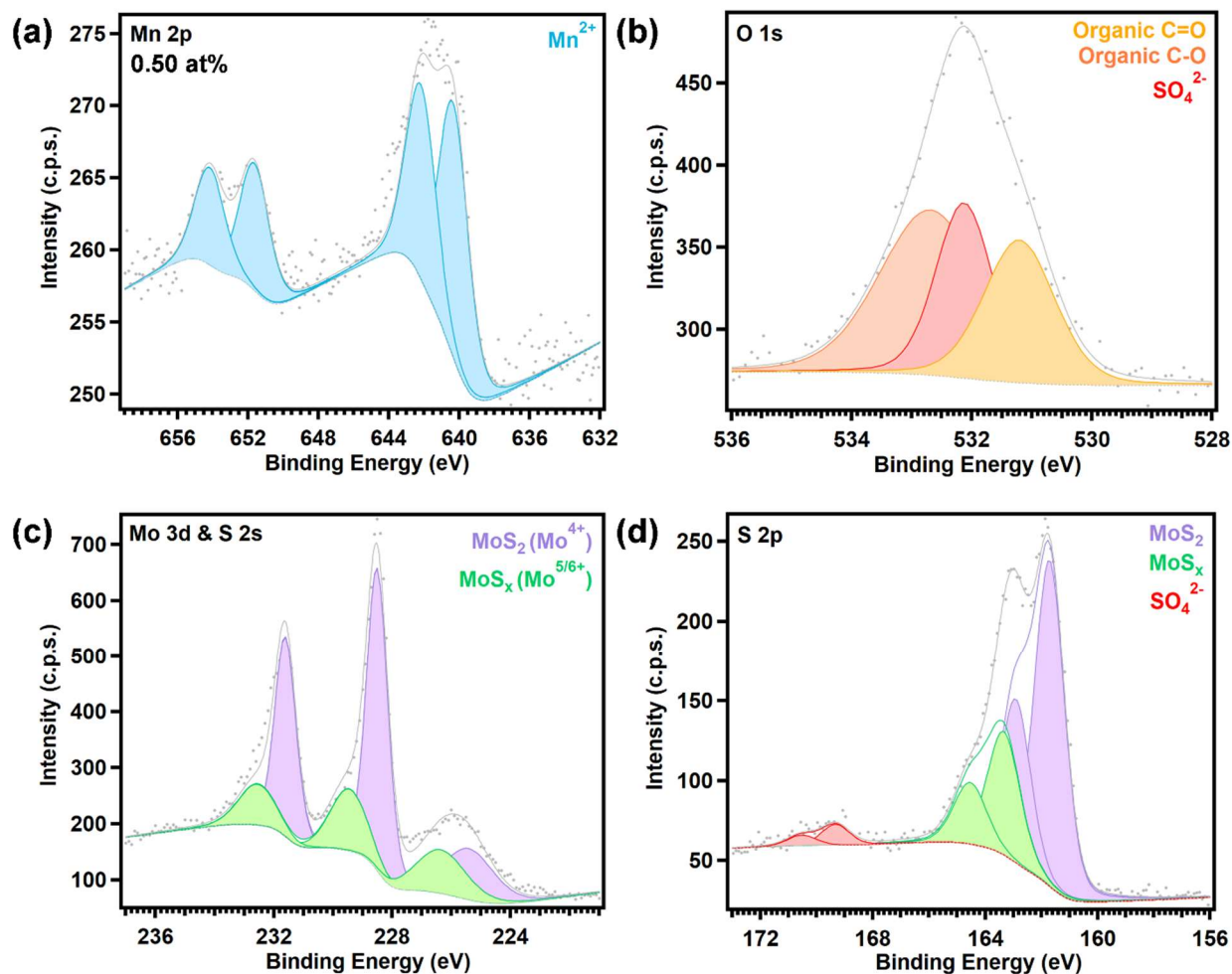
**Figure S5.12:** XPS data and peak assignments for HS Mn SAs/1T-MoS$_2$ on CFP before running 3,000 CV cycles.
**(a)** Mn 2p spectrum. **(b)** O 1s spectrum. **(c)** Mo 3d and S 2s spectra. **(d)** S 2p spectrum.
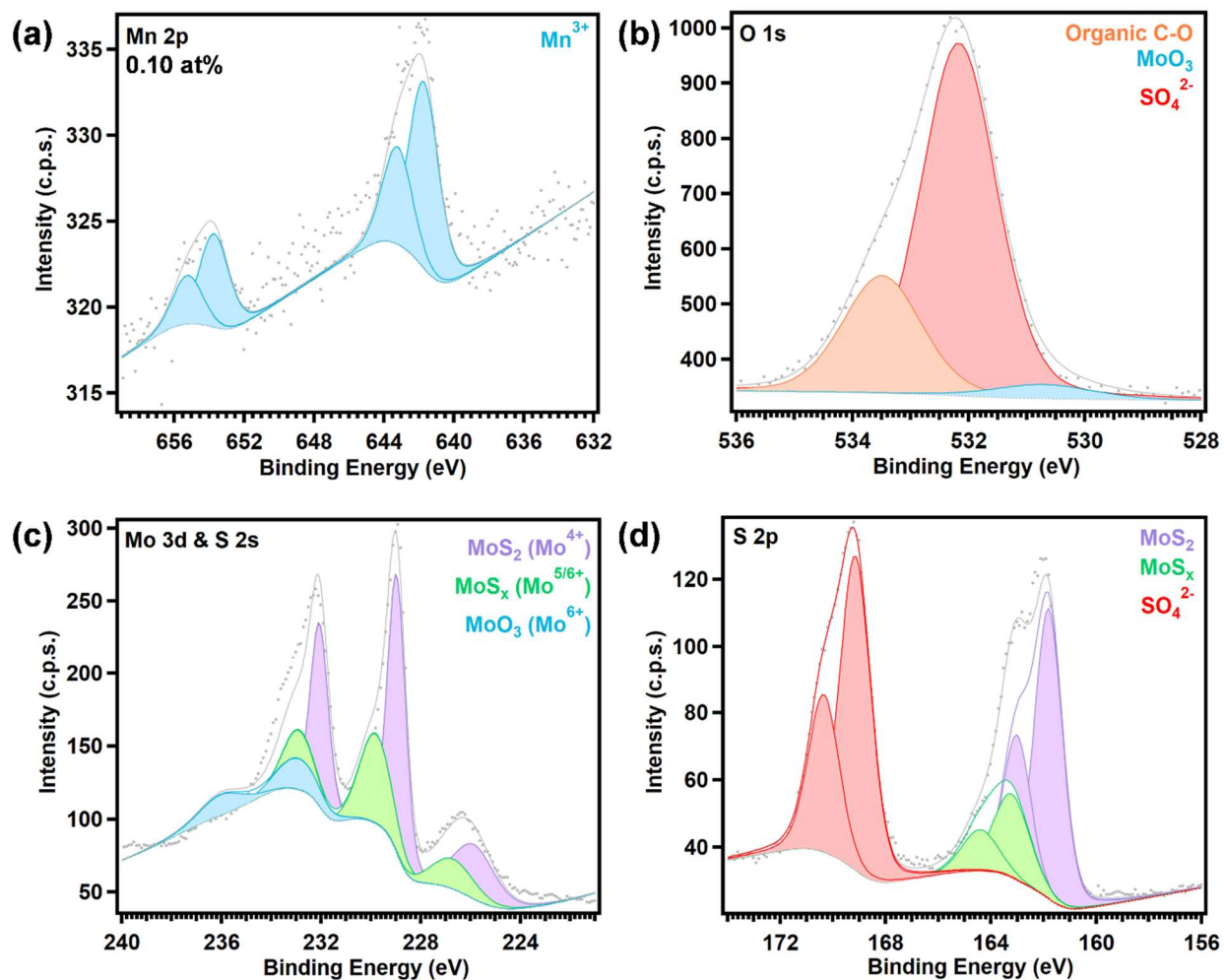
**Figure S5.13:** XPS data and peak assignments for HS Mn SAs/1T-MoS$_2$ on CFP after running 3,000 CV cycles.
**(a)** Mn 2p spectrum. **(b)** O 1s spectrum. **(c)** Mo 3d and S 2s spectra. **(d)** S 2p spectrum.
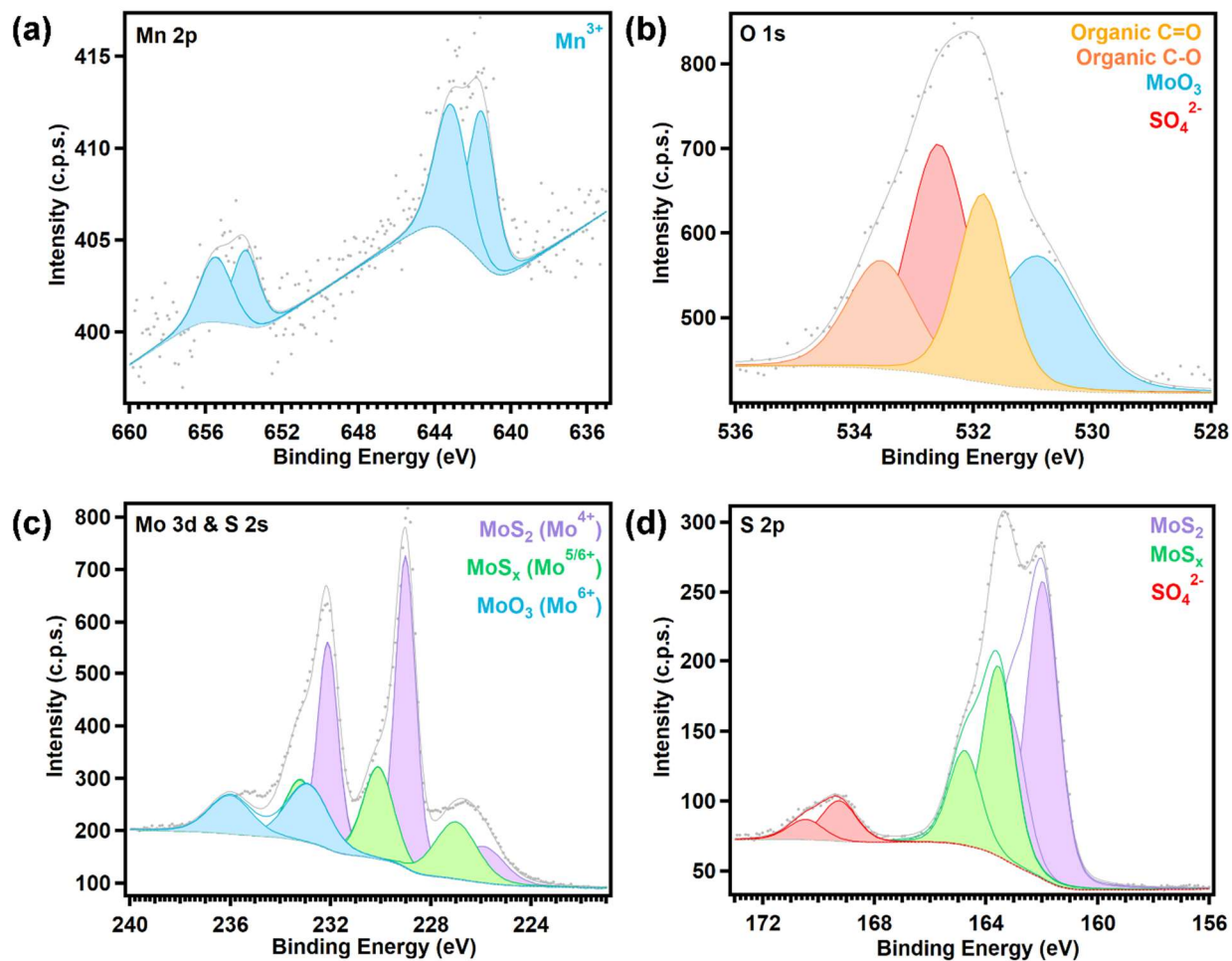
**Figure S5.14:** XPS data and peak assignments for LS Mn SAs/1T-MoS$_2$ on CFP before running 3,000 CV cycles.
**(a)** Mn 2p spectrum. **(b)** O 1s spectrum. **(c)** Mo 3d and S 2s spectra. **(d)** S 2p spectrum.
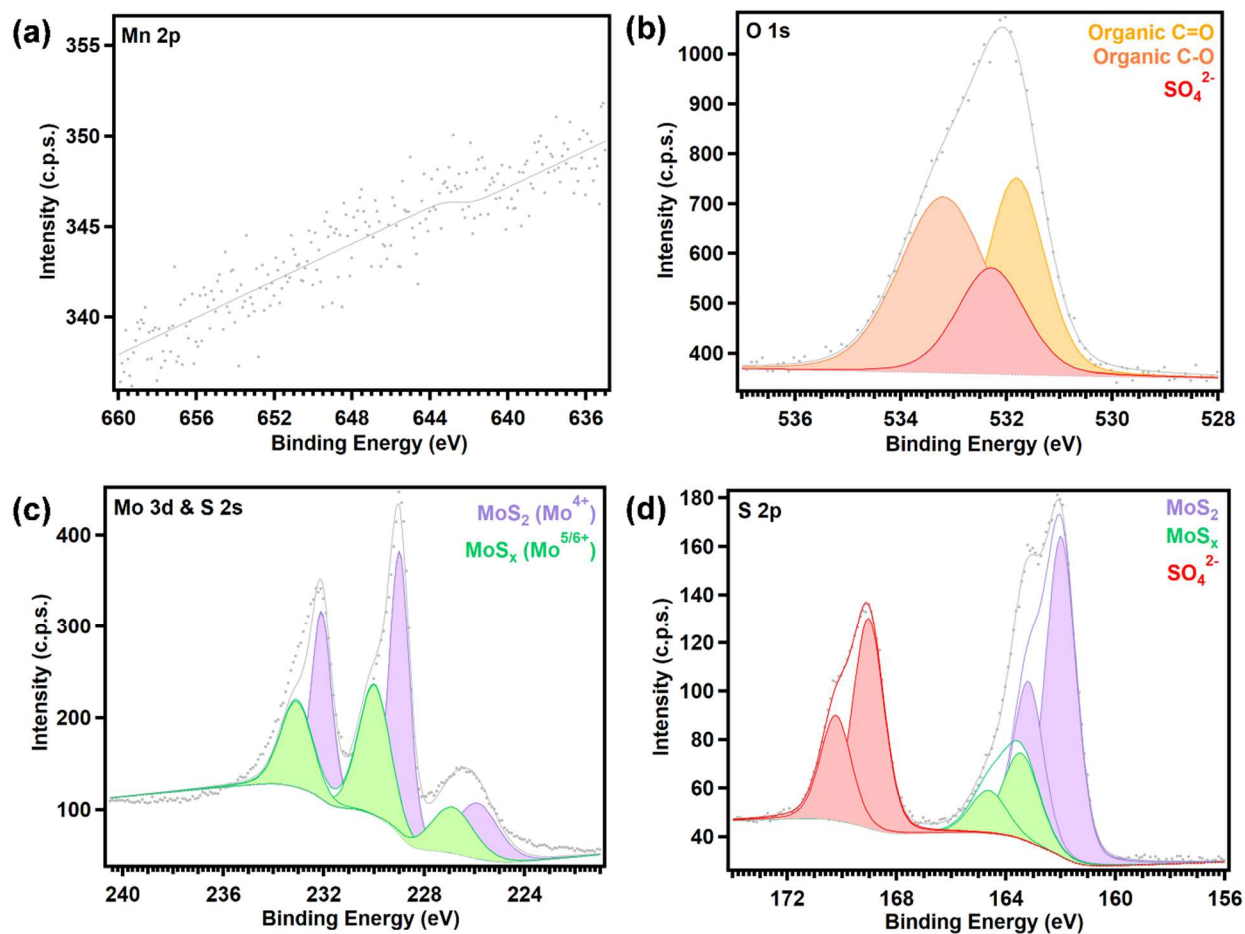
**Figure S5.15:** XPS data and peak assignments for LS Mn SAs/1T-MoS$_2$ on CFP after running 3,000 CV cycles.
**(a)** Mn 2p spectrum. **(b)** O 1s spectrum. **(c)** Mo 3d and S 2s spectra. **(d)** S 2p spectrum.
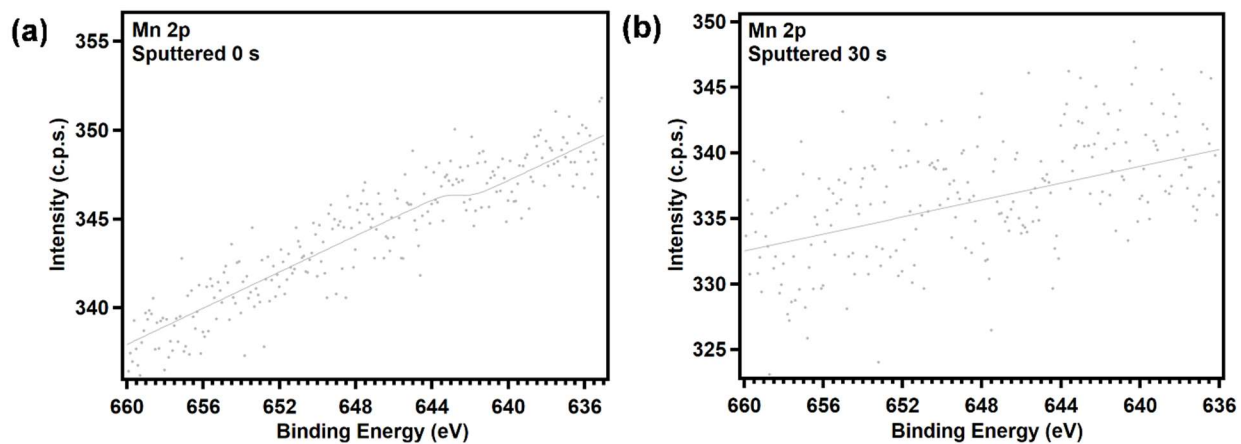
**Figure S5.16:** XPS analysis of the Mn 2p spectrum for LS Mn SAs/1T-MoS$_2$ after running 3,000 CV cycles after sputtering the sample for **(a)** with 0 s and **(b)** 30 s.

**Table S5.1:** Raman peak assignments for HS Mn SAs/1T-MoS$_2$, LS Mn SAs/1T-MoS$_2$, and 1T-MoS$_2$

| Peak Positions (cm$^{-1}$) | | | Peak Assignments |
|---|---|---|---|
| 1T-MoS$_2$ | HS Mn SAs/1T-MoS$_2$ | LS Mn SAs/1T-MoS$_2$ | |
| 113 | 113 | 115 | TA |
| 125 | 123 | 125 | TA |
| 149 | 147 | 150 | J$_1$ |
| 195 | 194 | 196 | LA |
| 213 | 214 | 215 | LA |
| 237 | 236 | 240 | J$_2$ |
| 284 | 283 | 284 | E$_{1g}$ |
| 336 | 335 | 337 | J$_3$ |
| 377 | 375 | 378 | E$^1_{2g}$ |
| 402 | 401 | 404 | A$_{1g}$ |

**Table S5.2:** Assignments of experimental g-values for HS Mn SAs/1T-MoS$_2$ and LS Mn SAs/1T-MoS$_2$

| g-values | | Assignment |
|---|---|---|
| HS Mn SAs/1T-MoS$_2$ | LS Mn SAs/1T-MoS$_2$ | |
| 2.031 | | Paramagnetic S in short chains |
| | 2.017 | Mo$^{5+}$ species coordinated to S atoms |

**Table S5.3:** XPS data and peak assignments for HS Mn SAs/1T-MoS$_2$, LS Mn SAs/1T-MoS$_2$, and 1T-MoS$_2$

| Peak | Binding Energy (eV) | | | Peak Assignment |
|---|---|---|---|---|
| | 1T-MoS$_2$ | HS Mn SAs/1T-MoS$_2$ | LS Mn SAs/1T-MoS$_2$ | |
| Mn 2p$_{3/2}$ | -- | 640.24 | -- | Mn$^{2+}$ |
| | -- | 641.62 | -- | Mn$^{2+}$ |
| | -- | -- | 641.62 | Mn$^{3+}$ |
| | -- | -- | 643.17 | Mn$^{3+}$ |
| Mn 2p$_{1/2}$ | -- | 651.39 | -- | Mn$^{2+}$ |
| | -- | 653.02 | -- | Mn$^{2+}$ |
| | -- | -- | 654.00 | Mn$^{3+}$ |
| | -- | -- | 655.54 | Mn$^{3+}$ |
| Mo 3d$_{5/2}$ | 229.05 | 228.98 | 229.05 | MoS$_2$, Mo$^{4+}$ |
| | 229.93 | 229.93 | 229.94 | MoS$_x$, Mo$^{5/6+}$ |
| | -- | -- | -- | MoO$_3$, Mo$^{6+}$ |
| Mo 3d$_{3/2}$ | 232.15 | 232.08 | 232.15 | MoS$_2$, Mo$^{4+}$ |
| | 233.03 | 233.03 | 232.94 | MoS$_x$, Mo$^{5/6+}$ |
| | -- | -- | -- | MoO$_3$, Mo$^{6+}$ |
| S 2p$_{3/2}$ | 161.90 | 161.80 | 161.98 | MoS$_2$, S$^{2-}$ |
| | 163.45 | 163.28 | 163.33 | MoS$_x$, S$^{2-}$ |
| | -- | -- | -- | SO$_4$$^{2-}$ |
| S 2p$_{1/2}$ | 163.10 | 163.00 | 163.18 | MoS$_2$, S$^{2-}$ |
| | 164.65 | 164.48 | 164.53 | MoS$_x$, S$^{2-}$ |
| | -- | -- | -- | SO$_4$$^{2-}$ |
| S 2s | 225.95 | 225.88 | 225.95 | MoS$_2$ |
| | 226.83 | 226.83 | 226.84 | MoS$_x$ |
| O 1s | -- | -- | -- | MoO$_3$ |
| | 531.20 | 531.56 | 531.24 | Organic C=O |
| | -- | -- | -- | SO$_4$$^{2-}$ |
| | 532.48 | 533.18 | 532.73 | Organic C-O |

**Table S5.4:** Comparison of the overpotentials and Tafel slopes observed for HS Mn SAs/1T-MoS$_2$, LS Mn SAs/1T-MoS$_2$, 1T-MoS$_2$, Pt/C, and CFP

| Sample | Overpotential (mV *vs.* RHE) | Tafel slope (mV/dec) |
|---|---|---|
| CFP | -- | -- |
| Pt/C | 37 | 34.0 |
| 1T-MoS$_2$ | 265 | 107.2 |
| HS Mn (5 mg) SAs/1T-MoS$_2$ | 264 | -- |
| HS Mn (10 mg) SAs/1T-MoS$_2$ | 201 | 99.0 |
| HS Mn (15 mg) SAs/1T-MoS$_2$ | 219 | -- |
| LS Mn SAs/1T-MoS$_2$ | 241 | 106.4 |

**Table S5.5:** Equivalent circuit fittings for EIS data reported for HS Mn SAs/1T-MoS$_2$ and LS Mn SAs/1T-MoS$_2$

| Sample | R$_s$ ($\Omega$) | R$_{ct}$ ($\Omega$) | CPE-T | CPE-P | A$_w$ ($\Omega$ s$^{-1/2}$) |
|---|---|---|---|---|---|
| 1T-MoS$_2$ | 2.289 | 127.5 | 0.0247 | 0.923 | -- |
| HS Mn (5 mg) SAs/1T-MoS$_2$ | 1.113 | 1.226 | $6.09 \times 10^{-4}$ | 0.941 | -- |
| HS Mn (10 mg) SAs/1T-MoS$_2$ | 1.397 | 0.0186 | 0.767 | 0.972 | -- |
| HS Mn (15 mg) SAs/1T-MoS$_2$ | 1.371 | 1.445 | 0.00986 | 0.755 | -- |
| LS Mn SAs/1T-MoS$_2$ | 0.125 | 1.292 | $5.72 \times 10^{-5}$ | 0.972 | 1.268 |

**Table S5.6:** XPS data and peak assignments for HS Mn SAs/1T-MoS$_2$ before and after collecting 3,000 CV scans

| Peak | HS Mn SAs/1T-MoS$_2$ | | Peak Assignment |
| --- | --- | --- | --- |
| | Pre-CV | Post-CV | |
| Mn 2p$_{3/2}$ | 640.33 | -- | Mn$^{2+}$ |
| | 642.17 | -- | Mn$^{2+}$ |
| | -- | 641.71 | Mn$^{3+}$ |
| | -- | 643.23 | Mn$^{3+}$ |
| Mn 2p$_{1/2}$ | 651.63 | -- | Mn$^{2+}$ |
| | 654.17 | -- | Mn$^{2+}$ |
| | -- | 653.71 | Mn$^{3+}$ |
| | -- | 655.23 | Mn$^{3+}$ |
| Mo 3d$_{5/2}$ | 228.88 | 228.97 | MoS$_2$, Mo$^{4+}$ |
| | 229.83 | 229.82 | MoS$_x$, Mo$^{5/6+}$ |
| | -- | 232.93 | MoO$_3$, Mo$^{6+}$ |
| Mo 3d$_{3/2}$ | 231.98 | 232.07 | MoS$_2$, Mo$^{4+}$ |
| | 232.93 | 232.92 | MoS$_x$, Mo$^{5/6+}$ |
| | -- | 236.03 | MoO$_3$, Mo$^{6+}$ |
| S 2p$_{3/2}$ | 161.71 | 161.81 | MoS$_2$, S$^{2-}$ |
| | 163.34 | 163.22 | MoS$_x$, S$^{2-}$ |
| | 169.33 | 169.15 | SO$_4^{2-}$ |
| S 2p$_{1/2}$ | 162.91 | 163.01 | MoS$_2$, S$^{2-}$ |
| | 164.54 | 164.42 | MoS$_x$, S$^{2-}$ |
| | 170.53 | 170.35 | SO$_4^{2-}$ |
| S 2s | 225.78 | 225.87 | MoS$_2$ |
| | 226.73 | 226.72 | MoS$_x$ |
| O 1s | -- | 530.72 | MoO$_3$, O$^{2-}$ |
| | -- | -- | Organic C=O |
| | 532.13 | 532.17 | SO$_4^{2-}$ |
| | 532.69 | 533.49 | Organic C-O |

**Table S5.7:** XPS data and peak assignments for LS Mn SAs/1T-MoS$_2$ before and after collecting 3,000 CV scans

| Peak | LS Mn SAs/1T-MoS$_2$ | | Peak Assignment |
| --- | --- | --- | --- |
| | **Pre-CV** | **Post-CV** | |
| Mn 2p$_{3/2}$ | -- | -- | Mn$^{2+}$ |
| | -- | -- | Mn$^{2+}$ |
| | 641.52 | -- | Mn$^{3+}$ |
| | 643.12 | -- | Mn$^{3+}$ |
| Mn 2p$_{1/2}$ | -- | -- | Mn$^{2+}$ |
| | -- | -- | Mn$^{2+}$ |
| | 653.90 | -- | Mn$^{3+}$ |
| | 643.12 | -- | Mn$^{3+}$ |
| Mo 3d$_{5/2}$ | 229.01 | 229.01 | MoS$_2$, Mo$^{4+}$ |
| | 230.10 | 230.10 | MoS$_x$, Mo$^{5/6+}$ |
| | 232.91 | -- | MoO$_3$, Mo$^{6+}$ |
| Mo 3d$_{3/2}$ | 232.11 | 232.11 | MoS$_2$, Mo$^{4+}$ |
| | 233.20 | 233.20 | MoS$_x$, Mo$^{5/6+}$ |
| | 236.01 | -- | MoO$_3$, Mo$^{6+}$ |
| S 2p$_{3/2}$ | 161.97 | 161.99 | MoS$_2$, S$^{2-}$ |
| | 163.57 | 163.45 | MoS$_x$, S$^{2-}$ |
| | 169.27 | 169.03 | SO$_4^{2-}$ |
| S 2p$_{1/2}$ | 163.17 | 163.19 | MoS$_2$, S$^{2-}$ |
| | 164.77 | 164.65 | MoS$_x$, S$^{2-}$ |
| | 170.47 | 170.23 | SO$_4^{2-}$ |
| S 2s | 225.91 | 225.91 | MoS$_2$ |
| | 227.00 | 227.00 | MoS$_x$ |
| O 1s | 530.92 | -- | MoO$_3$, O$^{2-}$ |
| | 531.84 | 531.30 | Organic C=O |
| | 532.58 | 532.29 | SO$_4^{2-}$ |
| | 533.55 | 533.20 | Organic C-O |

**Table S5.8:** Electrochemical comparison of each sample evaluated in this dissertation

| Sample | d-orbital Occupation | Overpotential (mV *vs.* RHE) | Tafel slope (mV/dec) | $R_s$ ($\Omega$) | $R_{ct}$ ($\Omega$) | CPE-T | CPE-P |
|---|---|---|---|---|---|---|---|
| Pt/C | -- | 37 | 34.0 | -- | -- | -- | -- |
| 1T-MoS$_2$ | -- | 265 | 107.2 | 2.289 | 127.5 | 0.0247 | 0.923 |
| Zn SAs/1T-MoS$_2$ | $d^{10}$ | 177 | 84.9 | 2.191 | 18.41 | 0.00410 | 0.897 |
| HS Mn SAs/1T-MoS$_2$ | $d^5$ | 201 | 99.0 | 1.397 | 0.0186 | 0.767 | 0.972 |
| LS Mn SAs/1T-MoS$_2$ | $d^4$ | 241 | 106.4 | 0.125 | 1.292 | $5.72\times10^{-5}$ | 0.972 |
| Sc SAs/1T-MoS$_2$ | $d^0$ | 262 | 108.7 | 1.728 | 42.87 | 0.00830 | 0.611 |

## 5.8 References

17.     Shi, Y.; Zhou, Y.; Yang, D. R.; Xu, W. X.; Wang, C.; Wang, F. B.; Xu, J. J.; Xia, X. H.; Chen, H. Y., Energy Level Engineering of Mos2 by Transition-Metal Doping for Accelerating Hydrogen Evolution Reaction. **2017,** *139*, 15479-15485.

31.     Li, H.; Xiao, J.; Fu, Q.; Bao, X., Confined Catalysis under Two-Dimensional Materials. *Proc Natl Acad Sci U S A* **2017,** *114* (23), 5930-5934.

63.     Naumkin, A. V.; Kraut-Vass, A.; Gaarenstroom, S. W.; Powell, C. J., Nist X-Ray Photoelectron Spectroscopy Database. National Institute of Science and Technology: 2012; Vol. 20899, p 20899.

64.     Baker, M. A.; Gilmore, R.; Lenardi, C.; Gissler, W., Xps Investigation of Preferential Sputtering of S from Mos2 and Determination of Mosx Stoichiometry from Mo and S Peak Positions. *Applied Surface Science* **1999,** *150* (1-4), 255-262.

172.    Lei, S.; Wang, X.; Li, B.; Kang, J.; He, Y.; George, A.; Ge, L.; Gong, Y.; Dong, P.; Jin, Z.; Brunetto, G.; Chen, W.; Lin, Z.-T.; Baines, R.; Galvão, D. S.; Lou, J.; Barrera, E.; Banerjee, K.; Vajtai, R.; Ajayan, P., Surface Functionalization of Two-Dimensional Metal Chalcogenides by Lewis Acid–Base Chemistry. *Nature Nanotechnology* **2016,** *11* (5), 465-471.

180.    Yang, D.-Q.; Sacher, E., S-P Hybridization in Highly Oriented Pyrolitic Graphite and Its Change on Surface Modification, as Studied by X-Ray Photoelectron and Raman Spectroscopies. *Surface Science* **2002,** *504*, 125-137.

181.    Housecroft, C.; Sharpe, A. G., *Inorganic Chemistry*. 4th Ed ed.; Pearson: 2012.

182.    Zhang, W.; Fu, Q.; Luo, Q.; Sheng, L.; Yang, J., Understanding Single-Atom Catalysis in View of Theory. *JACS Au* **2021,** *1* (12), 2130-2145.

183.    Gong, Y.-N.; Zhong, W.; Li, Y.; Qiu, Y.; Zheng, L.; Jiang, J.; Jiang, H.-L., Regulating Photocatalysis by Spin-State Manipulation of Cobalt in Covalent Organic Frameworks. *Journal of the American Chemical Society* **2020,** *142* (39), 16723-16731.

184.    Li, Y.; Ji, Y.; Zhao, Y.; Chen, J.; Zheng, S.; Sang, X.; Yang, B.; Li, Z.; Lei, L.; Wen, Z.; Feng, X.; Hou, Y., Local Spin-State Tuning of Iron Single-Atom Electrocatalyst by S-Coordinated Doping for Kinetics-Boosted Ammonia Synthesis. *Advanced Materials* **2022,** *34* (28), 2202240.

185.    Rajapakse, M.; Karki, B.; Abu, U. O.; Pishgar, S.; Musa, M. R. K.; Riyadh, S. M. S.; Yu, M.; Sumanasekera, G.; Jasinski, J. B., Intercalation as a Versatile Tool for Fabrication, Property Tuning, and Phase Transitions in 2d Materials. *Npj 2d Mater Appl* **2021,** *5* (1).

186.    Bonke, S. A.; Risse, T.; Schnegg, A.; Bruckner, A., In Situ Electron Paramagnetic Resonance Spectroscopy for Catalysis. *Nature Reviews Methods Primers* **2021,** *1*.

187.    Singh, M. K.; Chettri, P.; Tripathi, A.; Tiwari, A.; Mukherjee, B.; Mandal, R. K., Defect Mediated Magnetic Transitions in Fe and Mn Doped Mos$_2$. *Physical Chemistry Chemical Physics* **2018,** *20* (23), 15817-15823.

188.    Biesinger, M. C.; Payne, B. P.; Grosvenor, A. P.; Lau, L. W. M.; Gerson, A. R.; Smart, R. S. C., Resolving Surface Chemical States in Xps Analysis of First Row Transition Metals, Oxides and Hydroxides: Cr, Mn, Fe, Co and Ni. *Applied Surface Science* **2010,** *257* (7), 2717-2730.

189.    Jacobson, A. J., *Intercalation Chemistry*. Academic Press, Inc.: 1982.

190.    Tran, P. D.; Thu; Orio, M.; Torelli, S.; Truong, Q. D.; Nayuki, K.; Sasaki, Y.; Sing; Yi, R.; Honma, I.; Barber, J.; Artero, V., Coordination Polymer Structure and Revisited Hydrogen Evolution Catalytic Mechanism for Amorphous Molybdenum sulfide. *Nature Materials* **2016,** *15* (6), 640-646.

191.    Busetto, L.; Vaccari, A.; Martini, G., Electron Spin Resonance of Paramagnetic Species as a Tool for Studying the Thermal Decomposition of Molybdenum Trisulfide. *The Journal of Physical Chemistry* **1981,** *85* (13), 1927-1930.

192.    Bensimon, Y.; Belougne, P.; Giuntini, J. C.; Zanchetta, J. V., Electron Spin Resonance of Water Adsorption on Amorphous Molybdenum Sulfide. *The Journal of Physical Chemistry* **1984,** *88* (13), 2754-2757.

193.    Laursen, A. B.; Kegnæs, S.; Dahl, S.; Chorkendorff, I., Molybdenum Sulfides—Efficient and Viable Materials for Electro - and Photoelectrocatalytic Hydrogen Evolution. *Energy & Environmental Science* **2012,** *5* (2), 5577.

194.    Mei, B.-A.; Munteshari, O.; Lau, J.; Dunn, B.; Pilon, L., Physical Interpretations of Nyquist Plots for Edlc Electrodes and Devices. *The Journal of Physical Chemistry C* **2018,** *122* (1), 194-206.

195.    Benson, E. E.; Zhang, H.; Schuman, S. A.; Nanayakkara, S. U.; Bronstein, N. D.; Ferrere, S.; Blackburn, J. L.; Miller, E. M., Balancing the Hydrogen Evolution Reaction, Surface Energetics, and Stability of Metallic Mos$_2$ Nanosheets Via Covalent Functionalization. *Journal of the American Chemical Society* **2018,** *140* (1), 441-450.

# CHAPTER 6: Recommendations for Future Work

## 6.1 Introduction

The goal in this chapter is to identify remaining experiments that would be worth exploring. Likewise, future research directions of this project that may be of interest to future generations of graduate students continuing this research are discussed.

### 6.1.1 Further Magnetic Analysis of 1T-MoS$_2$ Intercalated HS and LS Mn SAs

Based on the results discussed in Chapter 5, further analysis of the magnetic properties of HS Mn SAs/1T-MoS$_2$ and LS Mn SAs/1T-MoS$_2$ is necessary to truly understand the magnetic interactions occurring between the Mn SAs and 1T-MoS$_2$. In Fall 2022, a new graduate student joined Dr. Gu's research group with the intention of continuing my research project. I have mentored her for the last year and have trained her to successfully continue these studies. Likewise, in-depth DFT analysis of the magnetic interactions between the substrate and intercalants, along with changes in kinetic properties related to the effects of confining Mn SAs in each type of spin state, will be vital to fully understand the results reported herein. Collaborations with our colleagues in Dr. Xiangheng Xiao's research group at Wuhan University to perform these calculations are already underway. Once these studies are complete, we intend to publish the findings reported in Chapter 5 so that the knowledge gained from our discoveries may benefit our scientific community.

### 6.1.1 Chiral-Induced Spin Selectivity (CISS)

The most attractive aspect of quantum confinement involves the ability to manipulate the electronic and optical properties of materials when they reach the nanoscale. Compared to bulk

materials, the enhancement of these properties observed in nanomaterials is highly sought after to achieve next-generation devices for quantum information science, smart materials, and semiconductors.[196-198]

Similarly, the discovery of CISS has exposed the ability to manipulate spin orientation in chiral molecules in the absence of magnetic fields, which enables the development of novel spintronic applications in next-generation devices.[199] As low-symmetry molecules that lack inversion and mirror symmetry, chiral molecules often exhibit unique optical properties with respect to circular polarization. Therefore, in the next phase of this research project, Dr. Gu is interested in marrying these two concepts and pursuing the intercalation of chiral molecules within 2D substrates.

### 6.1.2 Spatial Confinement of Chiral Molecules within 1T-MoS$_2$

2D materials such as 1T-MoS$_2$ provide an ideal platform for spatial confinement of chiral molecules due to the non-bonding van der Waals forces that exist between layers of nanosheets. These unique van der Waals gaps allow guest species to intercalate between layers without breaking the in-plane crystalline ordering of the nanosheets' covalently-bonded atomic layers.[200] Synthetic methods of 2D materials intercalated with chiral molecules are similar to those that were employed in this thesis work, such as syringe injection synthesis.

Preliminary research conducted thus far involves spatial confinement of R-methylbenzylamine or S-methylbenzylamine within the van der Waals gaps of 1T-MoS$_2$ (**Figure**
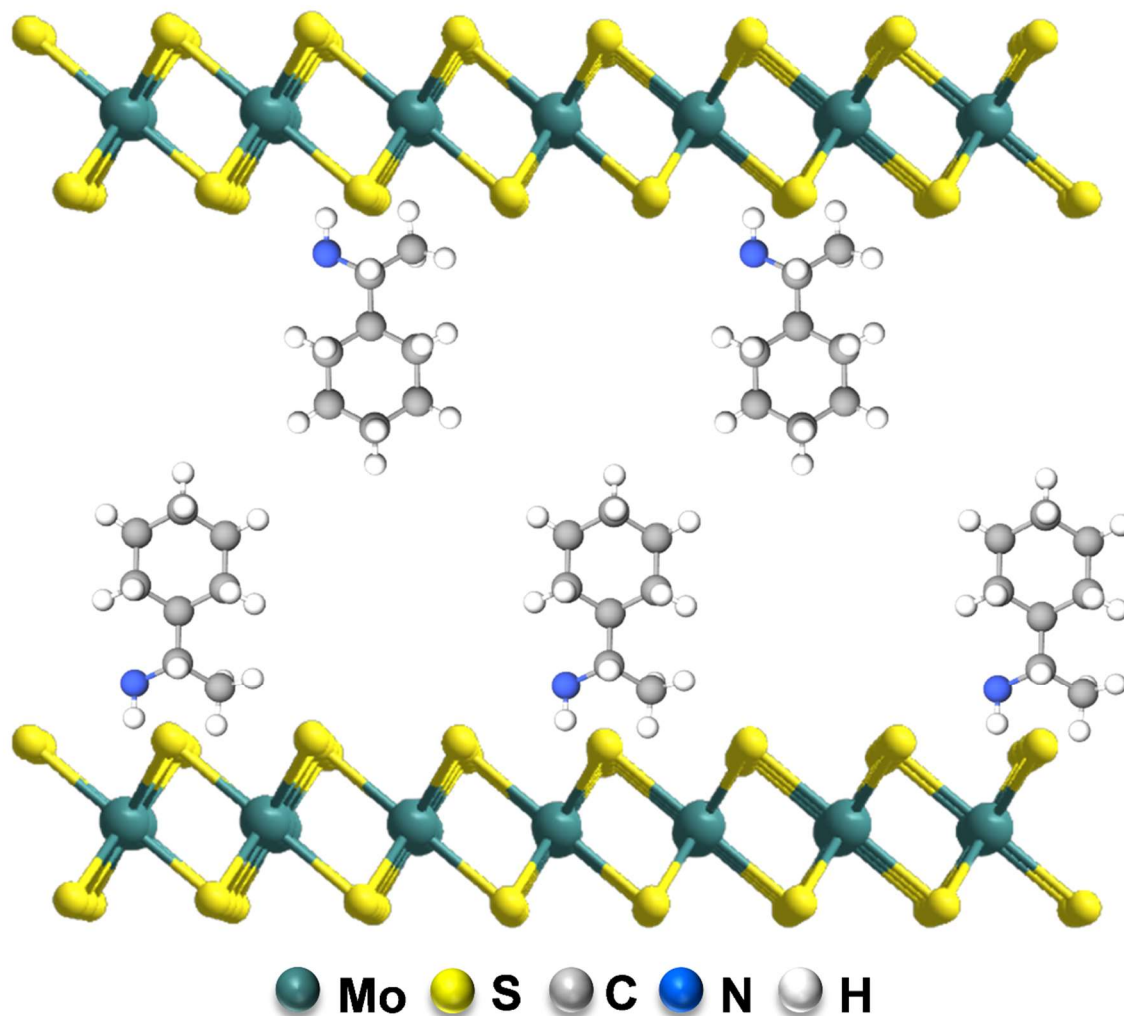
**Figure 6.1**: Schematic drawing of 1T-MoS$_2$ intercalated with methylbenzylamine. In R-methylbenzylamine, -NH$_2$ points into the screen. In S-methylbenzylamine, -NH$_2$ points out of the screen.

**6.1**). Characterization is in the preliminary stage and will include techniques such as XRD, STEM, CD, Raman spectroscopy, and UV-Vis spectroscopy. These techniques will elucidate changes in interlayer spacing, confirm the direction of circularly polarized light induced by the heterostructure, identify changes in interlayer interactions or identify phase changes in the bulk material if they arise, and identify excitonic transitions from the valence band to the conduction band in the 2D substrate.

*6.3 Impact of Chiral Molecular Intercalation on 2D Properties*

A vital detail of the future work proposed in this chapter involves the potential applications of the proposed future work. One of the key aspects that influences the efficiency of electrochemically-driven catalytic reactions involves electron transport. The reaction rate driving catalytic reactions is highly dependent on the speed at which electrons can move through the electrochemical circuit. Thanks to recent advances in the CISS effect, the efficiency of electron transport through chiral molecules, which depends on the electron's spin, was found to change with the enantiomeric form of the chiral molecule and the direction of the electron's linear momentum.[201] Therefore, we hypothesize that controlling the enantiomeric form of the chiral molecule confined within active site microenvironments may allow the catalyst's reaction kinetics to be altered/enhanced accordingly. It is important to note that since this concept arises from small spin-orbit coupling contributions, there are some concerns that this spin contribution to the total angular momentum of molecular collisions is not effective enough to control chemical processes.[202] While this view is valid for achiral molecules, recent experiments have shown that chiral catalysts display prominent spin selectivity effects.[203] Specifically, they demonstrated spin-selective electron transport through chiral films adsorbed on electrodes.

Another potential application involves incorporating CISS effects into solar energy conversion processes. Molecules that form long-lasting charge-separated states via photo-induced electron transfer are ideal systems for artificial photosynthesis.[204] Intercalating chiral molecules into catalytic substrates has the potential to enhance charge separation, which in turn could enhance charge collection and PEC-driven reactions such as HER. These examples are just a taste of the potential applications that hybridizing CISS effects with confinement effects could have in the field of catalysis and beyond.

## 6.2 Conclusion

Future research directions related to confinement of guest species for enhanced electronic and/or optical properties of 2D materials are discussed in this chapter. The primary research gaps to be addressed include further DFT analysis and experimental magnetic studies of HS and LS Mn SAs under 1T-MoS$_2$ confinement to provide new insights into the catalytic and electronic effects of confining guest metals with differing spin states within the local microenvironments of 1T-MoS2 active sites. Likewise, a brief discussion of future research directions involving chiral molecular intercalation into 2D lattice structures is provided.

## 6.3 Acknowledgements

Chapter 6 contains unpublished material describing future directions in this field. The dissertation author was the primary author of this chapter.

## 6.3 References

196.    Liu, X.; Hersam, M. C., 2d Materials for Quantum Information Science. *Nature Reviews Materials* **2019,** *4* (10), 669-684.

197.    Wilson, N. P.; Yao, W.; Shan, J.; Xu, X., Excitons and Emergent Quantum Phenomena in Stacked 2d Semiconductors. *Nature* **2021,** *599* (7885), 383-392.

198.    Yu, X.; Cheng, H.; Zhang, M.; Zhao, Y.; Qu, L.; Shi, G., Graphene-Based Smart Materials. *Nature Reviews Materials* **2017,** *2* (9), 17046.

199.    Qian, Q.; Ren, H.; Zhou, J.; Wan, Z.; Zhou, J.; Yan, X.; Cai, J.; Wang, P.; Li, B.; Sofer, Z.; Li, B.; Duan, X.; Pan, X.; Huang, Y.; Duan, X., Chiral Molecular Intercalation Superlattices. *Nature* **2022,** *606* (7916), 902-908.

200.    Chhowalla, M.; Shin, H. S.; Eda, G.; Li, L.-J.; Loh, K. P.; Zhang, H., The Chemistry of Two-Dimensional Layered Transition Metal Dichalcogenide Nanosheets. *Nature Chemistry* **2013,** *5* (4), 263-275.

201.    Naaman, R.; Paltiel, Y.; Waldeck, D. H., Chiral Induced Spin Selectivity Gives a New Twist on Spin-Control in Chemistry. *Accounts of Chemical Research* **2020,** *53* (11), 2659-2667.

202.    Kalogerakis, K. S.; Zare, R. N., Energy and Angular Momentum Control of the Specific Opacity Functions in the Ba+Hi→Bai+H Reaction. *The Journal of Chemical Physics* **1996,** *104*, 7947-7964.

203.    Bloom, B. P.; Lu, Y.; Metzger, T.; Yochelis, S.; Paltiel, Y.; Fontanesi, C.; Mishra, S.; Tassinari, F.; Naaman, R.; Waldeck, D. H., Asymmetric Reactions Induced by Electron Spin Polarization. *Physical Chemistry Chemical Physics* **2020,** *22* (38), 21570-21582.

204.    Hore, P. J.; Ivanov, K. L.; Wasielewski, M. R., Spin Chemistry. *The Journal of Chemical Physics* **2020,** *152*.